The University Of Sheffield.

On the use of the Theory of Critical Distances to design notched metallic components against dynamic loading

By:

Taixiang Yin

A thesis submitted in partial fulfilment of the requirements for the degree of Doctor of Philosophy

The University of Sheffield
Faculty of Engineering
Department of Civil and Structural Engineering

28 February 2017

Contents

List of Figures

List of Tables

Acknowledgements

I would like to take this opportunity to express my deepest gratitude to my supervisors Prof. Luca Susmel and Prof. Andrew Tyas for their persistent encouragement, guidance, support and for giving me the opportunity to pursue my doctoral studies under their supervision. I would also like to thank my parents for their crucial financial, love and support during my study, which is beyond my word.

Nomenclature

a	The half of crack length
A	Instantaneous area of cross-section
A_g	Gross section
A_n	Net section
A_o	Original area of cross-section
b	Burgers Vector
d	distance from notch tip
d_g	Gross diameter
d_n	Net diameter
D	Notch depth
D_f	Failure displacement
E	Young's modulus
F	Remote axial force
F_f	Failure force
$\dot{F}$	Nominal loading rate
EPFM	Elasto-plastic fracture mechanics
G	The energy release rate
G_c	The critical energy release rate
J	J integral
J_c	The critical value of J intgral
K	Stress intensity factor
K_C	Fracture toughness (Critical stress intensity factor)

K_{cm}	Measured fracture toughness using a notch of finite root radius instead of a crack
K_I	Stress intensity factor (mode I loading)
K_{IC}	Fracture toughness (model I loading)
K_{Id}	Dynamic fracture toughness
$K_{Id,c}$	Dynamic fracture toughness
K_t	Stress concentration factor of a notch
K_{tg}	Gross stress concentration factor
K_{tn}	Net stress concentration factor
K_σ	Effective stress concentration factor
K_ε	Effective strain concentration factor
$\dot{K}$	Stress intensity factor rate
l	Instantaneous length
l_o	Original length
L	The critical distance
LEFM	Linear elastic fracture mechanics
LM	The line method
N	Element size
PM	The point method
r	Distance measured from the point of maximum stress for any stress concentration feature
r_n	Notch root radius
r_p	The further extension of the plastic zone size
r_y	The plastic zone size

T	Working temperature
T_1	Transition temperature
T_{room}	Room temperature
T_{melt}	Melting temperature
T_f	Failure time
T^*	Homologous temperature
v_d	Dynamic safety factor
W	Width of component
W_g	Gross width
W_n	Net width
$\dot{Z}$	Denoting loading rate, strain rate, displacement rate and stress intensity factor rate
α	Notch angle
σ	Uniform remote tensile stress
σ_f	Failure strength: the nominal stress to cause brittle fracture in a cracked body
σ_{eff}	Effective stress
$\sigma_{g,nom}$	Gross nominal stress
$\sigma_{L,eff}$	Local effective stress
σ_{max}	Maximum stress
$\sigma_{n,nom}$	Net nominal stress
σ_{nom}	Nominal stress
σ_o	Material inherent strength used with the PM and LM
σ_{true}	True stress
σ_{UTS}	Ultimate tensile strength

σ_{xx}	Stress in x direction
σ_{ys}	Yield strength
σ_{yy}	Stress in y direction
$\bar{\sigma}_{VM}$	Plain Von Mises strength
$\bar{\sigma}_{0,VM}$	Inherent material V-M strength
ε_f	Failure strain
ε_{EPS}	Effective plastic strain
ε_{nom}	Nominal strain
$\dot{\varepsilon}$	Strain rate
$\dot{\varepsilon}_{L,eff}$	Local effective strain rate
$\dot{\varepsilon}_{nom}$	Nominal strain rate
$\bar{\varepsilon}^p$	Effective plastic strain in Jonson-Cook material model constitutive law
$\dot{\bar{\varepsilon}}^p$	Effective plastic strain rate in Jonson-Cook material model constitutive law
$\dot{\varepsilon}^*$	Normalized effective strain rate
τ	Shear stress
Δ	Displacement
$\dot{\Delta}$	Nominal displacement rate
$\dot{\Delta}_f$	Displacement rate at time of failure
ρ	Square root of notch radius
$\emptyset$	Diameter

Abstract

The Theory of Critical Distances (TCD) is a well-known design method allowing the strength of notched/crack components to be estimated accurately by directly post-processing the entire linear elastic stress fields damaging the material in the vicinity of the stress raisers being designed. By taking full advantage of the TCD's unique features, in this thesis the TCD is reformulated to make it suitable for predicting the strength of notched metallic materials subjected to dynamic loading by post-processing both linear elastic and elasto-plastic stress distributions. The accuracy and reliability of the proposed reformulation of the linear elastic TCD was checked against a number of experimental results generated by testing, under different loading/strain/displacement rates, notched cylindrical samples of aluminium alloy 6063-T5, titanium alloy Ti－6Al－4V, aluminium alloy AlMg6, and an AlMn alloy. To further validate the proposed design method also different data sets taken from the literature were considered. Such an extensive validation exercise allowed us to prove that the proposed reformulation of the TCD is successful in predicting the dynamic strength of notched metallic materials falling within an error interval of $\pm 20\%$. Such a high level of accuracy is certainly remarkable, especially in light of the fact that it was reached without the need for explicitly modelling the stress vs. strain dynamic behaviour of the investigated ductile metals. Additionally, the FEM with Simplified-Johnson Cook elasto-plastic material model was used to predict the dynamic strength of notched metallic material falling within an error interval of $\pm 20\%$. Moreover, the elasto-plsastic TCD was also provided to be capable of predicting the dynamic strength of notched metallic materials falling within an error interval of $\pm 6\%$.

Introduction

Since about the beginning of the last century, the behaviours of engineering materials subjected to high rates of loading has been investigated by many researchers. The international scientific community has made a tremendous effort to understand and model the mechanical/cracking behaviour of engineering materials subjected to high rates of loading. In situations of practical interest (such as car crashes, forging and rolling, and sudden impacts as shown in Figure 1), many engineering components and structures containing notches are widely used in everyday products, which have to be designed to withstand high rates of loading. In light of the importance of this complex structural engineering problem. This large body of work shows that this problem has been extensively addressed by tackling it both from an experimental and a theoretical angle.

Figure 1 Example of car crash test.

According to the effort done by international scientific community, we can conclude that, at room temperature, the failure stress tends to change with an increase in the loading/strain/displacement rate; this holds true for the majority of metallic materials (Lindholm, 1964, Lindholm et al., 1971, Oosterkamp et al., 2000, Lee and Kim, 2003, Zhang et al., 2008, Sakino, 2008, Wiesner and MacGillivray, 1999). Moreover, according to the studies about structural integrity analysis (Pilkey, 2008), it is also can be found that stress concentration phenomena have significant influence on a material's behaviour, the notches in structural components could affect the generation of dislocations locally. However, in spite of knowledge which is available to structural engineers engaged in designing real structures containing various stress raisers against dynamic loading, only a few studies can be found in the technical literatures which investigate the behaviour of notched samples subjected to high rates of loading (Noda et al., 2015). Examination of the state of the art shows that a commonly accepted design strategy has not yet been agreed by the international scientific community to design dynamic strength of notched samples.

It is well known that under quasi-static loading, notches have a detrimental effect on the overall static strength of engineering materials. Accordingly, appropriate design methods have to be used to accurately design components experiencing stress concentration phenomena. In this context, it is recognised that the so-called Theory of Critical Distances (TCD) is the most effective tools which can be used by structural engineers to take into account the weakening effect of notches of all kinds.

Independently from the structural integrity ambit in which it is used, the most important feature of the TCD is that, similar to other existing local approaches (Berto and Lazzarin, 2014, Vartnica et al, 2010), this theory is seen to be capable of accommodating any kind of material non-linarites into a linear- elastic framework, this allowing the time and costs associated with the design process to be reduced remarkably (Susmel and Taylor, 2004). Another important aspect which is worth being mentioned is that, by nature, the TCD can be calibrated by using pieces of experimental information generated via conventional testing equipment.

Aims:

Owing to its unique features, in this complex scenario, the challenging aims of this thesis is to reformulate the linear-elastic TCD to make it suitable for designing notched metallic components under dynamic loading, the material behaviour being, by nature, highly non-linear. Additionally, elasto-plastic simulation and elasto-plastic Theory of Critical Distances are also been used to assess the dynamic strength of notched metallic material.

Objectives:

In order to achieve these aims, we need to complete the following **objectives**, which are

- To understand the fundamental theory of the Theory of Critical Distances methods and its applications.
- To understand the dynamic material behaviours by testing two series of aluminium alloy 6063-T5 notched samples at University of Sheffield Buxton laboratory.
- To reformulate the linear elastic Theory of Critical distances method and make it suitable of estimating the dynamic material strength of tested material samples by post-processing linear elastic stress distributions with the help of FEM simulations.
- With the help of elasto-plastic FE modelling, to reuse the reformulated Theory of Critical Distances by post-processing elasto-plastic stress distributions to estimate the dynamic material strength of tested material samples
- To make suggestions for further research.

Methodologies:

In this thesis, the FEM will be used to produce linear elastic stress fields for tested samples, and the linear elastic Theory of Critical Distances (TCD) will be reformulated to predict the dynamic strength of metallic material components having different stress raisers. Additionally, FEM elasto-plastic simulations will be carried out to estimate the dynamic strength of notched metallic components, and the elasto-plastic Theory of Critical Distances will be conducted to predict the dynamic strength of notched samples.

Outline of the thesis:

The content of this thesis will be structured as follows: in Chapter 1, fundamental concepts including stress–strain definition, the dynamic behaviour of plain and notched materials, stress concentration phenomena and the development of fracture mechanics will be briefly introduced. Chapter 2 describes the basis of the theory of critical distance (TCD) and its application under quasi-static conditions. Chapter 3 includes the experimental data from tests carried out at the University of Sheffield and in the laboratory of the Institute of Continuous Media Mechanics UB RAS, Perm, Russia. In Chapter 4, a novel reformulation of the linear-elastic TCD suitable for designing notched metallic materials against dynamic loading will be proposed and validated by using the experimental results described in Chapter 3. Chapter 5 summarises the results from the elasto-plastic simulations performed by using commercial code LS-DYNA, whilst Chapter 6 investigates the accuracy of the elasto-plastic FE solutions in predicting the dynamic strength of the notched specimens being tested. Finally, Chapter 7 gives the discussion and conclusion to the whole thesis.

References

LEE, O. S. & KIM, M. S. 2003. Dynamic material property characterization by using split Hopkinson pressure bar (SHPB) technique. *Nuclear Engineering and Design,* 226**,** 119-125.

LINDHOLM, U. S. 1964. Some experiments with the split hopkinson pressure bar. *Journal of the Mechanics and Physics of Solids,* 12**,** 317-335.

LINDHOLM, U. S., BESSEY, R. L. & SMITH, G. V. 1971. Effect of Strain Rate on Yield Strength, Tensile Strength, and Elongation of Three Aluminium Alloys. *J Mater,* 6**,** 119-133.

NODA, N. A., OHTSUKA, H., ZHENG, H., SANO, Y., ANDO, M., SHINOZAKI, T. & GUAN, W. 2015. Strain rate concentration and dynamic stress concentration for double-edge-notched specimens subjected to high-speed tensile loads. *Fatigue & Fracture of Engineering Materials & Structures,* 38**,** 125-138.

OOSTERKAMP, L. D., IVANKOVIC, A. & VENIZELOS, G. 2000. High strain rate properties of selected aluminium alloys. *Materials Science and Engineering: A,* 278**,** 225-235.

PILKEY, W. D. 2008. *Peterson's stress concentration factors,* Hoboken, N.J., Hoboken, N.J. : John Wiley, c2008.

SAKINO, K. 2008. Strain rate dependence of dynamic flow stress of 2017 aluminum alloy at very high strain rates. *International Journal of Modern Physics B,* 22**,** 1209-1214.

WIESNER, C. S. & MACGILLIVRAY, H. 1999. Loading Rate Effects on Tensile Properties and Fracture Toughness of Steel. *1999 TAGSI Seminar, Cambridge, IoM Publication***,** 149.

ZHANG, X. M., LI, H. J., LI, H. Z., GAO, H., GAO, Z. G., LIU, Y. & LIU, B. 2008. Dynamic property evaluation of aluminum alloy 2519A by split Hopkinson pressure bar. *Transactions of Nonferrous Metals Society of China (English Edition),* 18**,** 1-5.

Chapter 1 Fundamental Concepts

1.1 Introduction

Because it has the advantages of being lightweight, durable and ductile, the use of metallic material has increased dramatically during the last century. 'Material mechanical properties' is the term for a material's response to applied loading. A material's mechanical properties and limitations must be well understood by engineers in order to select the right material for a specific application (Ashby and Jones, 1996, Sharma, 2003). Material mechanical properties are classified into two categories: structure-sensitive properties and structure-insensitive properties. Specifically, structure-sensitive properties include yield strength, tensile strength, ductility, fracture toughness, etc., all of which are dependent on a material's microstructure. Structure-insensitive properties include elastic modulus, Poisson's ratio, density, etc. (Ashby and Ashby, 1998, Sharma, 2003, Groover, 2010). Mechanical properties are very important information that can be used to determine a material's behaviour when subjected to all types of external forces. It can be measured by a basic relationship called a stress–strain curve. Before continuing, it is worth giving definitions of stress and strain.

1.2 Stress/strain: basic definitions

Stress and strain are the most fundamental quantities that are used to describe the response of an object subjected to applied loads (Brinson and Brinson, 2015). Specifically, stress is defined as internal force per unit area, while strain is a dimensionless quantity that expresses the relative change per unit length of an object due to the deformation caused by externally applied forces. Normally, there are three kinds of stresses: tensile, compressive and shear. Tensile stress is the force per unit area when the object is pulled apart, whereas the compressive stress is opposite to tensile stress, rather than stretching, it tends to squeeze the object. Shear refers to stresses which are caused by forces parallel to the area (Groover, 2010).

The stress–strain relationship is the most important measure of a material's mechanical properties. It has been used extensively by researchers and designers in order to understand the response of a material to applied forces. Therefore, determining the stress–strain status of a structural component is a very important procedure in studying a material's behaviour. In order to obtain stress–strain curves, the tensile test is the most commonly used method in determining stress–strain relationships and choosing materials for engineering applications (Groover, 2010, Testing and Materials, 2015)

For example, Figure 1.1(a) shows a homogeneous cylindrical bar loaded by a remote axial force, F, that is applied at both ends. According to the equilibrium diagram shown Figure 1.1(b), the nominal (or engineering stress), σ_{nom}, can be expressed as follows:

$$\sigma_{nom} = F/A_o \quad (1.1)$$

The corresponding nominal (or engineering) strain, ε_{nom}, can be calculated using Equation (1.2):

$$\varepsilon_{nom} = (l - l_o)/l_o \quad (1.2)$$

where A_o and l_o indicate the original area of the cross-section and original length before the bar was loaded. l is the instantaneous length during deformation.

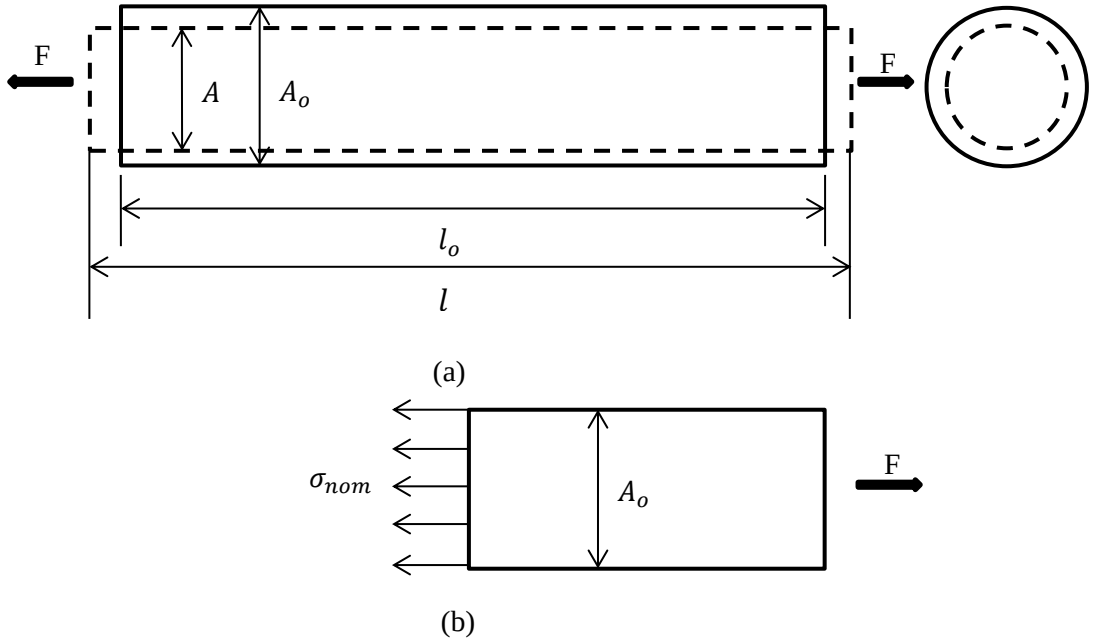

Figure 1.1 Homogeneous plate loaded in tension.

If the instantaneous area of the cross-section and length of the bar during deformation are used instead of the original values, as the dashed-line shows in Figure 1.1, the values of the stress and strain components will be different from the ones calculated from Equations (1.1) and (1.2); we call these *true stress* and *true strain*, which can be expressed as follows:

$$\sigma_{true} = F/A \quad (1.3)$$

$$\varepsilon_{true} = \ln(l/l_o) \quad (1.4)$$

where A indicates the instanteous area of the cross-section when the sample is stretching. Generally speaking, the nominal stress–strain curves and true stress–strain curves are plotted as shown in Figure 1.2, and it is easy to calculate the elastic modulus, material yield strength and material ultimate strength from this figure.

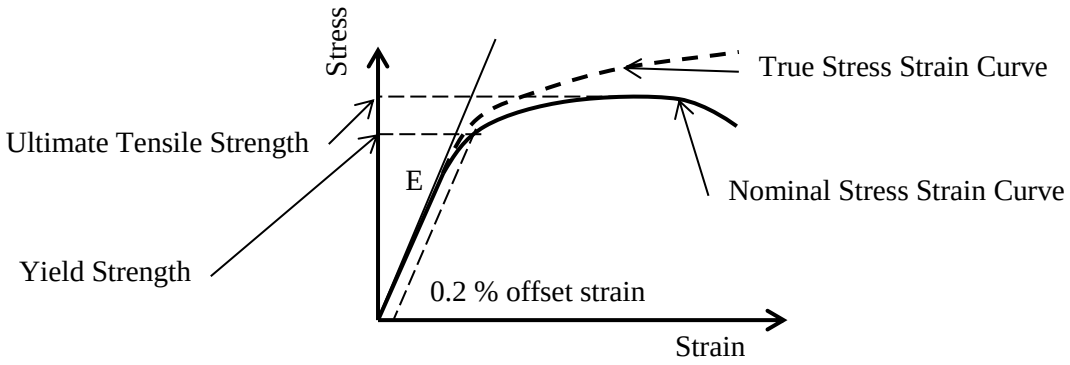

Figure 1.2 Nominal and true stress strain curves.

In order to understand the material mechanical properties of metallic materials and the plastic deformation mechanism from a fundamental level, we need to understand the material at the microstructural level. This will be introduced briefly in the next section.

1.3 Material microstructure and deformation mechanisms

Metallic materials are generally held together by metallic or covalent bonds theoretically, these can provide a high modulus for the metals. However, the stiffness of the metallic bonds cannot completely explain the metal's strength, atomic arrangement is another important factor that influences a metal's stiffness (Ashby and Jones, 1996). In terms of the atomic arrangement in metallic materials, Ashby and Jones used a simple and intuitive way to pack the atoms into two-dimensional close-packed planes before stacking these planes on top of one another to generate a perfect three-dimensional crystal (Ashby and Jones, 1996). The majority of metals follow the least energy principle when their crystal structures are formed by tacking the close-packed patterns together in a repeating and regular way. Normally, two different crystal structures can be obtained by stacking the close-packed pattern in two different sequences for metals. These sequences are face-centred cubic (f.c.c.) and close-packed hexagonal (c.p.h.) as shown in Figures 1.3 (a) and (b).

Specifically, the crystal structure of Al, Cu and Ni have an f.c.c. structure, whereas Mg, Zn and Ti are made up of a c.p.h. crystal structure (Ashby and Jones, 1996). Another important crystal structure called body-centred cubic (b.c.c.) (as shown in Figure 1.3 (c)) provides less density to the crystal structure than the two close-packed structures (f.c.c. and c.p.h.). The close-packed plane with three directions makes the best use of space for crystal structures. Therefore, the density of a crystal with close-packed planes is higher than one without it. Generally speaking, due to their close-packed structures and heavy atoms, metals have higher densities than other materials such as polymers and ceramics.

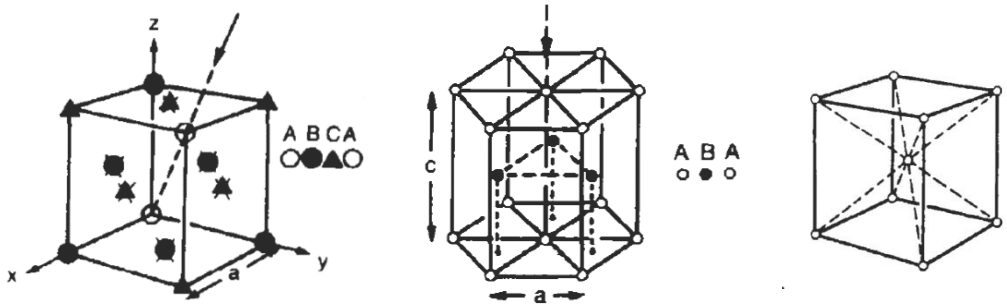

(a) f.c.c. crystal structure (b) c.p.h. crystal structure (c) b.c.c. crystal structure

Figure 1.3 Visualisation of the atomic positions in a unit cell for three different types of crystal structure (Ashby and Jones, 1996).

According to the theoretical calculation of the strength of a perfect crystal that has been carried out by Ashby and Jones (1996), we have learned that if the crystal structure of a metal is assembled by stacking the atoms together in a perfect pattern, the material will have an ideal strength. However, such a perfect crystal is impossible to find in nature. In reality, the calculated value of the theoretical strength of a material is much higher than the actual strength of the material tested in the laboratory (Ashby and Jones, 1996). Hence, there must be some defects which exist in the crystal structure of metallic materials that reduce material strength. This can give a proper explanation about the mechanism of material plastic deformation.

1.3.1 Dislocations

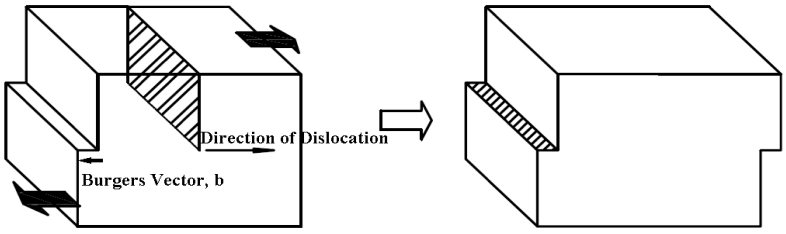

(a) Edge dislocation

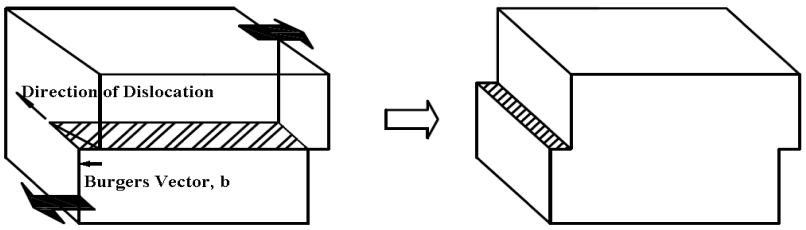

(b) Screw dislocation

Figure 1.4 Two types of dislocation: (a) edge dislocation; and (b) screw dislocation.

A dislocation is a linear defect which can reduce the required stress level for plastic deformation dramatically. Basically, the migration of a dislocation inside a crystal structure is explained as a

plastic carrier for material components when the applied load exceeds the material yield stress, and its presence has a significant effect on the material mechanical properties.

The dislocation concept was first mentioned by Volterra (1907), and thereafter it was used and developed as a defect inside a material by Orowan (1934), Taylor (1934) and Polanyi (1934) in 1934. These papers give full explanations of the plastic deformation of ductile materials by referring to the dislocation concept (Taylor, 1934, Orowan, 1934, Polanyi, 1934). There are two primary types of dislocations: edge dislocations and screw dislocations, which are demonstrated in Figure 1.4.

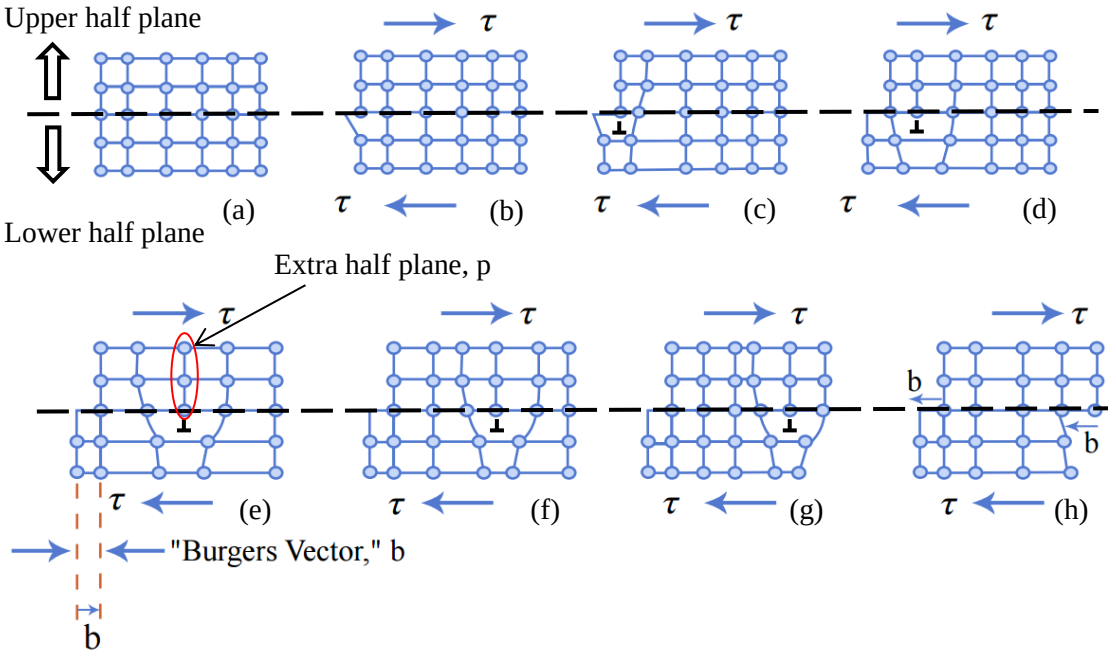

Figure 1.5 Migration of an edge dislocation through a crystal (Ashby and Jones, 1996).

Figure 1.5 shows the process of atomic rearrangement of an edge dislocation passing through a crystal when a shear force τ is applied parallel to the dislocation line, resulting in plastic deformation. The edge dislocation in this crystal is visualised as the edge of a half plane (the extra half plane p shown in Figure 1.5(e)) of atoms inserted into the upper half of the crystal (Ashby and Jones, 1996, Jaswon and El-Damanawi, 1991). When the shear force τ is applied, the dislocation starts to move through the crystal structure and the atoms in the line of the dislocation slip over each other. When the dislocation migrates across the crystal, the lower half plane is forced with respect to the upper half plane by a vector slip b (as shown in Figure 1.5(h)), which is called the Burgers vector of the dislocation (Ashby and Jones, 1996, Morris, 2001).

In general, edge and screw dislocations are two components which in reality can act simultaneously inside the material. Due to the existence of these defects inside real materials,

extra behaviours can be observed when a very high strain rate loading is applied to the component, such as the appearance of dislocation movement, twinning, adiabatic shear banding, the transition from plastic flow (the mobility of dislocation density) to plasticity (the dislocation and twin generation, which are generated by the shock front) and so on. All of these additional deformation features might be considered as the causes for different responses between static and dynamic loading. As observed by Armstrong and Walley (2008), dislocation mechanics dominate the high loading rate sensitivity of flow stress in metals and alloys. For example, some may argue that the dislocation evolution is enhanced by the increase of strain rate, because under high strain rate loading, more dislocations accumulation will increase the work-hardening rate (Liang et al., 2015). In next section, material behaviours under high rates of loading will be discussed in detail.

1.4 Dynamic behaviour of plain materials

Since about the beginning of the last century, the international scientific community has made a tremendous effort to understand and model the mechanical/cracking behaviour of engineering materials subjected to high rates of loading. For example, In 1914, Hopkinson (1914) developed the Hopkinson pressure bar, which is suitable for measuring the impulse and pressure generated by the impact of bullets or the detonation of explosives. Thirty years later, Davies (1948) revisited Hopkinson's pressure bar method, developing the theoretical basis of the wave propagation analysis required to understand the results, and introducing electronic measurement of the stress waves in the bar. In 1949, Kolsky (1949) developed what has become known as the Split-Hopkinson Pressure Bar or Kolsky bar test, in which a small sample of material is sandwiched between the ends of two long cylindrical bars. When an axial dynamic load is induced in one bar, this partially reflects and partially transmits through the sample. By analysing the incident, reflected and transmitted waves, Kolsky showed that it is possible to determine the dynamic stress, strain and strain rate which the specimen experiences during the loading phase.

This pioneering work has been followed by a multitude of subsequent investigations further confirming the validity of Kolsky's findings, that generally, the mechanical behaviour of metallic materials is strain rate dependent. There are a number of experimental studies (Lindholm, 1964, Lindholm et al., 1971, Oosterkamp et al., 2000, Lee and Kim, 2003, Zhang et al., 2008, Sakino, 2008, Wiesner and MacGillivray, 1999, Lindholm and Yeakley, 1965, Zhu et al., 2011, Cao et al., 2015, El-Magd, 1994, Jiang and Chen, 1974) which have proven that, at room temperature, the failure stress tends to increase with the increase of the loading or strain rate; this holds true for many metallic materials.

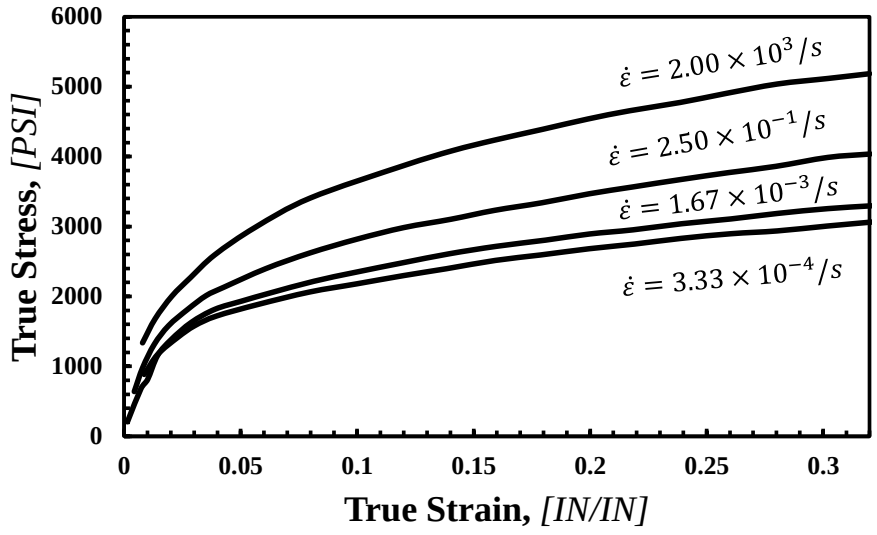

Figure 1. 6 Stress–strain curves under four different rates of loading for material lead [Figures area adopted from Lindholm, 1964]..

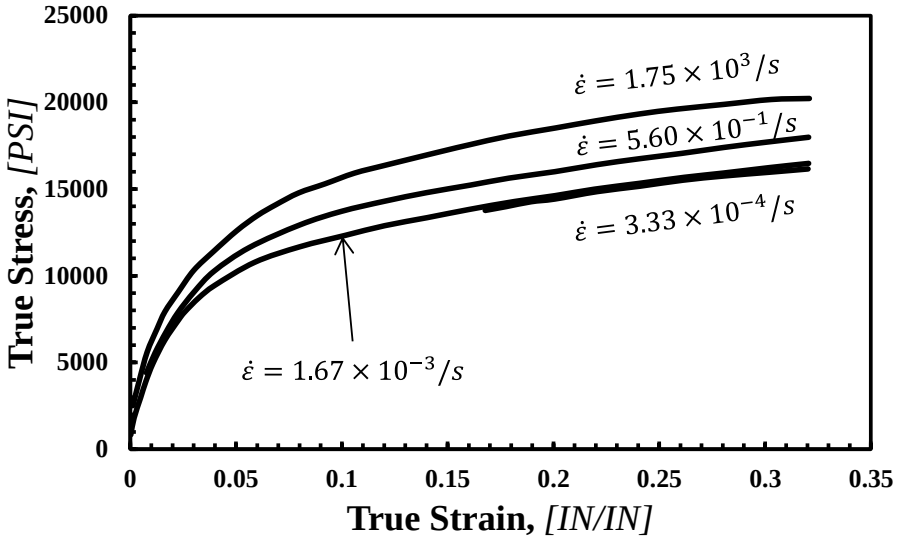

Figure 1. 7 Stress–strain curves under four different rates of loading for mateiral aluminium [Figures are adopted from Lindholm, 1964]..

Specifically, in 1964, Lindholm tested three annealed f.c.c. metals, which were lead, aluminium, and copper, by using the Split–Hopkinson Pressure Bar (SHPB) method in order to understand the rate sensitivity of these metallic materials subjected to strain rates ranging from $10^{-4}s^{-1}$ to $10^{3}s^{-1}$ (Lindholm, 1964). For example, the graphs reported in Figure 1.6, 1.7 and 1.8 show the true stress–true strain curves of the three investigated metals generated from the tests under four different strain rates. These graphs make it evident that the stress increases as the strain rate increases for the three investigated metals. In 1971, Lindholm, Bessey and Smith tried to understand the basic material properties of three wrought aluminium alloys subjected to strain

rates ranging from $0.0001s^{-1}$ to $1000s^{-1}$ at room temperature (Lindholm et al., 1971). The graphs reported in Figure 1.9 show the material yield strength and ultimate tensile strength versus logarithmic strain rate for aluminium alloys 5454-O, 5454-H34, 6061-T651 and 6351-T51. This figure indicates the fact that, in a general way, the 0.2% offset yield strength and the ultimate strength of these aluminium alloys increase slightly (of the order of a 10% increase over a wide range of strain rates from $10^{-4}s^{-1}$ to $10^{3}s^{-1}$) as the strain rate increases.

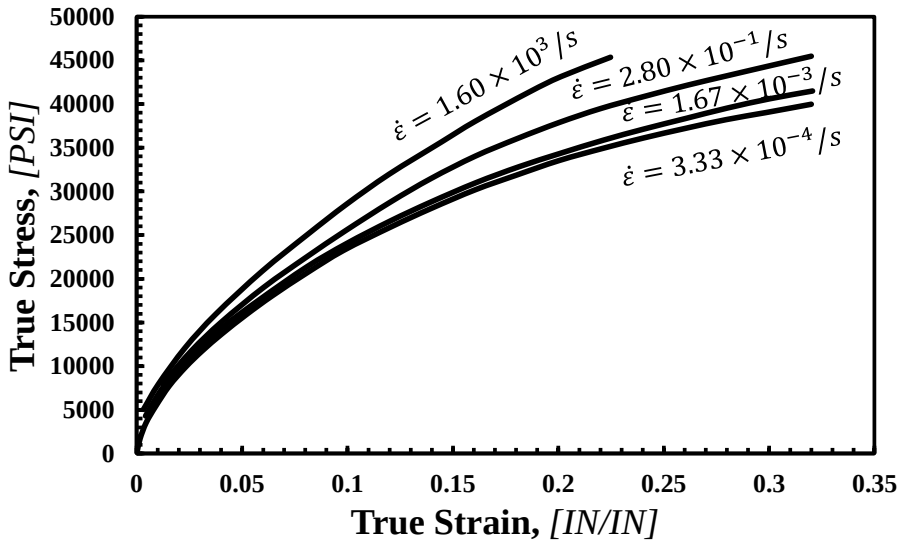

Figure 1.8 Stress–strain curves under four different rates of loading for material copper [Figures area adopted from Lindholm, 1964].

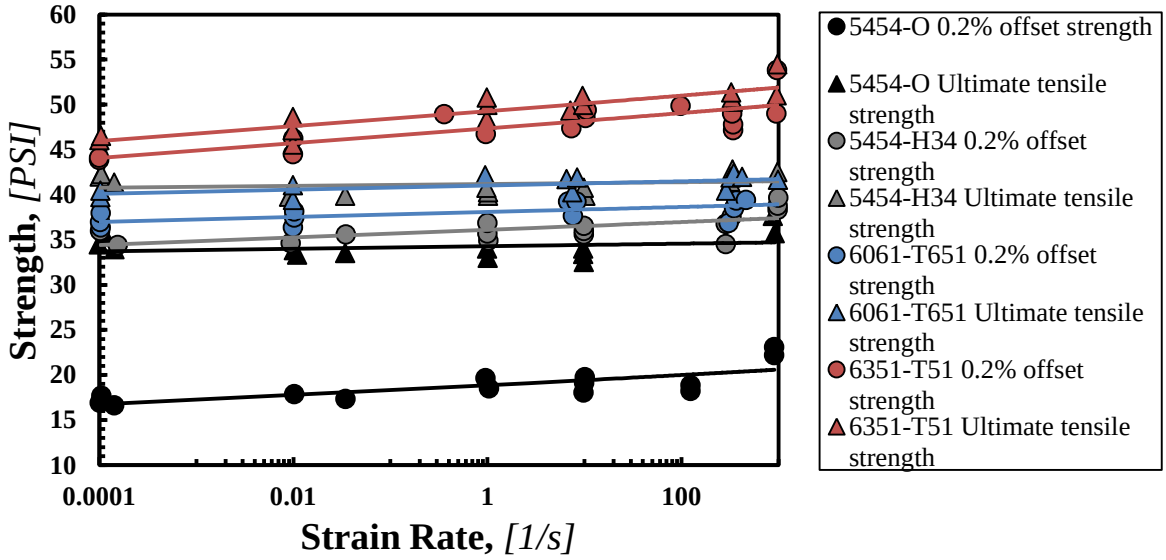

Figure 1.9 Strength vs strain rate for four aluminium alloys 5454-O; 5454-H34; 6061-T651 and 6351-T5 [adopted from Lindholm et al., 1971].

Additionally, Oosterkamp et al. also tested the response of commercial aluminium alloys AA6082-T6 and AA7108-T79 over a wide range of strain rates ranging from $0.1s^{-1}$ to $3000s^{-1}$ at various temperatures (Oosterkamp et al., 2000). The graphs reported in Figure 1.10 show the flow stress at 5% plastic strain versus log strain rate curves of these aluminium alloys when tested at different temperatures. The flow stress used here indicates instantaneous value of stress required to continue reformatting the material to keep the metal flowing plastically. According to these graphs, positive but low strain rate sensitivity can be observed. These results have similar strain rate sensitivity to the results published by Lindholm et al. (1971).

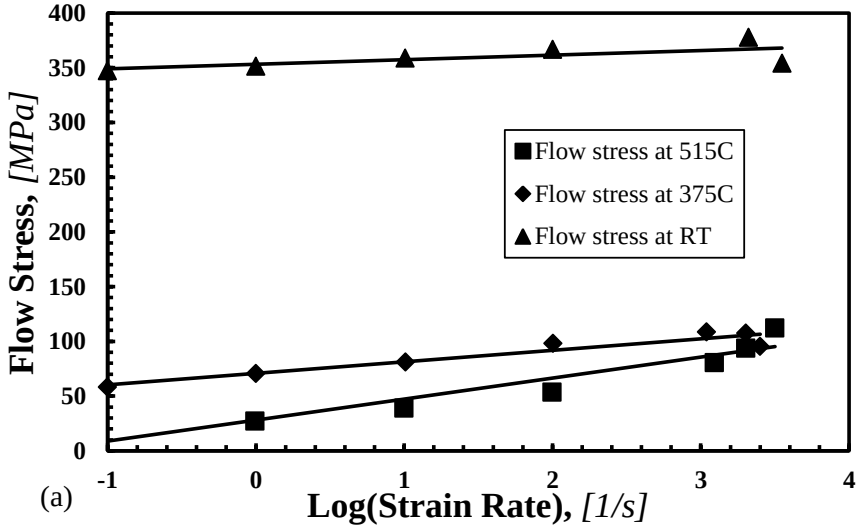

(a)

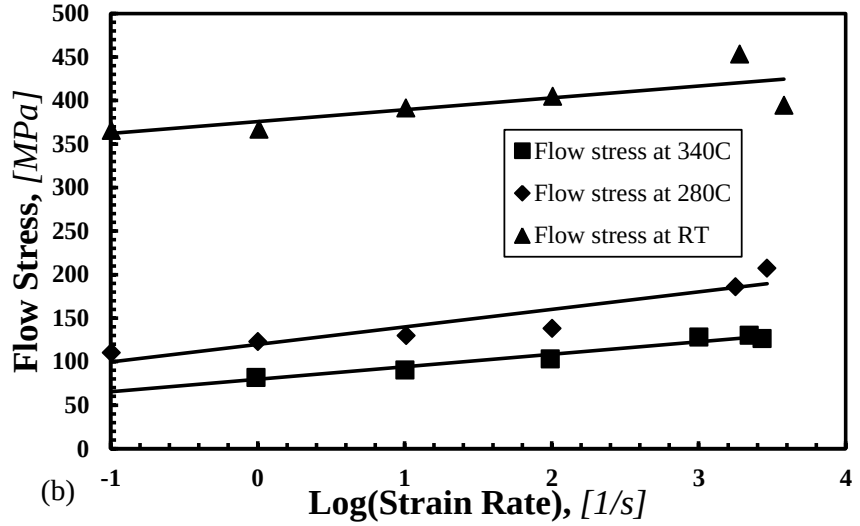

(b)

Figure 1.10 Flow stress at 5% of plastic strain versus logarithmic strain rate for aluminium alloys: (a) AA6082-T6 at room temperature, $375^{o}C$ and $515^{o}C$; and (b) AA7108-T79 at room temperature, $280^{o}C$ and $340^{o}C$ [adopted from Oosterkamp et al., 2000].

Lee and Kim (2003) used the split-Hopkinson pressure bar (SHPB) technique to test the dynamic strength of aluminium alloys Al2024-T4 and Al7075-T6 in 2003 under both high strain rate compressive and tensile loading conditions, and the results are shown in the graphs reported in Figure 1.11. This figure makes it evident that the dynamic material strength of the tested aluminium alloys (Al2024-T4 and Al7075-T6) becomes higher when the strain rate is increasing. It is also interesting to observe from this figure that the rate sensitivity under compressive loading is higher than the one under tensile loading (Lee and Kim, 2003), which means the mechanical deformation behaviours of metallic material under high rate of tensile loading and compressive are very different.

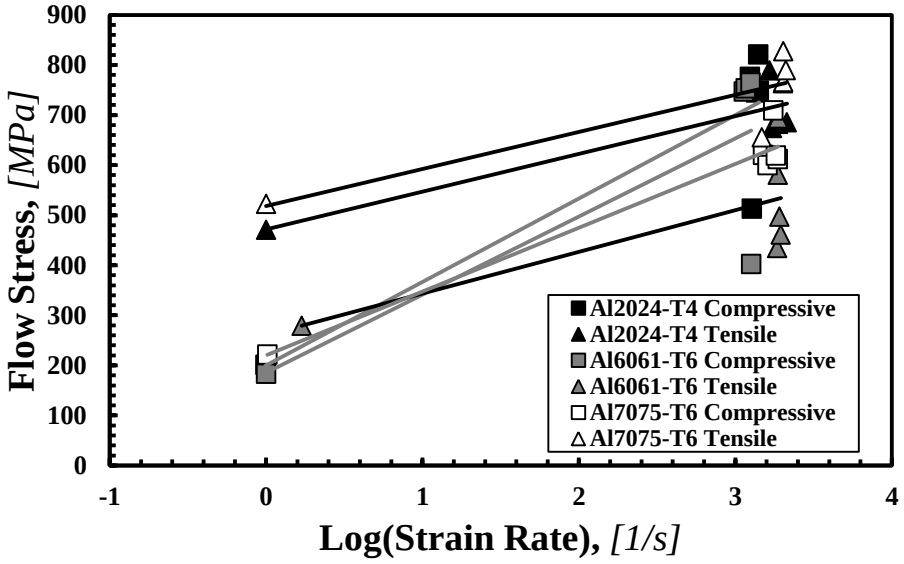

Figure 1.11 Dynamic compressive stress–strain curves of materials Al2024-T4, Al6061-T6 and Al7075-T6 [adopted from Lee and Kim, 2003].

Due to the rapid development of numerical methods during the last three decades, the advent of finite element analysis has promoted the progress of stress and strength analysis. In 2008, Zhang et al. used both experimental and numerical techniques to understand the impact behaviours of aluminium alloy 2519A subjected to strain rates from $600s^{-1}$ to $7000s^{-1}$ at various temperatures (Zhang et al., 2008). The graph in Figure 1.12 shows the results of the true stress versus strain rate for aluminium alloy 2519A obtained from both experimental work and FE analysis at room temperature. This figure again shows that the strain rate sensitivity of this type of aluminium alloy is positive.

The ultimate tensile strength/yield stress versus strain rate curves for mild steel tested at different temperatures, published by Wiesner and MacGillivray in 1999, are shown in Figure 1.13 (Wiesner and MacGillivray, 1999). These curves make it evident that the material ultimate tensile strength and the yield stress of the steel tested under higher rates of loading are higher

than the results obtained under quasi-static conditions, and the rate sensitivity of strength increases as the strain rate increases (Wiesner and MacGillivray, 1999).

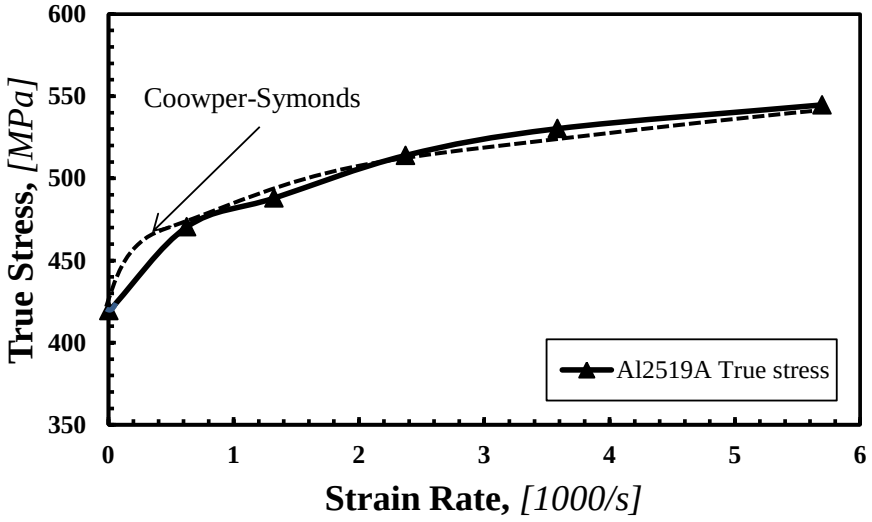

Figure 1.12 True stress–strain rate curves obtained from both experiment and FE analysis at room temperature (Zhang et al., 2008).

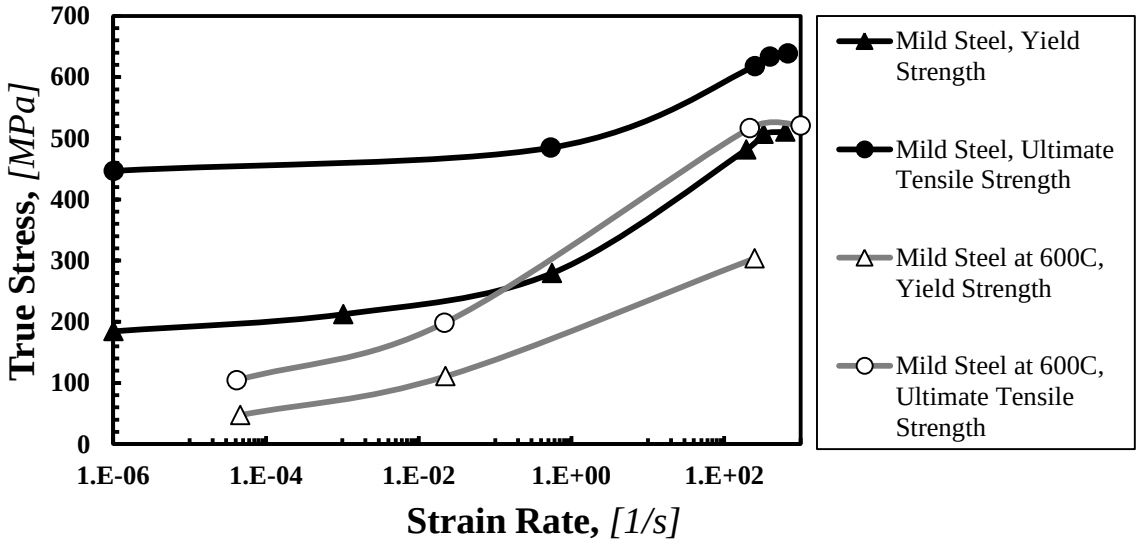

Figure 1.13 True stress vs. strain rate of materials mild steel at room temperature and 600°C (Wiesner and MacGillivray, 1999).

In this section, the dynamic behaviour of plain material has been discussed. We can conclude that in general, the material strength increases as the loading rate increases. This phenomenon can be attributed to the fact that the high rate of loading has the effect to promote the dislocation denervation and annihilation, which therefore increase the work-hardening rate. Additionally,

the deformation twinning resulted from high rate of loading also contributes to the increase of work-hardening rate (Liang et al., 2015).

However, in practice, plain (i.e., un-notched) components are not often to be found, as most material components have irregular shapes, which can change the stress distribution. As a result, the material behaviour of these components with complex geometry under dynamic loading will be different. In the next section, the stress concentration phenomena will be introduced briefly, with this being followed by a discussion focussing on the dynamic behaviour of notched metals.

1.5 Stress concentration phenomena

Stress concentration, which is measured by the stress concentration factor K_t, is a localised effect caused by geometrical discontinuities such as grooves, holes, fillets, notches and other stress raisers, which exist in a linear elastic material body. Stress concentration has the effect of redistributing the stress state in which the magnitude of maximum stress at the notch tip is much larger than the average stress across the section and the stress in the mid part is lower than the average stress (Young and Budynas, 2002, Roark, 1975, Dieter and Bacon, 1986, Peterson, 1974). If a crack exists in a linear elastic material body, the stress concentration factor K_t is equal to infinity. Stress concentration phenomena are one of the reasons leading to fatigue crack initiation as well as to the static and dynamic failure of real components. In reality, stress concentration can be seen in various forms in structural applications (Pilkey and Pilkey, 2008).

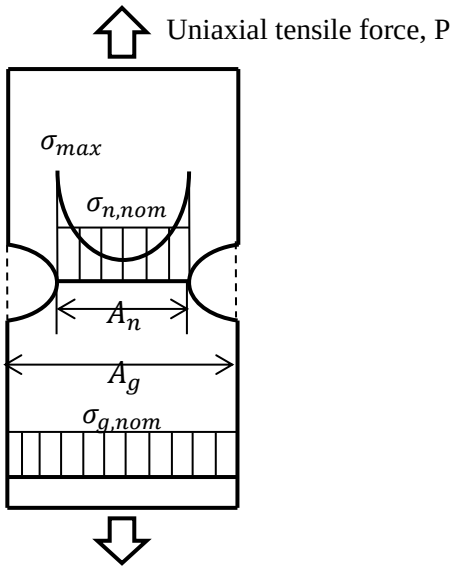

Figure 1.14 Stress concentration factor for double edge notches.

As an example, Figure 1.14 shows the two-dimensional linear elastic stress distribution for a plate containing double edge notches subject to a uniaxial tensile force P. In the absence of notches, a uniform stress across the section can be simply calculated as $\sigma = P/A_g$. However, in

this case, the stress at the notch tip increases to a maximum stress, σ_{max}, and decreases to a lower value away from the notch tip towards the centre. To account for the increased level of this maximum stress, the theoretical gross and net stress concentration factors K_{tg} and K_{tn} can be calculated as follows:

$$K_{tg} = \frac{\sigma_{max}}{\sigma_{g,nom}} \quad (1.5)$$

$$K_{tn} = \frac{\sigma_{max}}{\sigma_{n,nom}} \quad (1.6)$$

From equations (1.5) and (1.6), the theoretical stress concentration factors are calculated as the maximum stress (σ_{max}) divided by the nominal stress (either $\sigma_{g,nom}$ or $\sigma_{n,nom}$). The gross nominal stress $\sigma_{g,nom}$ is calculated as P/A_g (as shown in Figure 1.14), whereas net nominal stress is calculated as $\sigma_n = P/A_n$. The magnitude of the maximum stress, σ_{max}, is dependent on both the loading type and the geometrical features (Pilkey and Pilkey, 2008), In this thesis, the general term $\sigma = P/A$ will be assumed as net nominal stress.

When the stress around the stress concentrator exceeds the yield stress, the stress and strain redistributes due to plastic deformation in the vicinity of the stress raiser, and the local strain increases with little stress increase. Hence, the equations (1.5) and (1.6) above are no longer applicable to ductile materials (Topper et al., 1967, Roark, 1975, Dieter and Bacon, 1986). According to the analyses developed by Stowell (1950) and Neuber (1961), the theoretical stress concentration factor for material with nonlinear behaviour can be calculated as follows:

$$K_\sigma \cdot K_\varepsilon = K_t^2 \quad (1.7)$$

Where K_σ (taken to be equal to $\sigma_{max}/\sigma_{nom}$) indicates the effective stress concentration factor, which is obtained experimentally; K_ε is defined as the effective strain concentration factor, which can be calculated as $K_\varepsilon = \varepsilon_{max}/\varepsilon_{nom}$. ε_{max} means the strain corresponding to the maximum stress, σ_{max}.

1.6 Dynamic behaviour of notched materials

As we discussed above, both the rate of loading and stress concentration phenomena have influence on a material's behaviour. It would be interesting to discover how the loading rate influences the material when stress concentration phenomena occur. However, in contrast with the dynamic behaviour of plain samples, only a few studies can be found in the technical literature which investigate the behaviour of notched samples subjected to high rates of loading.

Back in the 60s, the experimental investigation carried out at the Wright-Patterson Air Force Base, Ohio (Brisbane, 1963) involved three different metallic materials, i.e. 301XH stainless

steel with σ_{UTS} = 1392 MPa, RENE-41 alloy with σ_{UTS} = 1379 MPa and VASCO JET-1000 steel with σ_{UTS} = 1411 MPa. The specimens used in this investigation are shown in Figure 1.15. In particular, the un-notched flat samples had width equal to 12.7 mm and gauge length equal to

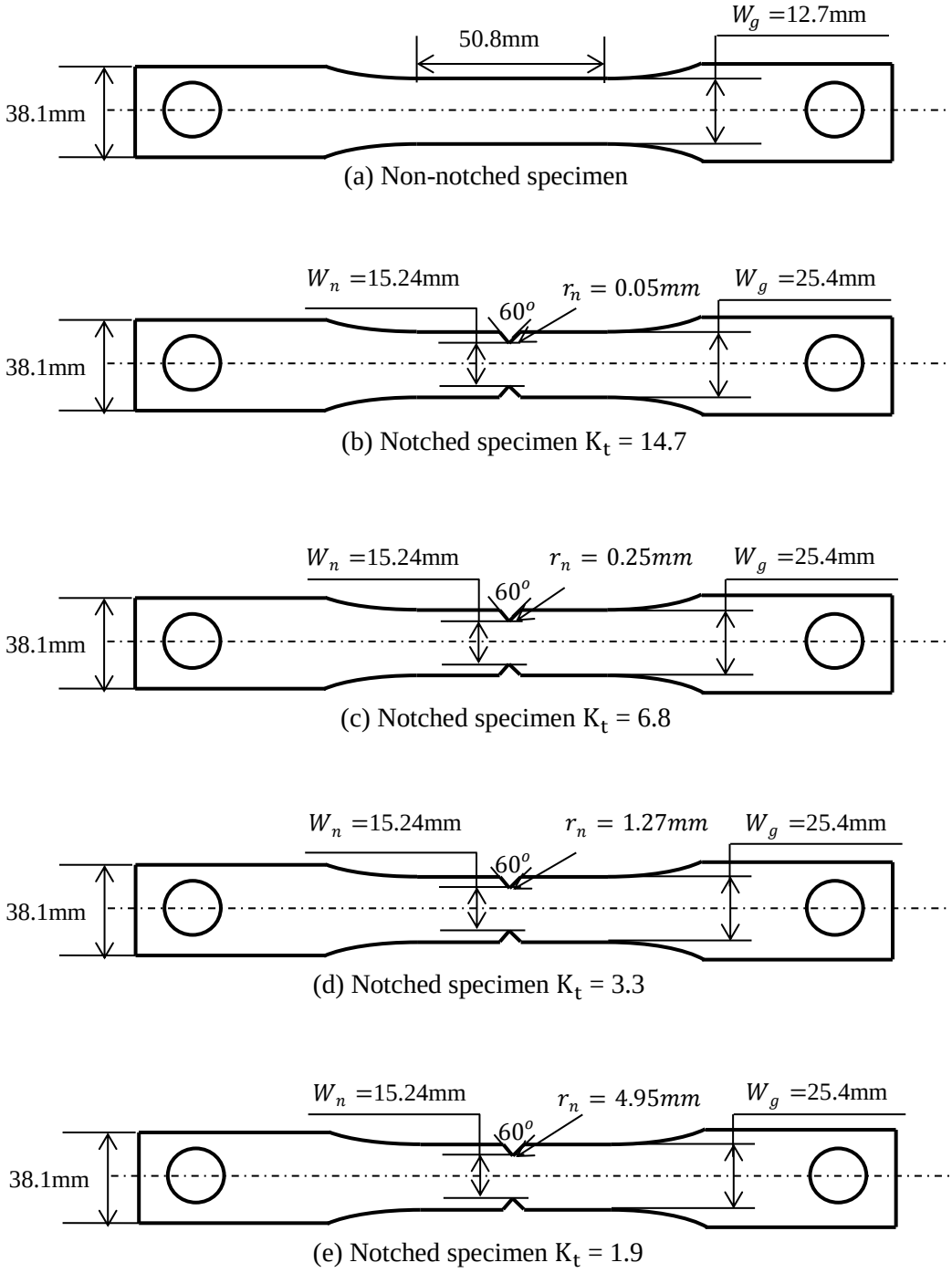

Figure 1.15 Geometries of the samples tested in the laboratory of Wright-Patterson Air Force Base, Ohio by Brisbane (1963) (dimensions in millimetres).

50.8 mm and the V-notched flat specimens had a net width W_n of 15.24 mm and a gross width W_g of 25.4 mm. Four different values of the root radius r_n were investigated, i.e. r_n = 0.05 mm (K_t = 14.7), r_n = 0.25 mm (K_t = 6.8), r_n = 1.27 mm (K_t = 3.3), and r_n = 4.95 mm (K_t = 1.9). The above samples were tested under the following values of the nominal displacement rate, $\dot{\Delta}$: $0.002\ \text{mm} \cdot s^{-1}$, $0.021\ \text{mm} \cdot s^{-1}$, $0.423\ \text{mm} \cdot s^{-1}$, and $3.387\ \text{mm} \cdot s^{-1}$. Table 1.1 summarises all of the results generated by Brisbane (1963), where $\sigma_{f,nom}$ is the nominal failure strength and refers to the net area of the samples. It is worth observing here that the $\sigma_{f,nom}$ values reported in Table 1.1 were supplied by Brisbane himself as the average from three different tests.

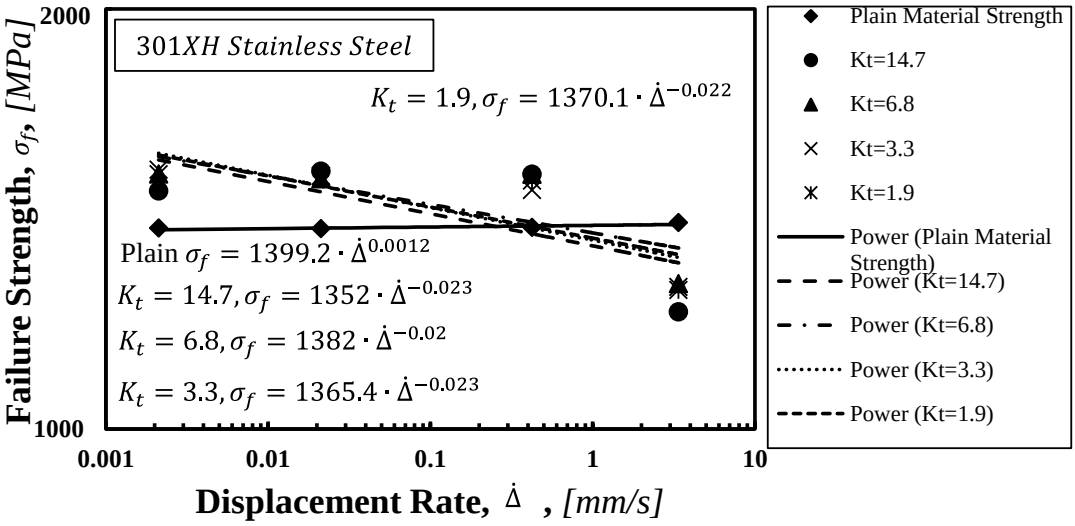

Figure 1. 16 Failure strength vs displacement rate of material 301XH stainless steel.

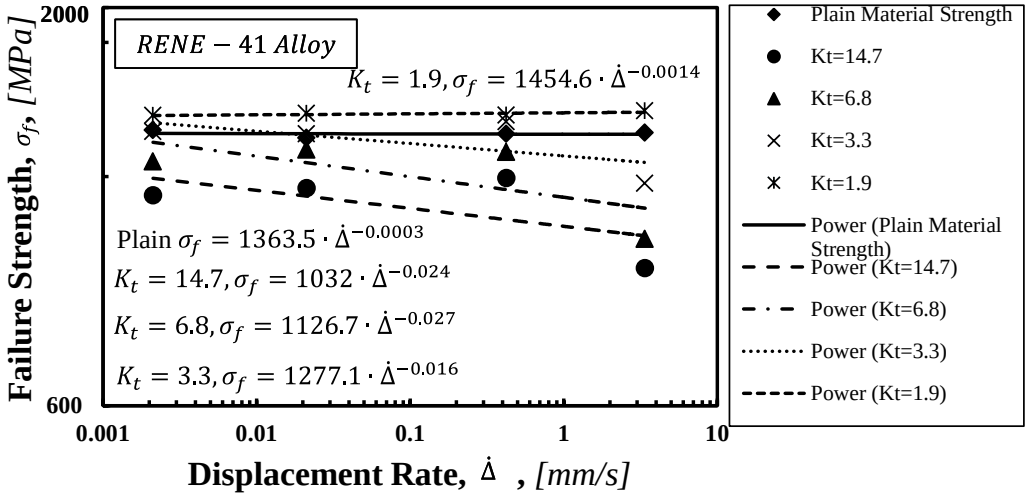

Figure 1. 17 Failure strength vs displacement rate of material RENE-41 alloy (Brisbane, 1963).

By plotting the failure strength against displacement rate for both un-notched and notched samples (Figure 1.14, 1,15 and 1.16), we can clearly see that the failure strength of no-notched sample increases as the displacement rate increases. However, in terms of notched samples, the failure strength decreases as long as the displacement rate decreases.

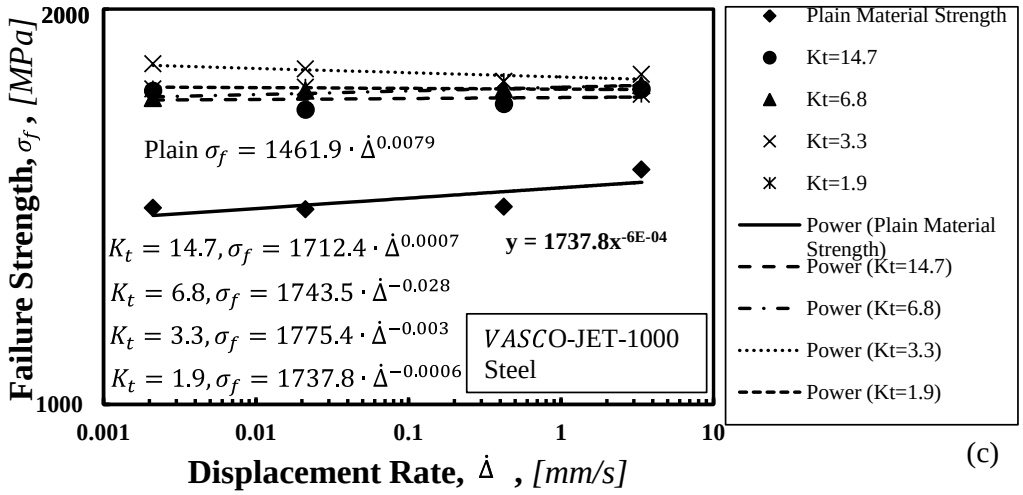

Figure 1.18 Failure strength vs displacement rate of material VASCO JET-1000 steel (Brisbane, 1963).

Moreover, with the help of finite element method, Noda et al. (2015) also analysed material behaviours of notched specimens subjected to dynamic loading. According to their analysis, the results suggested that the maximum dynamic stress at notch tip increases as the test speed increases when the tensile speed is less than $5000mm \cdot s^{-1}$. However, when the tensile speed is greater than $100000mm \cdot s^{-1}$, the maximum dynamic stress remains constant as the tensile speed increases. From the section above, we can see that the high rate of loading gives rise to big changes in material behaviours no matter whether the specimen contains notches or not. In the next section, the fundamental ideas of Linear Elastic Fracture Mechanics (LEFM) and Elastic Plastic Fracture Mechanics (EPFM) will be introduced.

Table 1.1 Summary of the results generated by Brisbane (1963) by testing plain and V-notched flat samples of 301XH stainless steel, René-41 alloy, and Jet-1000 steel.

w_g	w_n	r_n	K_t	$\dot{\Delta}$	301XH, $\sigma_{f,nom}$	René-41, $\sigma_{f,nom}$	Jet-1000, $\sigma_{f,nom}$
[mm]	[mm]	[mm]		[mm $\cdot s^{-1}$]	[MPa]	[MPa]	[MPa]
12.7	12.7	plain	1.0	0.002	1392.1	1379.0	1410.7
12.7	12.7	plain	1.0	0.021	1390.7	1347.2	1407.2
12.7	12.7	plain	1.0	0.423	1393.4	1363.8	1413.4
12.7	12.7	plain	1.0	3.387	1405.2	1368.6	1508.6
25.4	15.24	0.05	14.7	0.002	1481.0	1132.8	1732.0
25.4	15.24	0.05	14.7	0.021	1529.9	1157.6	1676.1
25.4	15.24	0.05	14.7	0.423	1522.4	1194.2	1692.7
25.4	15.24	0.05	14.7	3.387	1212.8	909.4	1737.5
25.4	15.24	0.25	6.8	0.002	1522.4	1254.8	1709.9
25.4	15.24	0.25	6.8	0.021	1510.0	1300.4	1732.0
25.4	15.24	0.25	6.8	0.423	1521.7	1291.4	1737.5
25.4	15.24	0.25	6.8	3.387	1270.0	992.8	1748.5
25.4	15.24	1.27	3.3	0.002	1532.7	1373.4	1816.1
25.4	15.24	1.27	3.3	0.021	1516.8	1363.8	1799.5
25.4	15.24	1.27	3.3	0.423	1482.4	1421.0	1760.2
25.4	15.24	1.27	3.3	3.387	1263.1	1174.2	1782.3
25.4	15.24	4.95	1.9	0.002	1521.7	1442.4	1737.5
25.4	15.24	4.95	1.9	0.021	1516.8	1450.7	1743.0
25.4	15.24	4.95	1.9	0.423	1503.1	1443.8	1760.2
25.4	15.24	4.95	1.9	3.387	1256.9	1462.4	1720.9

1.7 Linear Elastic Fracture Mechanics and Elastic Plastic Fracture Mechanics under static loading

1.7.1 Introduction

Fracture mechanics is a subfield of solid mechanics. It consists of two main parts: Linear Elastic Fracture Mechanics (LEFM) and Elastic Plastic Fracture Mechanics (EPFM). The former applies to cases where the plastic zone is confined to a small area in the vicinity of the crack tip, while the latter is developed for the fractures which are caused by large yielding around the crack tip when LEFM is no longer applicable to be used. LEFM has been developed for centuries and continues to occupy an important position in the design of material components.

1.7.2 Development of Linear Elastic Fracture Mechanics (LEFM)

Several centuries earlier, in order to find the fundamental causes of fracture, Leonardo da Vinci investigated the strength of iron wires in his laboratory. According to these results, he proposed that defects in the material can have a big influence on the strength of the material (Anderson, 2005). Later on, in 1898, based on Kirsch's linear elastic solution, the stress state around a hole in an infinite plate was calculated, and the stress concentration was observed and varied between 2 to 4 under different loading conditions (Welss, 1955). In 1912, Kommers discovered that the resistance of scratched specimens was 45%–50% lower than the resistance of polished specimens (Inglis, 1913). One year later, Inglis extended Kirsch's linear elastic solution to describe the stress state around an elliptic hole in a plate, which is well-known as a cornerstone of Linear Elastic Fracture Mechanics (LEFM). According to this linear elastic solution, the stress at the notch tip goes to infinity when the root radius of the notch tip goes to zero. In 1920, with the help of Inglis's work (Irwin, 1948) and the soap-film method developed by Griffith and Taylor (Zener and Hollomon, 1944), Griffith was able to calculate the stress and strain states around scratches in glass. From this calculation, Griffith also found that surface scratches have the effect of increasing the stress and strain of solids, and the material strength is decreased by such scratches. Based on an energy balance, Griffith proposed a fracture theory to predict the connection between fracture stress and flaw size in glass specimens (Griffith, 1921). In 1939, Westergaard proposed an easier solution to describe the stress states surrounding a crack in rectangular coordinates rather than the elliptical coordinates used in Inglis's solution (Westgaard, 1939). In this approach, Westergaard applied loads directly to cracks rather than applied loads to ellipses that approached cracks under the condition of the limit (Westgaard, 1939).

During World War 2, a large quantity of military equipment was manufactured and equipped in a very short time without being well designed and investigated. The destructive influence of cracks and notches became obvious in the case of non-ductile materials. For example, in 1943,

as shown in Figure 1.19, the all-welded cargo vessels (Liberty Ships) sudden broke in half when they moored at dock (Anderson, 2005); more than 200 out of 1031 damaged ships were completely sunk and fractured beyond all hope of repair (Kobayashi and Onoue, 1943). According to the accident report investigated by Hideo and Hisahiro (Kobayashi and Onoue, 1943), there are three factors which led to the destruction of the Liberty Ships (Anderson, 2005): 1. the appearance and development of crack-like defects in welded joints; 2. local stress concentrations on the deck; and 3. the lack of fracture toughness consideration, which marked the birth of fracture mechanics. Specifically, due to the low temperature in the North Atlantic, the fracture mode of the hull of the Liberty Ships transferred from ductile to brittle (Kobayashi and Onoue, 1943). As shown in Figure 1.20, for the steel used in welded structures, the energy required for fracture decreases dramatically when the temperature is lower than a certain value (as shown in Figure 1.20: transition temperature T1); this behaviour accelerated the fracture under very low stresses (Janssen et al., 2004).

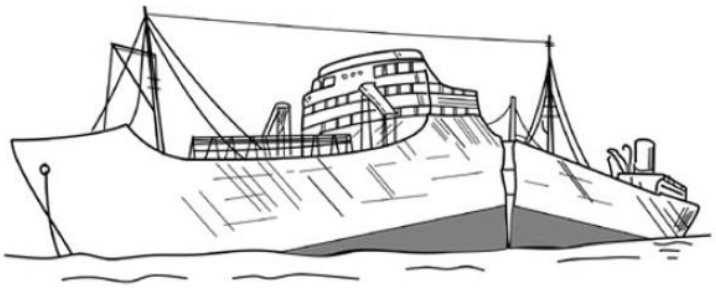

Figure 1.19 The failure of Liberty Ships during the Second World War (Kobayashi and Onoue, 1943).

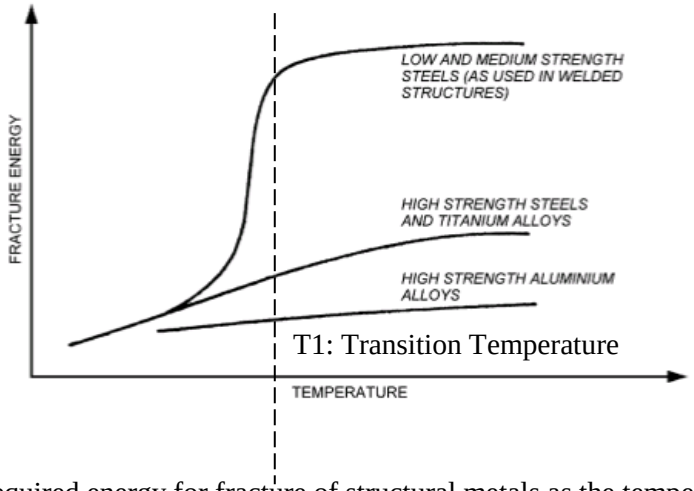

Figure 1.20 Required energy for fracture of structural metals as the temperature increases (Janssen et al., 2004).

Along with the development of engineering materials, during the Second World War, metallic materials were in high demand for national defence and engineering applications. However, the Griffith theory is only applied to the applications where pure brittle fracture happens. After the Second World War, promoted by the failure of the Liberty Ship described above, the Griffith theory has been used extensively and modified significantly in order to extend this approach to other engineering materials rather than just brittle materials (Rossmanith, 1995, Shrot and Bäker, 2012). In 1956, after studying the pioneering work of Inglis and Griffith (Irwin, 1948, Brinson and Brinson, 2015), Irwin extended Griffith's theory to metallic materials which experience plastic deformation and developed a more useful concept called the energy release rate (G) approach, based on representing the rate of energy change per unit of crack extension in a linear elastic body (can be calculated from equation 1.8) (Majzoobi et al., 2010). The critical value of energy release rate G_c is a measure of fracture toughness, which can be calculated using the critical remote strength σ_f through equation (1.9). Figure 1.21 shows an infinite plate with a through-thickness crack of length $2a$ subject to a uniform remote tensile stress σ, and the energy release rate would be

$$G = \frac{\pi\sigma^2 a}{E} \tag{1. 8}$$

where E is the elastic modulus; σ indicates the uniform remote tensile stress applied to the infinite plate; and a denotes the half length of the crack. The critical value G_c can be calculated as follows:

$$G_c = \frac{\pi\sigma_f^2 a}{E} \tag{1. 9}$$

The fracture can be avoided when the energy release rate G is equal to or less than the critical value of energy release rate G_c:

$$G \leq G_c \tag{1. 10}$$

Besides the energy approach, in 1957, based on linear elastic theory and Westergaard's solution (Westgaard, 1939), Irwin proposed an advanced concept called the stress intensity factor (SIF), which was considered to be one of the most important and useful concepts in fracture mechanics (Liang et al., 2015). In this approach, the stress intensity factor K is a single parameter, which is used to describe the magnitude of the stress field of an element in the vicinity of the crack tip. The general form of K is given by

$$K = \sigma\sqrt{\pi a} \cdot f(a/W) \tag{1. 11}$$

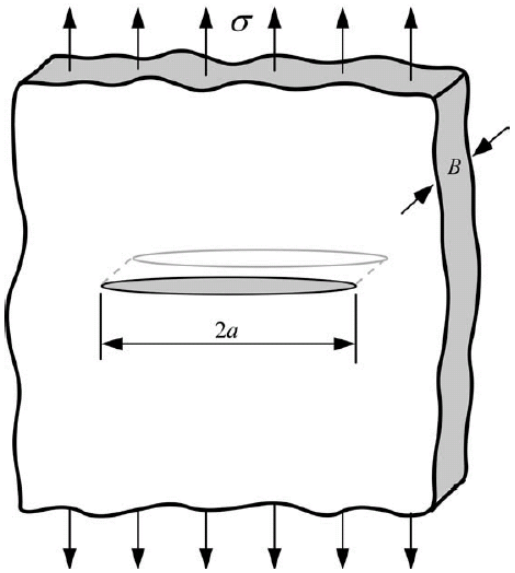

Figure 1.21 Through-thickness crack in an infinite plate subject to a remote tensile stress (Anderson, 2005).

where σ indicates the remote applied stress; and $f(a/W)$ is a function depending on the sizes of the plate and the position of the crack. W is the width of component. In the case shown in Figure 1.21, $f(a/W)$ was taken equal to 1, therefore the equation (1.11) can be rewritten as follows:

$$K = \sigma\sqrt{\pi a} \tag{1. 12}$$

The stresses in the vicinity of the tip of a crack can be described according to the following three basic modes: opening mode (mode I), sliding mode (mode II) and tearing mode (mode III), which are shown in Figure 1.22. Under mode I loading, the principal stress is applied perpendicular to the crack plane, and it leads to a crack opening mechanism acting parallel to the stress direction. The sliding mode (mode II) corresponds to the in-plane shear loading, which is perpendicular to the crack edge. The tearing mode (mode III) corresponds to out-of-plane shear.

In many practical situations, the opening mode (mode I) has been found as the most predominant mode. Under mode I loading conditions (Figure 1.22(a)), based on Westergaard's work, according to the Griffith energy balance approach (Brinson and Brinson, 2015) and Irwin's modification (Liang et al., 2015), Irwin concluded that material failure will not happen when the value of the stress intensity factor K_I is equal to or smaller than the critical stress intensity factor (fracture toughness), K_{Ic}:

$$K_I = \sigma\sqrt{\pi a} \leq K_{Ic} \tag{1. 13}$$

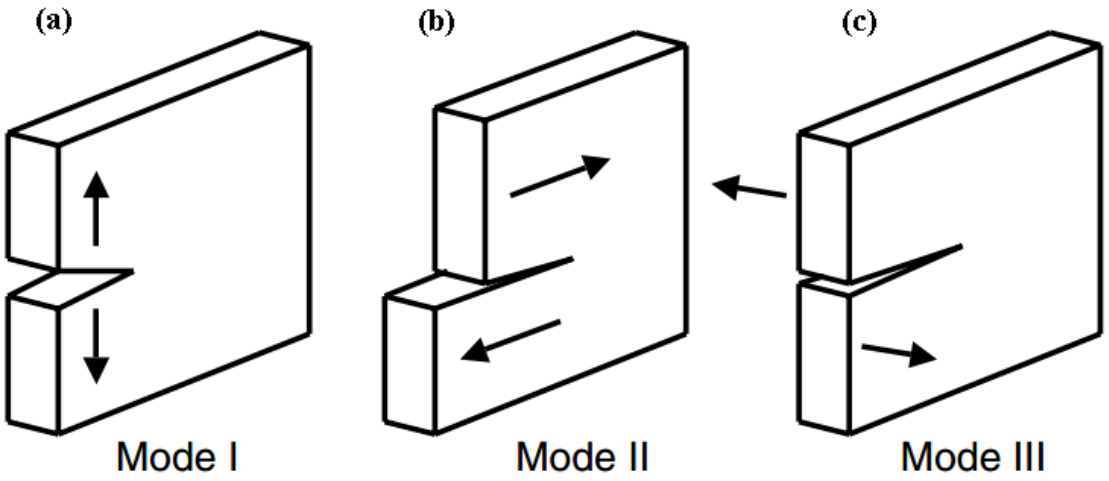

Figure 1.22 Three different loading modes of cracked specimens: (a) mode I: opening mode; (b) mode II: sliding mode; and (c) mode III: tearing mode (Mach et al., 2007).

where σ indicates the remote tensile stress applied to the infinite plate as shown in Figure 1.21; and a is the half length of the central crack in this infinite plate. From this equation, it can be seen that the stress intensity factor K_I is proportional to the remote stress σ and the square root of the half-length of the crack, $\sqrt{a}$.

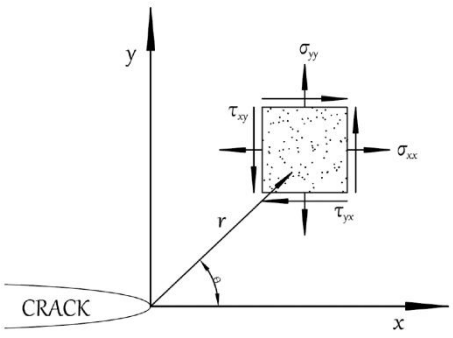

Figure 1.23 In-plane stresses of an element at the crack tip in an elastic material (Anderson, 2005).

The in-plane stress of an element around the tip of a crack in an isotropic linear elastic material is schematically shown in Figure 1.23 (Anderson, 2005), and the stress field under mode I loading can be expressed mathematically by equations (1.14), (1.15) and (1.16).

$$\sigma_{xx} = \frac{K_I}{\sqrt{2\pi r}} cos\left(\frac{\theta}{2}\right)\left[1 - sin\left(\frac{\theta}{2}\right) sin\left(\frac{3\theta}{2}\right)\right] \quad (1.\ 14)$$

$$\sigma_{yy} = \frac{K_I}{\sqrt{2\pi r}} cos\left(\frac{\theta}{2}\right)\left[1 + sin\left(\frac{\theta}{2}\right) sin\left(\frac{3\theta}{2}\right)\right] \quad (1.\ 15)$$

$$\tau_{xy} = \frac{K_I}{\sqrt{2\pi r}} cos\left(\frac{\theta}{2}\right) sin\left(\frac{\theta}{2}\right) cos\left(\frac{3\theta}{2}\right) \quad (1.\ 16)$$

where r and θ are the polar coordinates of the element at a point ahead of the crack tip. It can be seen from the equations 1.14 to 1.16 that the stresses σ_{xx}, σ_{yy} and τ_{xy} are all in proportion to the stress intensity factor K_I. It is clear that the stress field can be calculated once the stress intensity factor is known. When θ is taken equal to 0, the stresses in directions x and y are given by:

$$\sigma_{xx} = \sigma_{yy} = \frac{K_I}{\sqrt{2\pi r}} \quad (1.\ 17)$$

By combining equations (1.8) and (1.12), the relationship between the energy release rate G and stress intensity factor K can be simply derived, and their critical values can be expressed as equation (1.18) below:

$$G = \frac{K^2}{E},\ G_c = \frac{K_c^2}{E} \qquad (Joule/m^2) \quad (1.\ 18)$$

1.7.3 Crack tip plasticity

According to equations 1.14 to 1.16, it is clear that an infinite stress, which is called the stress singularity, is obtained at the crack tip (zero root radius and $r \to 0$). However, it is recognised that the stress singularity does not exist in real materials. This is because the minimum crack tip radius is about the interatomic distance, which is not zero, and the plastic material deformation around the crack tip relaxes stresses above the yield stress. Hence, a correction is required when yielding in the vicinity of the crack tip occurs (Broek, 1982, Janssen et al., 2004, Anderson, 2005).

By substituting the yield stress σ_y for σ_{yy} in equation 1.17, Irwin (1961) discovered that the plastic zone size, r_y, under plane stress conditions along the x-axis over the crack tip is given by:

$$r_y = \frac{1}{2\pi}\left(\frac{K_I}{\sigma_{ys}}\right)^2 \quad (1.\ 19)$$

Figure 1.24 shows the distributions of the linear elastic stress and yield stress σ_{ys} after local yielding over the corrected plastic zone. Irwin (1961) indicated that the original crack size should be extended to a longer effective crack length, $a_{eff} = a + r_y$, in order to maintain the equilibrium of forces. Hence, a further extension of the plastic zone is given by:

$$r_p = \frac{1}{\pi}\left(\frac{K_I}{\sigma_{ys}}\right)^2 \quad (1.\ 20)$$

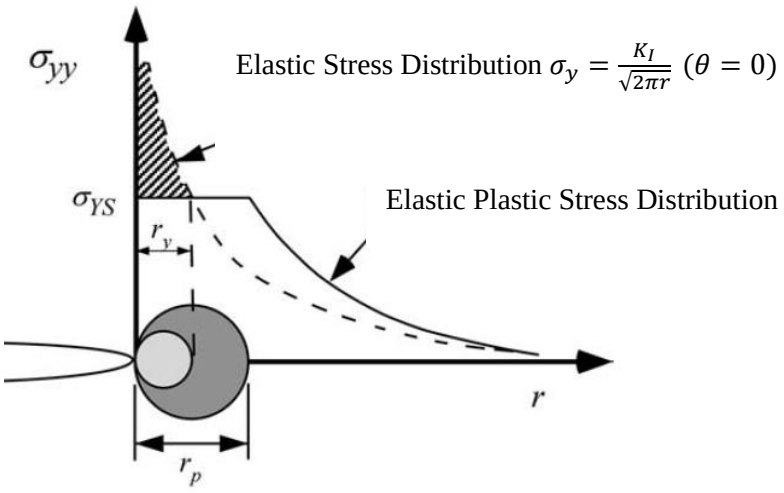

Figure 1.24 Linear elastic stress distribution and corrected elastic plastic stress distribution from the Irwin approach (Anderson, 2005).

By comparing equation 1.19 with 1.20, it can be seen that the second order plastic zone correction r_p is twice that of the first order plastic zone correction r_y.

For plane strain conditions, due to the tri-axial stress effect caused by the surrounding elastic parts, the Irwin corrected plastic zone size can be rewritten as (Anderson, 2005):

$$r_y = \frac{1}{6\pi}\left(\frac{K_I}{\sigma_{ys}}\right)^2 \qquad (1.\ 21)$$

By comparing equation (1.21) with (1.19), we can draw the conclusion that the Irwin plastic zone correction for plane stress is 3 times bigger than the one calculated under plane strain conditions.

1.7.4 Development of Elastic Plastic Fracture Mechanics (EPFM)

As described above, LEFM is developed for either the cases under elastic conditions or the cases where the plastic zone is confined to a small area in the vicinity of the crack tip (Anderson, 2005, Ewalds and Wanhill, 1984, Janssen et al., 2004). However, when the failure of ductile materials is preceded by a large plastic deformation, LEFM is not able to describe material behaviours correctly. In such circumstances, alternative methods must be proposed (Ewalds and Wanhill, 1984, Janssen et al., 2004, Anderson, 2005).

In addressing the problem of brittle fracture, a satisfactory result was obtained by using the linear elastic stress intensity factor approach. However, when a fracture occurs in ductile material, large-scale yielding can be observed around the crack tip, and the stress increases slowly with the high increase of plastic deformation. Hence, the use of strain or displacement as

physical parameters for characterising ductile fracture may be more appropriate for calculating the elastic plastic problem.

In 1961, Wells proposed a plastic strain control concept called crack tip opening displacement (CTOD) as a measure of fracture toughness when LEFM is not applicable to materials experiencing large plastic deformation (Wells, 1961). According to this concept, the sharp crack is blunted by plastic deformation surrounding the sharp crack tip, which leads to an opening displacement $\boldsymbol{\delta}$ perpendicular to the crack, as shown in Figure 1.25.

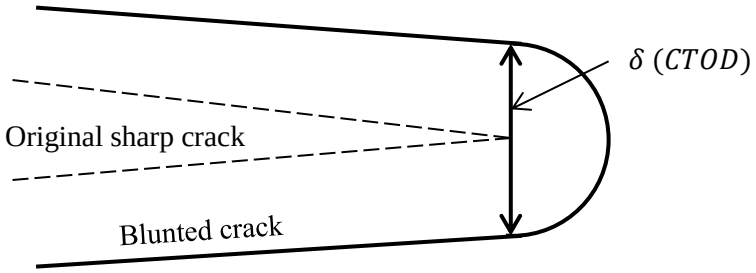

Figure 1.25 Crack tip opening displacement (CTOD) [adopted from (Janssen et al., 2004)].

According to the CTOD criterion, the fracture is expected not to happen when the critical crack tip opening displacement $\boldsymbol{\delta_c}$,exceeds or equals the crack tip opening displacement δ.

$$\delta \leq \delta_c \qquad (1.\ 22)$$

In the case of linear elasticity, the CTOD is related to the stress intensity factor K_I and energy release rate G which is shown as follows:

$$\delta = \frac{1}{E}\frac{{K_I}^2}{\sigma_{ys}} = \frac{G}{\sigma_{ys}} \qquad (1.\ 23)$$

Apart from CTOD, another important concept for elastic plastic fracture mechanics has also been developed. In 1968, Rice extended linear elastic fracture mechanics and proposed a new parameter called the J integral, which is a path independent line integral around a crack tip for linear or nonlinear elastic materials which characterises the intensity of stresses and strains around the crack tip (Rice, 1968, Janssen et al., 2004). Based on the energy approach, the J integral can be considered as the elastic plastic energy release rate, which was used to predict the initiation of cracks (Janssen et al., 2004). In 1976, Shih and Hutchinson developed the mathematical framework for the J integral approach to make this approach applicable to the design process (Shih and Hutchinson, 1976). Hence, there is a critical value of J, J_c, which leads to material failure, as follows:

$$J \leq J_c \tag{1. 24}$$

For linear elastic cases, the J integral is compatible with LEFM. In this case, J is taken equal to the energy release rate G (Janssen et al., 2004):

$$J = G = \begin{cases} \frac{K^2}{E} & (plane\ stress) \\ \frac{K^2}{E/(1-\nu^2)} & (plane\ strain) \end{cases} \tag{1. 25}$$

There are some limitations we need to consider when the J integral is used to predict the onset of crack extension. According to the deformation theory of plasticity (Jones, 2009), the difference between plastic behaviours and nonlinear elastic behaviours is the unloading behaviour. Specifically, nonlinear elastic behaviour is reversible whereas plastic behaviour is irreversible (as shown in Figure 1.26). Therefore, plastic behaviour can be modelled as nonlinear elastic behaviour only if the loading is kept applied to the material component. However, another assumption is also made for the J integral – that it is only suitable when the crack starts to extend. The J integral is not applicable to predict crack growth. This is because when crack growth occurs, the appearance of unloading is inevitable, in this case, the plastic deformation can no longer be modelled as nonlinear elastic behaviour (Janssen et al., 2004).

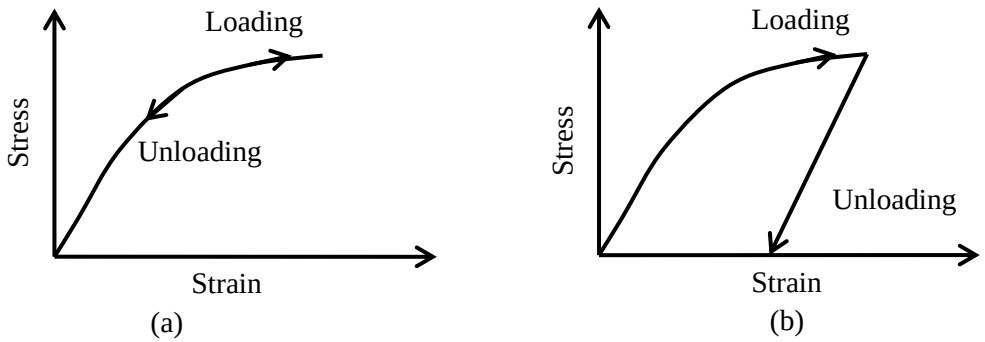

Figure 1.26 Stress–strain curves for (a) nonlinear elastic behaviour and (b) plastic behaviour (Janssen et al., 2004).

1.8 Dynamic Fracture Mechanics

Besides LEFM and EPFM, dynamic fracture mechanics is currently another important subfield of fracture mechanics that has been investigated by many researchers during the last few decades. It is focused on crack behaviour when a material is subjected to a high rate of loading. There are two main problems: crack initiation under rapidly increasing load and fast crack propagation under constant applied load, which dynamic fracture mechanics focuses on. Similar to fracture mechanics under quasi-static conditions, the stress–strain state around the crack tip are also the characteristic quantities for dynamic fracture mechanics. However, material under

dynamic loading is much more complicated than quasi-static loading both mechanically, mathematically and experimentally, because it is difficult to observe many key aspects during a very short time without interpreting the testing process. Also, data of stress and strain around the crack tip is difficult to obtain directly in a normal way (Freund, 1986). A well-known experimental rig based on a pendulum called the Charpy impact test has been used extensively in testing dynamic material behaviours of notched specimens subjected to impact loading. It was first proposed and invented by Georges Charpy in 1901 (Charpy, 1901, Siewert and Manahan, 2000). Since then, the Charpy test has become the most commonly used dynamic test by many researchers to investigate material dynamic fracture behaviours.

In most situations, the stress wave propagation, inertia effects and rate sensitivity of materials are three specific features (which are impossible to be seen in LEFM and EPFM) in dynamic fracture mechanics (Freund, 1990, Anderson, 2005). Specifically, the inertia effect occurs as a rapid load is applied or along with crack propagation. Due to this effect, the work applied to the material component will be converted to both strain energy and kinetic energy. For rate dependent materials, as discussed in section 1.4, the material strength increases as the rate of loading increases. When the stress wave generated from fast loading transfers and reflects between boundaries (such as crack or notch flanks, or the free surface), the local stress and strain fields are changed by these waves, which leads to a much more complicated fracture behaviour (Anderson, 2005, Freund, 1990).

1.8.1 Experimental techaniques used for dynamic behaviour of notched samples

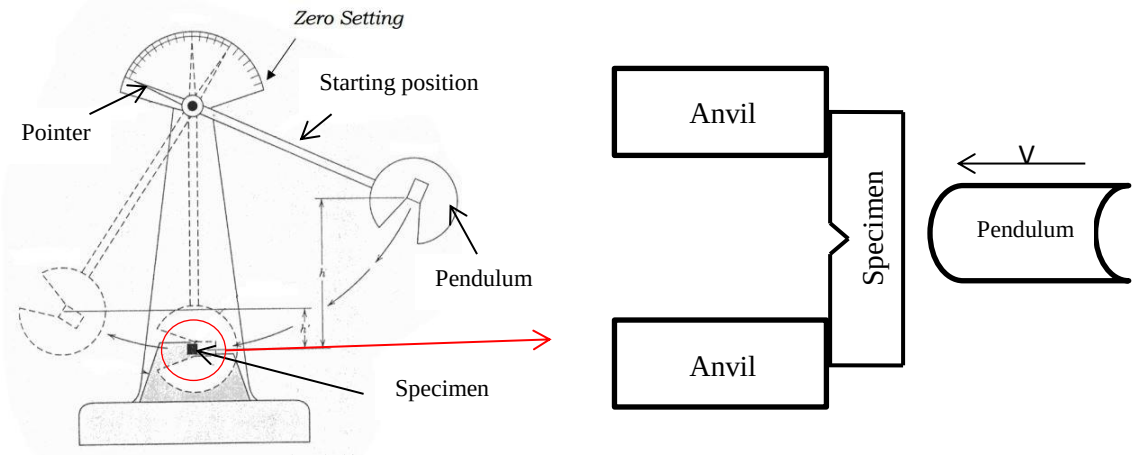

Figure 1. 27 Charpy testing rig proposed by Charpy (Charpy, 1901).

The Charpy impact test method is based on the use of a pendulumto apply an impact load to a specimen, it is one of the most cost-efficient material dynamic testing program, which involves striking a notched specimen with a controlled weight pendulum swung from a set height (as the schematic representation of the Charpy test shown in Figure 1.27). The specimen is supported

by its two anvils and struck on the opposite face to the notch by the pendulum. The fracture toughness can be given by measuring the amount of absorbed energy in damaging the specimen. The pendulum swings through during the test, the height of the swing being a measure of the amount of energy absorbed in fracturing the specimen. Generally, the results from three specimens tested at any one temperature will be averaged. Alternatively, tests are carried out at a range of temperatures in order to generate a ductile to brittle transition curve (Figure 1.20).

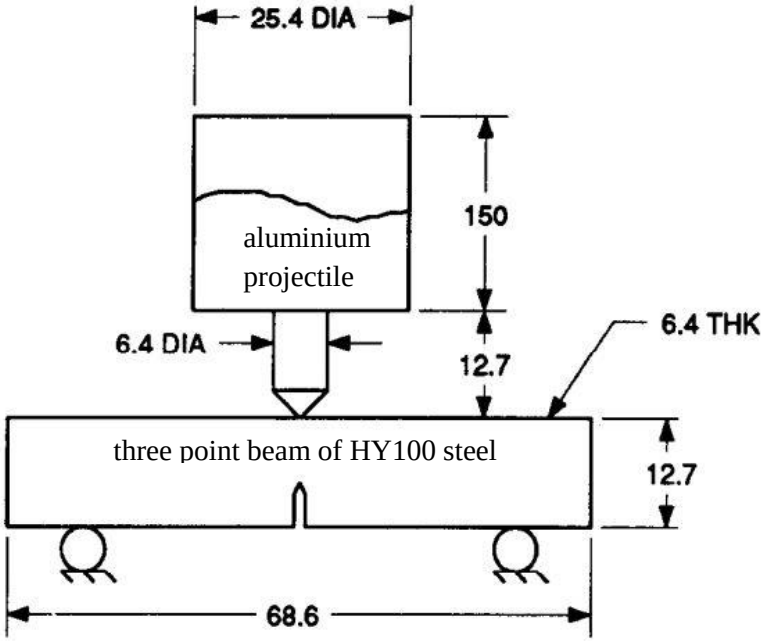

Figure 1. 28 Impact fracture toughness test using three-point bend fracture specimen (all dimensions are in millimetres) (Premack and Douglas, 1993).

Additionally, three-point bending test method has also been used widely in order to investigate the dynamic behaviours of materials. Specifically, Permack and Douglas (1993) tested dynamic fracture toughness of a pre-cracked three point beam of HY100 steel subjected to impact load. As shown in Figure 1.28, an aluminium projectile is fired from a gas gun into the hardened steel top that is held against the three point bend fracture specimen. Moreover, based on the three-point bending test method, a classical Split Hopkinson Pressure Bar was modified and performed to measure the dynamic fracture toughness of material aluminium alloy 7075-T651 (Rubio, et.al, 2003). As shown in Figure 1.29, the input bar was impacted by a projectile and transfer the compressive wave to the specimen to product the impact load.

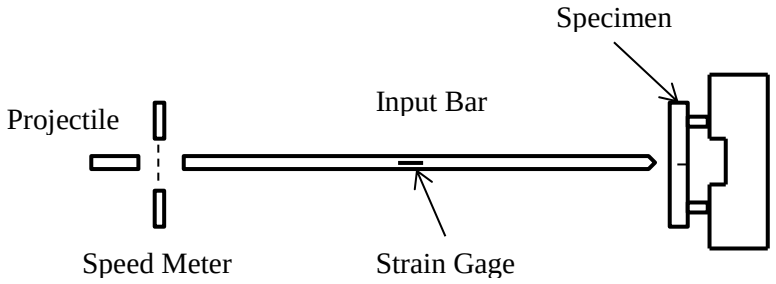

Figure 1. 29 Modified Split Hopkinson Pressure Bar based on three-point bending test method.

1.8.2 LEFM under dynamic loading

As introduced in section 1.7, LEFM describes the relationship between stress fields in the vicinity of the crack tip and applied loads. However, if the loads are applied suddenly, the inertial effects must be considered together with material stiffness in order to balance the loads. When the material is assumed as linear, dynamic fracture mechanics can be simplified as dynamic linear elastic fracture mechanics, which is expressed as elasto-dynamic fracture mechanics (Freund, 1990).

In terms of a stationary crack under rapid loading, in this context, the dynamic fracture toughness is an important parameter to characterise dynamic fractures; it has been investigated by many researchers during the last half century. (Nakamura et al., 1986, Nakamura et al., 1988, Rice et al., 1973). After the advent of Linear Elastic Fracture Mechanics (LEFM), accurate investigations were also carried out to study the relationship between material fracture toughness and the rate of applied loading. As to this aspect, examination of the state of the art (Wiesner and MacGillivray, 1999, Yokoyama and Kishida, 1989, Li, 1999, Chen et al., 1993, Ravi-Chandar and Knauss, 1984, Foster et al., 2011) suggests that, at room temperature, the fracture toughness can either decrease, increase, or remain constant as the stress intensity factor rate (SIFR) increases, this mainly depends on the microstructural features of the metallic material being investigated.

For example, Wiesner and MacGillivray employed the Charpy test to determine the fracture toughness behaviours of some steels. From their point of view, increases in yield and tensile strength results in reducing the brittle fracture toughness of most steels and an increasing loading rate has an effect equivalent to decreasing the temperature (Wiesner and MacGillivray, 1999). In detail, Wiesner and MacGillivray concluded in their paper that the fracture toughness of BS11 rail steel (Figure 1.30) and A533B steel (Figure 1.31) decreases with a rise in loading rate (in the form of stress intensity factor rate $\dot{K}$).

However, the negative loading rate sensitivity for fracture toughness does not always happen in steels. For instance, from the results plotted in Figure 1.32, the material 0.4%C Cr Mo steel shows a positive rate sensitivity of dynamic fracture toughness to the loading rate (Wiesner and MacGillivray, 1999). Additionally, the fracture toughness sensitivity to loading rate can change from negative to positive when the test temperature exceeds a certain value.

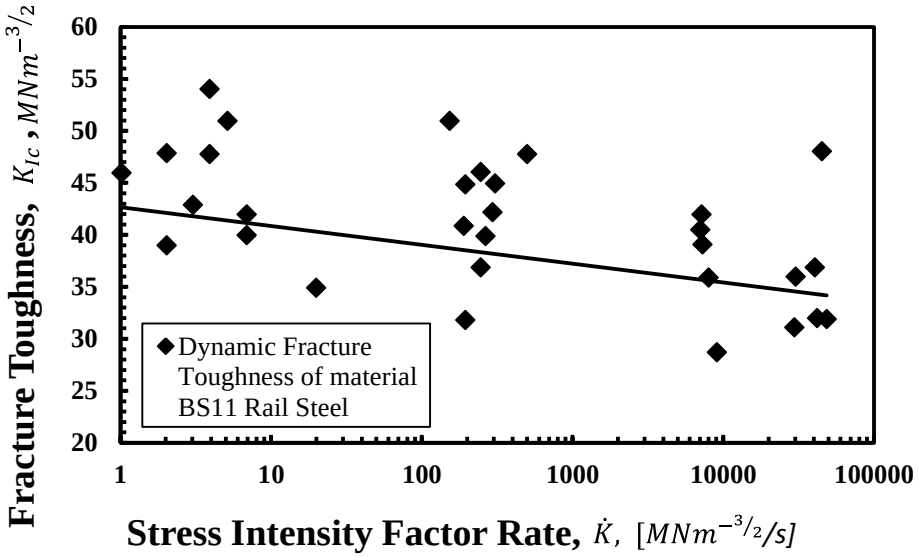

Figure 1. 30 Effect of loading rate (in the form of stress intensity factor rate) on dynamic fracture toughness of BS11 rail steel (MacGillivray, 1990).

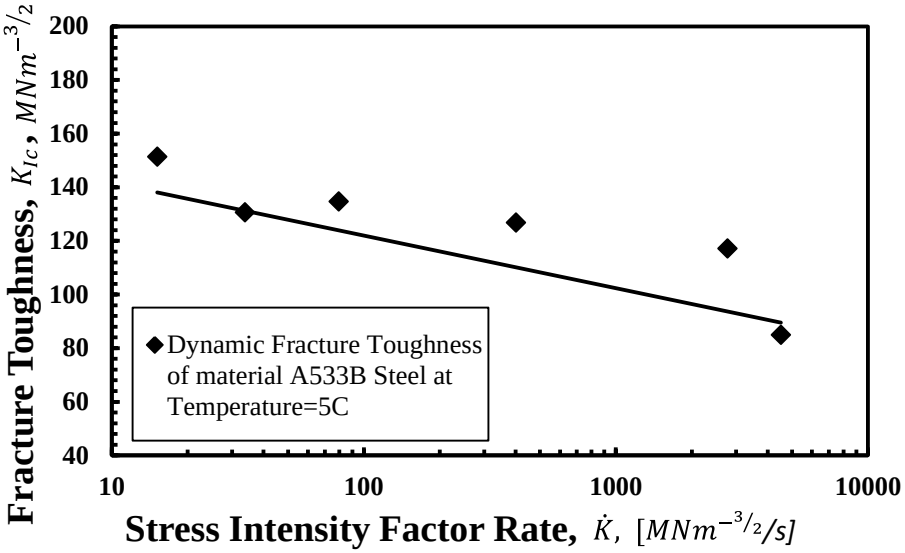

Figure 1. 31 Effect of loading rate (in the form of stress intensity factor rate) on dynamic fracture toughness of A533B steel (Ireland, 1977).

Moreover, according to the results published by Yokoyama and Kishida (1989), the fracture toughness of aluminium alloy 7075-T6 subjected to dynamic loading remains the same as the fracture toughness tested under quasi-static conditions. In other words, this means that the fracture toughness for the alloy 7075-T6 is rate independent (as shown in Figure 1.33). On the contrary, due to the adiabatic heating and low thermal conductivity of the alloy Ti-6246, during testing (Yokoyama and Kishida, 1989) at a loading rate of log $\dot{K}_I$=6$MNm^{-3/2} \cdot s^{-1}$, the fracture toughness of this alloy was about 50 percent higher ($K_{Id}/K_{Ic} \approx 1.5$) than the fracture toughness obtained under quasi-static conditions, and the results are plotted in Figure 1.34.

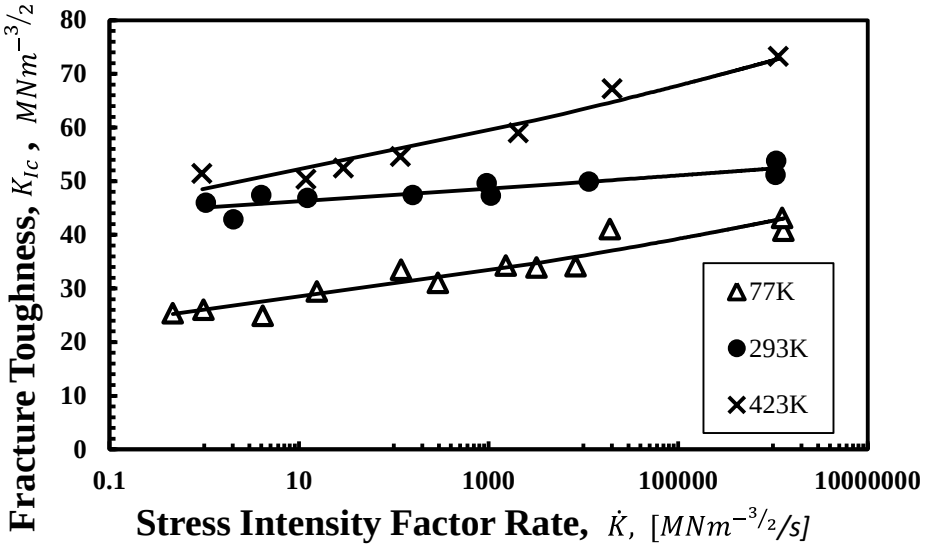

Figure 1. 32 Effect of loading rate (in the form of stress intensity factor rate) on dynamic fracture toughness of 0.4%C Cr Mo steel; (Wiesner and MacGillivray, 1999).

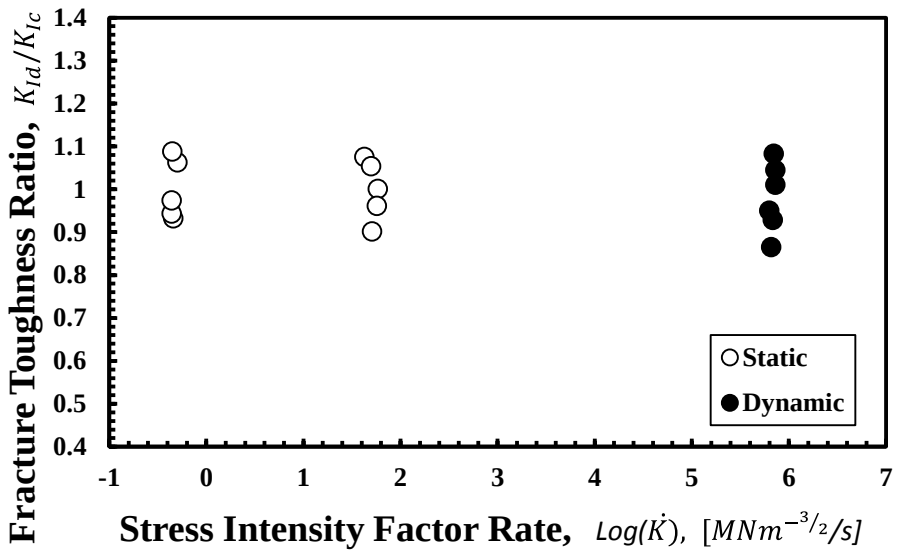

Figure 1. 33 Effect of loading rate on fracture toughness of 7075-T6 aluminium alloy (Yokoyama and Kishida, 1989).

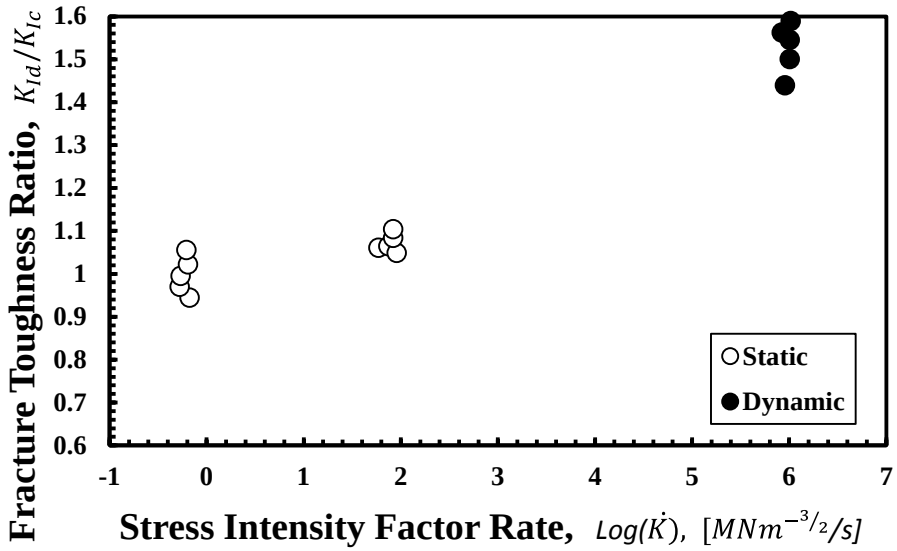

Figure 1.34 Effect of loading rate on fracture toughness of Ti-6246 alloy (Yokoyama and Kishida, 1989).

Therefore, according to the rate sensitivity of fracture toughness, the stress field under mode I dynamic loading in the vicinity of the crack tip can be described as similar to the one under quasi-static conditions. The only difference between them is the time dependent stress intensity factor (Freund, 1990, Ravi-Chandar, 2004). The stress components under mode I loading conditions can be expressed as follows:

$$\sigma_{xx} = \frac{K_I(t)}{\sqrt{2\pi r}} cos\left(\frac{\theta}{2}\right)\left[1 - sin\left(\frac{\theta}{2}\right) sin\left(\frac{3\theta}{2}\right)\right] \quad (1.\ 26)$$

$$\sigma_{yy} = \frac{K_I(t)}{\sqrt{2\pi r}} cos\left(\frac{\theta}{2}\right)\left[1 + sin\left(\frac{\theta}{2}\right) sin\left(\frac{3\theta}{2}\right)\right] \quad (1.\ 27)$$

$$\tau_{xy} = \frac{K_I(t)}{\sqrt{2\pi r}} cos\left(\frac{\theta}{2}\right) sin\left(\frac{\theta}{2}\right) cos\left(\frac{3\theta}{2}\right) \quad (1.\ 28)$$

Moreover, due to difficulty of dynamic testing discussed above, the FE analysis is playing a pivotal role in understanding dynamic behaviours, in next section, one of the most widely used material model called Johnson-Cook model will be introduced.

1.9 Johnson-Cook material model

The **Johnson-Cook** flow stress model is one of the most commonly used material model in analysing dynamic material responses subjected to large strain, high strain rate and elevated temperature (Hallquist, 2007). The constitutive law of this model was first proposed and used by Johnson and Cook in 1983 (1983) which is given by:

$$\sigma_y = (A + B\bar{\varepsilon}^{p\,n})(1 + C\ln\dot{\varepsilon}^*)(1 - T^{*m}) \quad (1.\ 29)$$

A, B, n, and C are all assumed as material constants, where A indicates the yield stress at 0.2% offset strain under quasi-static conditions; constants B and n are related to the strain hardening effect of the material. According to the investigations done by the pioneering researchers, the strain hardening parameters A, B, and n can be determined by fitting the model to sets of quasi-static experimental data (Kang et al., 1998, Milani et al., 2009, Milani et al., 2006, Børvik et al., 2001, Majzoobi et al., 2010, Shrot and Bäker, 2012), this method will be discussed in chapter 5 in detail. $\bar{\varepsilon}^p$ is the effective plastic strain. In the second set of brackets, C is the strain rate sensitivity. The value C can be determinated experimentally by using Split Hopkinson Pressure Bar (SHPB). $\dot{\varepsilon}^*$ is the normalised effective strain rate, which can be calculated as follows:

$$\dot{\varepsilon}^* = \frac{\dot{\bar{\varepsilon}}^p}{\dot{\varepsilon}_0} \quad (1.\ 30)$$

where $\dot{\bar{\varepsilon}}^p$ is effective plastic strain rate, and $\dot{\varepsilon}_0$ is reference strain rate. In the third set of beackets, T^* indicates homologous temperature, which can be calculated as follows:

$$T^{*m} = \frac{T - T_{room}}{T_{melt} - T_{room}} \quad (1.\ 31)$$

where T, T_{room}, and T_{melt} are working temperature room temperature and melting temperature. When the thermal effects and damage are ignored, a much less expensive model call Simplified Johnson-Cook material model is recommended, which is given by:

$$\sigma_y = (A + B\bar{\varepsilon}^{p\,n})(1 + C\ln\dot{\varepsilon}^*) \quad (1.\ 32)$$

In terms of elasto-plastic simulations, which will be discussed in chapter 5, the Simplified Johnson-Cook material model will be used.

1.10 Conclusion

To conclude, from the content discussed above, in a very general way, we can say that the dynamic failure strength of metallic materials increases as the loading rate increases. However, some metals may actually exhibit decreased strength with increased strain rate. This holds true for both plain and notched samples.

In terms of the dependence of material properties on the loading rate applied in tests, researchers had given explanations regarding the mechanisms affected by stain rate. For instance, the complex dynamic material behaviours can be attributed to different deformation mechanisms, such as thermal activating mechanism, enhanced rate of dislocation generation and viscous drag mechanism. Under dynamic loading, the plastic deformation was confined to a restricted area that called Adiabatic Shear Band (ASB), this area always occurred along with internal cracks that result in final material failure (Zhang et al., 2015). Moreover, to the role of thermal activation in control of deformation mechanisms , some may argue that this phenomenal can be associated with the increase in the thermal component of the flow stress (Lindholm et al., 1971), and the complex precipitation alloys also have significant effect on the strain rate sensitivity.

Finally, it can be found that the dynamic behaviour of metallic material subjected to high rate of loading has been investigated and studied a lot. but only a few cases had tried to understand the dynamic behaviours of material components having stress concentration phenomenon. Moreover, there is no an acceptable commonly design methodology has been agreed by the international scientific community to design dynamic mateiral strength of notched components. This is the main reason why we are going to make a big effort in order to find a simply analysical solution for predicting dynamic failure of notched samples. In order to better understand the main features of the TCD, it is worth summarising briefly the dundamental idea this theory is based on, as discussed in next Chapter.

References

ANDERSON, T. L. 2005. *Fracture mechanics: fundamentals and applications*, CRC press.

ARMSTRONG, R. & WALLEY, S. 2008. High strain rate properties of metals and alloys. *International Materials Reviews,* 53**,** 105-128.

ASHBY, M. F. & ASHBY, M. F. 1998. *Engineering materials 2 : an introduction to microstructures, processing and design,* Oxford, Oxford : Butterworth-Heinemann, 1998.

ASHBY, M. F. & JONES, D. R. H. 1996. *Engineering materials 1 : an introduction to their properties and applications,* Oxford, Oxford : Butterworth-Heinemann, 1996.

BØRVIK, T., HOPPERSTAD, O., BERSTAD, T. & LANGSETH, M. 2001. A computational model of viscoplasticity and ductile damage for impact and penetration. *European Journal of Mechanics-A/Solids,* 20**,** 685-712.

BRINSON, H. F. & BRINSON, L. C. 2015. Stress and strain analysis and measurement. *Polymer Engineering Science and Viscoelasticity.* Springer.

BRISBANE, A. 1963. The Investigation of the Effects of Loading Rate and Stress Concentration Factors on the Notch Properties of Three Sheet Alloys at Subzero Temperatures. DTIC Document.

BROEK, D. 1982. *Elementary engineering fracture mechanics,* The Hague, Martinus Nijhoff Publisher.

CAO, Y., AHLSTRÖM, J. & KARLSSON, B. 2015. The influence of temperatures and strain rates on the mechanical behavior of dual phase steel in different conditions. *Journal of Materials Research and Technology,* 4**,** 68-74.

CHARPY, G. 1901. Note sur l'essai des métaux à la flexion par choc de barreaux entaillés. *Mémoires et comptes rendus de la société des ingénieurs civils de France***,** 848-877.

CHEN, G., WANG, Y., YANG, W., ZHUQING, S., REN, R., ZHU, S. & AL, S. 1993. Effect of strain rate on the mechanical properties of Ti-24Al-11Nb. *Journal of Materials Science and Technology,* 9**,** 219-222.

DAVIES, R. 1948. A critical study of the Hopkinson pressure bar. *Philosophical Transactions of the Royal Society of London. Series A. Mathematical and Physical Sciences***,** 375-457.

DIETER, G. E. & BACON, D. J. 1986. *Mechanical metallurgy*, McGraw-Hill New York.

EL-MAGD, E. 1994. Mechanical properties at high strain rates. *JOURNAL DE PHYSIQUE IV,* 4**,** C8-149 - C8-170.

EWALDS, H. L. & WANHILL, R. J. H. 1984. *Fracture mechanics,* London, London : Edward Arnold, 1984.

FOSTER, J., CHEN, W. & LUK, V. 2011. Dynamic crack initiation toughness of 4340 steel at constant loading rates. *Engineering Fracture Mechanics,* 78**,** 1264-1276.

FREUND, L. 1986. The mechanics of dynamic fracture. DTIC Document.

FREUND, L. B. 1990. *Dynamic Fracture Mechanics*, Cambridge, Cambridge University Press.

GRIFFITH, A. A. 1921. The phenomena of rupture and flow in solids. *Philosophical transactions of the royal society of london. Series A, containing papers of a mathematical or physical character*, 221**,** 163-198.

GROOVER, M. P. 2010. *Fundamentals of Modern Manufacturing: Materials, Processes, and Systems*, John Wiley & Sons.

HALLQUIST, J. O. 2007. LS-DYNA keyword user's manual. *Livermore Software Technology Corporation*, 970.

HOPKINSON, B. 1914. A Method of Measuring the Pressure Produced in the Detonation of High Explosives or by the Impact of Bullets. *Proceedings of the Royal Society of London. Series A, Containing Papers of a Mathematical and Physical Character*, 89**,** 411-413.

INGLIS, C. E. 1913. Stresses in a plate due to the presence of cracks and sharp corners. *Transactions of the Institute of Naval Architects*, 137**,** 219-241.

IRWIN, G. 1948. Fracture dynamics, Fracturing of Metals. American Society of Metals. Cleveland.

IRWIN, G. Plastic zone near a crack and fracture toughness. Sagamore Research Conference, 1961 Syracuse NY. Syracuse University Research Institute,, 63-78.

JANSSEN, M., ZUIDEMA, J. & WANHILL, R. J. H. 2004. *Fracture mechanics*, London

New York, London, 2004.

JASWON, M. & EL-DAMANAWI, K. 1991. What is a dislocation? *Mathematical and Computer Modelling*, 15**,** 205-213.

JIANG, C. & CHEN, M. 1974. Dynamic Properties of Materials. Part 2. Aluminum Alloys. DTIC Document.

JOHNSON, G. R. & COOK, W. H. A constitutive model and data for metals subjected to large strains, high strain rates and high temperatures. Proceedings of the 7th International Symposium on Ballistics, 1983. The Hague, The Netherlands, 541-547.

JONES, R. M. 2009. *Deformation theory of plasticity*, Bull Ridge Corporation.

KANG, W. J., CHO, S. S., HUH, H. & CHUNG, D. T. 1998. Identification of Dynamic Behavior of Sheet Metals for an Auto-Body with Tension Split Hopkinson Bar. SAE International.

KOBAYASHI, H. & ONOUE, H. 1943. Brittle Fracture of Liberty Ships. *Failure Knowledge Database*, 100.

KOLSKY, H. 1949. An investigation of the mechanical properties of materials at very high rates of loading. *Proceedings of the Physical Society. Section B*, 62**,** 676.

LEE, O. S. & KIM, M. S. 2003. Dynamic material property characterization by using split Hopkinson pressure bar (SHPB) technique. *Nuclear Engineering and Design,* 226**,** 119-125.

LI, C.-J. 1999. Effects of temperature and loading rate on fracture toughness of structural steels. *Materials & Design,* 21**,** 27-30.

LIANG, Z. Y., HUANG, W. & HUANG, M. X. 2015. Suppression of dislocations at high strain rate deformation in a twinning-induced plasticity steel. *Materials Science and Engineering: A,* 628**,** 84-88.

LINDHOLM, U. S. 1964. Some experiments with the split hopkinson pressure bar. *Journal of the Mechanics and Physics of Solids,* 12**,** 317-335.

LINDHOLM, U. S., BESSEY, R. L. & SMITH, G. V. 1971. Effect of Strain Rate on Yield Strength, Tensile Strength, and Elongation of Three Aluminium Alloys. *J Mater,* 6**,** 119-133.

LINDHOLM, U. S. & YEAKLEY, L. M. 1965. Dynamic deformation of single and polycrystalline aluminium†. *Journal of the Mechanics and Physics of Solids,* 13**,** 41-53.

MACGILLIVRAY, H. 1990. Project to Develop a Standard Method of Fracture Toughness Testing at Very High Loading Rates', Prepared by the European Group on Fracture Working Party on High Rate Conventional Fracture Testing, DTI Ref. Fracture Working Party.

MACH, K. J., NELSON, D. V. & DENNY, M. W. 2007. Techniques for predicting the lifetimes of wave-swept macroalgae: a primer on fracture mechanics and crack growth. *Journal of Experimental Biology,* 210**,** 2213-2230.

MAJZOOBI, G., FRESHTEH-SANIEE, F., KHOSROSHAHI, S. F. Z. & MOHAMMADLOO, H. B. 2010. Determination of materials parameters under dynamic loading. Part I: Experiments and simulations. *Computational Materials Science,* 49**,** 192-200.

MILANI, A., DABBOUSSI, W., NEMES, J. & ABEYARATNE, R. 2009. An improved multi-objective identification of Johnson–Cook material parameters. *International Journal of Impact Engineering,* 36**,** 294-302.

MILANI, A. S., DABBOUSSI, W., EL-LAHHAM, C., NEMES, J. A. & ABEYARATNE, R. C. 2006. On obtaining material parameters for general purpose finite element models. *Proceedings of the 17th IASTED international conference on Modelling and simulation.* Montreal, Canada: ACTA Press.

MORRIS, J. W. 2001. *Dislocation Plasticity: an Overview, in Encyclopedia of Materials Science and Technology*.

NAKAMURA, T., SHIH, C. & FREUND, L. 1986. Analysis of a dynamically loaded three-point-bend ductile fracture specimen. *Engineering Fracture Mechanics,* 25**,** 323-339.

NAKAMURA, T., SHIH, C. & FREUND, L. 1988. Three-dimensional transient analysis of a dynamically loaded three-point-bend ductile fracture specimen. *Nonlinear Fracture Mechanics: Volume I Time-Dependent Fracture.* ASTM International.

NEUBER, H. 1961. Theory of stress concentration for shear-strained prismatical bodies with arbitrary nonlinear stress-strain law. *Journal of Applied Mechanics,* 28**,** 544-550.

NODA, N. A., OHTSUKA, H., ZHENG, H., SANO, Y., ANDO, M., SHINOZAKI, T. & GUAN, W. 2015. Strain rate concentration and dynamic stress concentration for double-edge-notched specimens subjected to high-speed tensile loads. *Fatigue & Fracture of Engineering Materials & Structures,* 38**,** 125-138.

OOSTERKAMP, L. D., IVANKOVIC, A. & VENIZELOS, G. 2000. High strain rate properties of selected aluminium alloys. *Materials Science and Engineering: A,* 278**,** 225-235.

OROWAN, E. 1934. Mechanical strength properties and real structure of crystals. *Z. Kristallogr,* 89**,** 327-343.

PETERSON, R. E. 1974. *Stress Concentration Factors: Chart and Relations Useful in Making Strength Calculations for Machine Parts and Structural Element*, John Wiley and Sons.

PILKEY, W. D. & PILKEY, D. F. 2008. *Peterson's stress concentration factors*, John Wiley & Sons.

POLANYI, M. 1934. Über eine Art Gitterstörung, die einen Kristall plastisch machen könnte. *Zeitschrift für Physik,* 89**,** 660-664.

PREMACK, T. & DOUGLAS, A. S. 1993. An analysis of the crack tip fields in a ductile three-point bend specimen subjected to impact loading. *Engineering Fracture Mechanics,* 45**,** 717-728.

RAVI-CHANDAR, K. 2004. *Dynamic fracture*, Elsevier.

RAVI-CHANDAR, K. & KNAUSS, W. 1984. An experimental investigation into dynamic fracture: I. Crack initiation and arrest. *International Journal of Fracture,* 25**,** 247-262.

RICE, J., PARIS, P. & MERKLE, J. 1973. Some further results of J-integral analysis and estimates. *Progress in flaw growth and fracture toughness testing.* ASTM International.

RICE, J. R. 1968. A path independent integral and the approximate analysis of strain concentration by notches and cracks. *Journal of applied mechanics,* 35**,** 379-386.

ROARK, R. J. 1975. *Formulas for stress and strain*, New York, McGraw-Hill.

ROSSMANITH, H. 1995. AN INTRODUCTION TO K. WIEGHARDT'S HISTORICAL PAPER "ON SPLITTING AND CRACKING OF ELASTIC BODIES". *Fatigue & Fracture of Engineering Materials & Structures,* 18**,** 1367-1369.

SAKINO, K. 2008. Strain rate dependence of dynamic flow stress of 2017 aluminum alloy at very high strain rates. *International Journal of Modern Physics B,* 22**,** 1209-1214.

SHARMA, C. P. 2003. *Engineering materials: properties and applications of metals and alloys*, PHI Learning Pvt. Ltd.

SHIH, C. & HUTCHINSON, J. 1976. Fully plastic solutions and large scale yielding estimates for plane stress crack problems. *Journal of Engineering Materials and Technology,* 98**,** 289-295.

SHROT, A. & BÄKER, M. 2012. Determination of Johnson–Cook parameters from machining simulations. *Computational Materials Science,* 52**,** 298-304.

SIEWERT, T. A. & MANAHAN, M. P. 2000. *Pendulum impact testing: a century of progress*, ASTM International.

STOWELL, E. Z. 1950. Stress and strain concentration at a circular hole in an infinite plate.

TAYLOR, G. I. 1934. The mechanism of plastic deformation of crystals. Part I. Theoretical. *Proceedings of the Royal Society of London. Series A, Containing Papers of a Mathematical and Physical Character,* 145**,** 362-387.

TESTING, A. S. F. & MATERIALS. ASTM designation E8/E8m-13a Standard Test Methods for Tension Testing of Metallic Materials. 2015. ASTM.

TOPPER, T., WETZEL, R. & MORROW, J. 1967. Neuber's rule applied to fatigue of notched specimens. DTIC Document.

VOLTERRA, V. Sur l'équilibre des corps élastiques multiplement connexes. Annales scientifiques de l'École normale supérieure, 1907. Société mathématique de France, 401-517.

WELLS, A. A. Unstable crack propagation in metals: cleavage and fast fracture. Proceedings of the crack propagation symposium, 1961.

WELSS, A. 1955. *The Conditions for Fast Fracture in Aluminium Alloys with Particular Reference to the Comet Failures*, British Welding Research Assoc.

WESTGAARD, H. 1939. Bearing pressure and cracks. *J. Appl. Maths Mech,* 6**,** 49-53.

WIESNER, C. S. & MACGILLIVRAY, H. 1999. Loading Rate Effects on Tensile Properties and Fracture Toughness of Steel. *1999 TAGSI Seminar, Cambridge, IoM Publication***,** 149.

YOKOYAMA, T. & KISHIDA, K. 1989. A novel impact three-point bend test method for determining dynamic fracture-initiation toughness. *Experimental Mechanics,* 29**,** 188-194.

YOUNG, W. C. & BUDYNAS, R. G. 2002. *Roark's formulas for stress and strain*, McGraw-Hill New York.

ZENER, C. & HOLLOMON, J. 1944. Effect of strain rate upon plastic flow of steel. *Journal of Applied physics,* 15**,** 22-32.

ZHANG, X. M., LI, H. J., LI, H. Z., GAO, H., GAO, Z. G., LIU, Y. & LIU, B. 2008. Dynamic property evaluation of aluminum alloy 2519A by split Hopkinson pressure bar. *Transactions of Nonferrous Metals Society of China (English Edition),* 18**,** 1-5.

ZHANG, Y., OUTEIRO, J. C. & MABROUKI, T. 2015. On the Selection of Johnson-cook Constitutive Model Parameters for Ti-6Al-4 V Using Three Types of Numerical Models of Orthogonal Cutting. *Procedia CIRP,* 31**,** 112-117.

ZHU, D., MOBASHER, B., RAJAN, S. & PERALTA, P. 2011. Characterization of Dynamic Tensile Testing Using Aluminum Alloy 6061-T6 at Intermediate Strain Rates. *Journal of Engineering Mechanics,* 137**,** 669-679.

Chapter 2 Introduction to the Theory of Critical Distances under Static Loading

2.1 Introduction

As discussed in Chapter 1, LEFM and EPFM are simplified theories which deal with the behaviours of sharp cracks (i.e., root radius tending to 0) in material components. LEFM only applies to situations where the plastic deformation is limited to a small area around the crack tip. EPFM is suitable for the cases where the material exhibits a large area of nonlinear deformation in the vicinity of the crack tip. However, it was found that these theories are not applicable to many practical applications. For example, LEFM and EPFM cannot be used to assess the failure of structures and components containing notches, which form a stress state in between those for plain and sharp cracks. Therefore, it is interesting to develop an applicable method that is suitable for all kinds of stress raisers (for example cracks, notches, smooth samples and some other non-standard geometrical features). It is well known that under quasi-static loading, notches have a detrimental effect on the overall static strength of engineering materials (Nui et al., 1994, Toth, 1998). Accordingly, appropriate design methods have to be used to accurately design components experiencing stress concentration phenomena. In this context, it is recognised that the so-called Theory of Critical Distances (TCD) is the most effective tool which can be used by structural engineers to take into account the weakening effect of all kinds of notches (Taylor, 2007). In this chapter, the development and basic methodology of the TCD will introduced, a simplest form of this method will be shown to demonstrate how it can be used.

2.2 Development of the Theory of Critical Distance

The fundamental idea on which the TCD is based was first proposed in about the middle of the last century to specifically estimate the high-cycle fatigue strength of notched components. In more detail, Neuber (1936) suggested performing the high-cycle fatigue assessment of metals containing notches through an effective stress calculated by averaging the linear- elastic stress over a straight line emanating from the notch tip. A few years later, Peterson (1959) observed that the problem could greatly be simplified by directly using, as effective stress, the linear-elastic stress evaluated at a given distance from the notch apex. In both Neuber's and Peterson's approach, this length scale parameter was treated as a material property. Late in the 1960s, Novozhilov (1969) has proven that Neuber's method could also be derived by using an elegant energy argument. In 1974, Whitney and Nuismer (1974) showed that the TCD could be used to estimate the static strength of notched composite, the material critical length being directly determined through the LEFM fracture toughness and the ultimate tensile strength. Toward the end of the last century, Tanaka (1983) and Taylor (1999) have proven that the TCD could

successfully be employed to estimate notch fatigue limits also by calculating the necessary critical distance via the threshold value of the stress intensity factor and the plain fatigue limit. Owing to its accuracy in assessing the detrimental effect of notches, in recent years, the TCD has gained new popularity being used to address a variety of structural integrity problems (Taylor, 2007). For instance, the TCD applied along with the so-called Modified Wöhler Curve Method was seen to be capable of accurately designing notched components against multiaxial fatigue (Susmel and Taylor, 2003b, Susmel, 2004, Susmel and Taylor, 2006b). Recently, it was also proven that the TCD is successful in estimating the static strength of both ductile and brittle notched materials subjected to uniaxial as well as to multiaxial static loading (Susmel and Taylor, 2008, Susmel and Taylor, 2010c). Finally, Cicero et al. (Madrazo et al., 2012, Cicero et al., 2012, Cicero et al., 2013) have successfully used the TCD to model the effect of the notch sharpness on the apparent fracture toughness.

2.3 The TCD methodology

The TCD methodology includes a group of methods: Point Method (PM), Line Method (LM), Area Method (AM) and Volume Method (VM), which have a common feature: the material length parameter called critical distance L. Point Method (PM) is the simplest form of TCD, whereas the LM, AM and VM are slightly more complex. The TCD postulates that the static strength of notched components can be estimated by directly post-processing the entire linear-elastic stress field acting on the material in the vicinity of the stress raiser being assessed. (Taylor, 2007).

If attention is focussed on notches subjected to Mode I quasi-static loading, as shown in Figure 2.1, according to the TCD, breakage takes place as soon as a critical distance depending effective stress, σ_{eff}, becomes larger than the material inherent strength, σ_0 (Susmel and Taylor, 2008). Therefore, the notched component being designed is supposed to be capable of withstanding the applied loading as long as the following condition is assured:

$$\sigma_{eff} \leq \sigma_0 \qquad (2.1)$$

One of the most interesting features of the TCD is that effective stress σ_{eff}, which can be estimated by adopting a simple linear-elastic constitutive law (Taylor, 1999 and 2007), this holding true independently from the level of ductility characterising the material under investigation (Susmel and Taylor, 2008, Susmel and Taylor, 2010c). This results in a great simplification of the design problem, allowing structural engineers to perform the required stress analysis via simple linear-elastic models done using commercial Finite Element (FE) software packages.

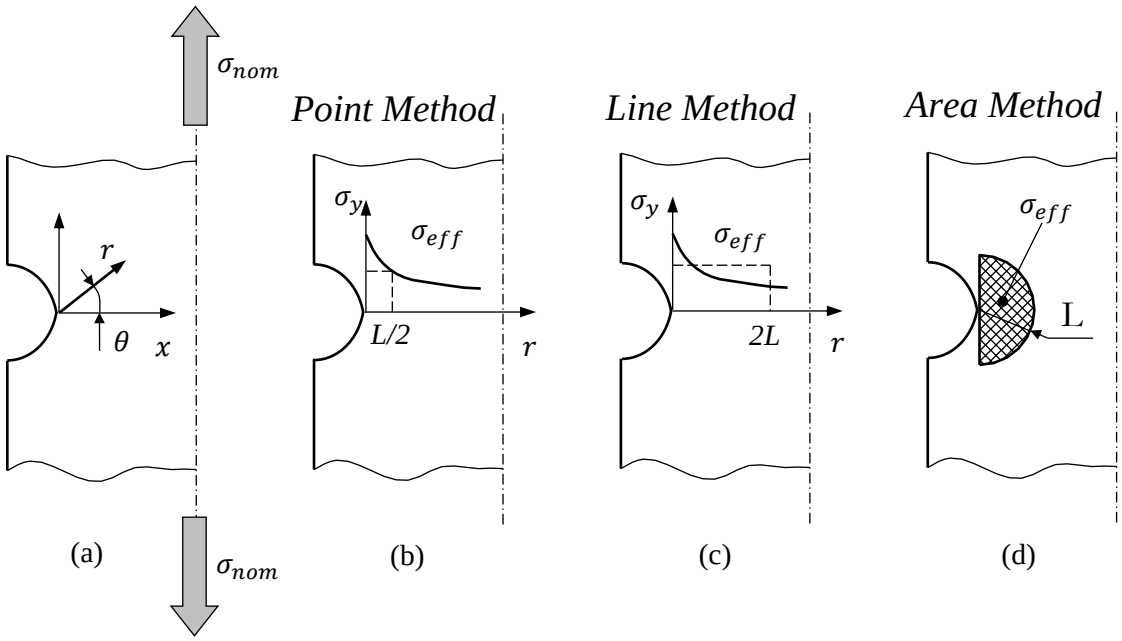

Figure 2.1 (a) Definition of the local systems of coordinates; (b) Effective stress, $\boldsymbol{\sigma_{eff}}$, calculated according to the Point Method; (c) Line Method and (d) Area Method

According to condition (2.1), to properly use the TCD in situations of practical interest, the second important information which is needed is the material inherent strength, σ_0. As to the expected values for σ_0, it is worth recalling here that the inherent strength equals the conventional ultimate tensile strength, σ_{UTS}, solely under particular circumstances, this mainly depending on the mechanical behaviour as well as on the microstructural features of the material being designed. In particular, when breakage is preceded by a certain amount of plastic deformation, σ_0 takes on a value which is larger than the ultimate tensile strength (Taylor, 2007). This obviously applies also to metallic materials (Susmel and Taylor, 2010b), even if, for certain metals, σ_0 is seen to be so close to σ_{UTS} (Susmel and Taylor, 2008) that the TCD can successfully be used by simply taking $\sigma_0=\sigma_{UTS}$. On the contrary, as far as brittle materials (such as ceramics (Taylor, 2004)) or quasi-brittle materials (such as fibre composites (Whitney and Nuismer, 1974)) are concerned, σ_0 is seen to be invariably equal to σ_{UTS}. Lastly, it should be noted that σ_0 is seen to be different from σ_{UTS} also in those situations where the presence of stress raisers leads to different failure mechanisms to those resulting in the breakage of the un-notched material (Taylor et al., 2005). These considerations clearly suggest that the most accurate way to estimate material inherent strength σ_0 is by running appropriate experiments, the recommended experimental procedure for the determination of σ_0 being explained below.

Turning back to the different formalisations of the TCD, effective stress σ_{eff} can be calculated according to either the Point Method (PM), the Line Method (LM), or the Area Method (AM) as follows (Taylor, 1999):

$$\sigma_{eff} = \sigma_y\left(\theta = 0, r = \frac{L}{2}\right) \qquad \text{(PM)} \qquad (2.\ 2)$$

$$\sigma_{eff} = \frac{1}{2L}\int_0^{2L} \sigma_y(\theta = 0, r)\, dr \qquad \text{(LM)} \qquad (2.\ 3)$$

$$\sigma_{eff} = \frac{2}{\pi L^2}\int_{-\pi/2}^{\pi/2}\int_0^{L} \sigma_1(\theta, r)\, r dr d\theta \qquad \text{(AM)} \qquad (2.\ 4)$$

The meaning of the adopted symbols as well as of the effective stress calculated according to definitions (2.2), (2.3), and (2.4) is explained in Figures from 2.1(a) to 2.1(d). Equations (2.2) to (2.4) show that, independently from the strategy adopted to determine σ_{eff}, the TCD makes use of a length scale parameter which can be estimated via the LEFM plane strain fracture toughness, K_{Ic}, and the material inherent strength, σ_0, as follows (Taylor, 2007):

$$L = \frac{1}{\pi}\left(\frac{K_{Ic}}{\sigma_0}\right)^2 \qquad (2.\ 5)$$

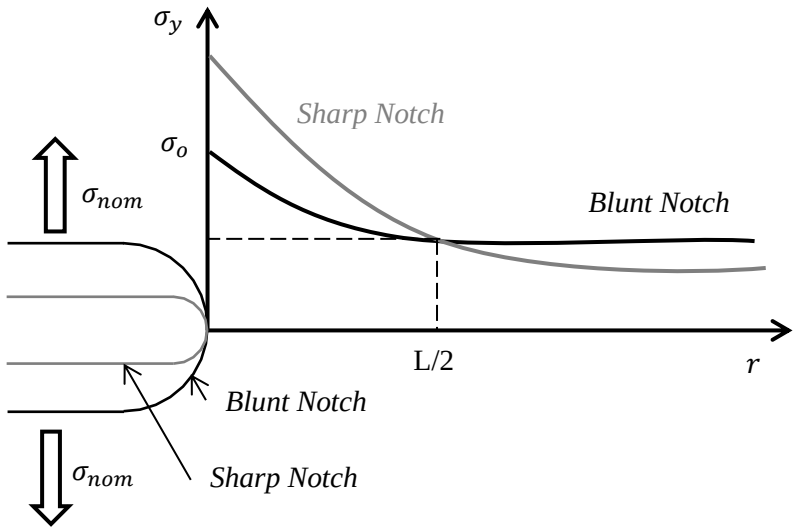

Figure 2.2 Determination of length scale parameter L and inherent strength σ_0 through experimental results generated by testing notches of different sharpness.

According to definition (2.5), as soon as K_{Ic} is known from the experiments, the determination of critical distance L is straightforward solely for those materials for which inherent material strength σ_0 is invariably equal to the ultimate tensile strength, σ_{UTS}. On the contrary, when $\sigma_0 \neq \sigma_{UTS}$, the only way to determine L is by testing samples containing notches of different sharpness (Susmel and Taylor, 2008, Susmel and Taylor, 2010c). This procedure is summarised in Figure 2.2: As postulated by the PM, the coordinates of the point at which the two linear-elastic stress-distance curves, plotted in the incipient failure condition, intersect each other allow length scale parameter L and inherent strength σ_0 to be estimated directly.

2.4 Standard procedure to predict material strength by using PM

In this subsection, the PM will be used as an example to introduce predictions of brittle fracture. For example, as flow chats plotted in Figure 2.3, a notched sample is strengthened by a uniaxial tensile stress:

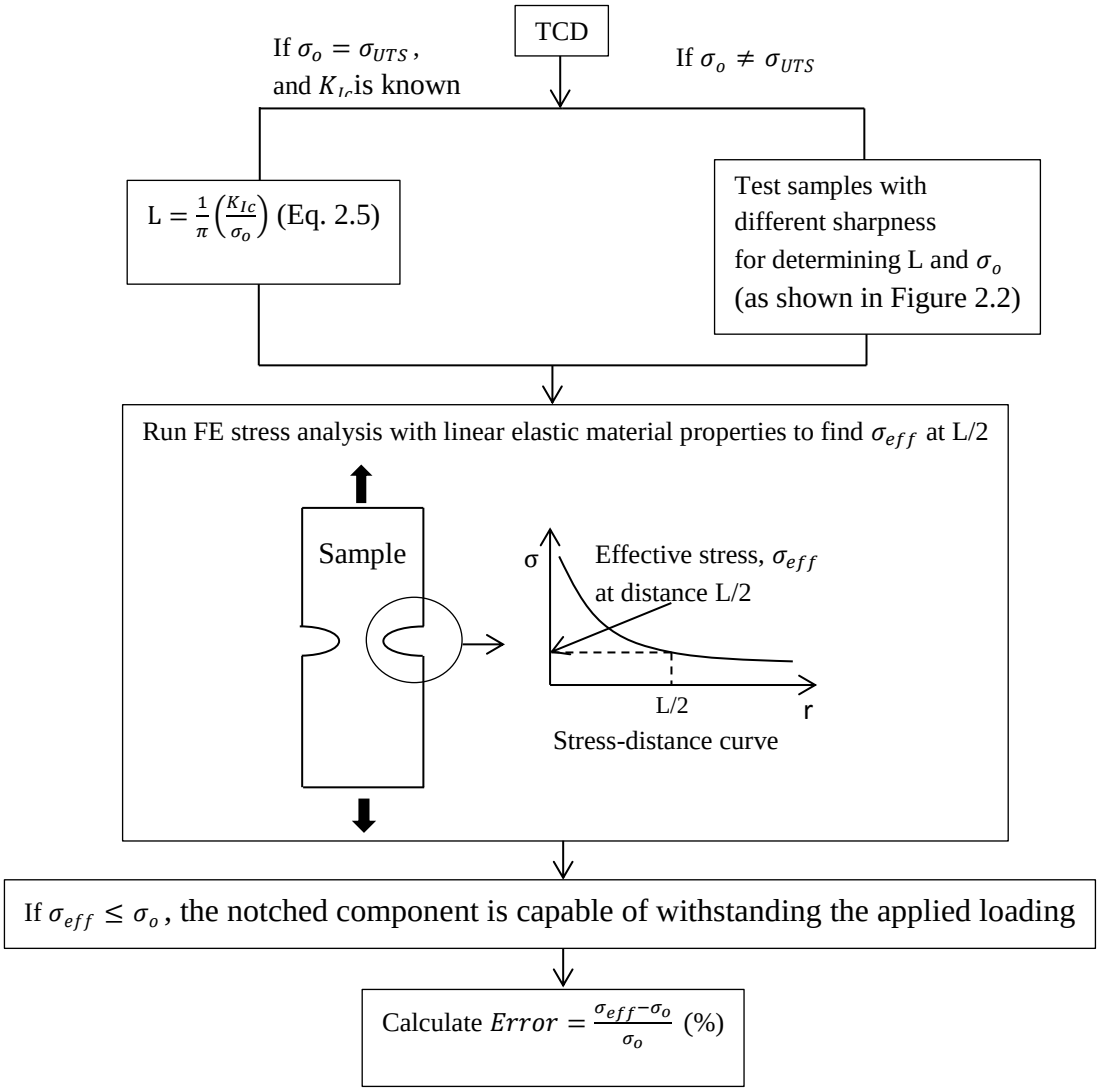

Figure 2. 3 Flow chart of TCD procedures in its simplest form of Point Method.

To conclude, it is worth observing that such an experimental procedure (Figure 2.2) based on notches of different sharpness was seen to be very accurate also to estimate the LEFM plane strain fracture toughness (Susmel and Taylor, 2010a). In fact, after determining both L and σ_0, according to the procedure schematically depicted in Figure 2.2, K_{Ic} can directly be estimated via Equation (2.5), the LEFM plane strain fracture toughness obviously becoming the unknown variable in the problem.

2.5 Applications of the Theory of Critical Distance (TCD)

As briefly introduced above, over the last century, the TCD has been employed by many researchers from different areas to assess static and fatigue failures of samples containing different types of stress raisers. In this section, the applications of the TCD will be discussed in detail. For instance, Taylor (2007) considered the practical applications of the TCD in some specific fields to predict experimental data from the literature and his own work, to prove that this methodology can be used as a design tool to accurately estimate the failure of material components containing different geometrical features and subjected to both static and fatigue loading.

2.5.1 The predictions for notched non-metallic materials

As an example, ceramic is a non-metallic material which has the properties of high hardness, wear resistance and chemical stability. This type of material has been used massively in many different applications. Mechanically, ceramic materials normally have high strength but low fracture toughness, which result in high sensitivity to the presence of material defects (Taylor, 2007, Taylor, 2013).

The scatter plot in Figure 2.4 shows the material strength in the form of measured fracture toughness versus square root of the notch radius for pre-notched alumina tested at room temperature by Tsuji et al. (1999). The solid lines in this figure are the predictions calculated using both the PM and the LM (Taylor, 2007). When applying the PM, assuming $\sigma(r) = \sigma_{UTS}$ at a distance *r=L/2*, according to the stress distance distribution described by Creager and Paris (Creager and Paris, 1967) and the investigation done by Taylor (2007), the measured fracture toughness K_{cm} can be calculated as follows:

$$K_{cm} = \sigma_{UTS}\sqrt{\pi}\left[\frac{\sqrt{(L+\rho)^3}}{L+2\rho}\right] \quad (2.6)$$

where the measured K_{cm} is the value of fracture toughness K_c calculated by replacing the half of crack length a to the notch length D. The relationship between measured K_{cm} and experimental K_c was calculated as follows (Creager and Paris, 1967, Taylor, 2007):

$$\frac{K_{cm}}{K_c} = \frac{\left(1+\frac{\rho}{L}\right)^{3/2}}{\left(1+2\frac{\rho}{L}\right)} \quad (2.7)$$

In terms of LM, when the average stress was applied over the distance from 0 to 2L, the relationship between true toughness K_{cm} and K_c was given by:

$$\frac{K_{cm}}{K_c} = \sqrt{\frac{\rho}{4L} + 1} \qquad (2.8)$$

Following the same strategy, David Taylor (2007) continued to use LM to estimate the failure strength of many other ceramics containing notches, which have been investigated by many researchers (Takahashi et al., 1985, Clark Jr and Logsdon, 1974, Bertolotti, 1973, Damani et al., 1996, Tsuji et al., 1999). The experimental data and predictions are summarised in Figure 2.5, and indicate that the LM can be employed to predict the material strength of various ceramics accurately.

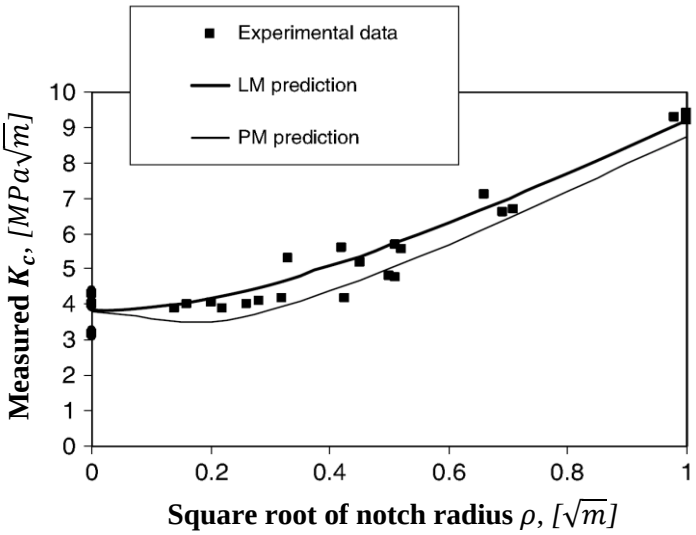

Figure 2.4 Predictions of measured fracture toughness versus square root of notch radius for alumina calculated using both PM and LM (Taylor, 2007).

According to the results plotted in Figures 2.4 and 2.5, it is obvious that both the PM and the LM can give accurate predictions for fracture toughness for the investigated alumina; the fracture toughness for notched material components can be calculated by assuming the material inherent strength $\sigma_o = \sigma_{UTS}$. However, the predictions are only applicable when the root radius ρ and the distance r are much less than the notch length D.

Moreover, the TCD has also been applied to predict brittle fracture of notched polymeric components under monotonic loading successfully by slightly modifying the TCD approach as discussed above. Different from ceramics, polymers have relatively low material strength and toughness. The scatter diagrams reported in Figure 2.6 show the experimental data for polycarbonate (PC) (Figure 2.6 (a)), un-modified epoxy (Figure 2.6 (b)) and rubber-modified epoxy (Figure 2.6 (c)) tested by Tsuji et al. (1999) and Kinloch et al. (1983) respectively. The solid lines reported in this figure indicate the accurate predictions calculated using modified PM. Specifically, in terms of the material PC, by assuming the material inherent strength σ_o is taken

to be equal to the ultimate tensile strength σ_{UTS}, according to equation 2.5, the critical distance was calculated as L=0.78mm. However, when the square root of the notch radius is higher than about 0.5 $mm^{1/2}$, the prediction is very poor; the predicted fracture toughness (the dotted line shown in Figure 26 (a)) is much lower than the experimental data. Hence, some modifications must be made in order to allow the TCD to work correctly.

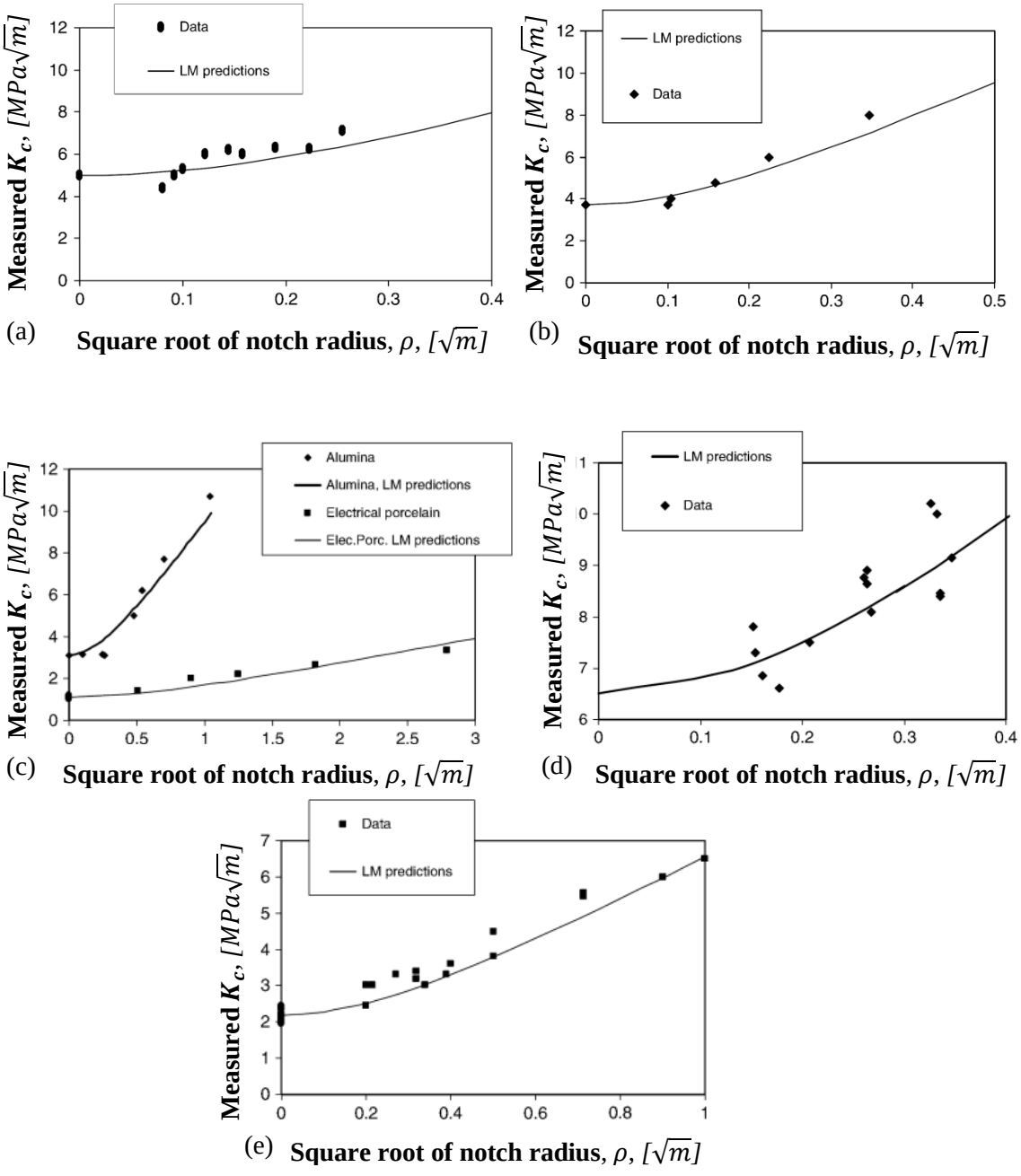

Figure 2.5 Experimental data and predictions calculated using LM (Taylor, 2007): (a) Silicon Nitride (Takahashi et al., 1985); (b) Silicon Carbide (Takahashi et al., 1985); (c) Alumina (Bertolotti, 1973); (d) MgPSZ (Damani et al., 1996); (e) Alumina at 1000^{o}C (Tsuji et al., 1999).

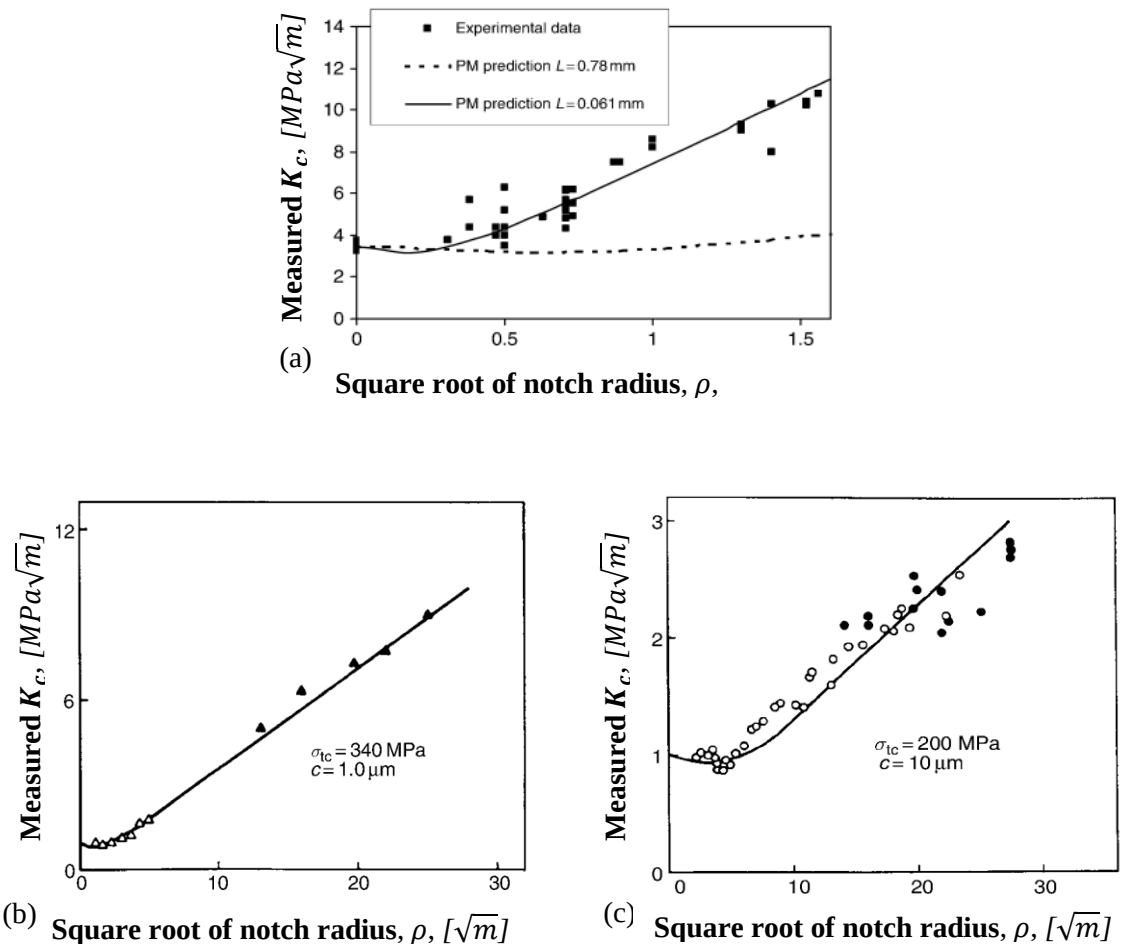

Figure 2.6 Experimental data of polymers and predictions calculated using the TCD (a) polycarbonate (PC) (Tsuji et al., 1999); (b) un-modified epoxy (Kinloch et al., 1983); (c) rubber-modified epoxy (Kinloch et al., 1983).

By trying different values of critical distance L, a best prediction was found by choosing an optimum value of L=0.061mm. Consequently, the corresponding material inherent strength σ_o must be different from the ultimate tensile strength σ_{UTS}. Additionally, Taylor also tested some notched polymer samples in his laboratory, and the results further confirmed that the modified TCD is successful in predicting the fracture strength of polymers containing stress raisers (Taylor et al., 2004, Taylor, 2007); the material inherent strength σ_o is higher than the ultimate tensile strength σ_{UTS}. It is worth noting here that, generally speaking, as far as polymers are concerned, the material inherent strength σ_o should be higher than the material ultimate tensile strength in order to make the TCD work correctly for the polymers being investigated.

2.5.2 The predictions for metallic materials

Besides ceramics and polymers, the brittle failure of metals has also been predicted by employing the TCD in Taylor's book (2007). As shown in Figure 2.7 (a), after trying different

values of critical distance for PM, an optimum critical distance of L=0.035mm was found to give rise to the best prediction for the experimental data for mild steel bar with a 2mm depth of notch, tested at a temperature of -196^{o}C (Taylor, 2007, Wilshaw et al., 1968). The curves reported in Figure 2.7(b) show the predictions from the LM and the experimental data from a specific aluminium alloy, DISPAL-2, tested at 4 different temperatures. The optimum values of critical distances L=0.045mm for the tests carried out at the three lower temperatures and L=0.075mm for tests at T=350^{o}C were obtained for the material to predict the measured fracture toughness correctly.

Moreover, with the help of linear elastic FE models, it has also been proved that the TCD can be used to predict static fracture in ductile metallic materials containing various stress raisers and subjected to both uniaxial and multiaxial loading (Susmel and Taylor, 2003a, Susmel and Taylor, 2003b, Susmel and Taylor, 2006a, Susmel and Taylor, 2008, Susmel, 2009, Susmel and Taylor, 2010b, Susmel and Taylor, 2010c, Susmel and Taylor, 2010a, Cicero et al., 2013, Louks and Susmel, 2015, Susmel and Taylor, 2015).

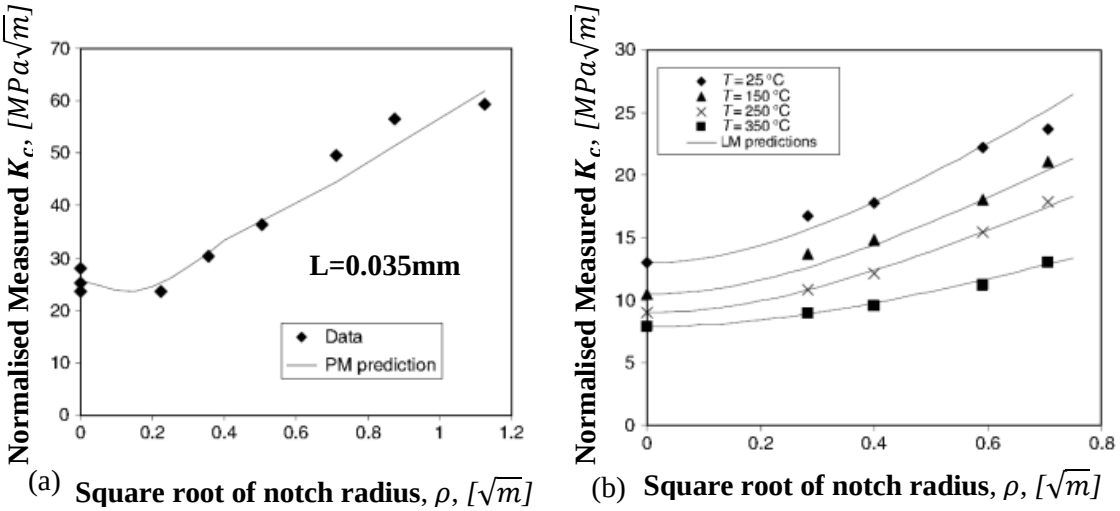

Figure 2.7 (a) Experimental data for mild steel and the predictions calculated using PM; (b) experimental data for an aluminum alloy tested at 4 different temperatures and the predictions calculated using LM.

For instance, with the help of linear elastic FE models, Susmel and Taylor (2008) used the TCD to predict static failure accurately in notched ductile materials in which the final breakage was preceded by large scale plastic deformation, by taking the inherent material strength σ_o equal to the ultimate tensile strength σ_{UTS}.

2.6 Conclusion

From the content discussed above, it is evident to say that the TCD is able to be used to predict the failure strength of ceramics by taking the ultimate tensile strength σ_{UTS} equal to σ_o. Additionally, by adjusting the critical distance L or the material inherent strength, σ_o, the TCD can also be used to assess static failure of polymers and some metals. Moreover, when the failure of notched metallic material specimens was preceded by large-scale yielding, based on different assumptions, it is still possible to apply the TCD to predict the material failure by post-processing both linear elastic stress fields and elasto-plastic stress fields.

Independently from the structural integrity ambit in which it is used, the most important feature of the TCD is that, similar to other existing local approaches (Berto and Lazzarin, 2009, Berto and Lazzarin, 2014, Vratnica et al., 2010, Vratnica et al., 2013), this theory is seen to be capable of accommodating any kind of material non-linarites into a linear-elastic framework, thus allowing the time and costs associated with the design process to be reduced remarkably (Susmel and Taylor, 2010b).

Before we extend the TCD from static problem to dynamic problem, some experimental work related to notched components subjected to dynamic load will be introduced. Therefore, in next chapter, the experimental results from the tests carried out at the University of Sheffield and in the laboratory of the Institute of Continuous Media Mechanics UB RAS, Perm, Russia will be introduced.

References

BERTO, F. & LAZZARIN, P. 2009. A review of the volume-based strain energy density approach applied to V-notches and welded structures. *Theoretical and Applied Fracture Mechanics,* 52**,** 183-194.

BERTO, F. & LAZZARIN, P. 2014. Recent developments in brittle and quasi-brittle failure assessment of engineering materials by means of local approaches. *Materials Science and Engineering: R: Reports,* 75**,** 1-48.

BERTOLOTTI, R. L. 1973. Fracture toughness of polycrystalline Al2O3. *Journal of the American Ceramic Society,* 56**,** 107-117.

CICERO, S., MADRAZO, V. & CARRASCAL, I. A. 2012. Analysis of notch effect in PMMA using the Theory of Critical Distances. *Engineering Fracture Mechanics,* 86**,** 56-72.

CICERO, S., MADRAZO, V., GARCÍA, T., CUERVO, J. & RUIZ, E. 2013. On the notch effect in load bearing capacity, apparent fracture toughness and fracture mechanisms of polymer PMMA, aluminium alloy Al7075-T651 and structural steels S275JR and S355J2. *Engineering Failure Analysis,* 29**,** 108-121.

CLARK JR, W. & LOGSDON, W. 1974. The applicability of fracture mechanics technology to porcelain ceramics. *Fracture Mechanics of Ceramics.* Springer.

CREAGER, M. & PARIS, P. 1967. Elastic field equations for blunt cracks with reference to stress corrosion cracking. *International Journal of Fracture Mechanics,* 3**,** 247-252.

DAMANI, R., GSTREIN, R. & DANZER, R. 1996. Critical notch-root radius effect in SENB-S fracture toughness testing. *Journal of the European Ceramic Society,* 16**,** 695-702.

KINLOCH, A., SHAW, S., TOD, D. & HUNSTON, D. 1983. Deformation and fracture behaviour of a rubber-toughened epoxy: 1. Microstructure and fracture studies. *Polymer,* 24**,** 1341-1354.

LOUKS, R. & SUSMEL, L. 2015. The linear- elastic Theory of Critical Distances to estimate high- cycle fatigue strength of notched metallic materials at elevated temperatures. *Fatigue & Fracture of Engineering Materials & Structures,* 38**,** 629-640.

MADRAZO, V., CICERO, S. & CARRASCAL, I. A. 2012. On the Point Method and the Line Method notch effect predictions in Al7075-T651. *Engineering Fracture Mechanics,* 79**,** 363-379.

NEUBER, H. 1936. Theorie der technischen Formzahl. *Forschung auf dem Gebiet des Ingenieurwesens A,* 7**,** 271-274.

NOVOZHILOV, V. V. 1969a. On a necessary and sufficient criterion for brittle strength: PMM vol. 33, (2), 1969, pp. 212–222. *Journal of Applied Mathematics and Mechanics,* 33**,** 201-210.

NOVOZHILOV, V. V. 1969b. On the foundations of a theory of equilibrium cracks in elastic solids: PMM vol. 33, (5), 1969, pp. 797–812. *Journal of Applied Mathematics and Mechanics,* 33**,** 777-790.

NUI, L., CHEHIMI, C. & PLUVINAGE, G. 1994. Stress field near a large blunted tip V-notch and application of the concept of the critical notch stress intensity factor (NSIF) to the fracture toughness of very brittle materials. *Engineering Fracture Mechanics,* 49**,** 325-335.

PETERSON, R. 1959. Notch sensitivity. *Metal fatigue***,** 293-306.

SUSMEL, L. 2004. A unifying approach to estimate the high-cycle fatigue strength of notched components subjected to both uniaxial and multiaxial cyclic loadings. *Fatigue and Fracture of Engineering Materials and Structures,* 27**,** 391-411.

SUSMEL, L. 2009. *Multiaxial notch fatigue,* Elsevier.

SUSMEL, L. & TAYLOR, D. 2003a. Fatigue design in the presence of stress concentrations. *The Journal of Strain Analysis for Engineering Design,* 38**,** 443-452.

SUSMEL, L. & TAYLOR, D. 2003b. Two methods for predicting the multiaxial fatigue limits of sharp notches. *Fatigue and Fracture of Engineering Materials and Structures,* 26**,** 821-833.

SUSMEL, L. & TAYLOR, D. 2006a. Can the conventional high-cycle multiaxial fatigue criteria be re-interpreted in terms of the theory of critical distances. *Struct Durability Health Monit,* 2**,** 91-108.

SUSMEL, L. & TAYLOR, D. 2006b. A simplified approach to apply the theory of critical distances to notched components under torsional fatigue loading. *International Journal of Fatigue,* 28**,** 417-430.

SUSMEL, L. & TAYLOR, D. 2008. On the use of the Theory of Critical Distances to predict static failures in ductile metallic materials containing different geometrical features. *Engineering Fracture Mechanics,* 75**,** 4410-4421.

SUSMEL, L. & TAYLOR, D. 2010a. The Theory of Critical Distances as an alternative experimental strategy for the determination of KIc and ΔKth. *Engineering Fracture Mechanics,* 77**,** 1492-1501.

SUSMEL, L. & TAYLOR, D. 2010b. The Theory of Critical Distances to estimate the static strength of notched samples of Al6082 loaded in combined tension and torsion. Part I: Material cracking behaviour. *Engineering Fracture Mechanics,* 77**,** 452-469.

SUSMEL, L. & TAYLOR, D. 2010c. The Theory of Critical Distances to estimate the static strength of notched samples of Al6082 loaded in combined tension and torsion. Part II: Multiaxial static assessment. *Engineering Fracture Mechanics,* 77**,** 470-478.

SUSMEL, L. & TAYLOR, D. 2015. Estimating Lifetime of Notched Components Subjected to Variable Amplitude Fatigue Loading According to the Elastoplastic Theory of Critical Distances. *Journal of Engineering Materials and Technology,* 137**,** 011008.

TAKAHASHI, I., USAMI, S., NAKAKADO, K., MIYATA, H. & SHIDA, S. 1985. Effect of defect size and notch root radius on fracture strength of engineering ceramics. *J. Ceram. Soc. Japan,* 93**,** 186-194.

TANAKA, K. 1983. Engineering formulae for fatigue strength reduction due to crack-like notches. *International Journal of Fracture,* 22**,** R39-R46.

TAYLOR, D. 1999. Geometrical effects in fatigue: a unifying theoretical model. *International Journal of Fatigue,* 21**,** 413-420.

TAYLOR, D. 2004. Predicting the fracture strength of ceramic materials using the theory of critical distances. *Engineering Fracture Mechanics,* 71**,** 2407-2416.

TAYLOR, D. 2007. *The Theory of Critical Distances: A New Perspecive in Fracture Mechanics,* Elsevier Science Limited.

TAYLOR, D. Applications of the theory of critical distances to the prediction of brittle fracture in metals and non-metals. ECF15, Stockolm 2004, 2013.

TAYLOR, D., CORNETTI, P. & PUGNO, N. 2005. The fracture mechanics of finite crack extension. *Engineering Fracture Mechanics,* 72**,** 1021-1038.

TAYLOR, D., MERLO, M., PEGLEY, R. & CAVATORTA, M. P. 2004. The effect of stress concentrations on the fracture strength of polymethylmethacrylate. *Materials Science and Engineering: A,* 382**,** 288-294.

TOTH, L. 1998. Notch effect and brittle-ductile transition. *Materials Science,* 34**,** 619-629.

TSUJI, IWASE & ANDO 1999. An investigation into the location of crack initiation sites in alumina, polycarbonate and mild steel. *Fatigue & Fracture of Engineering Materials & Structures,* 22**,** 509-517.

VRATNICA, M., PLUVINAGE, G., JODIN, P., CVIJOVIĆ, Z., RAKIN, M. & BURZIĆ, Z. 2010. Influence of notch radius and microstructure on the fracture behavior of Al–Zn–Mg–Cu alloys of different purity. *Materials & Design,* 31**,** 1790-1798.

VRATNICA, M., PLUVINAGE, G., JODIN, P., CVIJOVIĆ, Z., RAKIN, M., BURZIĆ, Z. & GERIĆ, K. 2013. Notch fracture toughness of high-strength Al alloys. *Materials & Design,* 44**,** 303-310.

WHITNEY, J. M. & NUISMER, R. J. 1974. Stress Fracture Criteria for Laminated Composites Containing Stress Concentrations. *Journal of Composite Materials,* 8**,** 253-265.

WILSHAW, T., RAU, C. & TETELMAN, A. 1968. A general model to predict the elastic-plastic stress distribution and fracture strength of notched bars in plane strain bending. *Engineering Fracture Mechanics,* 1**,** 191-211.

Chapter 3 Experimental results

3.1 Introduction

In this chapter, four experimental trials were run in the testing laboratory of the Sheffield University at Harpur Hill, Buxton, UK and in the laboratory of the Institute of Continuous Media Mechanics UB RAS, Perm, Russia. The experimental investigation performed at the University of Sheffield involved plain and notched cylindrical samples of Al6063-T5, such samples being tested under both quasi-static and dynamic tensile loading. The tested results will be used to understand the dynamic behaviours of notched metallic material. Due to the limited number of samples, the uncertainty analysis has not been done in this case.

3.2 Experimental details and results by testing Al6063-T5 cylindrical bar

In terms of conventional quasi-static mechanical properties, the investigated aluminium alloy had an ultimate tensile stress, σ_{UTS}, equal to 205 MPa, a yield stress, σ_y, of 145 MPa, an elastic modulus, E, of 68900 MPa, and a Poisson's ratio, v, of 0.33. The geometries of the tested specimens are sketched in Figure. 3.1. The plain samples had net diameter, d_n, equal to 5 mm and gross diameter, d_g, to 10 mm. The bluntly notched specimens had d_n = 5 mm, d_g = 10 mm, and notch root radius r_n equal to 4 mm, these resulting in a net stress concentration factor, K_t, of 1.25.

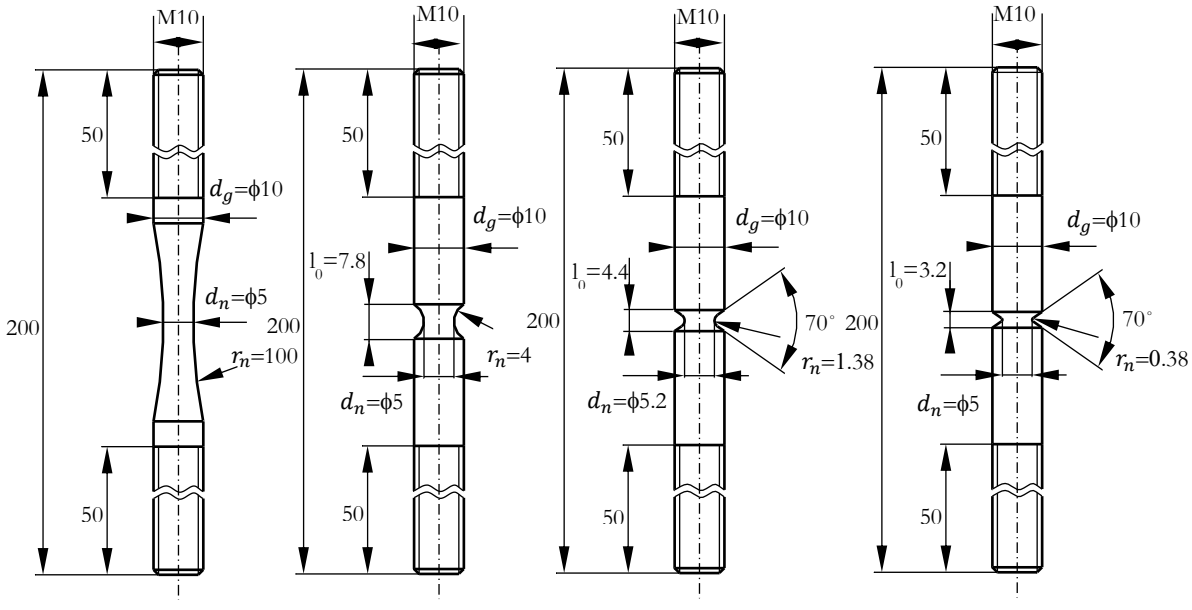

Figure 3.1 Geometries of the samples of Al6063-T5 tested at the University of Sheffield (dimensions in millimetres).

The samples containing both the intermediate and the sharp stress concentrators had d_n = 5.2 mm and d_g = 10 mm, the notch root radius being equal to 1.38 mm (K_t = 1.69) and to 0.38 mm (K_t = 2.93), respectively. In terms of notch radius, when the stress concentration factor K_t is beyond 2, the notched sample was treated as a very sharp notch, therefore, we choose one type of notch with K_t is bigger than 2, and two types of notches (K_t=1.69 and 1.25) between very sharp notch and plain samples.

Figure 3.2(a) shows the experimental arrangement which was used to generate the results summarised in Table 3.1. The specimens were mechanically attached to two purpose-built load cells by using nuts. The load cell B at the distal end of the sample was fixed to a stiff end-stop whilst the load cell A at the proximal, or loaded end of the specimen was connected through transfer bars to a pneumatic loading system. The transfer bars were constrained to travel axially by being passed through PTFE-coated holes in the flanges of a steel column section, and the proximal load cell was sat on a PTFE slider. In this way, the loading system was free to translate under the applied load, subject only to the resistance of the specimen. The pneumatic pressure was generated by releasing pressurised bottled nitrogen into a barrel of a ‘‘gas gun’’ where it reacted against a close-fitting nylon sealing piston, to drive the loading rod – cross-head – transfer bar system and hence apply a tensile load to the proximal load cell. Quasi-static loading was applied by slowly releasing the pneumatic pressure into the gas gun barrel. Dynamic loading was produced by releasing the pressurised nitrogen into a receiver vessel, separated from the gas gun barrel by a brass diaphragm which burst at a suitable pressure, causing a rapidly increasing load (typically of the order of 100–2000 kN $\cdot s^{-1}$) to be applied to the specimen. The dynamic loading rate was changed by using different thickness bursting diaphragms and introducing a choke to limit the rate of gas flow from the receiver to the loading system. Due to limitation of the testing rig and material samples, not so many material samples of each notch were fabricated, therefore, only three different sizes of diaphragms were used. Therefore, the range of loading rate applied during these tests is relative small. Moreover, the loading rate is very difficult to be kept exact same for two tested samples by using brass diaphragm, so the repeatability of each test was not been given.

The axial deformation and the cracking behaviour of the tested Al6063-T5 cylindrical samples were monitored by using a high speed camera which was synchronised with the signals gathered from the loading cell B, the accuracy of the load cell has been calibrated at University of Sheffield laboratory. With the help of the software CineView 2.0, the displacement and strain time history was obtained by post-processing the recorded high speed video and the displacement time history will be used as input data in Chapter 5. Camera Phantom V4.2 (8-bit image resolution, 2100 frames per second, recording at up to 90,000 frames per second

maximum) was used for Series 1 (S1 in Table 3.1), whereas camera Phantom V9.1 (14-bit image resolution, recording at up to 153846 fps) was employed for Series 2 (S2 in Table 3.1).

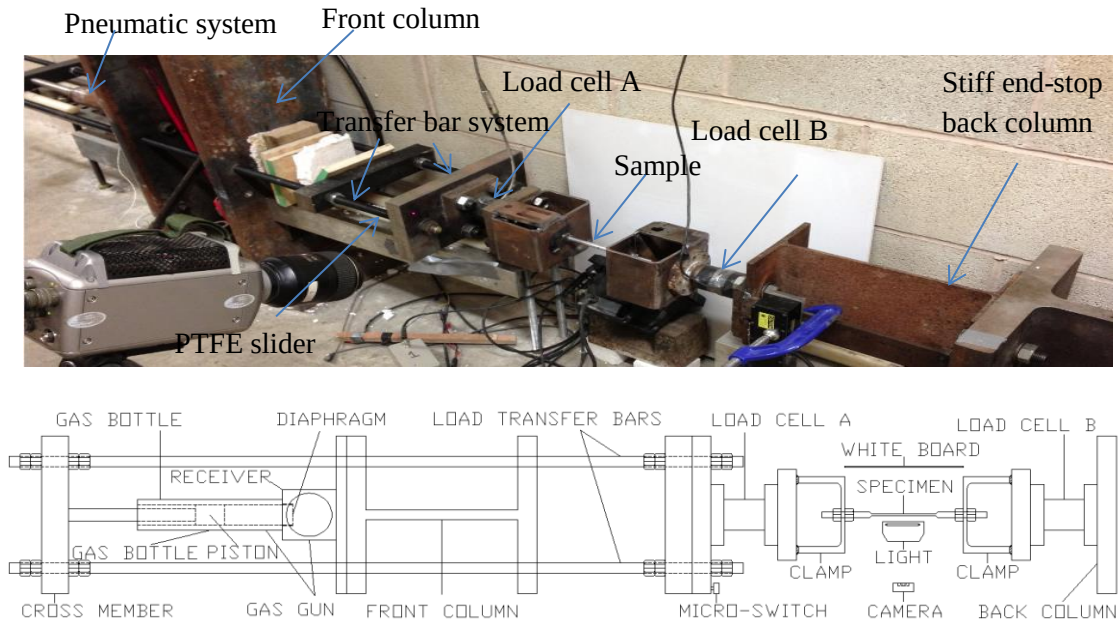

(a)

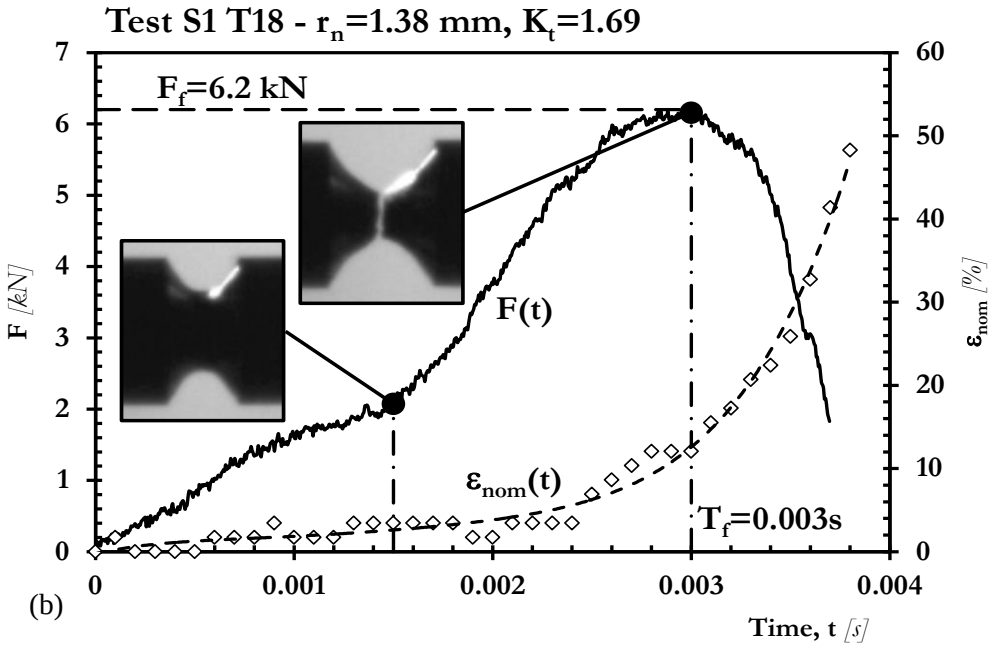

(b)

Figure 3.2 (a) Experimental rig used to test the notched cylindrical samples of Al6063-T5; (b) force vs. time and nominal strain vs. time curve for test S1 T18.

By post-processing the video of any test it was possible to confirm that, in the force vs. time curve, a sharp decrease of the load signal corresponded to the formation of a visible crack. Accordingly, because the data recorded by load cell A was affected by transfer system, the data

obtained from this load cell will be used for further study. Therefore, the maximum force recorded from load cell B during each test was taken as the failure force, F_f, the corresponding instant being used to define the time to failure, T_f.The force vs. time diagram reported in Figure 3.2 (b) shows the way the gathered signals were post-processed to determine F_f and T_f for test S1T18 (see also Table 3.1). Here, the load is that recorded by the distal load cell, i.e. the load which was transmitted through the specimen. It should be noted that the load does not immediately fall to zero on complete fracture of the specimen, due to inertia of the distal load cell which takes a few hundred microseconds to fully relax. The values for F_f and T_f determined according to the procedure briefly discussed above were then used to calculate the nominal loading rate, $\dot{F}$, as follows:

$$\dot{F} = \frac{F_f}{T_f} \tag{3.1}$$

Commercial software Cine viewer 2.14b was employed to post-process the high-speed videos in order to determine, for each test, the corresponding nominal strain, ε_{nom}, vs. time curve. For the notched samples, the gauge length was taken equal to the distance (measured along the axis) between the corners resulting from the intersection of the notch flanks with the cylindrical surface delimiting the gross volume of the specimens themselves. Accordingly, the gauge lengths, l_0, for the sharp, intermediate and blunt notches were equal to 3.2 mm, 4.4 mm and 7.8 mm, respectively (see Figure 3.1). For each test, by post-processing the high-speed videos, the actual distance, l, between the two reference points was measured frame by frame throughout the test, the corresponding nominal strain being calculated as follows:

$$\varepsilon_{nom} = \frac{l - l_0}{l_0} \tag{3.2}$$

The diagram reported in Figure 3.2(b) shows an example of the nominal strain, ε_{nom}, vs. time curve determined according to the procedure described above. Finally, from any ε_{nom} vs. time curve, the nominal failure strain, ε_f, was estimated at instant T_f, so that, the nominal strain rate, $\dot{\varepsilon}_{nom}$, could directly be calculated as follows:

$$\dot{\varepsilon}_{nom} = \frac{\varepsilon_f}{T_f} \tag{3.3}$$

Table 3.1 Summary of the experimental results generated by testing plain and notched cylindrical samples of Al6063-T5.

Code	d_g $[mm]$	d_n $[mm]$	r_n $[mm]$	K_t	F_f $[kN]$	T_f $[s]$	$\dot{F}$ $[kN \cdot s^{-1}]$	$\dot{\varepsilon}_{nom}$ $[s^{-1}]$
S1 T1	10	5	Plain	1.00	3.8	4.1	0.9268	0.02
S1 T2	10	5	Plain	1.00	4.8	0.08	60.00	1.3
S1 T3	10	5	Plain	1.00	4.1	35	0.1171	0.007
S1 T5	10	5	Plain	1.00	4.6	0.05	92.00	3.5
S1 T6	10	5	Plain	1.00	4	0.02	200.0	8.2
S1 T7	10	5	Plain	1.00	4.4	0.006	733.3	19.8
S1 T8	10	5	Plain	1.00	4.5	0.005	900.0	21.7
S1 T11	10	5	Plain	1.00	4.1	0.004	1600	30.66
S1 T12	10	5	Plain	1.00	4.7	0.01	470.0	11.33
S1 T9	10	5.2	0.38	2.93	5.4	22	0.2455	0.013
S1 T10	10	5.2	0.38	2.93	6.7	0.004	1675	125
S2 T1	10	5.2	0.38	2.93	6.8	0.007	971.4	52.15
S2 T2	10	5.2	0.38	2.93	6.7	0.007	957.1	32.35
S1 T17	10	5.21	1.38	1.69	4.6	29	0.1586	0.01
S1 T18	10	5.21	1.38	1.69	6.2	0.003	2066.7	89.29
S2 T5	10	5.21	1.38	1.69	5.3	21	0.2524	0.01
S2 T6	10	5.21	1.38	1.69	5.1	16	0.3188	0.019
S2 T7	10	5.21	1.38	1.69	6.7	0.007	957.1	61.59
S2 T9	10	5.21	1.38	1.69	6.2	0.009	688.9	49.42
S2 T10	10	5.21	1.38	1.69	6.9	0.007	985.7	56.43
S2 T11	10	5.21	1.38	1.69	4.9	11	0.4455	0.03
S2 T12	10	5.21	1.38	1.69	5.2	16	0.3250	0.017
S2 T13	10	5.21	1.38	1.69	6	0.007	857.1	48.17
S2 T14	10	5.21	1.38	1.69	5.9	0.009	655.6	42.62
S1 T15	10	5	4.00	1.25	3.7	30	0.1233	0.01
S1 T16	10	5	4.00	1.25	3.5	23	0.1522	0.01

3.3 Experimental details and results by testing Ti-6Al-4V, AlMn alloy and AlMg6 cylindrical bar

The experimental investigation carried out at the Institute of Continuous Media Mechanics UB RAS involved three different metallic materials, i.e. titanium alloy Ti–6Al–4V having $\sigma_{UTS} = 1031MPa$, aluminium alloy AlMg alloy having σ_{UTS} = 616 MPa and an AlMg6 having σ_{UTS} = 161 MPa. The geometries of the tested samples are shown in Figure 3.3. In particular, independently from the sharpness of the notch, the specimens had gross diameter, d_g, equal to 9 mm and net diameter, d_n, to 7.6 mm. The three stress raisers had root radius equal to 2 mm, 1 mm, and 0.1 mm, resulting in a net stress concentration factor, K_t, equal to 1.67, 2.08, and 5.2 respectively. The tensile tests under a nominal strain rate, $\dot{\varepsilon}_{nom}$, equal to $10^{-2}s^{-1}$, $10^{-1}s^{-1}$, and $10s^{-1}$ were ran using a 100 kN servo hydraulic machine Bi-00-100. The sharply notched samples instead were tested under $\dot{\varepsilon}_{nom} \approx 10^{4}s^{-1}$ by employing a classic Hopkinson-Kolsky split bar in the Nicholas's modification (Nicholas, 1981). The experimental setup is a typical compression setup with incident and transmission bars. The metallic specimens were threaded on both the incident and transmission ends, while placing a metal collar over the specimen. The specimen and the metal collar had a snug fit on the incident and transmission side in order to bypass an initial compression wave. The initial compression wave was generated by an impact in the incident bar with a striker. The compression wave would ideally pass through the metal collar and then reflect off the free end in tension. The tensile wave would then pull on the specimen.

The experimental setup in the Institute of Continuous Media Mechanics UB RAS includes two coaxial incident and transmitter bars with diameter of 25 mm and a 18-mm-caliber gas gun, which was used to accelerate a 200-mm-long projectile to a final velocity of 15–30 $m \cdot s^{-1}$. Two strain gauges fixed to the incident and transmitter bars were used to measure the stress waves in both bars. Following the classical consideration of elastic waves propagation in homogeneous bars proposed by Kolsky and assuming the uniform stress–strain state into the sample we can derive the equation for calculation of stress, strain and strain rate of the specimen during the test (Kolsky, 1949)

$$\sigma_s(t) = \frac{ES}{S_b}\varepsilon_T(t), \varepsilon_s(t) = -\frac{2C}{L}\int_0^t \varepsilon_R(t)dt,\ \dot{\varepsilon}_s(t) = -\frac{2C}{L}\varepsilon_R(t) \tag{3.4}$$

where t is time, C is the velocity of sound into the bars, L is the initial specimen length, $\sigma_s(t)$ is the stress in the specimen, $\varepsilon_s(t)$ and $\dot{\varepsilon}_s(t)$ the strain and strain rate, respectively, $\varepsilon_T(t)$ the strain wave into transmitter bar, and $\varepsilon_R(t)$ the strain wave reflected into incident bar. Parametric functions $\sigma_s(t)$, $\varepsilon_s(t)$ and $\dot{\varepsilon}_s(t)$ were used to directly calculate the stress–strain and strain rate-strain curves.

Finally, the results generated by testing plain and notched specimens of Ti–6Al–4V, AlMn alloy, and AlMg6 are summarised in Tables 3.2, 3.3 and 3.4, respectively, in terms of failure force, F_f, time to failure, T_f, nominal loading rate, $\dot{F}$, and nominal strain rate, $\dot{\varepsilon}_{nom}$.

In next chapter, a novel reformulation of the TCD will be formalised and the experimental results demonstrated in this chapter will be used and processed in order to validate the novel reformulation of TCD.

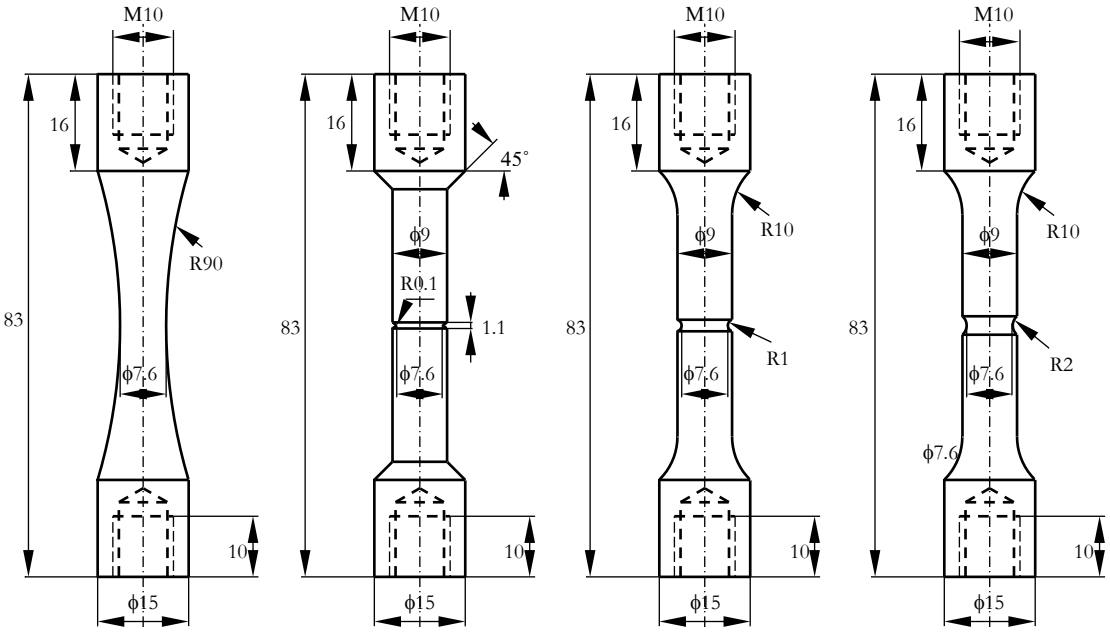

Figure 3.3 Geometries of the samples tested in the laboratory of the Institute of Continuous Media Mechanics, Perm, Russia (dimensions in millimetres).

Table 3.2 Summary of the experimental results generated by testing plain and notched cylindrical samples of Ti–6Al–4V.

Code	d_g [mm]	d_n [mm]	r_n [mm]	K_t	F_f [kN]	T_f [s]	$\dot{F}$ $[kN \cdot s^{-1}]$	$\dot{\varepsilon}_{nom}$ $[s^{-1}]$
Ti-P1	9	7.6	plain	1.00	65.5	32.86	1.994	0.01
Ti-P2	9	7.6	plain	1.00	65.6	30.55	2.147	0.01
Ti-P3	9	7.6	plain	1.00	65.7	38.42	1.710	0.01
Ti-P4	9	7.6	plain	1.00	67.3	3.25	20.71	0.1
Ti-P5	9	7.6	plain	1.00	68.2	3.23	21.10	0.1
Ti-P6	9	7.6	plain	1.00	67.6	3.13	21.60	0.1
Ti-P7	9	7.6	plain	1.00	70.4	0.15	469.5	10
Ti-P8	9	7.6	plain	1.00	70.6	0.26	271.6	10
Ti-P9	9	7.6	plain	1.00	69.3	0.24	288.9	10
Ti-B1	9	7.6	2.0	1.67	56.3	52.77	1.067	0.01
Ti-B2	9	7.6	2.0	1.67	55.9	43.91	1.274	0.01
Ti-B3	9	7.6	2.0	1.67	57.1	43.09	1.326	0.01
Ti-B4	9	7.6	2.0	1.67	58.1	5.12	11.35	0.1
Ti-B5	9	7.6	2.0	1.67	58.2	5.19	11.22	0.1
Ti-B6	9	7.6	2.0	1.67	56.8	4.93	11.52	0.1
Ti-B7	9	7.6	2.0	1.67	61.9	0.38	162.9	10
Ti-B8	9	7.6	2.0	1.67	61.7	0.19	324.5	10
Ti-B9	9	7.6	2.0	1.67	61.9	0.21	294.6	10
Ti-I1	9	7.6	1.0	2.08	59.0	45.96	1.284	0.01
Ti-I2	9	7.6	1.0	2.08	58.8	43.31	1.358	0.01
Ti-I3	9	7.6	1.0	2.08	60.2	46.92	1.282	0.01
Ti-I4	9	7.6	1.0	2.08	59.8	4.7	12.72	0.1
Ti-I5	9	7.6	1.0	2.08	60.2	5.06	11.91	0.1
Ti-I6	9	7.6	1.0	2.08	60.6	5.3	11.43	0.1
Ti-I7	9	7.6	1.0	2.08	63.7	0.21	303.4	10
Ti-I8	9	7.6	1.0	2.08	63.5	0.23	276.0	10
Ti-I9	9	7.6	1.0	2.08	63.8	0.21	304.0	10
Ti-S1	9	7.6	0.1	5.2	56.3	$2.6 \cdot 10^{-5}$	$2.2 \cdot 10^{6}$	10000
Ti-S2	9	7.6	0.1	5.2	71.2	$2.7 \cdot 10^{-5}$	$2.6 \cdot 10^{6}$	10000

Table 3.3 Summary of the experimental results generated by testing plain and notched cylindrical samples of AlMn alloy.

Code	d_g [mm]	d_n [mm]	r_n [mm]	K_t	F_f [kN]	T_f [s]	$\dot{F}$ $[kN \cdot s^{-1}]$	$\dot{\varepsilon}_{nom}$ $[s^{-1}]$
AlMn-P1	9	7.6	plain	1	10.3	58.52	0.1752	0.01
AlMn-P2	9	7.6	plain	1	10.2	87.78	0.1167	0.01
AlMn-P3	9	7.6	plain	1	10.2	60.35	0.1690	0.01
AlMn-P4	9	7.6	plain	1	10.5	4.12	2.560	0.1
AlMn-P5	9	7.6	plain	1	9.2	3.8	2.416	0.1
AlMn-P6	9	7.6	plain	1	10.5	4.25	2.462	0.1
AlMn-P7	9	7.6	plain	1	19.6	0.18	109.1	10
AlMn-P8	9	7.6	plain	1	10.5	0.18	58.07	10
AlMn-P9	9	7.6	plain	1	10.4	0.16	65.10	10
AlMn-B1	9	7.6	2.0	1.67	8.2	44.79	0.1840	0.01
AlMn-B2	9	7.6	2.0	1.67	8.1	57.64	0.1412	0.01
AlMn-B3	9	7.6	2.0	1.67	7.4	54.75	0.1354	0.01
AlMn-B4	9	7.6	2.0	1.67	8.4	4.11	2.054	0.1
AlMn-B5	9	7.6	2.0	1.67	8.3	4.49	1.856	0.1
AlMn-B6	9	7.6	2.0	1.67	8.4	4.5	1.857	0.1
AlMn-B7	9	7.6	2.0	1.67	8.0	0.21	38.29	10
AlMn-B8	9	7.6	2.0	1.67	7.1	0.2	35.72	10
AlMn-B9	9	7.6	2.0	1.67	8.9	0.18	49.47	10
AlMn-S1	9	7.6	0.1	5.2	5.0	$5.8 \cdot 10^{-5}$	$8.6 \cdot 10^{4}$	10000

Table 3.4 Summary of the experimental results generated by testing plain and notched cylindrical samples of AlMg6.

Code	d_g [mm]	d_n [mm]	r_n [mm]	K_t	F_f [kN]	T_f [s]	$\dot{F}$ $[kN \cdot s^{-1}]$	$\dot{\varepsilon}_{nom}$ $[s^{-1}]$
AlMg6-P1	9	7.6	plain	1	27.9	280.15	0.0996	0.01
AlMg6-P2	9	7.6	plain	1	27.8	269.69	0.1031	0.01
AlMg6-P3	9	7.6	plain	1	28.2	286.83	0.0982	0.01
AlMg6-P4	9	7.6	plain	1	27.7	26.22	1.058	0.1
AlMg6-P5	9	7.6	plain	1	27.7	26.98	1.027	0.1
AlMg6-P6	9	7.6	plain	1	27.7	26.064	1.061	0.1
AlMg6-P7	9	7.6	plain	1	26.2	0.31	84.5	10
AlMg6-P8	9	7.6	plain	1	26.2	0.29	90.41	10
AlMg6-P9	9	7.6	plain	1	26.1	0.32	81.47	10
AlMg6-B1	9	7.6	2.0	1.67	21.4	245.18	0.0874	0.01
AlMg6-B2	9	7.6	2.0	1.67	21.8	255.7	0.0853	0.01
AlMg6-B3	9	7.6	2.0	1.67	21.9	248.2	0.0882	0.01
AlMg6-B4	9	7.6	2.0	1.67	21.7	26.24	0.826	0.1
AlMg6-B5	9	7.6	2.0	1.67	21.6	25.08	0.860	0.1
AlMg6-B6	9	7.6	2.0	1.67	21.5	26.29	0.818	0.1
AlMg6-B7	9	7.6	2.0	1.67	20.9	0.32	65.31	10
AlMg6-B8	9	7.6	2.0	1.67	21.4	0.32	66.84	10
AlMg6-B9	9	7.6	2.0	1.67	21.0	0.32	65.72	10
AlMg6-I1	9	7.6	1.0	2.08	21.7	228.54	0.09	0.01
AlMg6-I2	9	7.6	1.0	2.08	21.4	220.5	0.10	0.01
AlMg6-I3	9	7.6	1.0	2.08	21.3	224.77	0.09	0.01
AlMg6-I4	9	7.6	1.0	2.08	21.5	24.46	0.88	0.1
AlMg6-I5	9	7.6	1.0	2.08	21.3	22.88	0.93	0.1
AlMg6-I6	9	7.6	1.0	2.08	21.2	22.82	0.93	0.1
AlMg6-I7	9	7.6	1.0	2.08	21.1	0.3	70.30	10
AlMg6-I8	9	7.6	1.0	2.08	21.1	0.3	70.37	10
AlMg6-I9	9	7.6	1.0	2.08	21.5	0.33	65.091	10

References

KOLSKY, H. 1949. An investigation of the mechanical properties of materials at very high rates of loading. Proceedings of the Physical Society. Section B, 62.

NICHOLAS, T. 1981. Tensile testing of materials at high rates of strain. Experimental Mechanics, 21, 177-185.

Chapter 4 Reformulating the TCD to Design Notched Materials against Dynamic Loading

4.1 Reformulating the TCD

As discussed in Chapter 2, the TCD postulates that the static assessment has to be performed by post-processing the entire stress field damaging the so-called process zone (i.e., that material portion controlling the overall strength of the component being assessed) (Taylor, 2007). Through length scale parameter *L*, the size of the process zone depends mainly on: (i) material microstructural features, (ii) local micro-mechanical properties, and (iii) characteristics of the processes resulting in the final breakage (Taylor, 2007). Examination of the state of the art (Kolsky, 1949, Lindholm, 1964, Lindholm et al., 1971, Djapic Oosterkamp et al., 2000, Lee and Kim, 2003, Zhang et al., 2008, Sakino, 2008, Wiesner and MacGillivray, 1999, Noda et al., 2015, Yokoyama and Kishida, 1989) suggests that, in general, the mechanical response, mechanical properties and cracking behaviour of metallic materials subjected to dynamic loading are different from the ones observed under quasi-static loading. If these universally accepted concepts are reinterpreted according to the TCD's philosophy, one may argue that, since both the dynamic failure stress, σ_f, and the dynamic fracture toughness, K_{Id}, vary as the applied load/strain/displacement rate increases, in the same way also the material inherent strength, σ_0, and the length scale parameter, *L*, have to vary. In particular, if $\dot{Z}$ is used to denote either the loading rate, $\dot{F}$, the strain rate, $\dot{\varepsilon}$, the displacement rate, $\dot{\Delta}$, or the Stress Intensity Factor (SIF) rate, $\dot{K}_I$, the effect of the dynamic loading on both the failure stress, σ_f, and the fracture toughness, K_{Id}, can be expressed as follows:

$$\sigma_f(\dot{Z}) = f_{\sigma_f}(\dot{Z}) \tag{4. 1}$$

$$K_{Id}(\dot{Z}) = f_{K_{Id}}(\dot{Z}) \tag{4. 2}$$

where $f_{\sigma_f}(\dot{Z})$ and $f_{K_{Id}}(\dot{Z})$ are functions which can be either estimated experimentally or derived theoretically. Since, under static loading, σ_o is seen to be proportional to σ_{UTS} (Taylor, 2007), the hypothesis can be formed that, similar to the dynamic failure stress, Equation 4.1, also the inherent material strength varies with $\dot{Z}$, i.e.:

$$\sigma_0(\dot{Z}) = f_{\sigma_0}(\dot{Z}) \tag{4. 3}$$

where again, function $f_{\sigma_0}(\dot{Z})$ can be either estimated experimentally or derived theoretically. If this assumption is correct, then, in the most general case, also the length scale parameter has to change with $\dot{Z}$. Therefore, by rewriting definition (2.5) for the dynamic case, *L* can directly be expressed as:

$$L(\dot{Z}) = \frac{1}{\pi}\left[\frac{K_{Id}(\dot{Z})}{\sigma_0(\dot{Z})}\right]^2 = f_L(\dot{Z}) \quad (4.4)$$

To design notched materials against dynamic loading, according to definitions (2.2)–(2.4), effective stress σ_{eff} can now be rearranged as follows:

$$\sigma_{eff}(\dot{Z}) = \sigma_y\left(\theta = 0,\ r = \frac{L(\dot{Z})}{2}\right) \quad \text{(PM)} \quad (4.5)$$

$$\sigma_{eff}(\dot{Z}) = \frac{1}{2L(\dot{Z})}\int_0^{2L(\dot{Z})} \sigma_y(\theta = 0,\ r)\ dr \quad \text{(LM)} \quad (4.6)$$

$$\sigma_{eff}(\dot{Z}) = \frac{2}{\pi L(\dot{Z})^2}\int_{\pi/2}^{\pi/2}\int_0^{L(\dot{Z})} \sigma_y(\theta, r) r dr d\theta \quad \text{(AM)} \quad (4.7)$$

where as postulated by the TCD (Taylor, 2007), the stress analysis is still done by using a simple linear-elastic constitutive law. In other words, the hypothesis is formed that the behaviour of notched metallic materials subjected to dynamic loading can directly be modelled via $\sigma_0(\dot{Z})$ and $L(\dot{Z})$ without taking into account the actual dynamic stress vs. strain response of the material being assessed.

Turning back to the design issue, according to the assumptions made above, notched components undergoing in-service dynamic loading are then supposed not to fail as long as the following conditions is assured:

$$\sigma_{eff}(\dot{Z}) \leq \sigma_0(\dot{Z}) \quad (4.8)$$

the dynamic safety factor, v_D, taking on the following value:

$$v_D = \frac{\sigma_0(\dot{Z})}{\sigma_{eff}(\dot{Z})} \geq 1 \quad (4.9)$$

4.2 Other theories related to critical distance L

Having reformulated the TCD to make it suitable for designing notched metals against dynamic loading, it is useful to recall here that, back in the 90s, Morozov and Petrov have proposed to estimate the dynamic strength of cracked brittle materials according to the so-called Structural-Time Criterion (Morozov, 1990, Petrov et al., 2003). If critical distance *L* is calculated via definition (2.5) independently from the rate of the applied loading, this failure criterion can be rewritten (according to the symbols adopted in the present thesis) as follows:

$$\frac{1}{\tau}\int_{T_f-\tau}^{T_f} \frac{1}{2L}\int_0^{2L} \sigma_y(\theta = 0, r, t) dr dt \leq \sigma_{UTS} \quad (4.10)$$

where t is time, T_f is the time to failure, and τ is the so-called incubation time (which is treated as a material property (Morozov, 1990, Petrov et al., 2003)). By comparing criterion (4.10) to the effective stress determined in terms of the LM, Equation (2.3), the existing similarities between Morozov and Petrov's approach and the TCD become evident. In particular, the Structural-Time Criterion postulates that the strength of a cracked material subjected to dynamic loading can be brought back to the static case by simply averaging over time the LM's effective stress, the temporal integration domain being defined via time-related material constant, τ. In other words, in Morozov and Petrov's criterion, the required critical distance is kept constant and equal to its value determined under quasi-static loading, the effect of the dynamic loading being assessed via the incubation time, τ. The reformulation of the TCD proposed in the present study assumes instead that both the reference material strength, Equation (4.3), and the size of the process zone, Equation (4.4), vary as the rate of the applied loading increases. This assumption can be justified by observing that, in metallic materials, the micro-mechanisms resulting in the formation of the fracture surface are seen to change as the rate of the applied loading increases, this resulting in a variation of the morphology of the fracture surface itself (Couque et al., 1988, Godse et al., 1989, Drar and Bergmark, 1993, Venkert et al., 2001). As recalled above, according to the TCD's modus operandi, the size of the process zone depends mainly on the characteristics of those processes resulting in the final fracture (Taylor, 2007). Therefore, since the microstructural mechanisms leading to dynamic breakage vary as the loading rate increases, the size of the process zone is expected to change accordingly. This phenomenon is modelled in the proposed reformulation of the TCD by forming the hypothesis that critical distance has to vary as the loading/strain/displacement rate increases, Equation (4.4).

As far as critical length based approaches are concerned, it is worth recalling here also that the closed form approach to describe the 'inertia' of fracture and introduce the characteristic length and time into the fracture mechanics problem was also proposed by Naimark and Plekhov (Naimark, 1998, Plekhov, 2003) as follows:

$$p(x,t) = \left(q_o(t-t_c)\right)^{-\frac{1}{\sigma}}\left(\frac{2(\sigma+1)}{\sigma(\sigma+2)}\sin^2\left[\frac{\pi r}{L_T}+\pi\theta\right]\right) \qquad (4.\ 11)$$

In this approach, the characteristic length L_T and characteristic time t of fracture were introduced based on the analysis of self-similar solutions of constitutive equations describing the defect evolution. It was shown that the processes resulting in the final breakage are accompanied by the collective modes of defect ensemble, which develop as instabilities with the blow-up kinetics localised on the spectrum of spatial scales. The Naimark and Plekhov's description includes the discrete spectrum of critical distances considered as characteristics of

both material structure and loading conditions. Each critical distance has own critical (incubation) time and can be realised under corresponding loading conditions (Plekhov, 2003).

4.3 Defining the governing equations

In order to find appropriate mathematical laws suitable for expressing functions $f_{\sigma_f}(\dot{Z})$, $f_{\sigma_0}(\dot{Z})$, $f_{K_{Id}}(\dot{Z})$, and $f_L(\dot{Z})$ in explicit form, a number of experimental data were selected from the technical literature. The log–log diagrams reported in Figure 4.1 show the way both engineering failure strength σ_f and dynamic fracture toughness K_{Id} vary as $\dot{Z}$ increases. The charts of Figure from 4.1 to 4.8 clearly support the idea that, independently from the way $\dot{Z}$ is defined, the selected experimental data can all be summarised by adopting simple power laws. This implies that both the σ_f vs. $\dot{Z}$ relationship and the K_{Id} vs. $\dot{Z}$ relationship can be rewritten as:

$$\sigma_f(\dot{Z}) = a_f \cdot \dot{Z}^{b_f} \tag{4. 12}$$

$$K_{Id}(\dot{Z}) = \alpha \cdot \dot{Z}^{\beta} \tag{4. 13}$$

where a_f, b_f, α, and β are material constants to be determined by running appropriate experiments.

Remembering that, under static loading, σ_0 is seen to be proportional to σ_{UTS} (Taylor, 1999, Susmel and Taylor, 2008), the hypothesis can be formed that also the σ_0 vs. $\dot{Z}$ relationship can be expressed by adopting a power law, i.e.:

$$\sigma_0(\dot{Z}) = a_0 \cdot \dot{Z}^{b_0} \tag{4. 14}$$

a_0 and b_0 being again material dependent constants.

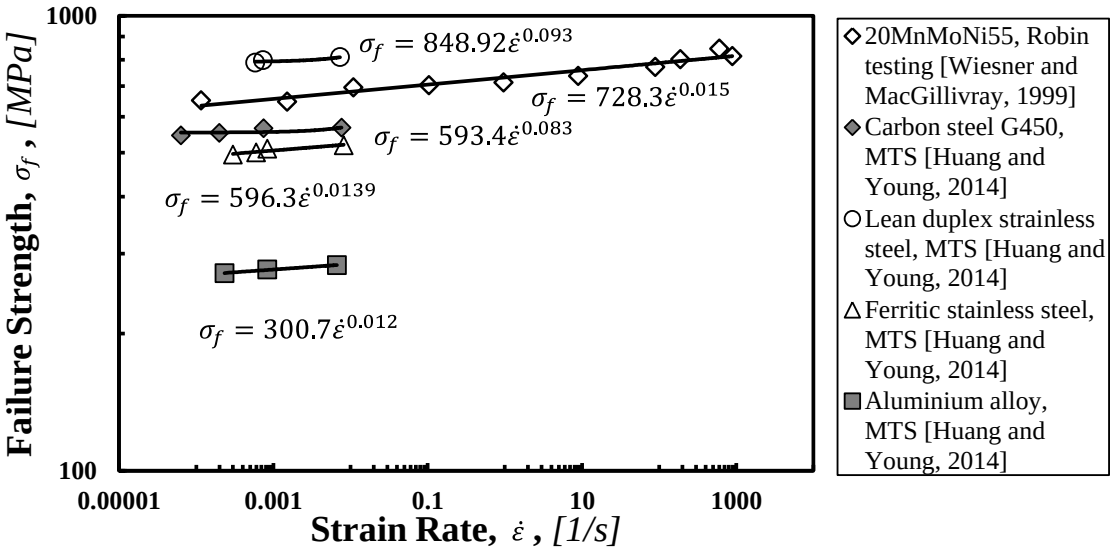

Figure 4. 1 Failure stress as function of strain rate taken from literatures (Wiesner and MacGillivray, 1999, Huang and Young, 2014).

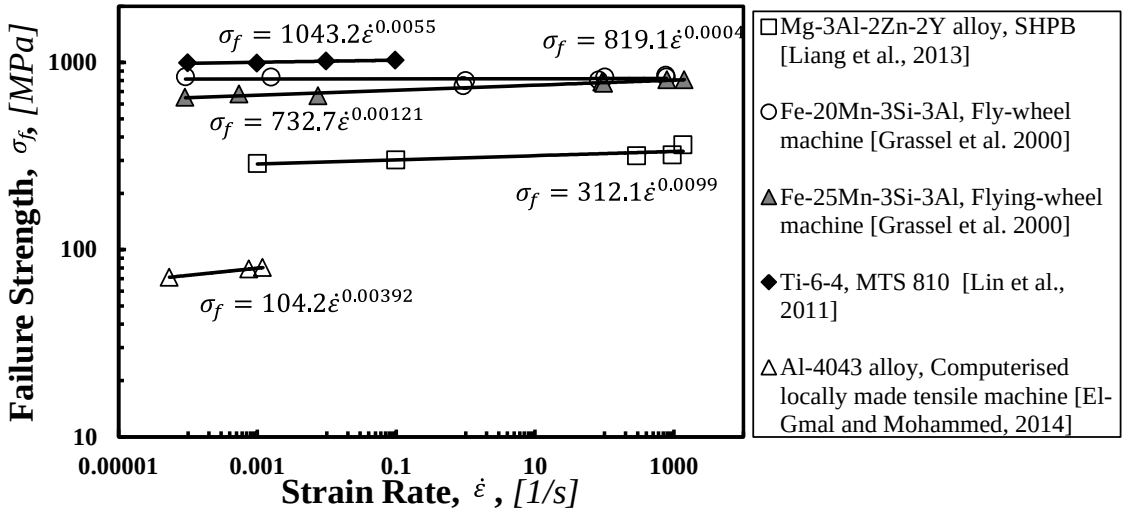

Figure 4. 2 Failure strength as function of strain rate taken from literatures (Grässel et al., 2000, Liang et al., 2013, Lin et al., 2011, El-Gamal and Mohammed, 2014).

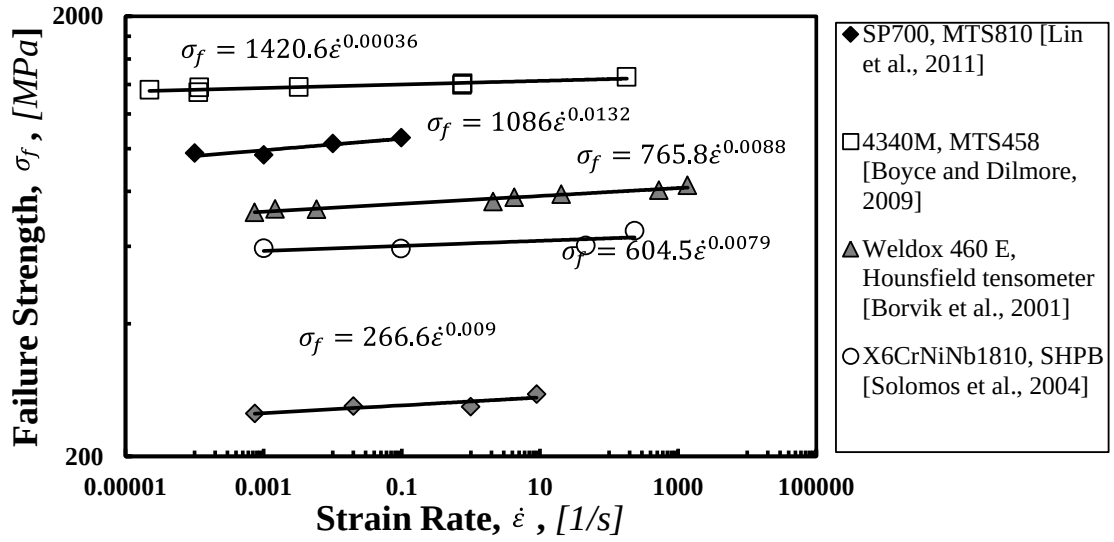

Figure 4. 3 Failure strength as function of strain rate taken from literatures (Lin et al., 2011, Boyce and Dilmore, 2009, Børvik et al., 2001, Solomos et al., 2004, Xu et al., 2009).

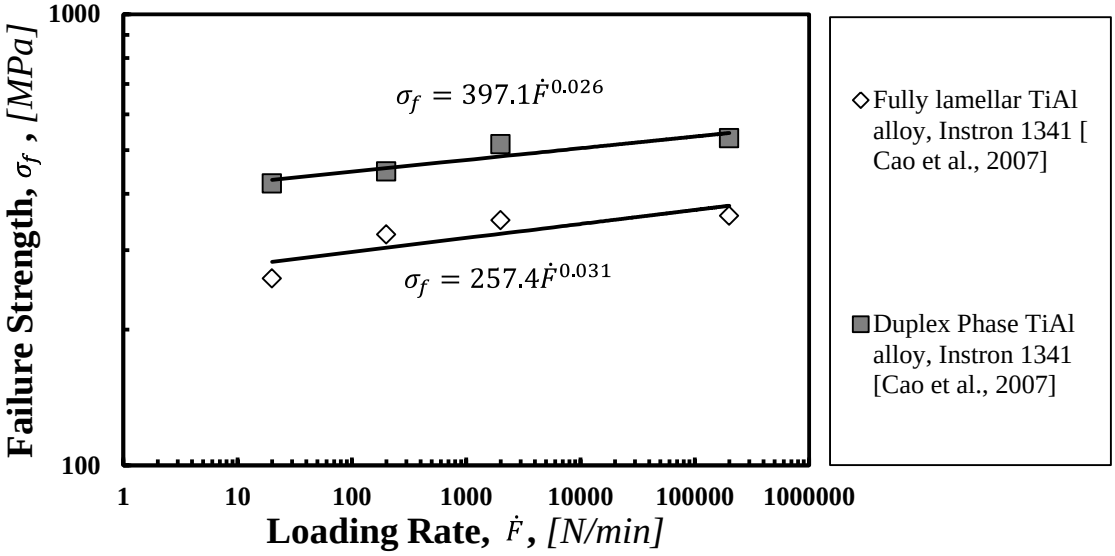

Figure 4. 4 Failure strength as function of loading rate taken from literature (Cao et al., 2007)

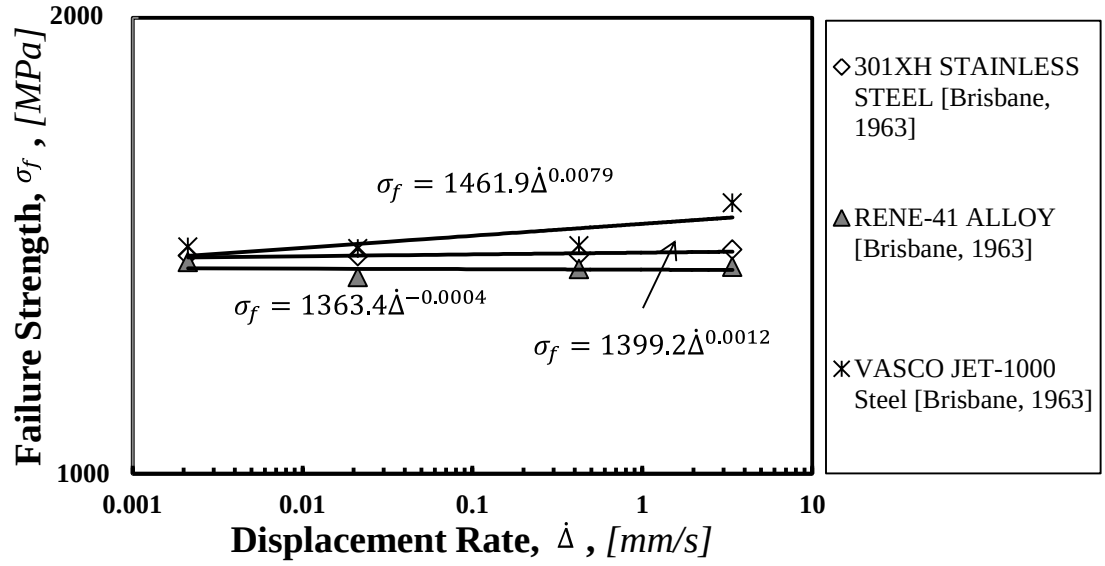

Figure 4. 5 Failure strength as function of displacement rate taken from literature (all of the tests were conducted on a 50000 pound capacity Baldwin Emery SR-4 testing machine) (Brisbane, 1963).

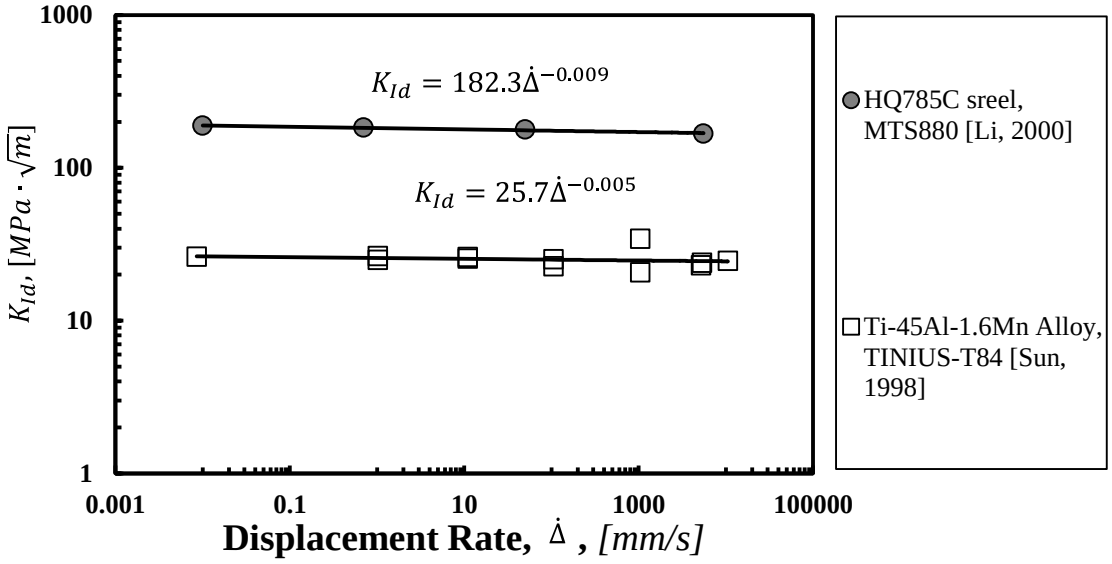

Figure 4. 6 Fracture toughness as function of displacement rate taken from literature (Sun et al., 1998, Li, 2000).

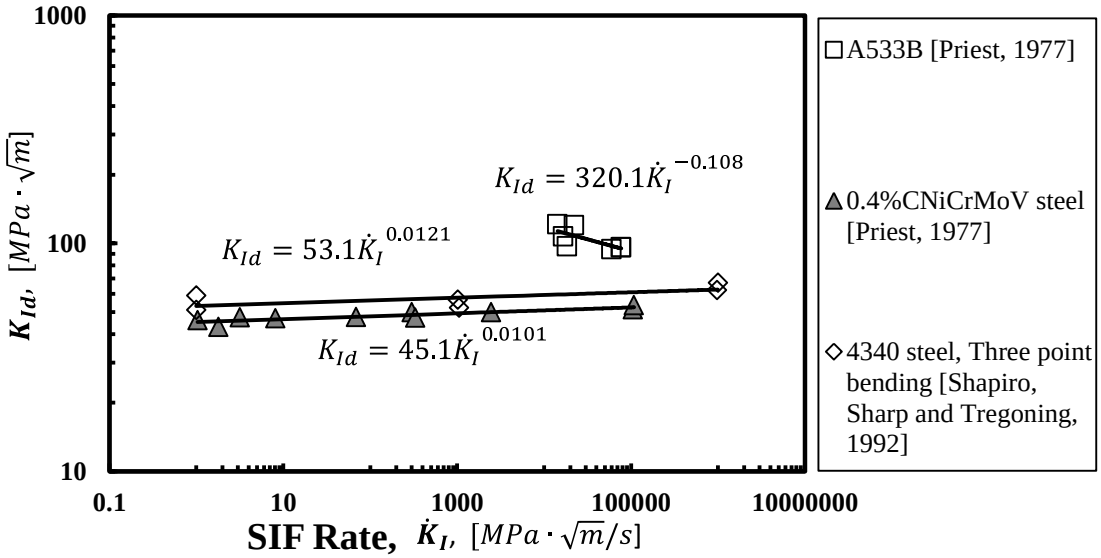

Figure 4. 7 Fracture toughness as function of stress intensity factor rate taken from literatures (Priest, 1977, Shapiro et al., 1992).

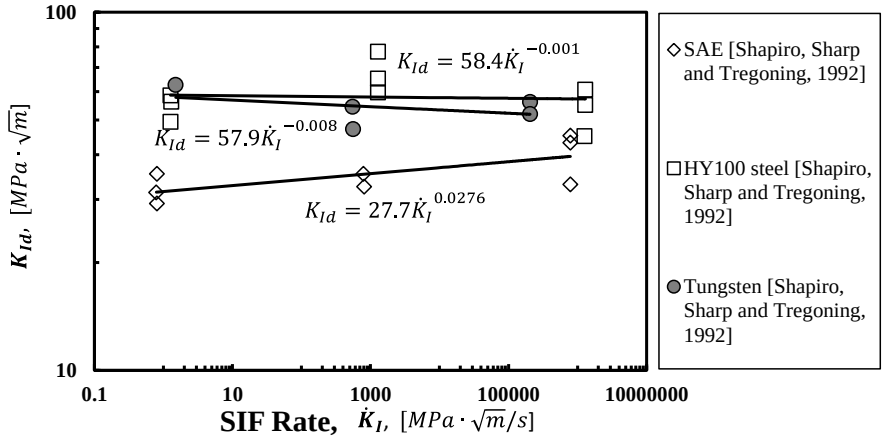

Figure 4. 8 Failure strength as function of displacement rate taken from literature(all of the tests were conducted by using three point bending test) (Shapiro et al., 1992).

According to Equation 4.4, length scale parameter $L(\dot{Z})$ can now be rewritten in explicit form as:

$$L(\dot{Z}) = f_L(\dot{Z}) = \frac{1}{\pi}\left[\frac{K_{Id}(\dot{Z})}{\sigma_0(\dot{Z})}\right]^2 = \left[\frac{\alpha \cdot \dot{Z}^{\beta}}{a_0 \cdot \dot{Z}^{b_0}}\right] = M \cdot \dot{Z}^{N} \qquad (4.\ 15)$$

In Equation 4.15, M and N are material constants which have to be determined by post-processing appropriate experimental results. In particular, if $\sigma_0(\dot{Z})$ equals $\sigma_f(\dot{Z})$, then constants M and N can directly be estimated as soon as function $K_{Id}(\dot{Z})$, Equation (4.13), is known from the experiments. On the contrary, for those situations in which $\sigma_0(\dot{Z})$ is different from $\sigma_f(\dot{Z})$, such constants are suggested to be determined by adopting a strategy similar to the one

summarised in Figure 2.2. To conclude, it should be noted that, in the latter case, at least two sets of results generated by testing two different notches under two different values of $\dot{Z}$ are required to determine constants M and N, the accuracy obviously increasing as the number of data used to calibrate the model increases.

Another important aspect which is worth being mentioned is that, by nature, the TCD can be calibrated by using pieces of experimental information generated via conventional testing equipment. Owing to its unique features, the reformulated linear-elastic TCD will be used to make it suitable for designing notched metallic components against dynamic loading, the material behaviour being, by nature, highly non-linear.

Turning back to the new reformulation of the TCD proposed in this chapter, it is possible to conclude by observing that, owing to the complexity of the reasoning on which the devised design method is based, a set of appropriate experimental results is obviously required to check the validity of the formed hypotheses.

4.4 Validation by Results for Notched Cylindrical Bars of Al6063-T5

4.4.1 Introduction

In order to check the accuracy of the proposed reformulation of the TCD for predicting the strength of the notched samples under both quasi-static and dynamic loading, attention was initially focussed on the stress analysis problem. The relevant stress fields in the vicinity of the investigated stress concentrators were determined by using the commercial FE software $ANSYS^{®}$. Under linear elastic constitutive law, only the models under load 1kN/m will be created, therefore, we can simply use the stress distance curve to generate the stress distribution for different cases. In order to check the accuracy of the novel reformulation of the TCD, in this chapter, the experimental data introduced in Chapter 3 (σ_{UTS}, equal to 205 MPa, a yield stress, σ_y, of 145 MPa, an elastic modulus, E, of 68900 MPa, and a Poisson's ratio, ν, of 0.33), will be post-processed to validate the reformulated TCD.

4.4.2 Mesh Convergence

In finite element analysis (FEA), according to FEA theory, element size determines the accuracy of the results and the computing time; a finer mesh can produce more accurate results but consumes much more time than a coarser mesh (Liu, 2013). Therefore, an appropriate level of mesh refinement is essential to yield sufficiently accurate results while saving computing time. In terms of the samples of Al6063-T5 (the geometrical features were shown in Figure 3.1), taking advantage of the axisymmetric features of the cylindrical bar, only a quarter of the sample was modelled using the axisymmetric bi-dimensional elements Plane183.

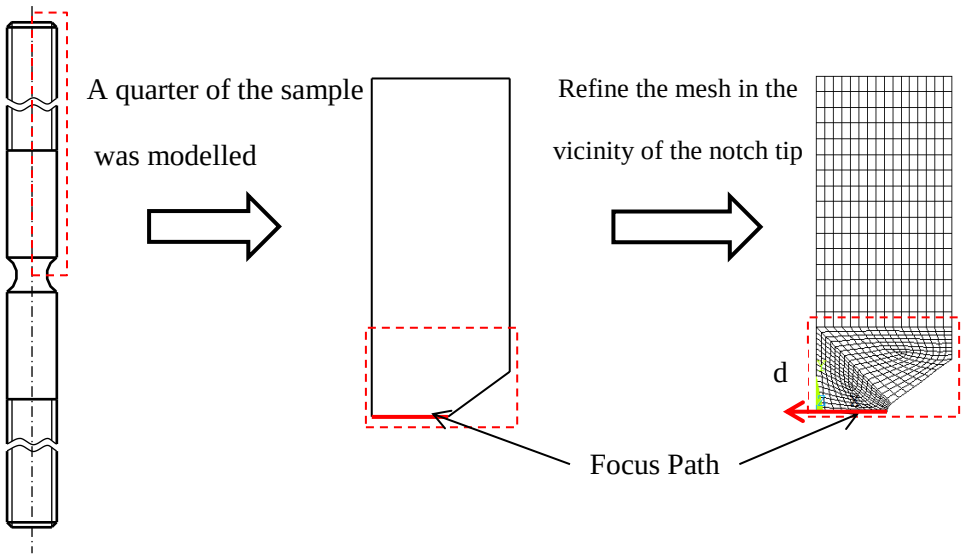

Figure 4.9 Mesh refined area of notched sample of material Al6063-T5.

In the present analysis, the most interesting information expected from the FE models is the linear elastic stress–distance curves along the focus path away from the notch tip (the solid red path shown in Figure 4.9). Therefore, mesh refinement in the vicinity of this path will be conducted until convergence occurs.

Figure 4.10 shows a series of FE models of sharply (K_t=2.93) notched samples meshed using element sizes from N=1.3mm to N=0.01mm. Figure 4.11 illustrates first principle stress–distance curves generated from these models. It is clear to see from this figure that as element size decreases, the difference in terms of first principal stress between two subsequent models decreases. Specifically, when the element size N is smaller than 0.16mm, the stress fields post-processed from the models nearly overlap each other. Figure 4.12 shows the maximum stress against element size. By comparing the maximum first principal stresses post-processed from models with two adjacent element sizes, the differences were calculated. It can be concluded that the maximum stress calculated from model with N=0.02mm and from the model with element size N=0.01mm is 0.99%, which is acceptable in engineering simulations.

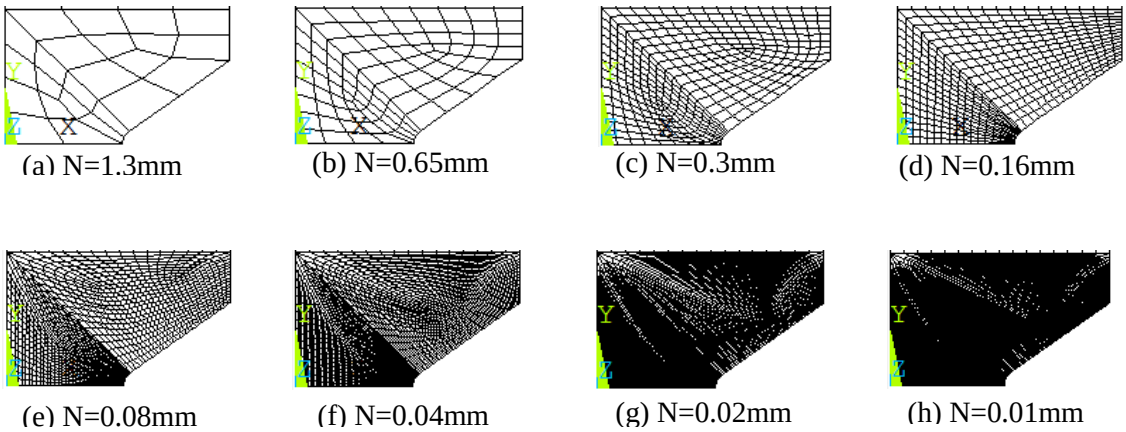

Figure 4.10 FE models of sharply (K_t=2.93) notched samples with various element sizes.

By applying the same procedure to the models of intermediately (K_t=1.69) (Figures 4.13, 4.14, and 4.15) and bluntly (K_t=1.25) (Figures 4.16, 4.17 and 4.18) notched samples, we can draw the conclusion from Figure 4.15 and Figure 4.18 that the values of N=0.08mm is the converged element size along the focus paths for the FE models of intermediately (K_t=1.69) and bluntly (K_t=1.25) notched samples, with difference of 0.93% and 0.31% respectively. The results of the convergence analysis for the models of all of the notched samples of material Al6063-T5 are summarised in Table 4.1. Owing to the simulations is based on linear elastic approach and the geometries are simple, the running time of the simulations are all less than 10s, even for a very fine mesh model. Therefore, there is no point to compare the computing time of each model.

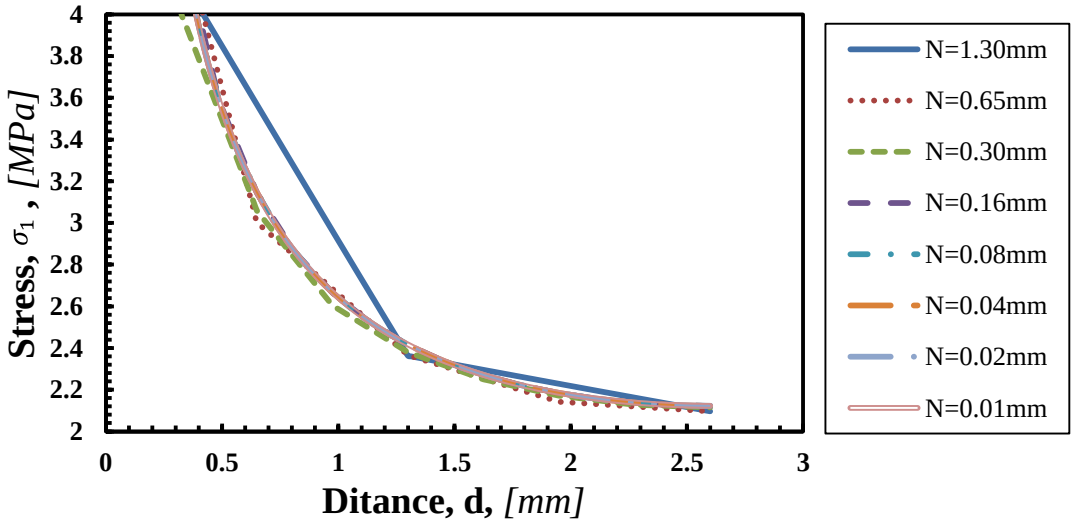

Figure 4.11 Stress distance curves of sharply (K_t=2.93) notched samples generated from FE models with different element sizes.

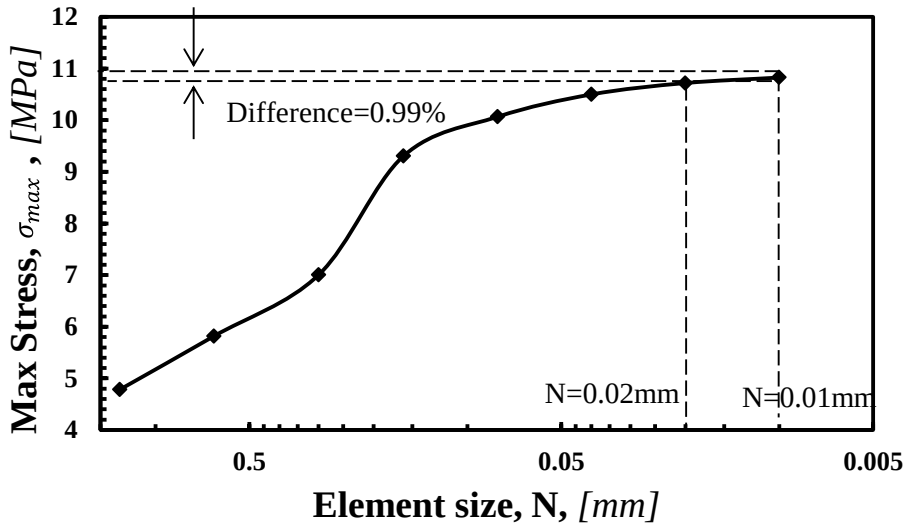

Figure 4.12 Maximum first principal stress in sharply notched samples (K_t=2.93) vs. element size.

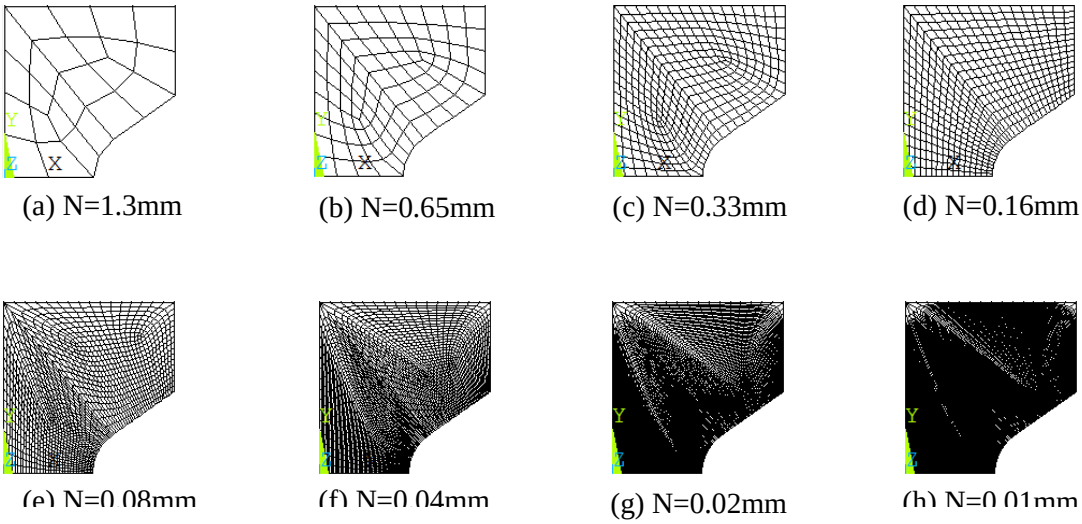

Figure 4.13 FE models of intermediately (K_t=1.69) notched sample with various element size.

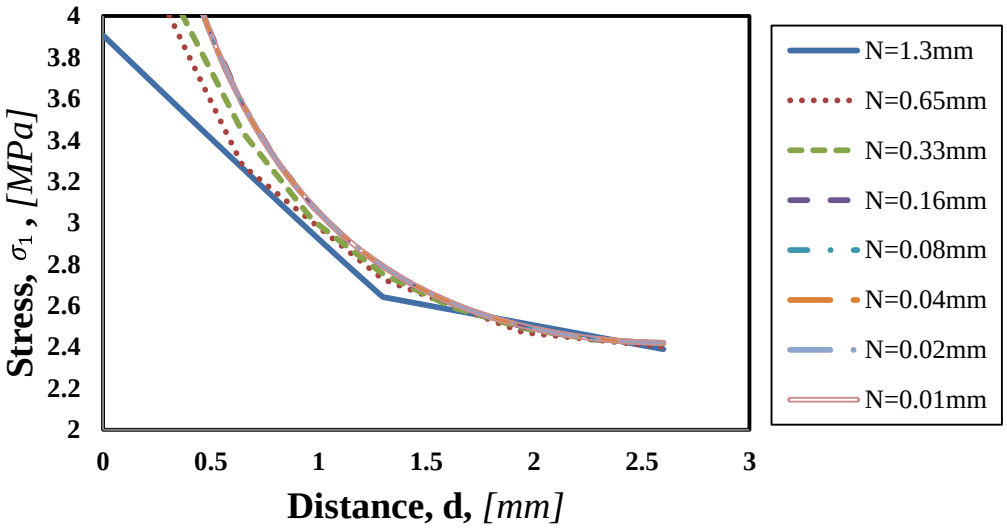

Figure 4.14 Stress distance curves of intermediately (K_t=1.69) notched sample generated from FE models with various element sizes.

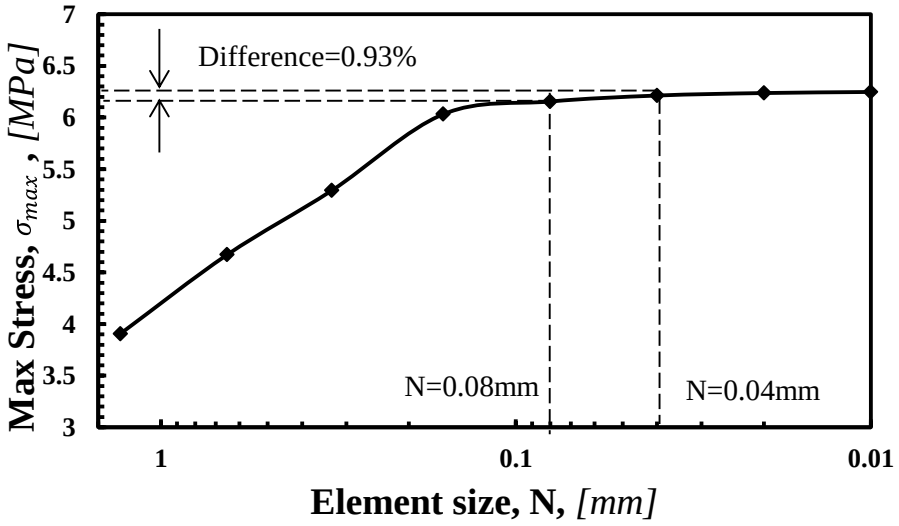

Figure 4.15 Accuracy of maximum first principal stress in intermediately notched sample (K_t=1.69) vs. element size.

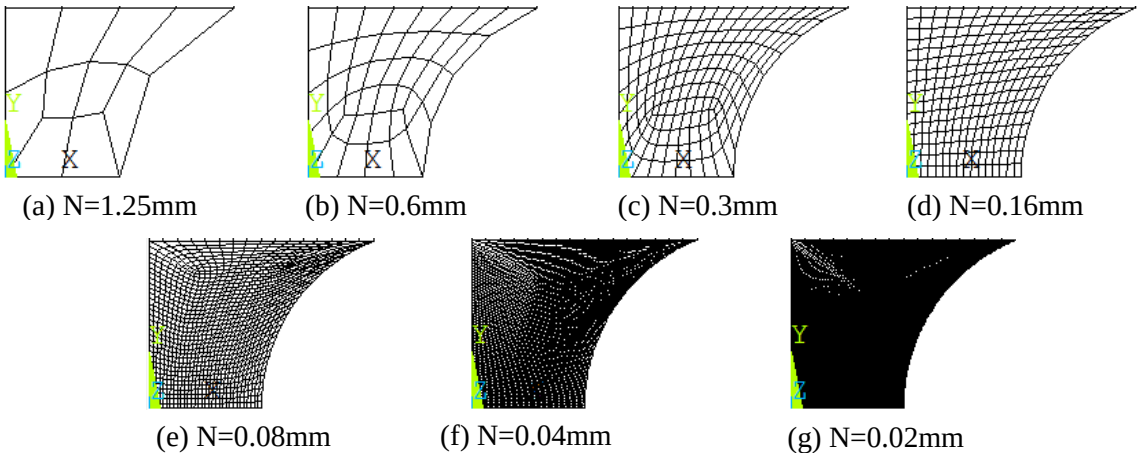

Figure 4.16 FE models of bluntly (K_t=1.25) notched sample with 8 different element size.

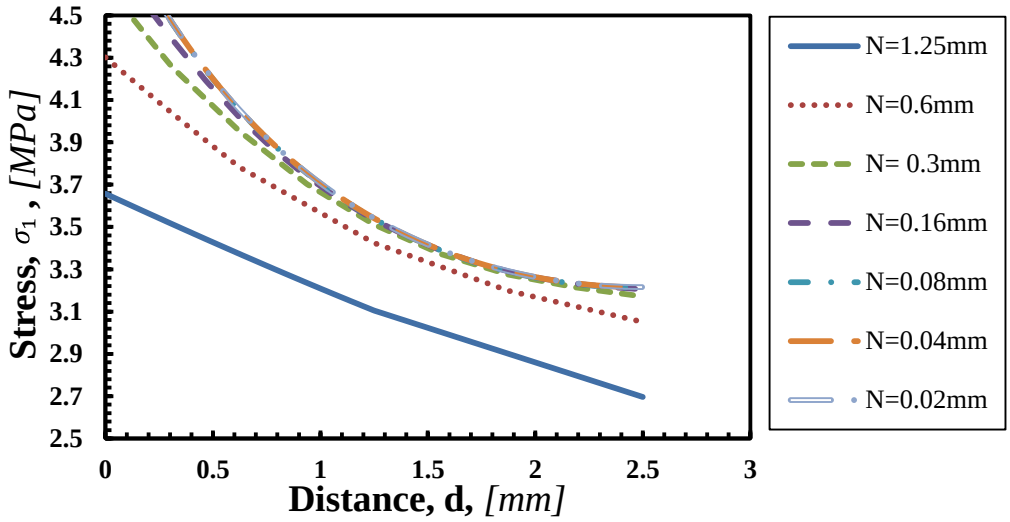

Figure 4.17 Stress distance curves of bluntly (K_t=1.25) notched sample generated from FE models with various element size.

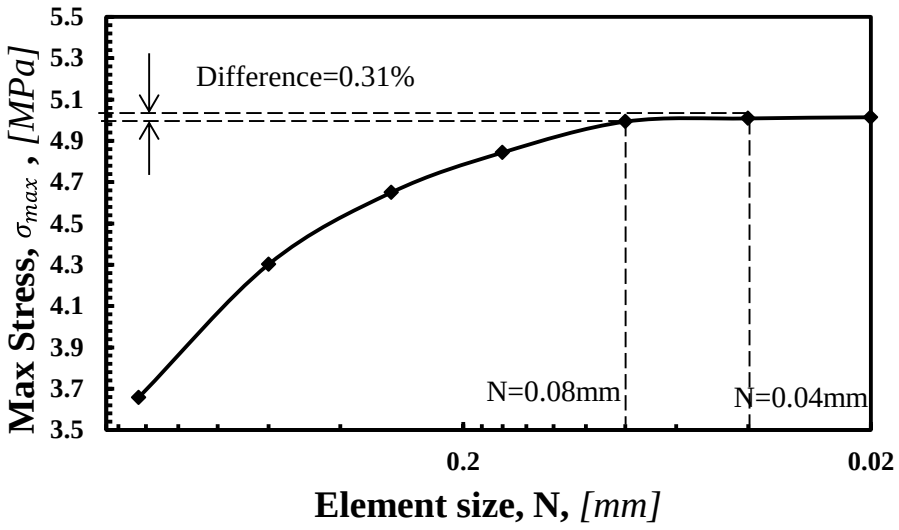

Figure 4.18 Accuracy of maximum first principal stress in bluntly notched sample (K_t=1.25) vs. element size.

Table 4.1 Results of mesh convergence for different notches of material Al6063-T5.

Notches	Selected Element Size *[mm]*	Difference *[%]*
Sharp (K_t = 2.93)	0.02	0.99
Intermediate (K_t = 1.69)	0.08	0.93
Blunt (K_t = 1.25)	0.08	0.31

4.4.3 Linear elastic TCD prediction

To use the TCD to re-analyse the results generated by testing the notched cylindrical samples of Al6063-T5 introduced in chapter 3, the initial assumption was made that the inherent strength could be taken equal to the corresponding parent material strength, that is:

$$\sigma_0\left(\dot{F}_{nom}\right) = \sigma_f\left(\dot{F}_{nom}\right) \text{ or } \sigma_0(\dot{\varepsilon}_{nom}) = \sigma_f(\dot{\varepsilon}_{nom}) \quad (4.\ 16)$$

According to the experimental results reported in Table 3.1, by using power law, the failure strength $\sigma_f\left(\dot{F}\right)$ and $\sigma_f(\dot{\varepsilon}_{nom})$ of plain and notched samples as function of nominal loading rate and strain rate were plotted in log-log graphs reported in Figure 4.19. The relationships by apply curve fitting can be expressed as follows:

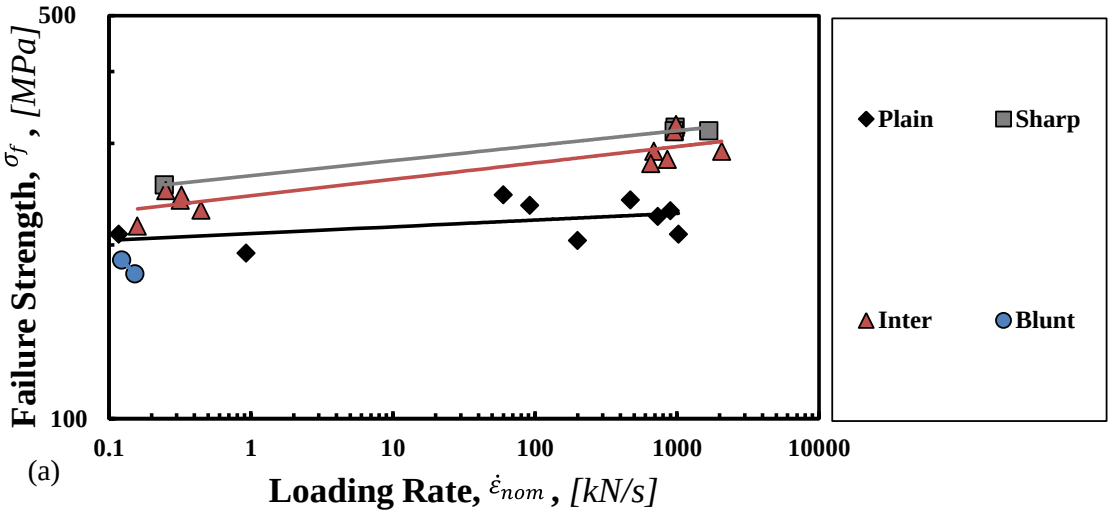

(a)

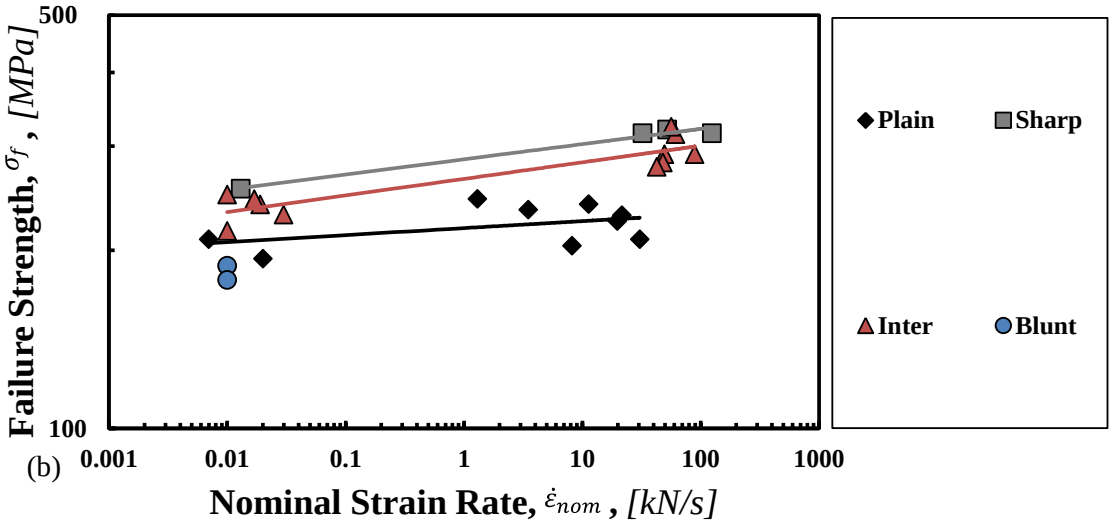

(b)

Figure 4.19 Log-log graphs of experimental failure strength of plain and notched samples of material Al6063-T5 as function of (a) nominal loading rate and (b) nominal strain rate.

- Failure strength as function of nominal loading rate:

$$\sigma_f(\dot{F}) = 209.9 \cdot \dot{F}^{0.0118} \quad \text{Plain} \quad \text{(MPa)} \qquad (4.\ 17)$$

$$\sigma_f(\dot{F}) = 264.0 \cdot \dot{F}^{0.0259} \quad \text{Sharp} \quad \text{(MPa)} \qquad (4.\ 18)$$

$$\sigma_f(\dot{F}) = 243.6 \cdot \dot{F}^{0.0284} \quad \text{Intermediate} \quad \text{(MPa)} \qquad (4.\ 19)$$

- Failure strength as function of nominal strain rate:

$$\sigma_f(\dot{\varepsilon}_{nom}) = 218.1 \cdot \dot{\varepsilon}_{nom}^{0.0118} \quad \text{Plain} \quad \text{(MPa)} \qquad (4.\ 20)$$

$$\sigma_f(\dot{\varepsilon}_{nom}) = 285.2 \cdot \dot{\varepsilon}_{nom}^{0.0257} \quad \text{Sharp} \quad \text{(MPa)} \qquad (4.\ 21)$$

$$\sigma_f(\dot{\varepsilon}_{nom}) = 264.2 \cdot \dot{\varepsilon}_{nom}^{0.0280} \quad \text{Intermediate (MPa)} \qquad (4.\ 22)$$

The bluntly notched samples were tested only at quasi-static condition, so there is no point to express the relationship between failure strength and loading or strain rate.

The chart of Figure 4.20 and Figure 4.21 show the linear-elastic stress–distance curves plotted, under quasi-static loading (i.e., $\dot{F} \approx 0.15kN \cdot s^{-1}$, $\dot{\varepsilon}_{nom} \approx 0.01 \cdot s^{-1}$) and dynamic loading (i.e., $\dot{F} \approx 2066.7kN \cdot s^{-1}$, $\dot{\varepsilon}_{nom} \approx 89.29 \cdot s^{-1}$), in the incipient failure condition. This diagram fully confirms that, for this aluminium alloy, the inherent material strength could be taken equal to σ_{UTS} with little loss of accuracy. In particular, as shown in Figure 4.20, the use of the material ultimate tensile strength (σ_{UTS} = 205 MPa) together with a conventional best fit procedure resulted in a value for the critical distance L equal to 1.37 mm. The same chart shows also that the use of the TCD applied in the form of the PM with $\sigma_0 = \sigma_{UTS}$ = 205 MPa and L = 1.37 mm resulted in estimates falling within an error interval of ±20%. Same results can also be observed in Figure 4.21, which results in critical distance L equal to 2.02mm, and the ultimate tensile strength $\sigma_{UTS} = 230MPa$ can also be taken equal to σ_0 within an error interval of±20%. Owing to the fact that this is the usual level of accuracy which is obtained when the TCD is used in other ambits of the structural integrity discipline (Taylor, 2007, Susmel, 2009b), hypothesis (4.15) was adopted to check the overall accuracy of TCD itself in estimating the strength of notched Al6063-T5 subjected to both quasi-static and dynamic loading.

After confirming the validity of assumption (4.16), by following the procedure in Figure 2.2 and 2.3, the necessary critical distance value was then directly estimated through the results generated by testing both the plain and the sharply notched specimens (see Figure 3.1 and Table 3.1). In particular, functions $L(\dot{F})$ and $L(\dot{\varepsilon}_{nom})$ were derived by post-processing the linear-elastic stress fields according to a procedure similar to the one summarised in Figure 2.2, the only difference being that $\sigma_0(\dot{F}) = \sigma_f(\dot{F})$ and $\sigma_0(\dot{\varepsilon}_{nom}) = \sigma_f(\dot{\varepsilon}_{nom})$ were assumed to be known a priori. By substituting value L generated from Figure 4.20 and 4.21 to Equation 4.15, this modus operandi allowed us to obtain the following relationships:

$$\mathrm{L}(\dot{\mathrm{F}}) = 1.541 \cdot \dot{\mathrm{F}}^{0.0368} \quad \text{(mm)} \qquad (4.\ 23)$$

$$\mathrm{L}(\dot{\varepsilon}_{nom}) = 1.695 \cdot \dot{\varepsilon}_{nom}^{\ 0.0343} \quad \text{(mm)} \qquad (4.\ 24)$$

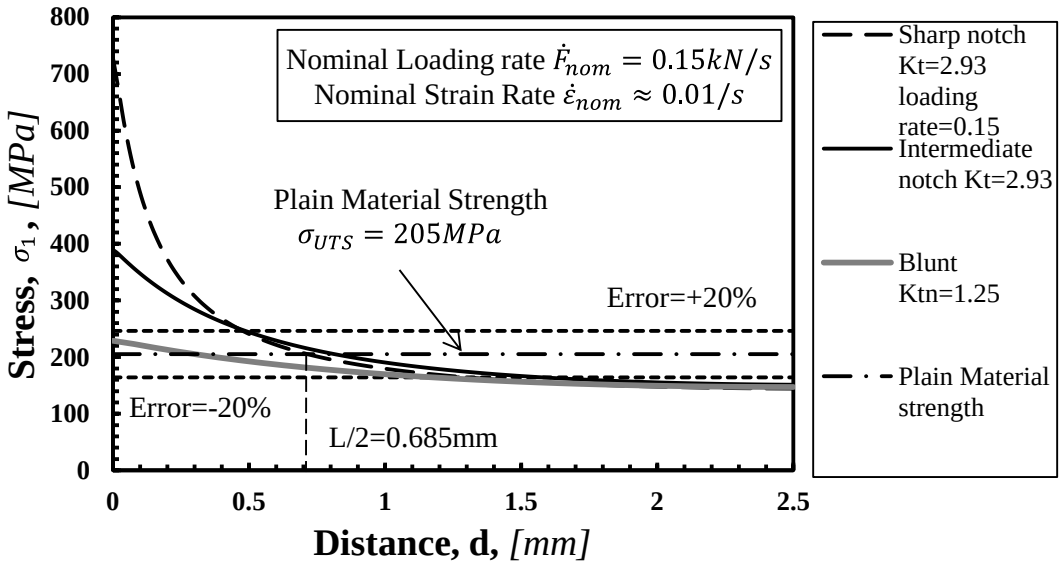

Figure 4.20 Local linear-elastic stress fields, in the incipient failure condition, under quasi-static loading ($\dot{\mathrm{F}} \approx 0.15\mathrm{kN} \cdot \mathrm{s}^{-1}$, $\dot{\varepsilon}_{\mathrm{nom}} \approx 0.01 \cdot \mathrm{s}^{-1}$) for notched Al6063-T5.

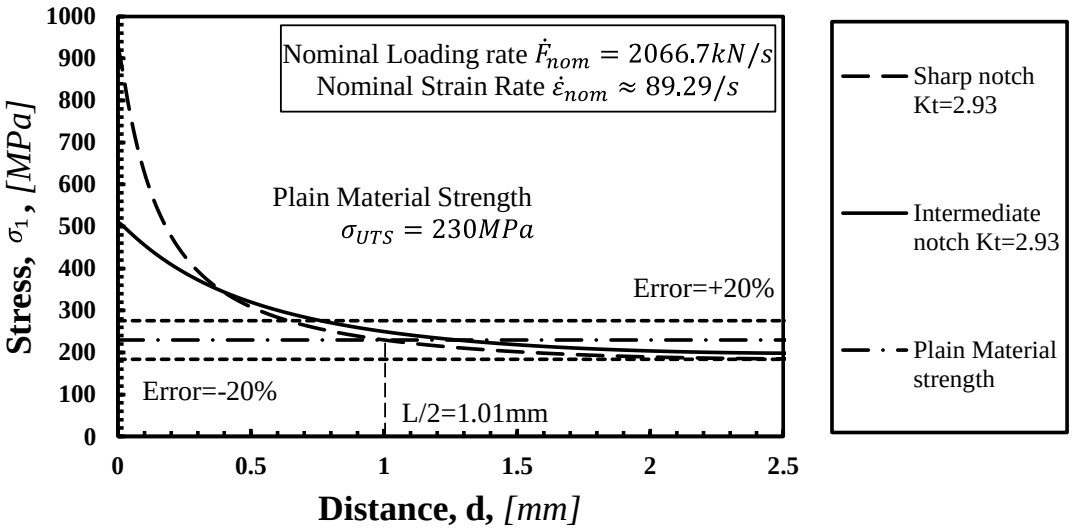

Figure 4. 21 Local linear-elastic stress fields, in the incipient failure condition, under dynamic loading ($\dot{\mathrm{F}} \approx 2066.7\mathrm{kN} \cdot \mathrm{s}^{-1}$, $\dot{\varepsilon}_{\mathrm{nom}} \approx 89.29 \cdot \mathrm{s}^{-1}$) for notched Al6063-T5.

By making use of power laws (4.23) and (4.24), the effective stress was then calculated from stress distribution curves (as shown in Figures in Appendix from A 4.1 to A4.16, in the incipient failure condition, according to both the PM, Equation 4.5, the LM, Equation 4.6, and the AM, Equation 4.7. The results of this final re-analysis are summarised in Table 4.2 and the two charts reported in Figures 4.23 and 4.24, where the error is calculated as:

$$\text{Error} = \frac{\sigma_{\text{eff}}(\dot{Z}) - \sigma_0(\dot{Z})}{\sigma_0(\dot{Z})} \ (\%) \qquad (4.\ 25)$$

The whole prediction procedure (as an example of nominal loading rate $\dot{F}_{nom}$) has been summarised in the flow chat as shown in Figure 4.22.

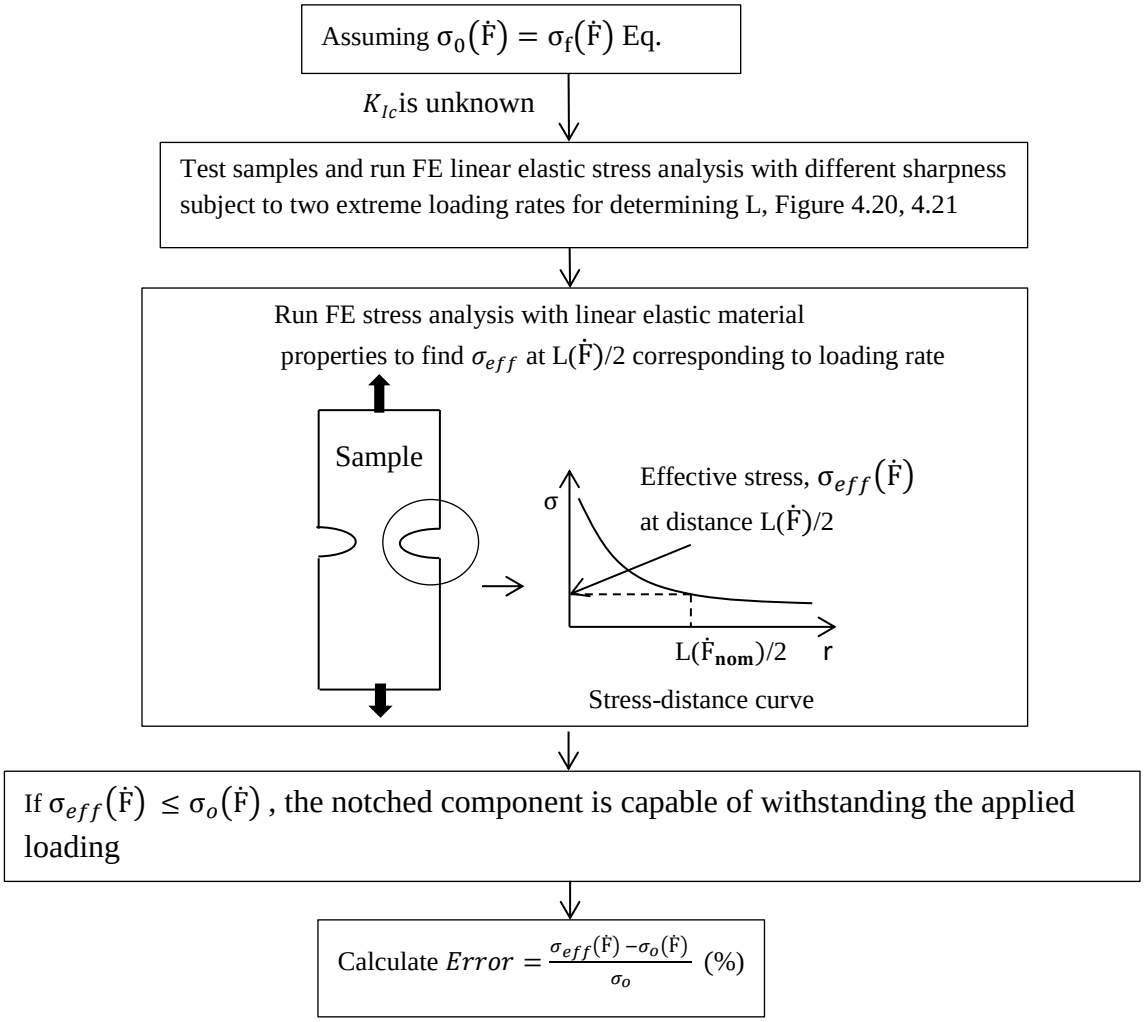

Figure 4. 22 Flow chart of TCD procedures in its simplest form of Point Method.

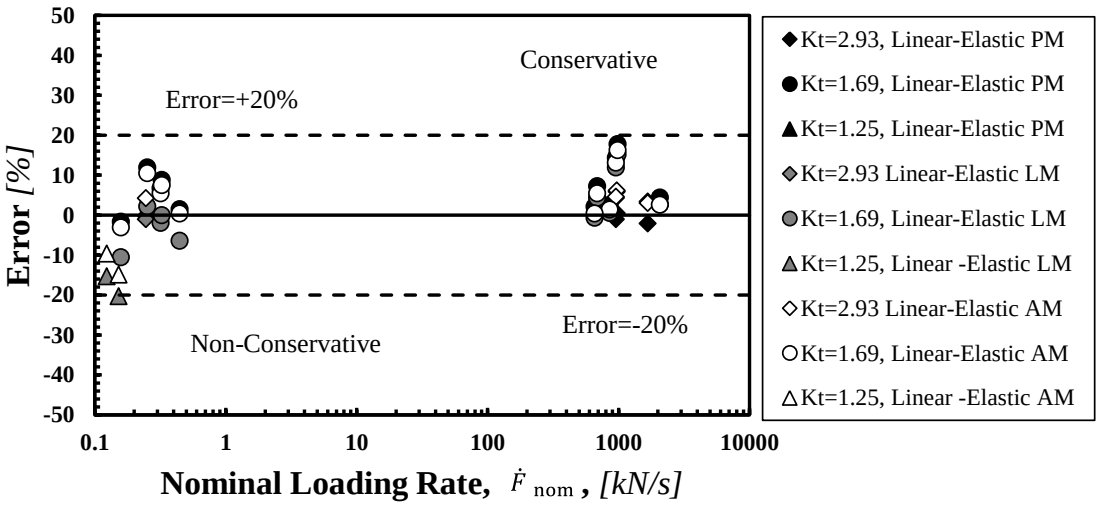

Figure 4. 23 Accuracy of the TCD applied in terms of loading rate in predicting the strength of notched Al6063-T5.

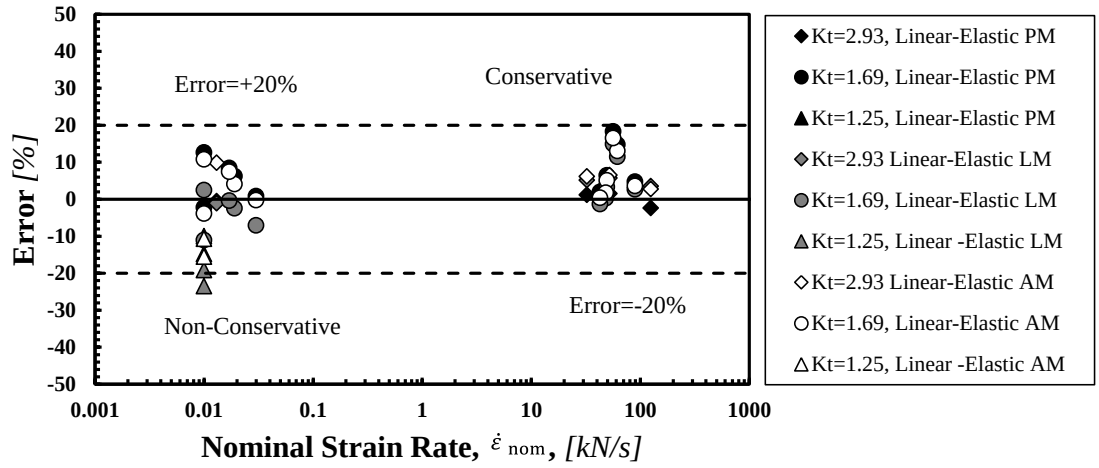

Figure 4.24 Accuracy of the TCD applied in terms of nominal strain rate in predicting the strength of notched Al6063-T5.

According to the above definition, when the error is positive, estimates are conservative, whilst, when the error is negative, estimates are non-conservative. The diagrams of Figure 4.23and 4.24 make it evident that the novel formalisation of the TCD proposed was highly accurate in predicting the dynamic strength of notched Al6063-T5, resulting in estimates falling within an error interval of ±20%. This level of accuracy is considered to be acceptable, because, in general, it is not possible to distinguish between an error of ±20% and an error of 0% due to the problems which are usually encountered during testing as well as during the numerical analyses, the local material morphology playing a role of primary importance in defining the

physiological level of scattering characterising the mechanical behaviour of engineering materials (Taylor, 2007).

Table 4. 2 Results of effective stresses and errors calculated from equation 4.25.

Code	σ_o *[MPa]*	σ_{eff} *[MPa]*, PM	Error *[%], PM*	σ_{eff} *[MPa]*, LM	Error *[%]*, LM	σ_{eff} *[MPa]*, AM	Error *[%]*, AM
S1T9	206.45	206.03	-0.20	204.27	-1.06	215.20	4.24
S1T10	229.12	224.25	-2.13	236.83	3.37	236.02	3.01
S2T1	227.65	228.68	0.45	240.98	5.86	241.67	6.16
S2T2	227.61	225.31	-1.01	237.43	4.32	238.11	4.62
S1T17	205.39	201.96	-1.67	183.74	-10.54	199.08	-3.07
S1T18	229.68	239.74	4.38	235.89	2.70	235.70	2.62
S2T5	206.52	231.17	11.94	211.01	2.17	228.17	10.48
S2T6	207.09	221.02	6.73	203.08	-1.93	218.42	5.47
S2T7	227.61	260.28	14.35	254.71	11.91	257.45	13.11
S2T9	226.73	243.14	7.24	236.49	4.31	239.11	5.46
S2T10	227.69	268.05	17.73	262.31	15.21	264.65	16.23
S2T11	207.91	211.01	1.49	194.49	-6.45	208.78	0.42
S2T12	207.13	225.35	8.80	207.06	-0.04	222.70	7.52
S2T13	227.31	233.09	2.54	228.54	0.54	230.55	1.42
S2T14	226.59	231.37	2.11	225.15	-0.64	227.54	0.42
S1T15	204.78	186.52	-8.92	173.38	-15.33	184.99	-9.67
S1T16	205.29	175.87	-14.33	163.55	-20.33	174.71	-14.90

4.5 Validation of Results for Notched Cylindrical Bars of Materials Ti-6Al-4V, an Al-Mn alloy and AlMg6

4.5.1 Mesh Convergence

To check the accuracy of the TCD against the data generated from testing the samples of Ti-6Al-4V, Al-Mn alloy and AlMg6 (see Tables 3.2, 3.3 and 3.4), again for this case, the initial hypothesis was formed that inherent strength could be taken equal to the corresponding plain material strength; the validity of this hypothesis being checked a posteriori via the notch results.

In order to obtain accurate results while saving computing time, according to the geometrical features of the group of samples described in Chapter 3 and the same as in the previous analysis,

one quarter of each sample was modelled by using axisymmetric bi-dimensional elements Plane183 (see Figure 4.25).

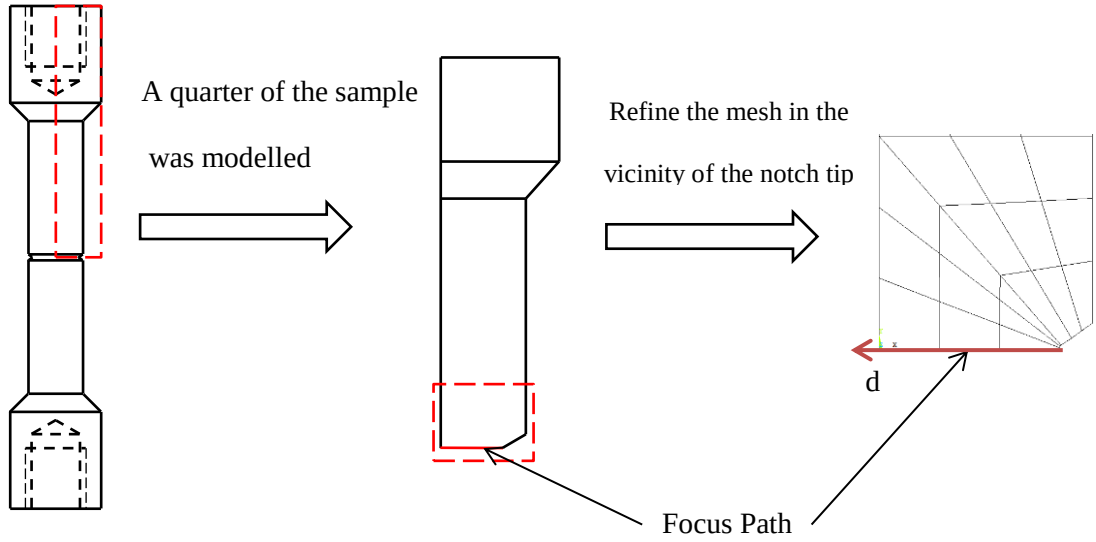

Figure 4.25 Mesh refined area of notched samples of materials Ti-6Al-4V, Al-Mn alloy and AlMg6.

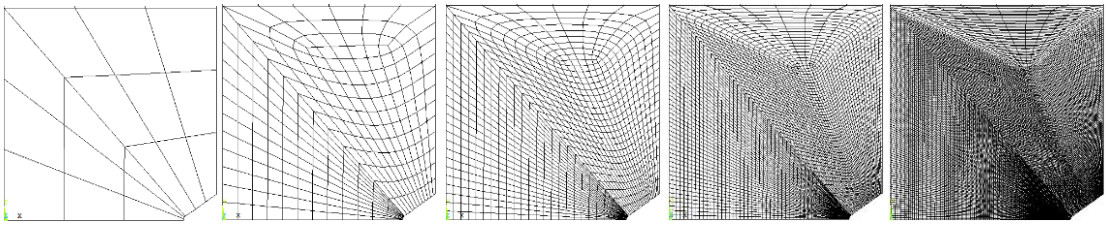

(a) N=1.3mm (b) N=0.3mm (c) N=0.16mm (d) N=0.08mm (e) N=0.04mm

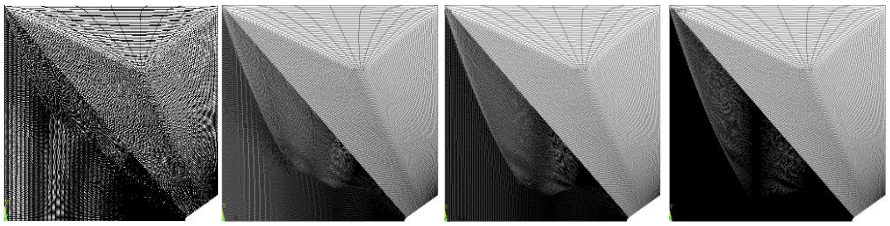

(f) N=0.02mm (g) N=0.01mm (h) N=0.007mm (i) N=0.004mm

Figure 4.26 FE models of sharply (K_t=5.2) notched samples with different element sizes.

Figure 4.26 shows a series of models of sharply notched samples ($K_t = 5.2$) meshed using various element sizes in the vicinity of the notch tip. After solving these models, the stress–distance curves were post-processed and plotted in Figure 4.27. It is clear to see from this figure that FE models with element sizes less than 0.16mm give much smoother results than the models whose element sizes are greater. As seen from the maximum stress against element size

graph for the K_t =5.2 notched samples shown in Figure 4.28, the difference between the maximum first principal stress from the model with element size N=0.007mm and from the model with element size N=0.004mm model is 1.04%. This result makes it evident that the element size N=0.007mm can be considered as the optimal element size to produce results accurately.

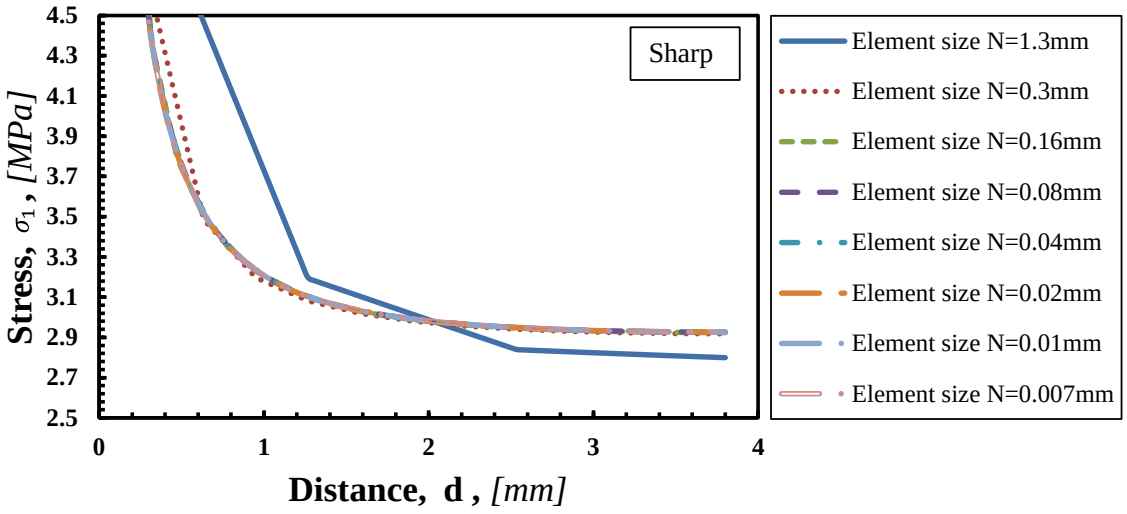

Figure 4.27 Stress distributions of sharply notched samples (K_t=5.2) calculated from the models with different element sizes.

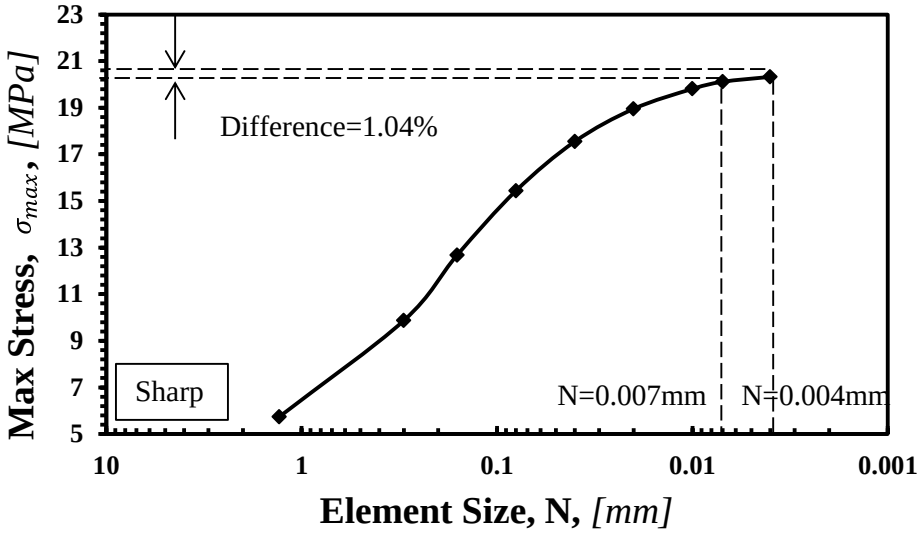

Figure 4.28 The maximum first principal stress in sharply notched samples (K_t=5.2) vs. element size.

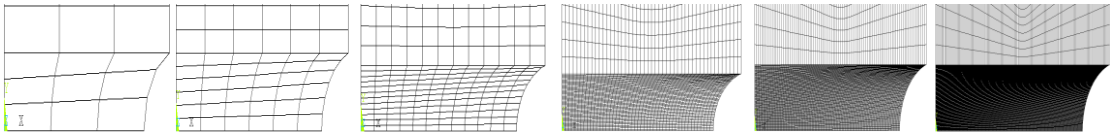

(a) N=1.3mm (b) N=0.6mm (c) N=0.3mm (d) N=0.08mm (e) N=0.04mm (f) N=0.02mm

Figure 4.29 FE models of intermediately (K_t=2.08) notched sample with different element sizes.

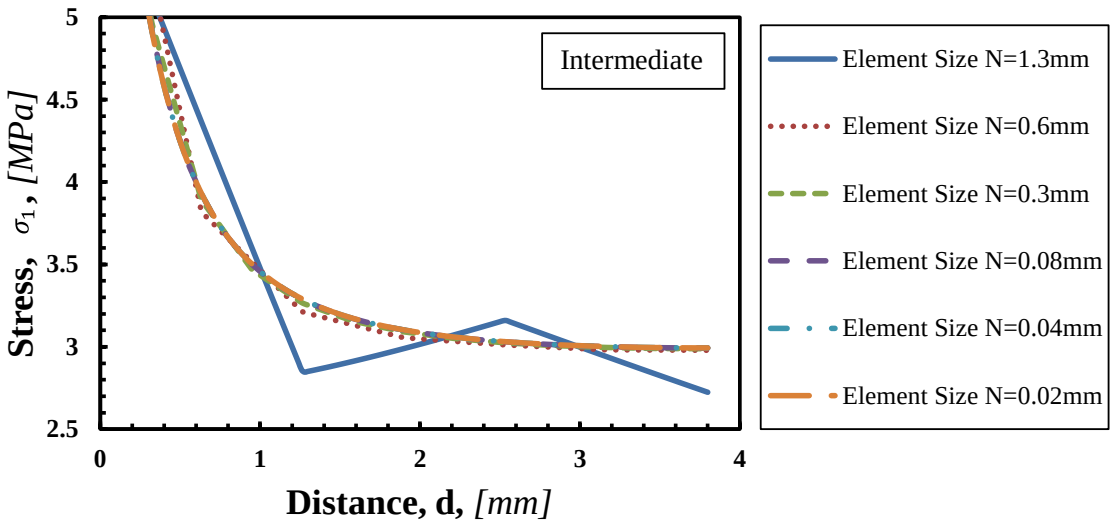

Figure 4.30 Stress distributions of intermediately notched samples (K_t=2.08) calculated from the models with different element sizes.

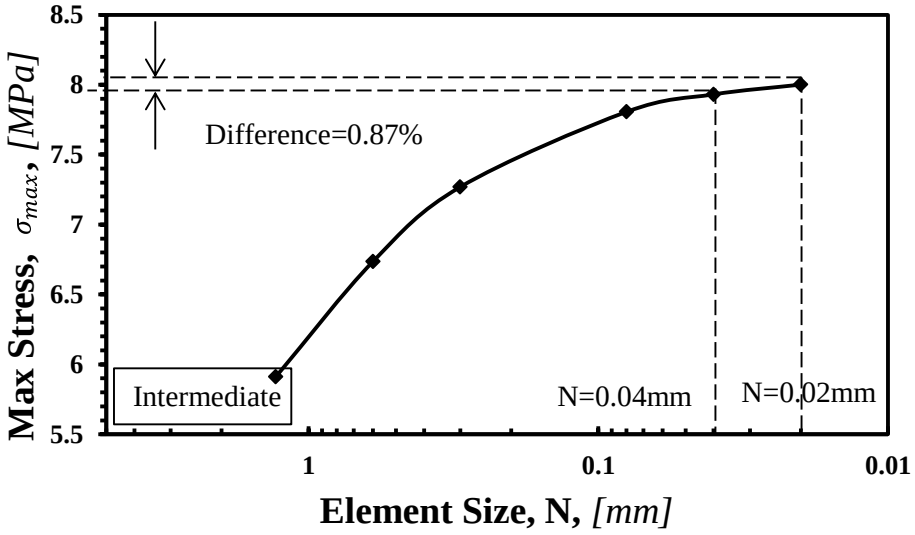

Figure 4.31 The maximum first principal stress in intermediately notched samples (K_t=2.08) vs. element size.

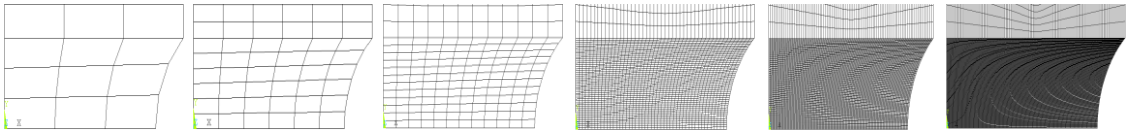

(a) N=1.3mm (b) N=0.6mm (c) N=0.3mm (d) N=0.08mm (e) N=0.04mm (f) N=0.02mm

Figure 4.32 FE models of bluntly (K_t=1.67) notched sample with different element sizes.

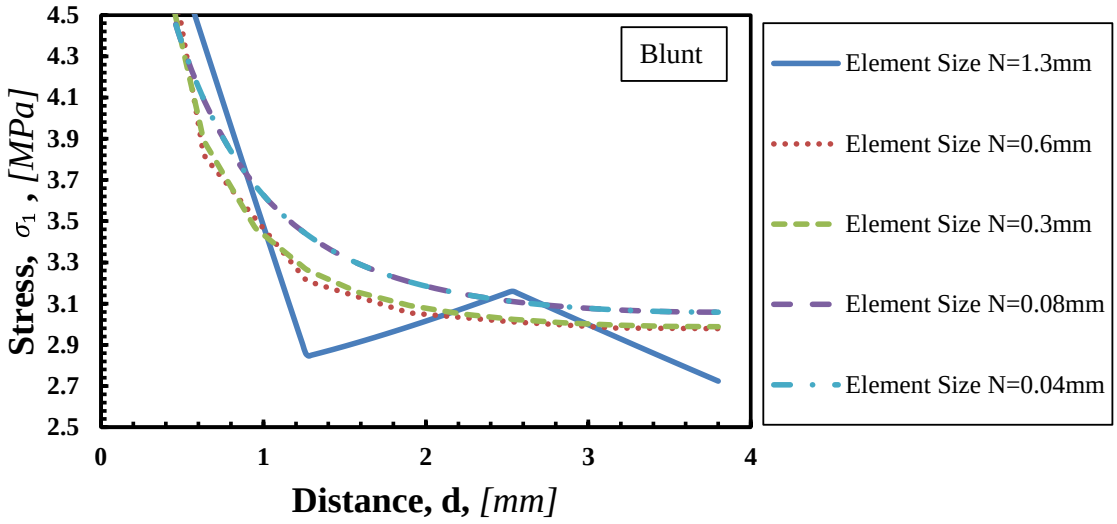

Figure 4.33 Stress distributions of bluntly notched samples (K_t=1.67) calculated from the models with different element sizes.

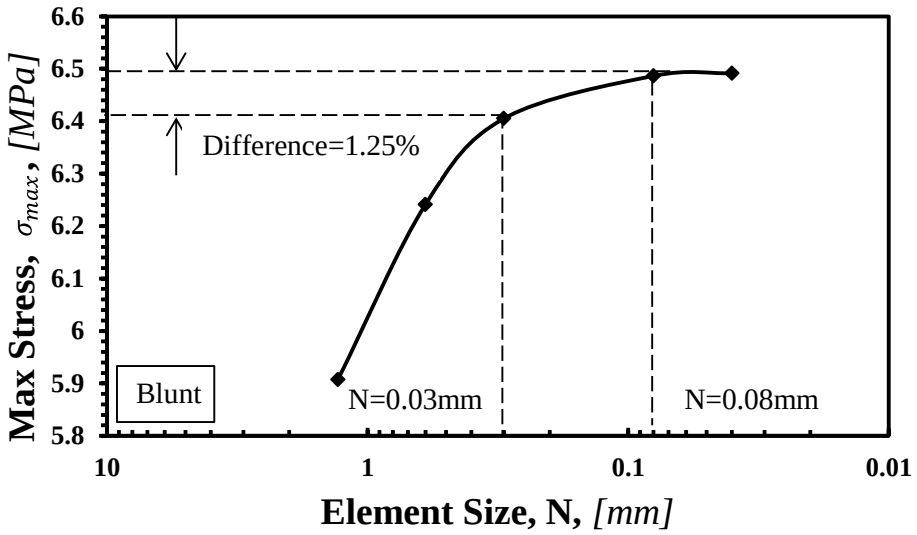

Figure 4.34 The maximum first principal stress in bluntly notched sample (K_t=1.67) vs. element size.

Similarly, by making use of the same procedure of convergence analysis with the models of other notched samples ($K_t = 2.08$, $K_t = 1.67$), we can draw the conclusion that the element sizes N=0.04mm and 0.30mm are converged sizes for the FE models of these two types of notched samples with errors of 0.87% and 1.25% respectively. The optimal element sizes for the models of the three types of stress raisers are summarised in Table 4.3.

Table 4.3 Results of mesh convergence for different notches of material Ti-6Al-4V.

Notches	Selected Element Size *[mm]*	Error *[%]*
Sharp (K_t = 2.93)	0.007	1.04
Intermediate (K_t = 1.69)	0.04	0.87
Blunt (K_t = 1.25)	0.30	1.25

4.5.2 Linear elastic TCD prediction

By using a conventional best fit procedure, graphs reported in Figure 4.35 plot the tested failure stress of un-notched and notched samples as function of nominal strain rate and loading rate.

Functions $\sigma_0(\dot{\varepsilon}_{nom})$ and $\sigma_0(\dot{F})$ were directly derived from the results generated by testing the all specimens:

- Failure strength as function of nominal strain rate:

$$\sigma_0(\dot{\varepsilon}_{\mathrm{nom}}) = \sigma_f(\dot{\varepsilon}_{\mathrm{nom}}) = 1080.8 \cdot \dot{\varepsilon}_{\mathrm{nom}}{}^{0.0094} \quad \text{Plain} \quad \text{(MPa)} \quad (4.\ 26)$$

$$\sigma_f(\dot{\varepsilon}_{\mathrm{nom}}) = 1319.0 \cdot \dot{\varepsilon}_{\mathrm{nom}}{}^{0.0134} \quad \text{Blunt} \quad \text{(MPa)} \quad (4.\ 27)$$

$$\sigma_f(\dot{\varepsilon}_{\mathrm{nom}}) = 1367.5 \cdot \dot{\varepsilon}_{\mathrm{nom}}{}^{0.0105} \quad \text{Intermediate} \quad \text{(MPa)} \quad (4.\ 28)$$

- Failure strength as function of nominal loading rate:

$$\sigma_0(\dot{\mathrm{F}}) = \sigma_f(\dot{\mathrm{F}}) = 1027 \cdot \dot{\mathrm{F}}^{0.0129} \quad \text{Plain} \quad \text{(MPa)} \quad (4.\ 29)$$

$$\sigma_f(\dot{\mathrm{F}}) = 1225.9 \cdot \dot{\mathrm{F}}^{0.0172} \quad \text{Blunt} \quad \text{(MPa)} \quad (4.\ 30)$$

$$\sigma_f(\dot{\mathrm{F}}) = 1290 \cdot \dot{\mathrm{F}}^{0.0134} \quad \text{Intermediate} \quad \text{(MPa)} \quad (4.\ 31)$$

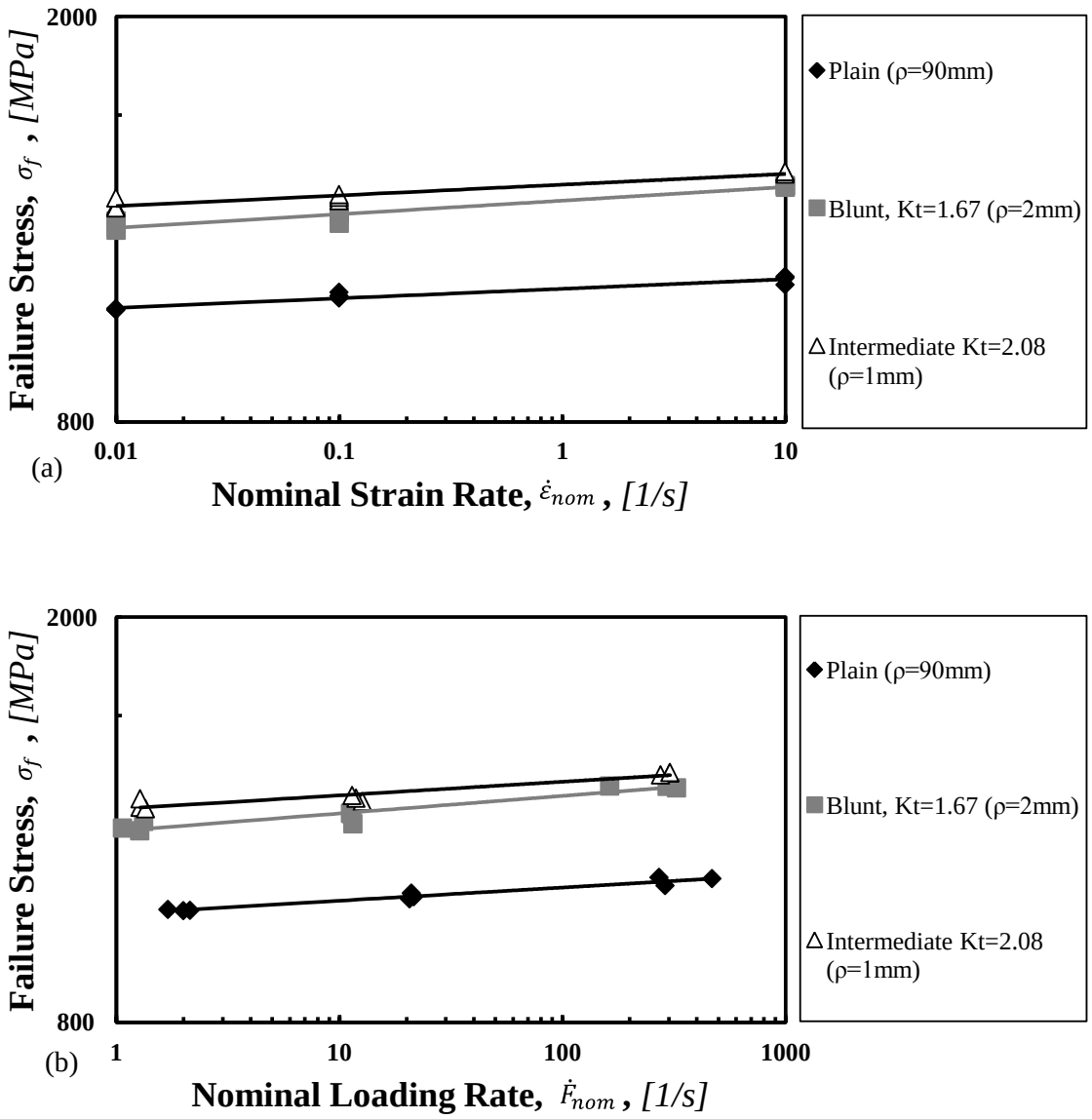

Figure 4.35 Log-log graphs of experimental failure strength of plain and notched samples of material Ti-6Al-4V as function of (a) nominal strain rate and (b) nominal loading rate.

The linear-elastic stress fields plotted, in the incipient failure condition, in the chart of Figure 4.36(a) fully confirm the validity of the formed hypothesis. In more detail, the two stress–distance curves reported in these graphs were determined by considering both the blunt (K_t = 1.67) and the intermediate (K_t = 2.08) stress raisers, the nominal failure force being calculated by averaging, for any notched geometry, the three results generated under $\dot{\varepsilon} = 0.01s^{-1}$ ($\dot{F} = 1.27kN \cdot s^{-1}$).

This simple procedure resulted in a critical distance value under quasi-static loading equal to 3.724 mm. The same strategy (Figure 4.36(b)) was followed also to estimate the critical distance value under $\dot{\varepsilon}_{nom} = 10000s^{-1}$ ($\dot{F} \approx 2.4 \cdot 10^6 kN \cdot s^{-1}$): the use of the liner-elastic stress–

distance curve determined by averaging the two results generated by testing the sharply notched samples (K_t = 5.2) together with the failure stress estimated according to Equation (4.26) resulted in a critical distance value of 1.792mm. Therefore, the two critical distance values estimated as described above allowed us to directly calculate constants M and N in Equation (4.15):

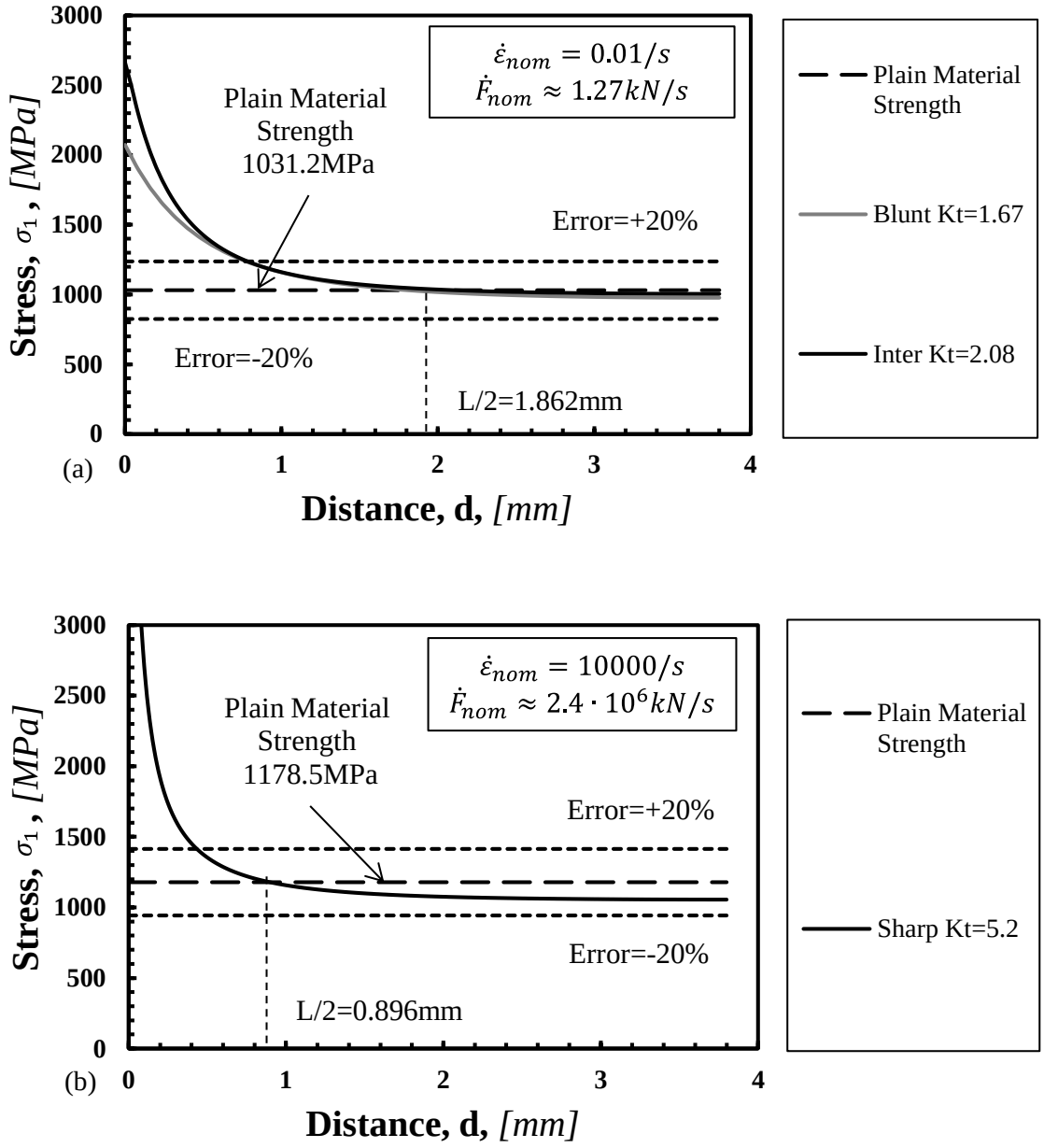

Figure 4.36 Local linear-elastic stress fields, in the incipient failure condition, under (a) $\dot{\varepsilon}_{nom} = 0.01\ s^{-1}$ ($\dot{F} \approx 1.27kN \cdot s^{-1}$) and (b) $\dot{\varepsilon}_{nom} = 10000\ s^{-1}$ ($\dot{F} \approx 2.4 \cdot 10^6 kN \cdot s^{-1}$) for notched Ti-6Al-4V;

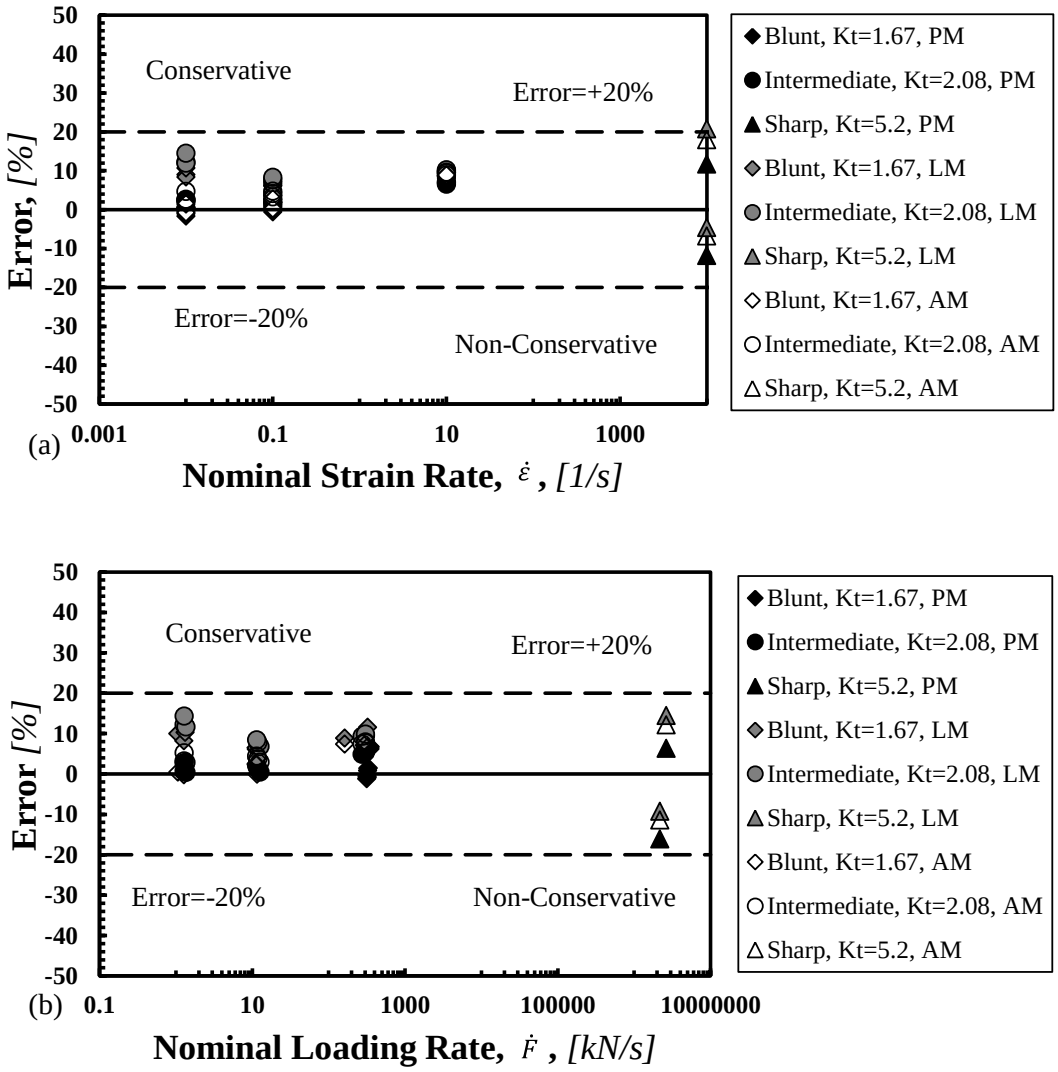

Figure 4.37 Accuracy of the TCD in predicting the strength of notched Ti-6Al-4V as function of (a) nominal strain rate and (b) nominal loading rate.

$$L(\dot{\varepsilon}_{nom}) = 2.92 \cdot \dot{\varepsilon}_{nom}{}^{-0.053} \quad \text{(mm)} \qquad (4.\ 32)$$

$$L(\dot{F}) = 3.77 \cdot \dot{F}^{-0.051} \quad \text{(mm)} \qquad (4.\ 33)$$

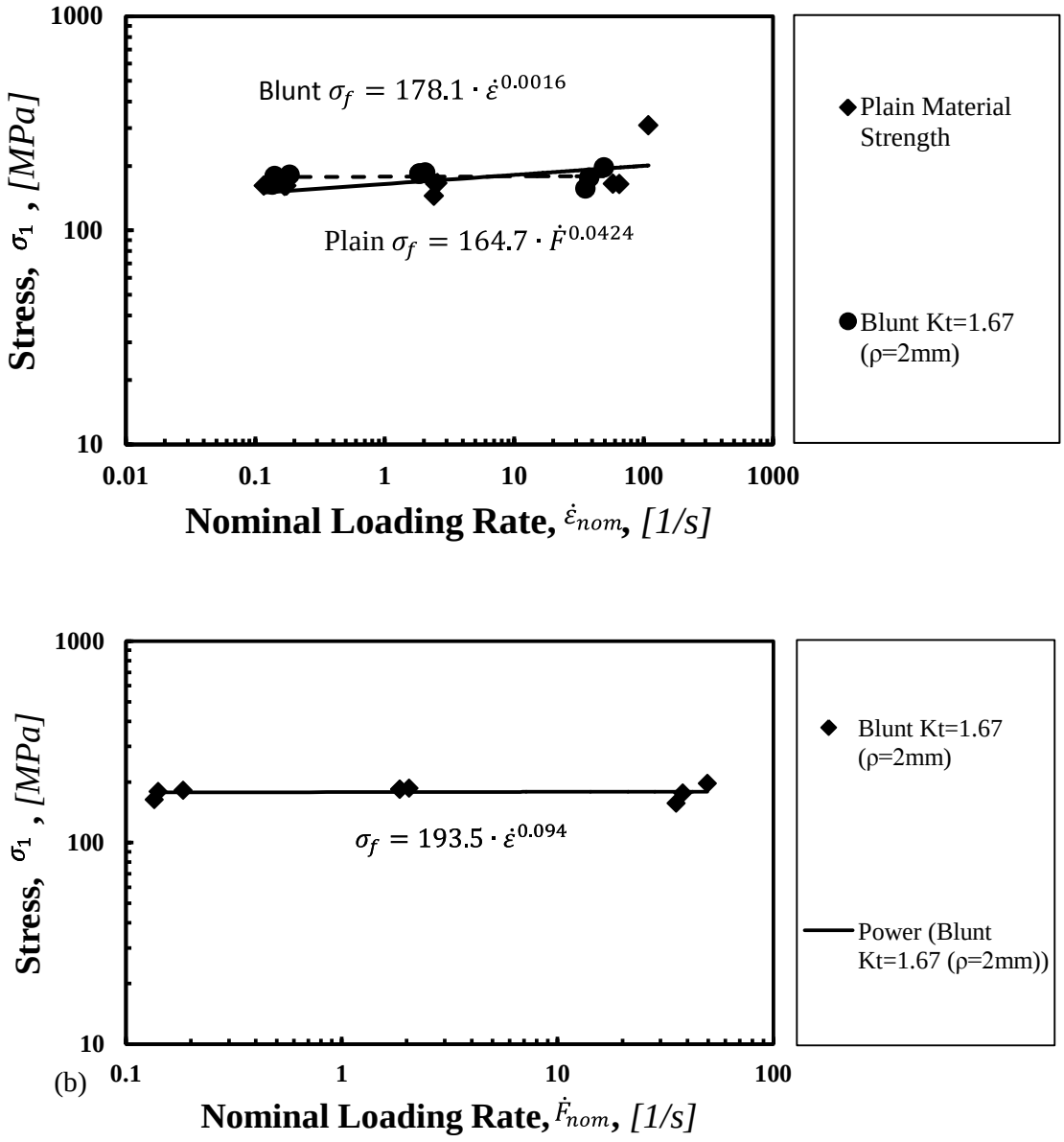

Figure 4.38 Log-log graphs of failure strength of plain and bluntly notched samples of material AlMn alloy as function of (a) nominal strain rate and (b) nominal loading rate.

The error diagrams reported in Figure 4.37(a) and (b) prove that the proposed reformulation of the TCD was capable of accurately estimating also the strength of the notched specimens of Ti–6Al–4V, with the estimates falling within an error interval of ±20%. It also interesting to point out that such a high level of accuracy was reached independently from the form in which the TCD was applied (i.e., in terms of either the PM, the LM, or the AM).

The results generated by testing the samples of the investigated AlMn alloy (Table 3.4) were re-analysed by adopting the same strategy as the one used to post-process the data obtained by

testing the Ti–6Al–4V specimens. In particular, initially the inherent strength was assumed to be equal to the plain material failure stress.

As shown in Figure 4.38(a) and (b), the relationship between failure strength for non-notched and notched samples as function of nominal strain rate and loading rare can be expressed as follow:

- In terms of nominal strain rate:

$$\sigma_0(\dot{\varepsilon}_{\mathrm{nom}}) = \sigma_f(\dot{\varepsilon}_{\mathrm{nom}}) = 182.5 \cdot \dot{\varepsilon}_{\mathrm{nom}}{}^{0.0363} \quad \text{Plain} \quad \text{(MPa)} \tag{4. 34}$$

$$\sigma_0(\dot{\varepsilon}_{\mathrm{nom}}) = \sigma_f(\dot{\varepsilon}_{\mathrm{nom}}) = 178.1 \cdot \dot{\varepsilon}_{\mathrm{nom}}{}^{0.0008} \quad \text{Blunt} \quad \text{(MPa)} \tag{4. 35}$$

- In terms of nominal loading rate:

$$\sigma_0(\dot{\mathrm{F}}) = \sigma_f(\dot{\mathrm{F}}) = 193.5 \cdot \dot{\varepsilon}_{\mathrm{nom}}{}^{0.094} \quad \text{Plain} \quad \text{(MPa)} \tag{4. 36}$$

$$\sigma_0(\dot{\mathrm{F}}) = \sigma_f(\dot{\mathrm{F}}) = 164.7 \cdot \dot{\mathrm{F}}^{0.0424} \quad \text{Blunt} \quad \text{(MPa)} \tag{4. 37}$$

where $\sigma_f(\dot{\varepsilon}_{nom})$ and $\sigma_0(\dot{F})$ were determined through a conventional best fit procedure by considering the un-notched results listed in Table 3.3.

The chart of Figure 4.39(a) reports the critical distance value determined under $\dot{\varepsilon}_{nom} = 0.01\ s^{-1}$ ($\dot{F} \approx 0.154 kN \cdot s^{-1}$) by averaging the three results generated by testing the bluntly notched specimens ($K_t = 1.67$) – see Table 3.3, the critical distance value was predicted to be equal to 2.09mm. The chart of Figure 4.39(b) plots instead the linear-elastic stress distance curve determined, in the incipient failure condition, from the result obtained by testing a sharply notched specimen ($K_t = 5.2$) under $\dot{\varepsilon}_{nom} \approx 10^4\ s^{-1}$ ($\dot{F} \approx 8.6 \cdot 10^4 kN \cdot s^{-1}$). According to this chart, the corresponding critical distance value was estimated to be equal to 0.136 mm. The L values reported in Figure 4.39(a) and (b) were then used to estimate constants M and N in Eq. (4.15), obtaining:

$$\mathrm{L}(\dot{\varepsilon}_{\mathrm{nom}}) = 0.841 \cdot \dot{\varepsilon}_{\mathrm{nom}}{}^{-0.198} \quad \text{(mm)} \tag{4. 38}$$

$$\mathrm{L}(\dot{\mathrm{F}}) = 1.42 \cdot \dot{\mathrm{F}}^{-0.206} \quad \text{(mm)} \tag{4. 39}$$

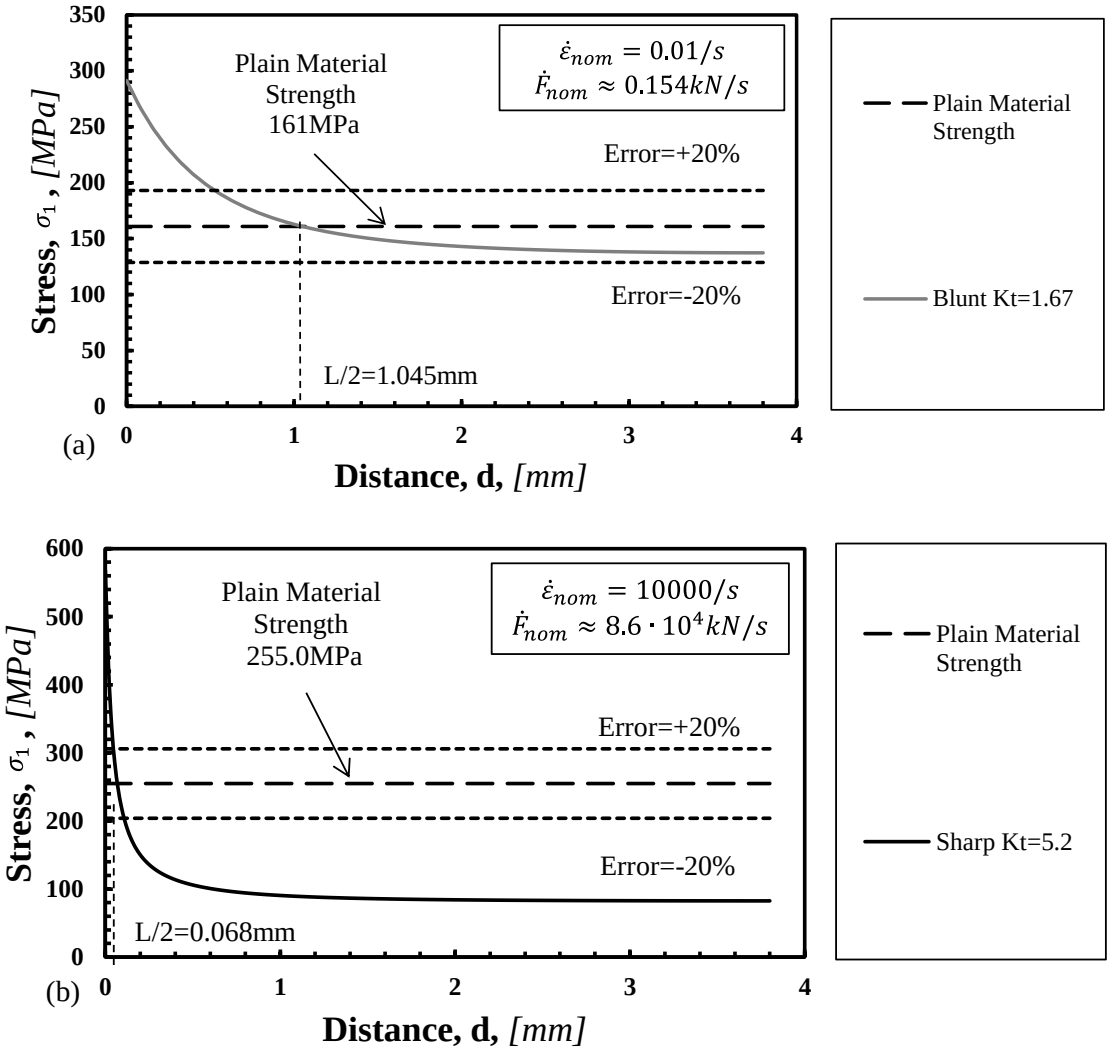

Figure 4.39 Local linear-elastic stress fields, in the incipient failure condition, under (a) $\dot{\varepsilon}_{\mathrm{nom}} = 0.01\ \mathrm{s}^{-1}$, and (b) $\dot{\varepsilon}_{\mathrm{nom}} = 10000\ \mathrm{s}^{-1}$ (b) for notched AlMn alloy.

The error diagrams reported in Figure 4.40(a)and (b) prove that the proposed reformulation of the TCD was highly accurate also in estimating the strength of the notched samples made of the investigated AlMn alloy, this holding true when the method was applied in terms of both nominal strain and loading rate.

The results generated by testing the samples of AlMg6 (Table 3.4) were post-processed by following the same strategy as the one adopted to re-analyse the data generated by testing the specimens made of both Ti–6Al–4V and AlMn alloy. By assuming that the inherent strength could be taken equal to the plain material failure stress, the following plain and notched material calibration functions were obtained via a conventional best fit procedure (Figure 4.41):

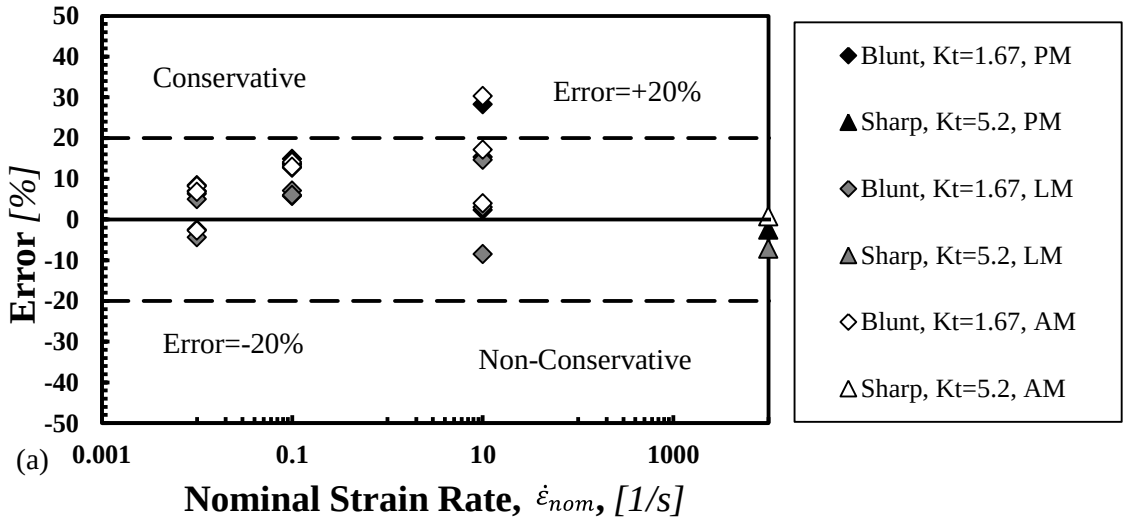

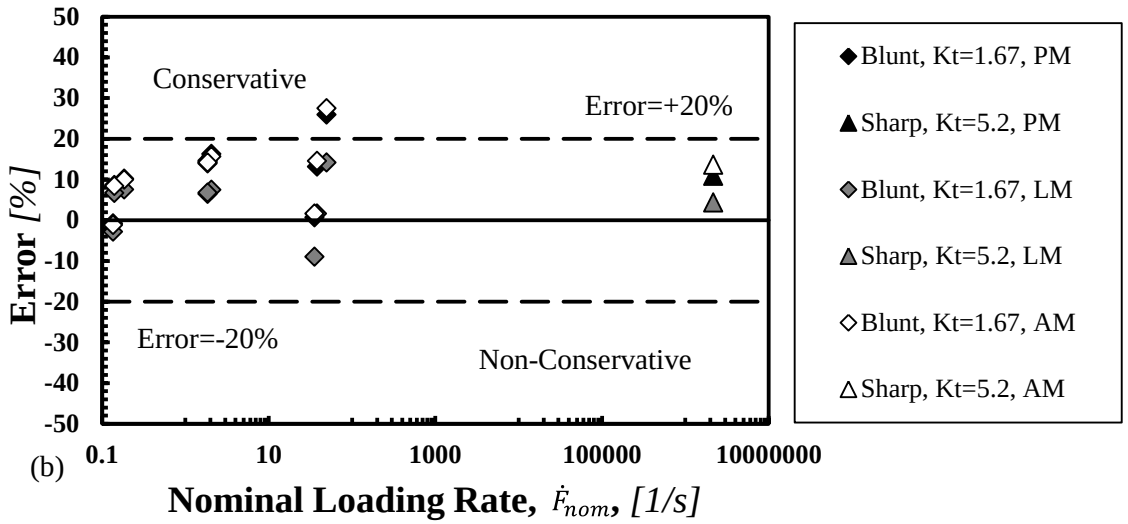

Figure 4.40 Accuracy of the TCD in predicting the strength of notched AlMn alloy as function of (a) nominal strain rate and (b) nominal loading rate.

The failure strength of plain and notched samples as function of nominal strain rate and loading rate are expressed as follows:

- In terms of nominal strain rate:

$$\sigma_0(\dot{\varepsilon}_{nom}) = \sigma_f(\dot{\varepsilon}_{nom}) = 591.8 \cdot \dot{\varepsilon}_{nom}{}^{-0.01} \quad \text{Plain} \quad \text{(MPa)} \qquad (4.\ 40)$$

$$\sigma_0(\dot{\varepsilon}_{nom}) = \sigma_f(\dot{\varepsilon}_{nom}) = 470.1 \cdot \dot{\varepsilon}_{nom}{}^{-0.004} \quad \text{Blunt} \quad \text{(MPa)} \qquad (4.\ 41)$$

$$\sigma_0(\dot{\varepsilon}_{nom}) = \sigma_f(\dot{\varepsilon}_{nom}) = 469.4 \cdot \dot{\varepsilon}_{nom}{}^{-0.02} \quad \text{Intermediate} \quad \text{(MPa)} \qquad (4.\ 42)$$

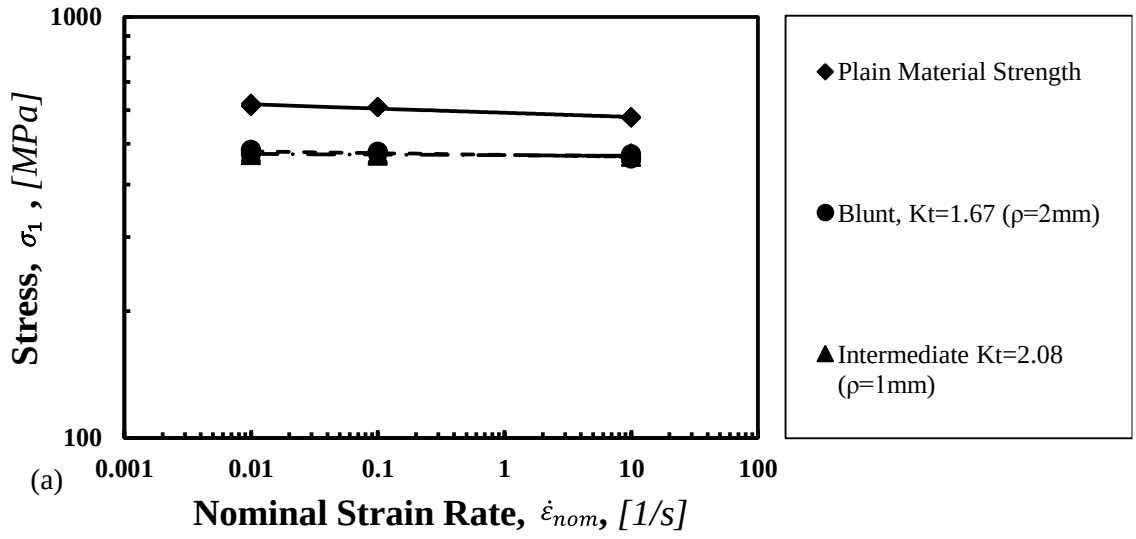

(a)

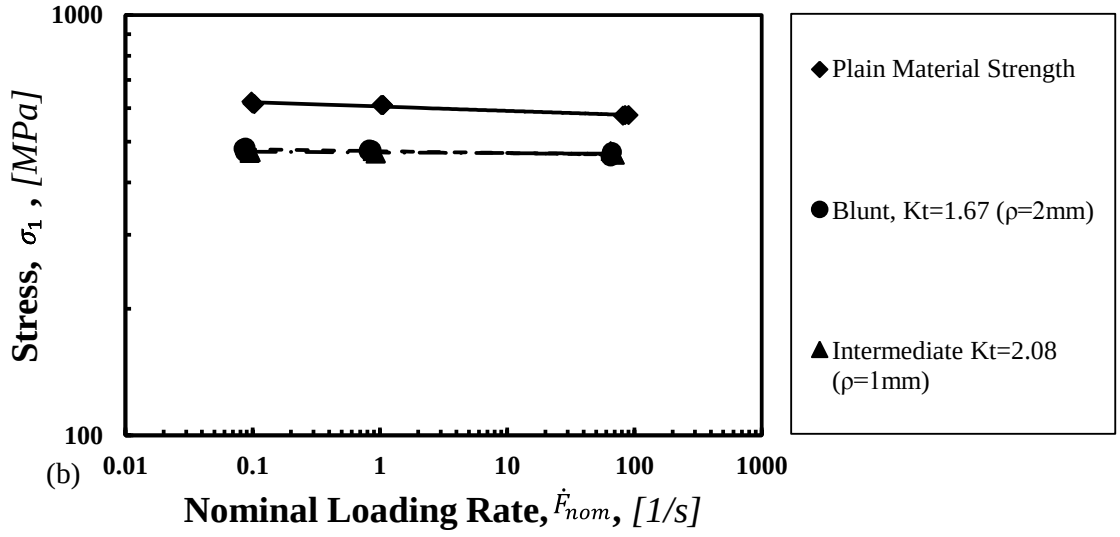

(b)

Figure 4.41 Log-log graphs of failure strength of plain and bluntly notched samples of material AlMg6 as function of (a) nominal strain rate and (b) nominal loading rate.

- In terms of nominal loading rate:

$$\sigma_0(\dot{F}) = \sigma_f(\dot{F}) = 605.4 \cdot \dot{F}^{-0.01} \quad \text{Plain} \quad \text{(MPa)} \quad (4.\ 43)$$

$$\sigma_0(\dot{F}) = \sigma_f(\dot{F}) = 474.2 \cdot \dot{F}^{-0.004} \quad \text{Blunt} \quad \text{(MPa)} \quad (4.\ 44)$$

$$\sigma_0(\dot{F}) = \sigma_f(\dot{F}) = 470.9 \cdot \dot{F}^{-0.002} \quad \text{Intermediate} \quad \text{(MPa)} \quad (4.\ 45)$$

The negative exponents in Equations from (4.40) to (4.45) make it evident that this material was characterised by an inverse strain rate sensitivity, this representing a very interesting condition to further validate the accuracy of the proposed approach.

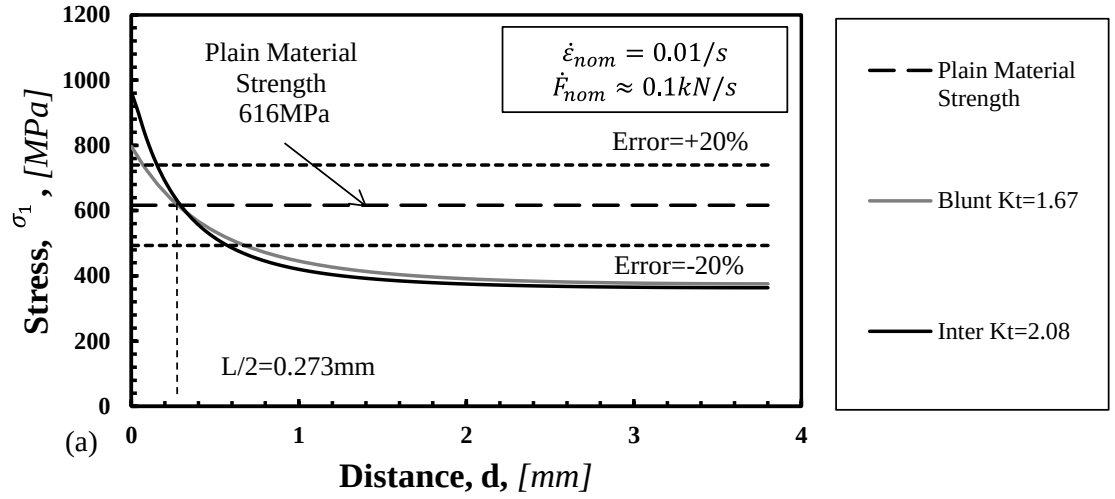

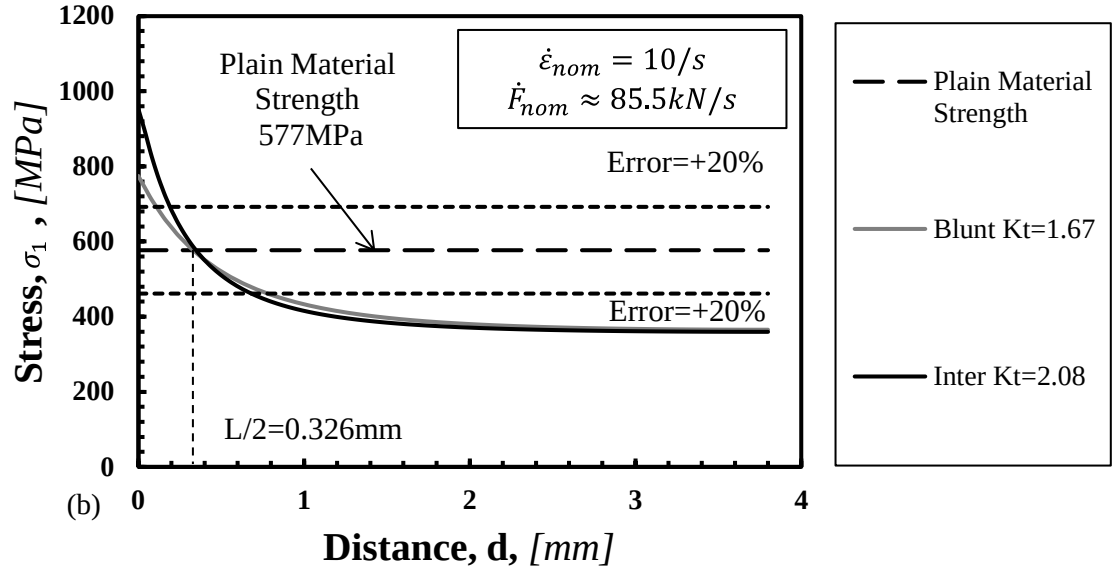

Figure 4.42 Local linear-elastic stress fields, in the incipient failure condition, (a) $\dot{\varepsilon}_{nom} = 0.01\ s^{-1}$ and (b) $\dot{\varepsilon}_{nom} = 10\ s^{-1}$ for notched AlMn6.

The chart of Figure 4.42(a) shows the L value determined under $\dot{\varepsilon}_{nom} = 0.01\ s^{-1}$ $(\dot{F} \approx 0.1kN/s)$ by using the results obtained by testing the notched specimens having K_t equal to 1.67 and 2.08 – see Table 3.4. The diagram reported in Figure 4.42(b) shows instead the linear-elastic stress distance curves determined, in the incipient failure condition, by post-processing the result generated by testing, under $\dot{\varepsilon}_{nom} = 10\ s^{-1}$ ($\dot{F} \approx 85.5kN/s$), the notched specimens having stress concentration factor, K_t, equal to both 1.67 and 2.08, the corresponding critical distance value being equal to 0.652 mm. The L values estimated under $\dot{\varepsilon}_{nom} = 0.01\ s^{-1}$ as well as under$\dot{\varepsilon}_{nom} = 10\ s^{-1}$ were then used to calculate the constants in Equation (4.16) obtaining:

$$L(\dot{\varepsilon}_{nom}) = 0.614 \cdot \dot{\varepsilon}_{nom}{}^{0.0256} \quad \text{(mm)} \qquad (4.\ 46)$$

$$L(\dot{F}) = 0.614 \cdot \dot{F}^{0.0253} \quad \text{(mm)} \qquad (4.\ 47)$$

The error diagrams reported in Figure 4.41(a) and (b) make it clear that the proposed reformulation of the TCD was capable of accurately estimating the strength of the tested notched samples, even though aluminium AlMg6 was characterised by an inverse strain rate sensitivity.

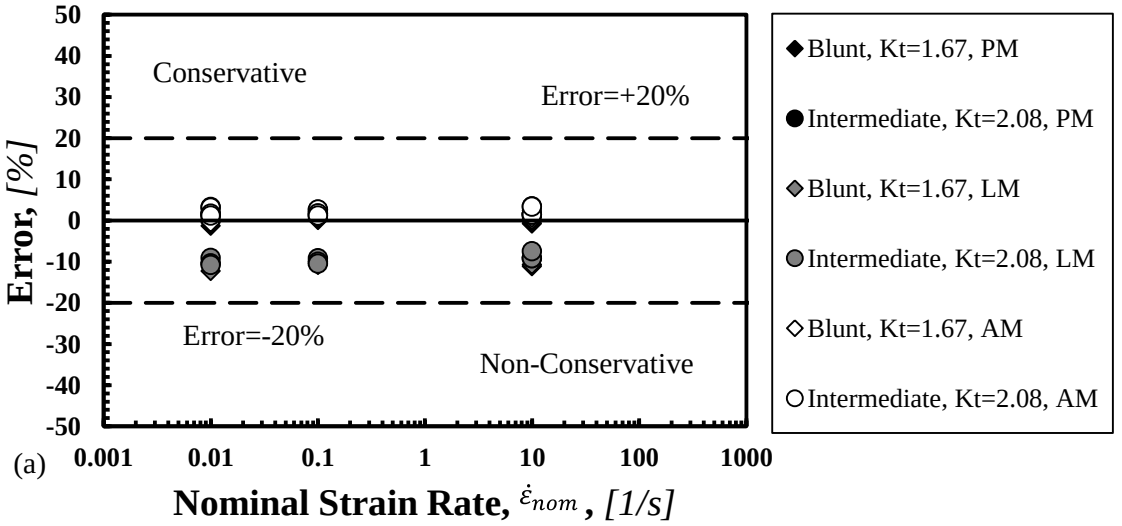

(a)

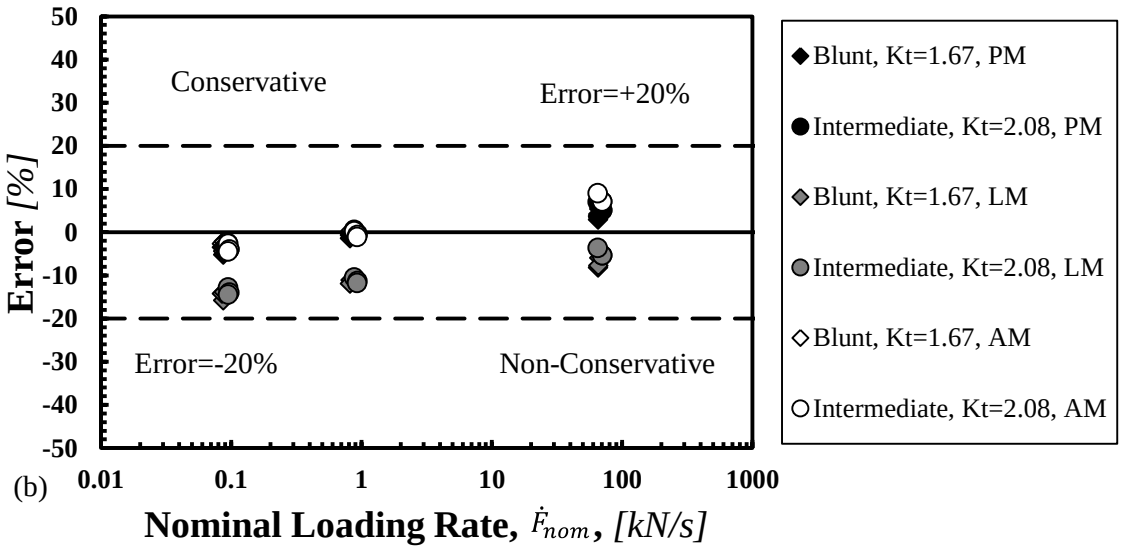

(b)

Figure 4.43 accuracy of the TCD in predicting the strength of notched AlMn6 as function of (a) nominal strain rate and (b) nominal loading rate.

4.6 Validation by Results Taken from the Literature

To further investigate the reliability of the proposed reformulation of the TCD, the accuracy of our approach was also checked against the experimental results generated, back in the 60s, by

Brisbane (1963) from testing, under quasi-static and dynamic tensile loading, notched specimens. The experimental investigation carried out at the Wright-Patterson Air Force Base, Ohio (Brisbane, 1963) involved three different metallic materials. The geometrical features and testing results were introduced in Section 1.6.

The linear-elastic stress fields needed to apply the TCD were calculated using bi-dimensional FE models and the commercial software $ANSYS^{®}$, and the mesh in the vicinity of the stress raiser apices was gradually refined until convergence occurred.

4.6.1 Mesh Convergence

Similar to the previous analysis, as shown in Figure 4.44, one quarter of each of the notched samples was modelled in order to save computing time and space. Models with various element sizes (Figure 4.45) were created until convergence occurred. Looking at the stress–distance curves reported in Figure 4.46, it is hard to observe a difference in these stress–distance curves when the value of the element size is less than 1.1mm. According to the graphs plotted in Figure 4.47, the model with an element size N=0.54mm can be chosen as the optimal element size for $K_t = 1.9$ notched samples to give accurate stress–distance curves.

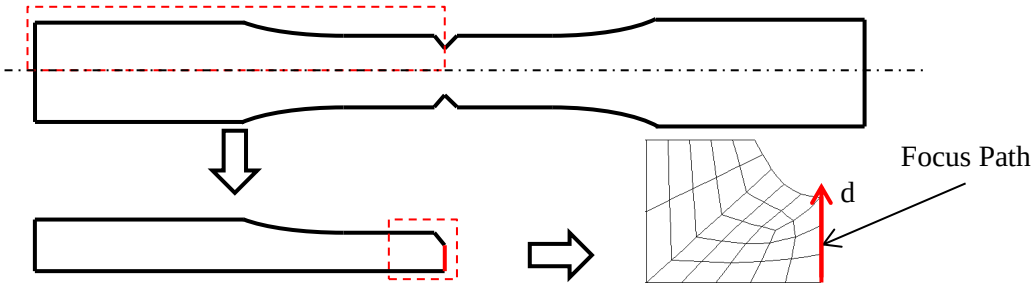

Figure 4.44 Area of refined mesh for notched samples of materials 301XH stainless steel, RENE-41 alloy and VASCO Jet-1000 steel.

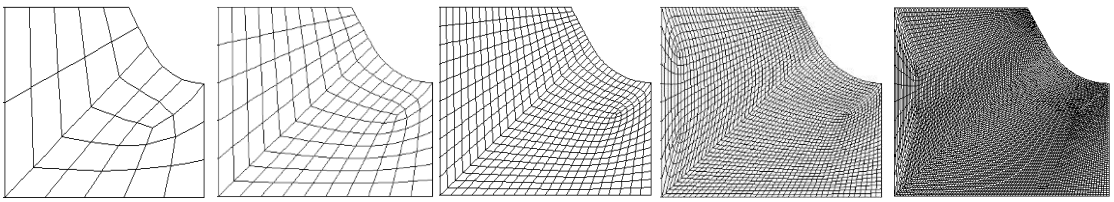

(a) N=2.54mm (b) N=1.1mm (c) N=0.54mm (d) N=0.27mm (e) N=0.14mm

Figure 4.45 FE models of K_t=1.9 notched samples with different element sizes.

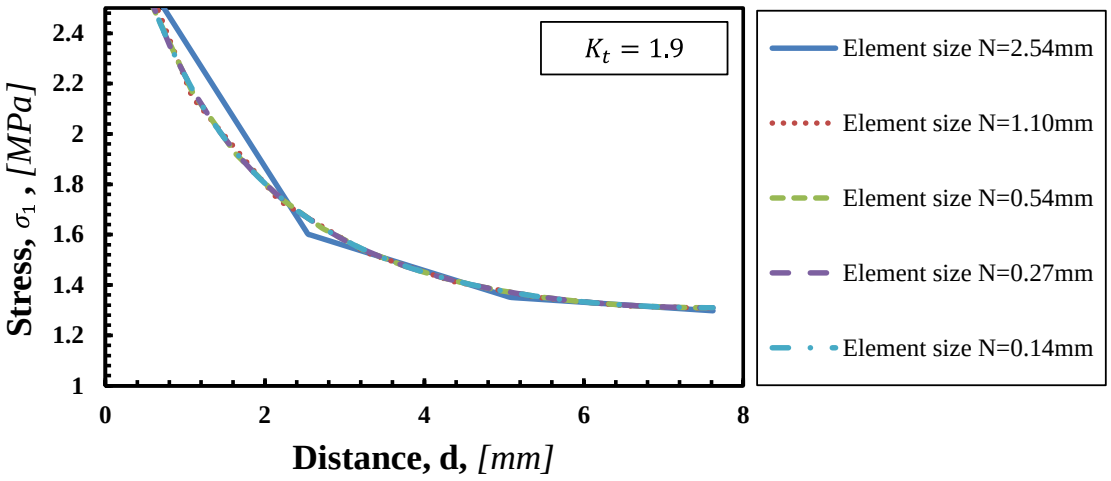

Figure 4.46 Stress distributions calculated from the models of notched samples (K_t=1.9) with different element sizes.

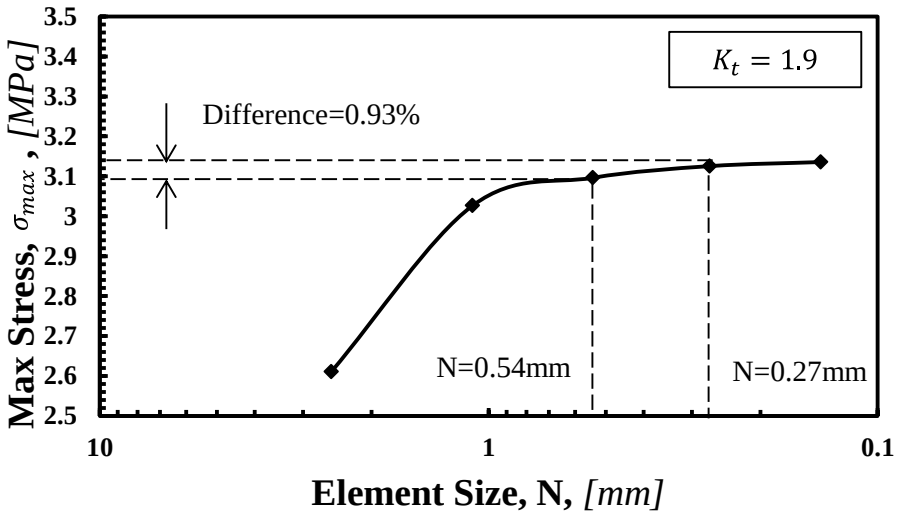

Figure 4.47 The maximum first principal stress in notched samples (K_t=1.9) vs. element size.

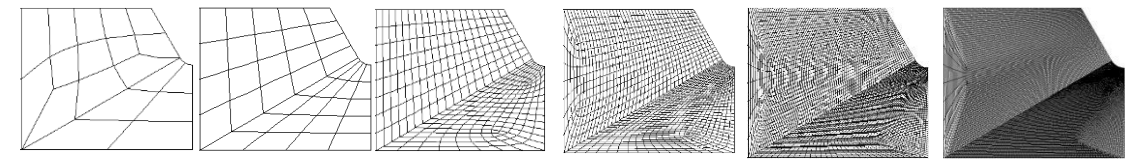

(a) N=2.54mm (b) N=1.27mm (c) N=0.64mm (d) N=0.32mm (e) N=0.16mm (f) N=0.08mm

Figure 4.48 FE models of K_t=3.3 notched samples with different element sizes.

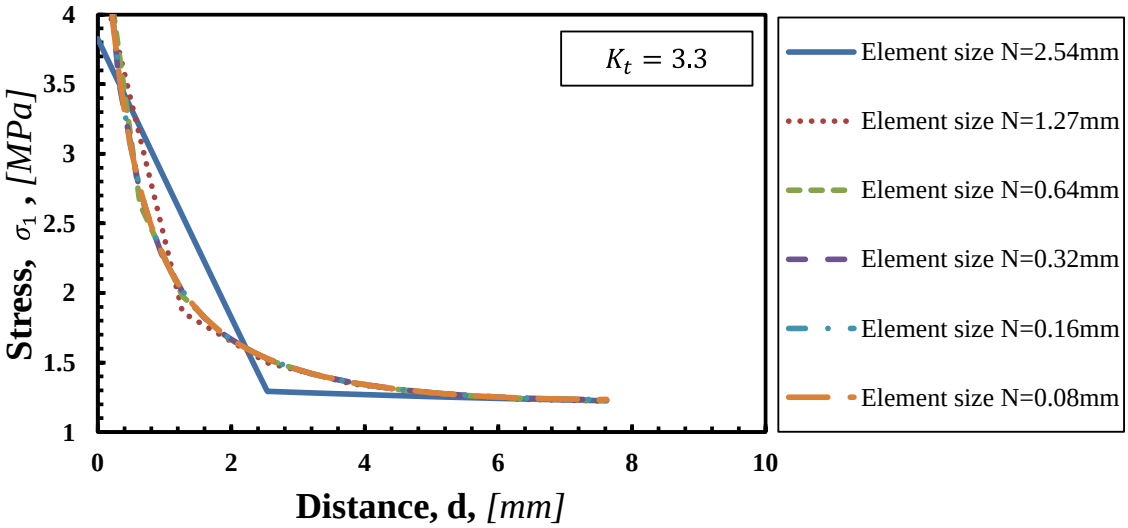

Figure 4.49 Stress distributions calculated from the models of notched samples (K_t=3.3) with different element sizes.

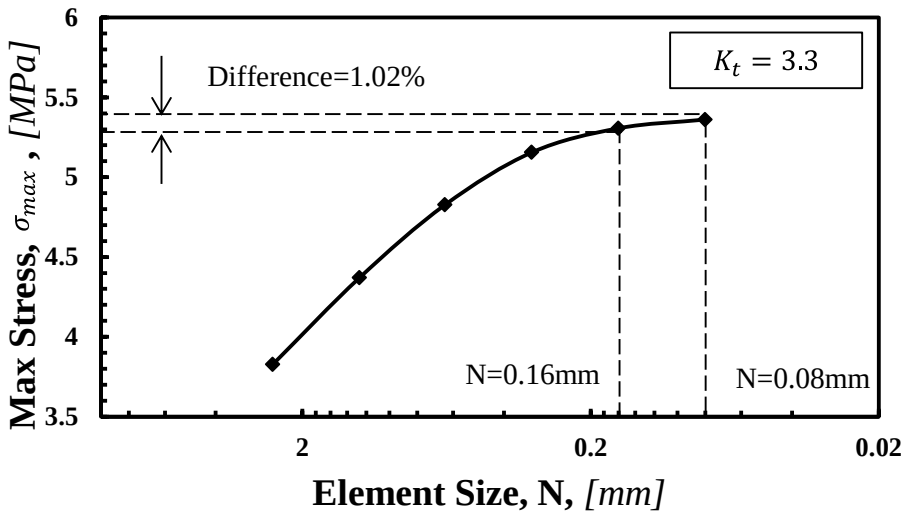

Figure 4.50 The maximum first principal stress in notched samples (K_t=3.3) vs. element size.

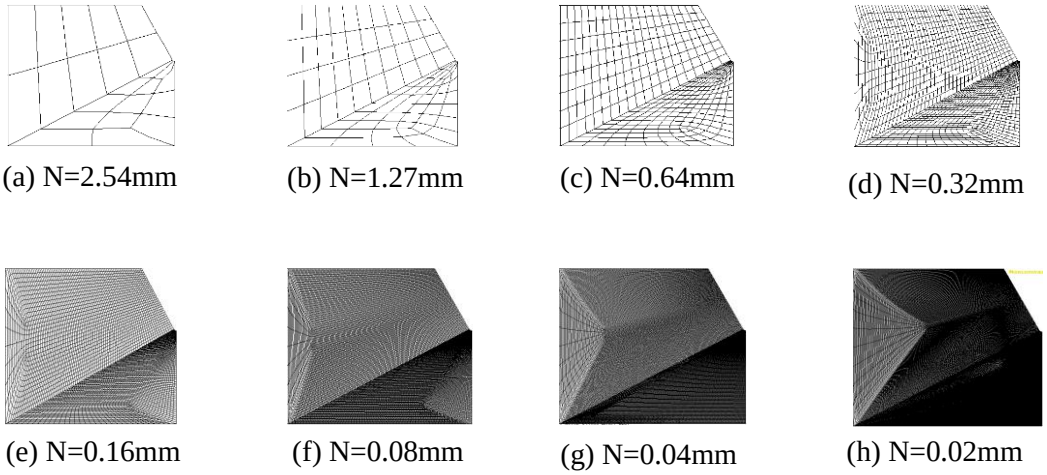

Figure 4.51 FE models of K_t=6.8 notched samples with different element sizes.

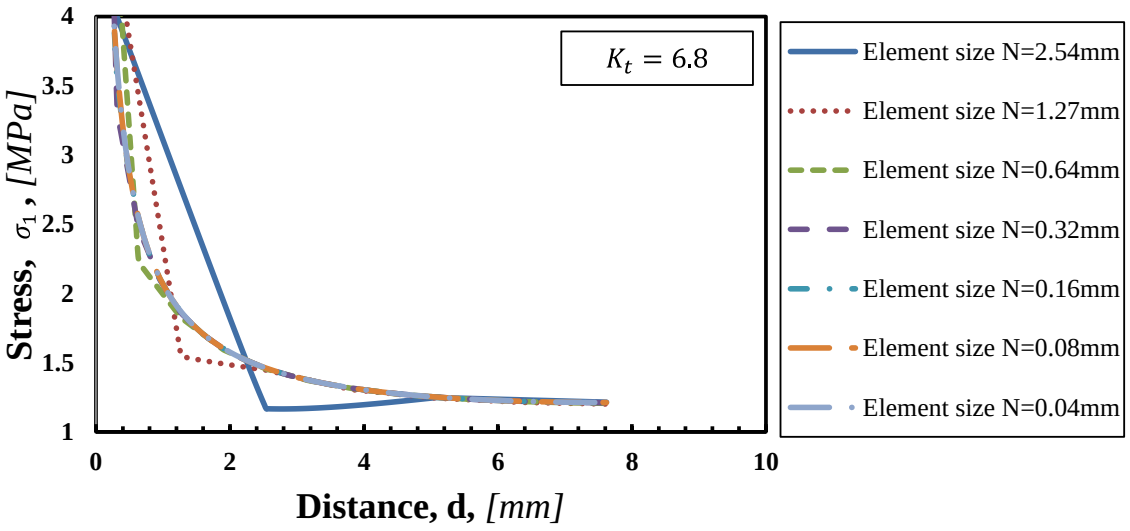

Figure 4.52 Stress distributions calculated from the models of notched samples (K_t=6.8) with different element sizes.

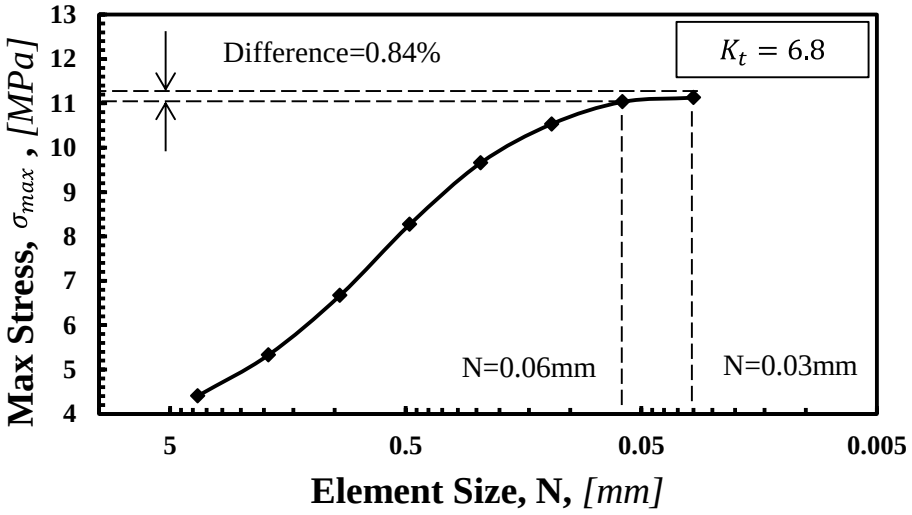

Figure 4.53 The maximum first principal stress in notched samples ($\mathbf{K_t}$=6.8) vs. element size.

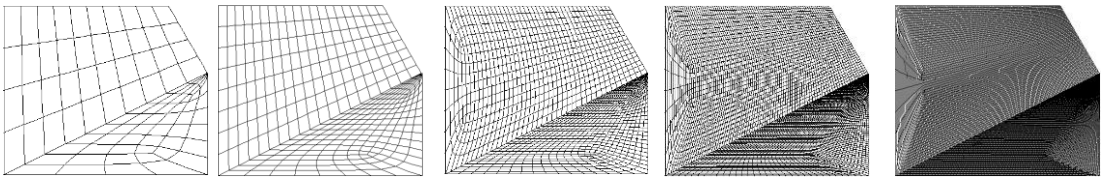

(a) N=1.27mm (b) N=0.64mm (c) N=0.32mm (d) N=0.16mm (e) N=0.08mm

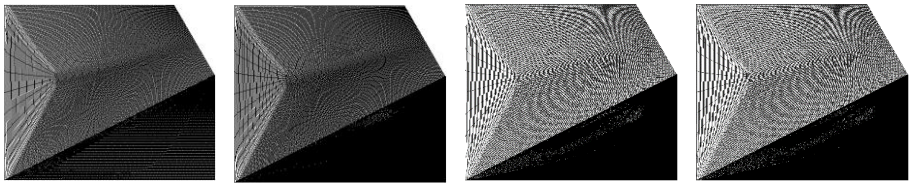

(f) N=0.04mm (g) N=0.02mm (h) N=0.015mm (i) N=0.013mm

Figure 4.54 FE models of K_t=14.7 notched samples with different element sizes.

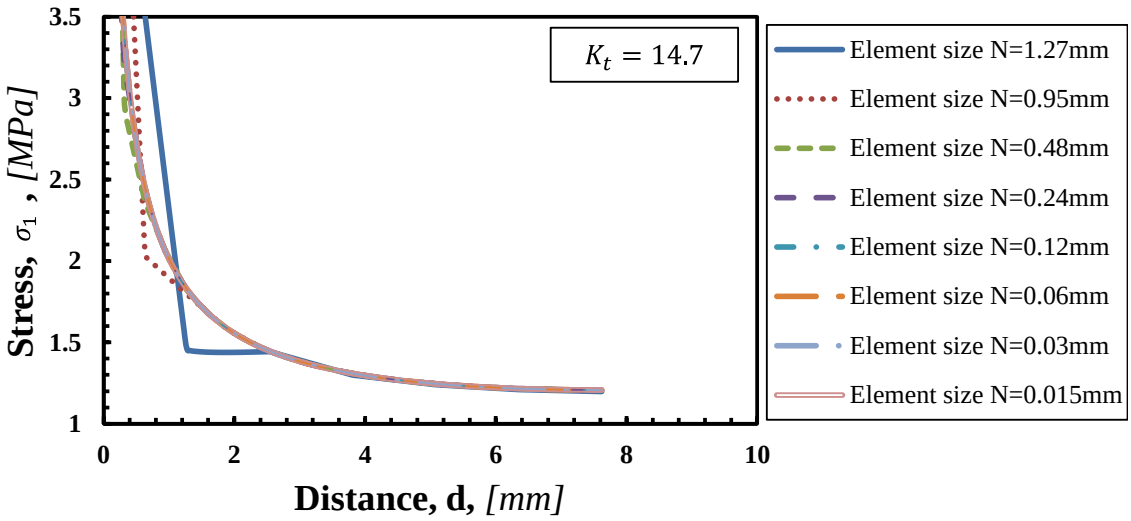

Figure 4.55 Stress distributions calculated from the models of notched samples (K_t=14.7) with different element sizes.

In terms of the models of other notched samples, Figures 4.48, 4.51 and 4.54 show a series of models meshed with various mesh sizes for notched samples having K_t=3.3, K_t=6.8 and K_t=14.7 respectively. It can be concluded from the results that the values of N=0.16mm, 0.06mm and 0.03mm are the converged mesh sizes for the models of notched samples having K_t=3.8, K_t=6.8 and K_t=14.7 respectively. All of the results are summarised in Table 4.4.

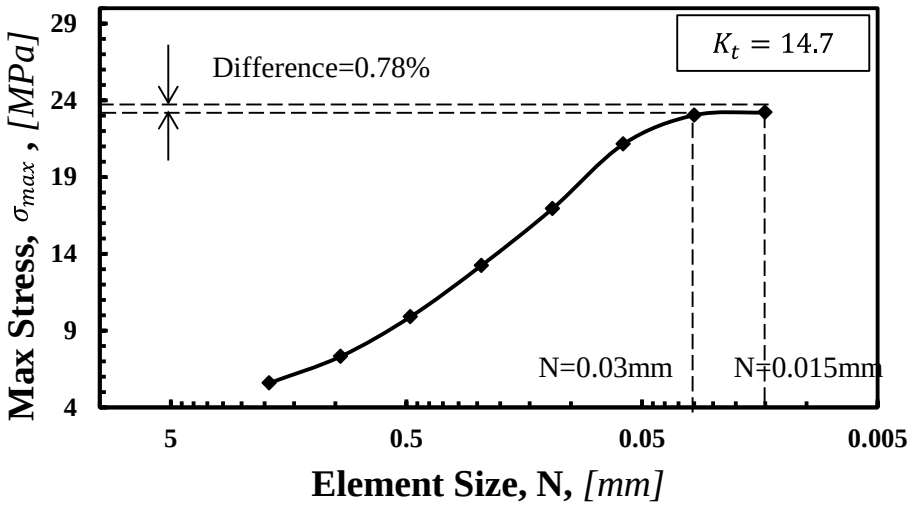

Figure 4.56 Accuracy of the maximum first principal stress in notched samples (K_t=14.7) vs. element size.

Table 4.4 Summary of mesh convergence results for different notches for materials 301XH stainless steel, Rene-41 alloy and Vasco Jet-1000 steel.

Notches	Optimal Element Size *[mm]*	Error *[%]*
K_t = 14.7	0.03	0.78
K_t = 6.8	0.06	0.84
K_t = 3.3	0.16	1.02
K_t = 1.9	0.54	0.93

4.6.2 Linear elastic TCD prediction

The stress–distance curves plotted, in the incipient failure condition, in the charts of Figure 4.57, 4.58 and 4.59 clearly prove that, for these three metallic materials, inherent strength $\sigma_0(\dot{\Delta})$ was larger than the corresponding failure strength, $\sigma_f(\dot{\Delta})$, this holding true independently from the considered value of the displacement rate. Accordingly, cases $\dot{\Delta}$ = $0.002 mm \cdot s^{-1}$ and $\dot{\Delta}$ =3.387 $mm \cdot s^{-1}$ were used to calibrate the constants not only in functions $L(\dot{\Delta})$ but also in functions $\sigma_0(\dot{\Delta})$, obtaining:

- 301XH Stainless steel

$$\sigma_0(\dot{\Delta}) = 1889.8 \cdot \dot{\Delta}^{-0.027} \quad (MPa) \tag{4.33}$$

$$L(\dot{\Delta}) = 1.449 \cdot \dot{\Delta}^{0.0051} \quad (mm) \tag{4.34}$$

- Rene-41 Alloy

$$\sigma_0(\dot{\Delta}) = 2477.9 \cdot \dot{\Delta}^{0.012} \quad (MPa) \tag{4.35}$$

$$L(\dot{\Delta}) = 0.529 \cdot \dot{\Delta}^{-0.084} \quad (mm) \tag{4.36}$$

- VASCO Jet-1000 Steel

$$\sigma_0(\dot{\Delta}) = 2503.3 \cdot \dot{\Delta}^{-0.005} \quad (MPa) \tag{4.37}$$

$$L(\dot{\Delta}) = 1.468 \cdot \dot{\Delta}^{0.0188} \quad (mm) \tag{4.38}$$

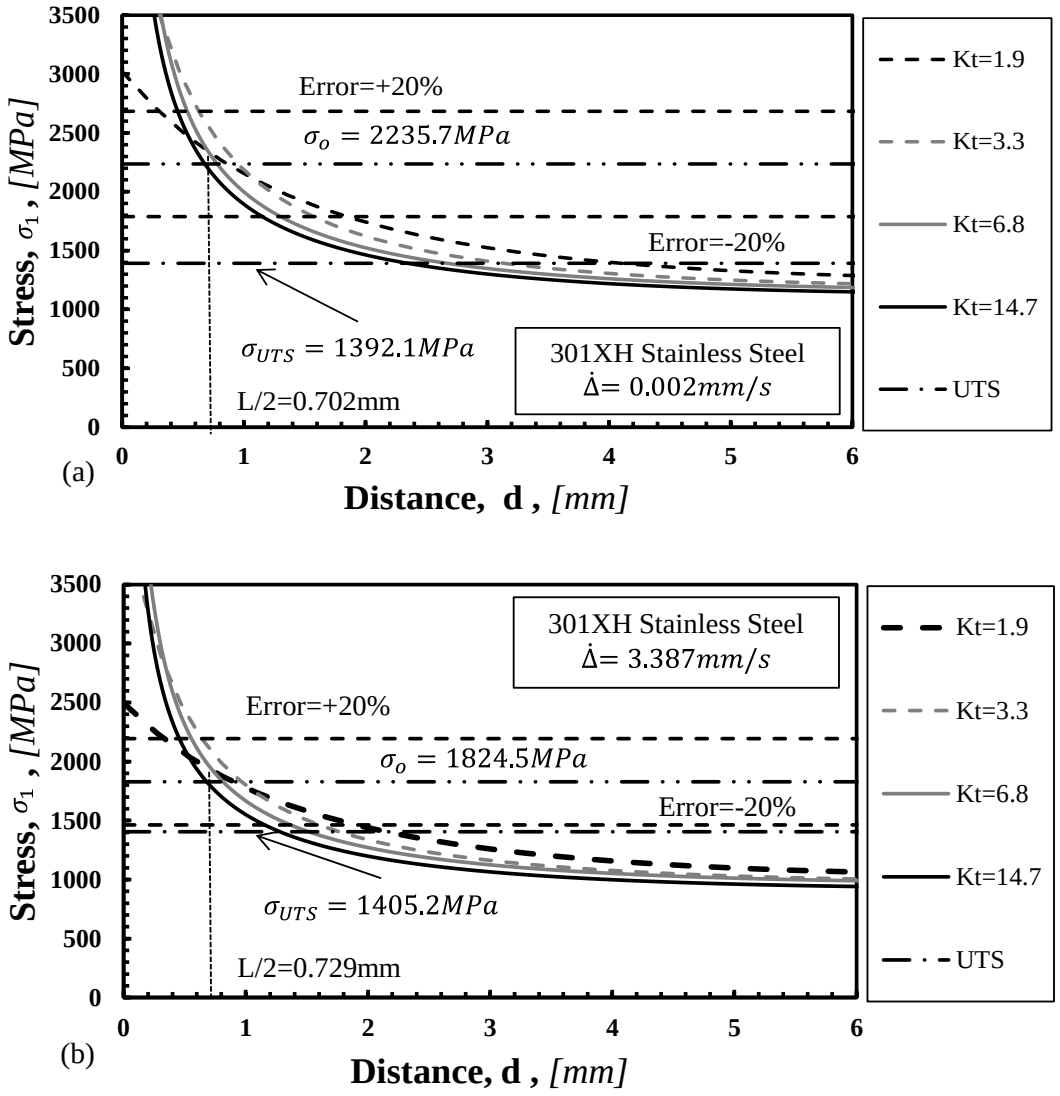

Figure 4.57 Local linear-elastic stress fields, in the incipient failure condition, under displacement rate (a) $\dot{\Delta} = 0.002mm \cdot s^{-1}$ and (b) $\dot{\Delta} = 3.387mm \cdot s^{-1}$ for notched metallic materials 301XH stainless steel (Brisbane, 1963).

The error charts reported in Figure 4.50 show that the proposed approach was successful also in estimating the strength of the notched samples tested by Brisbane (1963) under different values of the nominal displacement rate. It is worth concluding the present section by observing that the accuracy obtained by using the proposed reformulation of the TCD is certainly promising, especially in light of the fact that it allows notched metals subjected to dynamic loading to be designed without the need for explicitly modelling the stress vs. strain non-linear behaviour of ductile metals. Accordingly, this novel reformulation of the TCD can be seen as a powerful engineering tool allowing practitioners to safely and accurately design notched metallic components/structures against dynamic loading by remarkably reducing the time and costs associated with the design process.

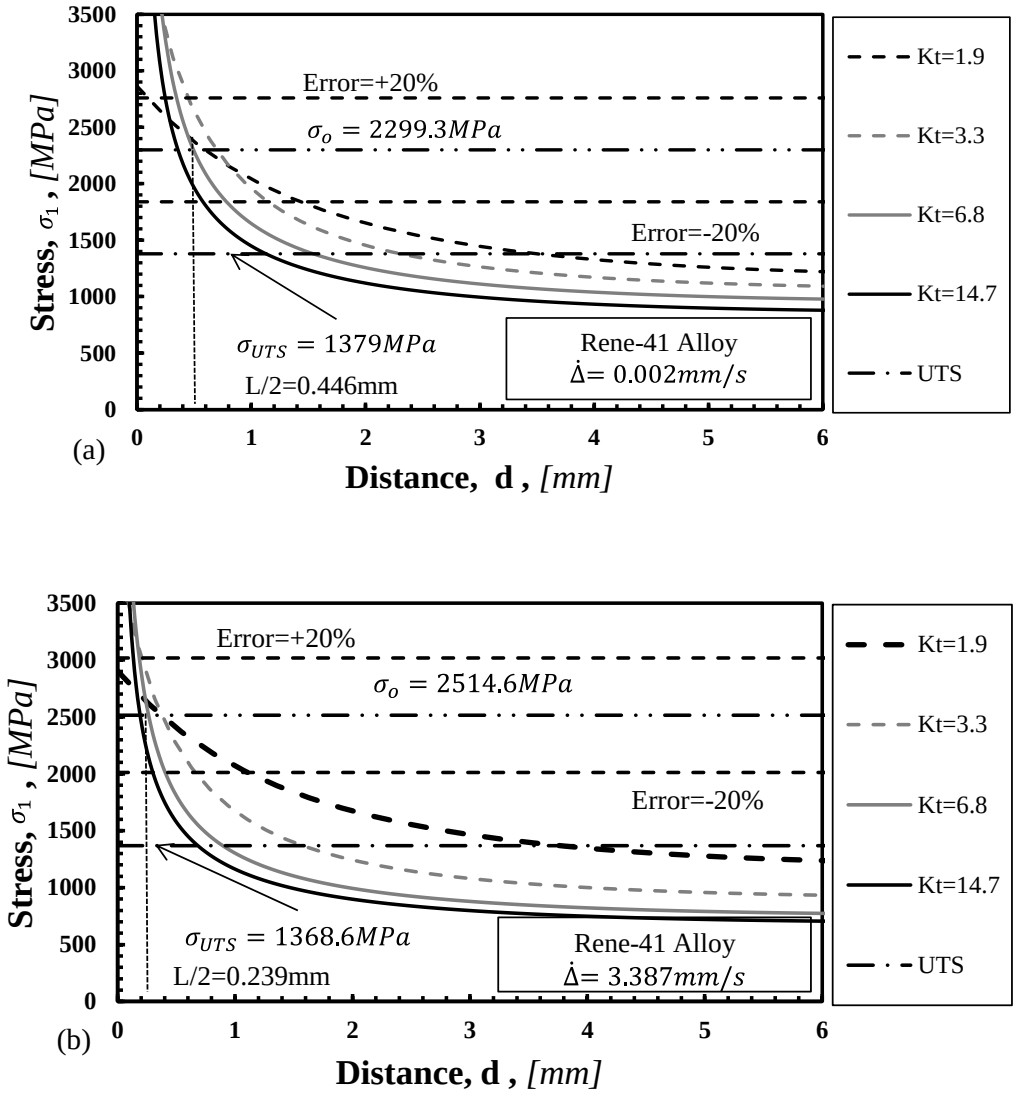

Figure 4.58 Local linear-elastic stress fields, in the incipient failure condition, under displacement rate (a) $\dot{\Delta} = 0.002mm \cdot s^{-1}$ and (b) $\dot{\Delta} = 3.387mm \cdot s^{-1}$ for notched metallic materials René-41 Alloy (Brisbane, 1963).

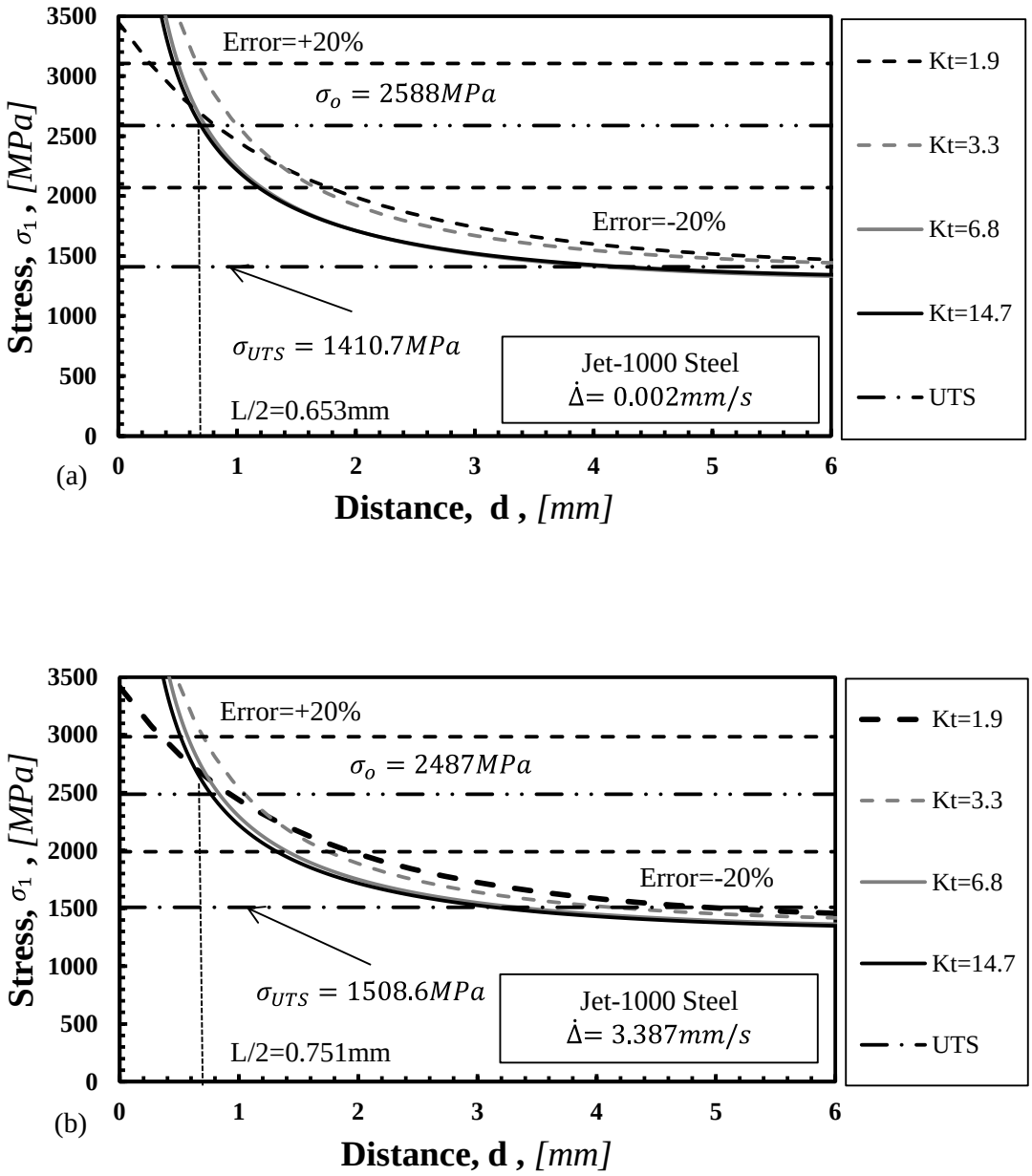

Figure 4.59 Local linear-elastic stress fields, in the incipient failure condition, under displacement rate (a) $\dot{\Delta}= 0.002mm \cdot s^{-1}$ and (b) $\dot{\Delta}= 3.387mm \cdot s^{-1}$ for notched metallic materials Jet-1000 Steel (Brisbane, 1963).

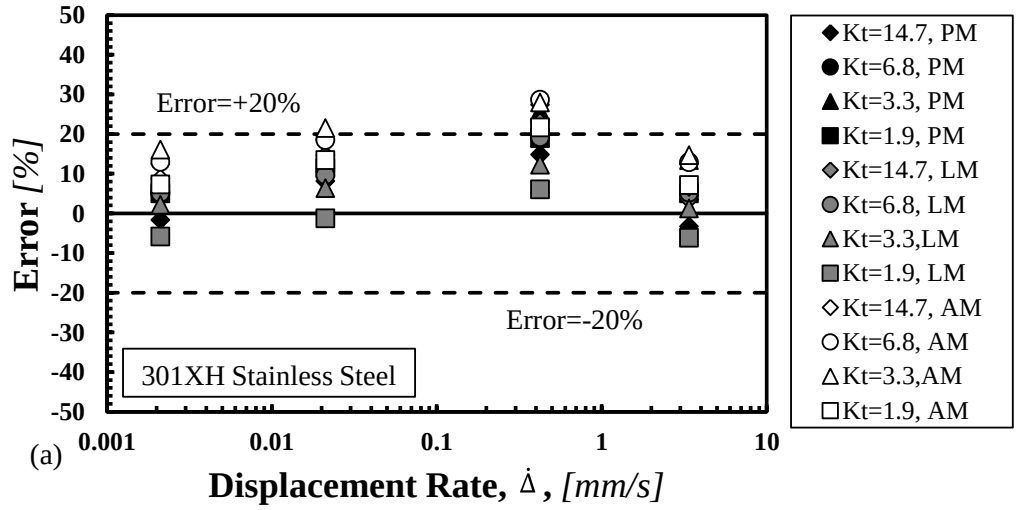

(a)

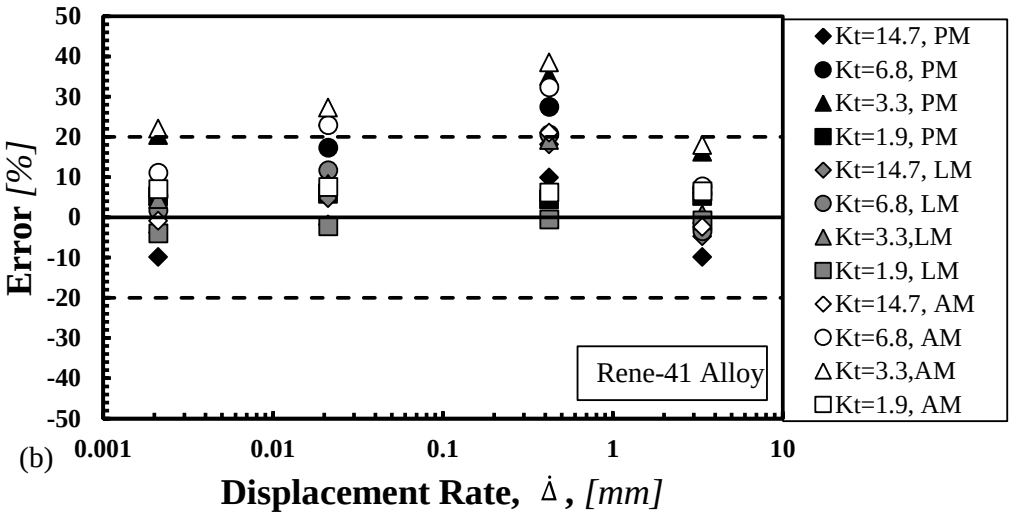

(b)

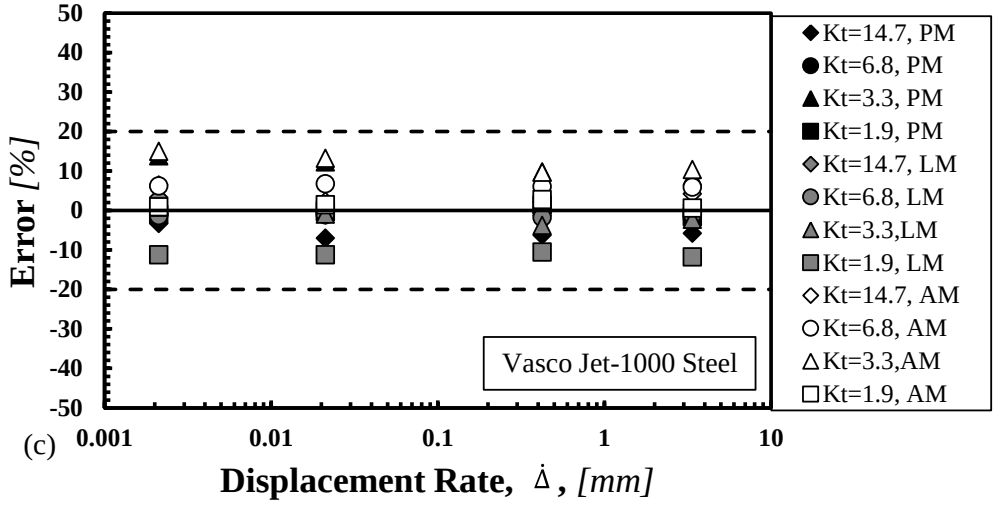

(c)

Figure 4.60 Accuracy of the TCD in predicting the strength of notched metallic materials (a) 301XH stainless steel, (b) René-41 alloy, and (c) VASCO Jet-1000 steel.

In this chapter, the reformulated TCD has been proposed and validated by our own experimental results and from literature. In terms of these metallic materials, the linear elastic TCD can be used as a simply tool to design material components. In order to understand the dynamic behaviour around notch tip, in next chapter, the elasto-plastic analysis will be introduced.

References

BØRVIK, T., HOPPERSTAD, O. S., BERSTAD, T. & LANGSETH, M. 2001. A computational model of viscoplasticity and ductile damage for impact and penetration. *European Journal of Mechanics - A/Solids,* 20**,** 685-712.

BOYCE, B. L. & DILMORE, M. F. 2009. The dynamic tensile behavior of tough, ultrahigh-strength steels at strain-rates from 0.0002 s−1 to 200 s−1. *International Journal of Impact Engineering,* 36**,** 263-271.

BRISBANE, A. 1963. The Investigation of the Effects of Loading Rate and Stress Concentration Factors on the Notch Properties of Three Sheet Alloys at Subzero Temperatures. DTIC Document.

CAO, R., LEI, M. X., CHEN, J. H. & ZHANG, J. 2007. Effects of loading rate on damage and fracture behavior of TiAl alloys. *Materials Science and Engineering: A,* 465**,** 183-193.

COUQUE, H., ASARO, R. J., DUFFY, J. & LEE, S. H. 1988. Correlations of microstructure with dynamic and quasi-static fracture in a plain carbon steel. *Metallurgical Transactions A,* 19**,** 2179-2206.

DJAPIC OOSTERKAMP, L., IVANKOVIC, A. & VENIZELOS, G. 2000. High strain rate properties of selected aluminium alloys. *Materials Science and Engineering: A,* 278**,** 225-235.

DRAR, H. & BERGMARK, A. 1993. Load rate influence on the fracture morphology of a ductile steel. *Engineering Fracture Mechanics,* 46**,** 225-233.

EL-GAMAL, S. & MOHAMMED, G. 2014. Effects of γ-irradiation and strain rate on the tensile and the electrical properties of Al-4043 alloy. *Radiation Physics and Chemistry,* 99**,** 68-73.

GODSE, R., RAVICHANDRAN, G. & CLIFTON, R. 1989. Micromechanisms of dynamic crack propagation in an AISI 4340 steel. *Materials Science and Engineering: A,* 112**,** 79-88.

GRÄSSEL, O., KRÜGER, L., FROMMEYER, G. & MEYER, L. W. 2000. High strength Fe–Mn–(Al, Si) TRIP/TWIP steels development-properties-application. *International Journal of Plasticity,* 16**,** 1391-1409.

HUANG, Y. & YOUNG, B. 2014. The art of coupon tests. *Journal of Constructional Steel Research,* 96**,** 159-175.

KOLSKY, H. 1949. An investigation of the mechanical properties of materials at very high rates of loading. *Proceedings of the Physical Society. Section B,* 62.

LEE, O. S. & KIM, M. S. 2003. Dynamic material property characterization by using split Hopkinson pressure bar (SHPB) technique. *Nuclear Engineering and Design,* 226**,** 119-125.

LI, C.-J. 2000. Effects of temperature and loading rate on fracture toughness of structural steels. *Materials & Design,* 21**,** 27-30.

LIANG, H., PAN, F., WANG, J. & YANG, J. 2013. Tensile and Compressive Properties of Mg-3Al-2Zn-2Y Alloy at Different Strain Rates. *Journal of Materials Engineering and Performance,* 22**,** 2681-2690.

LIN, Y.-H., WU, S.-M., KAO, F.-H., WANG, S.-H., YANG, J.-R., YANG, C.-C. & CHIOU, C.-S. 2011. Microtwin formation in the α phase of duplex titanium alloys affected by strain rate. *Materials Science and Engineering: A,* 528**,** 2271-2276.

LINDHOLM, U. S. 1964. Some experiments with the split hopkinson pressure bar. *Journal of the Mechanics and Physics of Solids,* 12**,** 317-335.

LINDHOLM, U. S., BESSEY, R. L. & SMITH, G. V. 1971. Effect of Strain Rate on Yield Strength, Tensile Strength, and Elongation of Three Aluminium Alloys. *J Mater,* 6**,** 119-133.

LIU, Y. 2013. CHOOSE THE BEST ELEMENT SIZE TO YIELD ACCURATE FEA RESULTS

WHILE REDUCE FE MODE'S COMPLEXITY. *British Journal of Engineering and Technology,* 1**,** 13-28.

MOROZOV, N. F., PETROV, Y.V. 1990. Dynamic fracture toughness in crack growth initiation problems. *AN SSSR MTT (Solid Mechanics),* 6**,** 108-11.

NAIMARK, O. B. 1998. Defect-induced instabilities in condensed media. *Journal of Experimental and Theoretical Physics Letters,* 67**,** 751-758.

NODA, N. A., OHTSUKA, H., ZHENG, H., SANO, Y., ANDO, M., SHINOZAKI, T. & GUAN, W. 2015. Strain rate concentration and dynamic stress concentration for double-edge-notched specimens subjected to high-speed tensile loads. *Fatigue & Fracture of Engineering Materials & Structures,* 38**,** 125-138.

PETROV, Y. V., MOROZOV, N. F. & SMIRNOV, V. I. 2003. Structural macromechanics approach in dynamics of fracture. *Fatigue and Fracture of Engineering Materials and Structures,* 26**,** 363-372.

PLEKHOV, O. A. 2003. Modeling of stochastic properties of fast cracks in quasi-brittle materials. *Computational Materials Science,* 28**,** 462-468.

PRIEST, A. Influence of strain rate and temperature on the fracture and tensile properties of several metallic materials. Dynamic fracture toughness an international conference arranged by the Welding Institute and the American Society for Metals. London, 5-7 July 1976. Vol. 1-papers, 1977.

SAKINO, K. 2008. Strain rate dependence of dynamic flow stress of 2017 aluminum alloy at very high strain rates. *International Journal of Modern Physics B,* 22**,** 1209-1214.

SHAPIRO, J. M., SHARPE, W. & TREGONING, R. L. 1992. Dynamic Crack-Tip Opening Displacement (CTOD) measurements with application to fracture toughness testing. *Rapid Load Fracture Testing.* ASTM International.

SOLOMOS, G., ALBERTINI, C., LABIBES, K., PIZZINATO, V. & VIACCOZ, B. 2004. Strain rate effects in nuclear steels at room and higher temperatures. *Nuclear Engineering and Design,* 229**,** 139-149.

SUN, Z. M., KOBAYASHI, T., FUKUMASU, H., YAMAMOTO, I. & SHIBUE, K. 1998. Tensile properties and fracture toughness of a Ti-45Al-1.6Mn alloy at loading velocities of up to 12 m/s. *Metallurgical and Materials Transactions A,* 29**,** 263-277.

SUSMEL, L. 2009. Multiaxial Notch Fatigue: From Nominal to Local Stress. *Strain Quantities*.

SUSMEL, L. & TAYLOR, D. 2008. On the use of the Theory of Critical Distances to predict static failures in ductile metallic materials containing different geometrical features. *Engineering Fracture Mechanics,* 75**,** 4410-4421.

TAYLOR, D. 1999. Geometrical effects in fatigue: a unifying theoretical model. *International Journal of Fatigue,* 21**,** 413-420.

TAYLOR, D. 2007. *The Theory of Critical Distances: A New Perspecive in Fracture Mechanics,* Elsevier Science Limited.

VENKERT, A., GUDURU, P. & RAVICHANDRAN, G. 2001. Effect of loading rate on fracture morphology in a high strength ductile steel. *Journal of engineering materials and technology,* 123**,** 261-267.

WIESNER, C. S. & MACGILLIVRAY, H. 1999. Loading Rate Effects on Tensile Properties and Fracture Toughness of Steel. *1999 TAGSI Seminar, Cambridge, IoM Publication***,** 149.

XU, S., TYSON, W. R., BOUCHARD, R. & GERTSMAN, V. Y. 2009. Effects of Strain Rate and Temperature on Tensile Flow Behavior and Energy Absorption of Extruded Magnesium AM30 Alloy. *Journal of Materials Engineering and Performance,* 18**,** 1091-1101.

YOKOYAMA, T. & KISHIDA, K. 1989. A novel impact three-point bend test method for determining dynamic fracture-initiation toughness. *Experimental Mechanics,* 29**,** 188-194.

ZHANG, X. M., LI, H. J., LI, H. Z., GAO, H., GAO, Z. G., LIU, Y. & LIU, B. 2008. Dynamic property evaluation of aluminum alloy 2519A by split Hopkinson pressure bar. *Transactions of Nonferrous Metals Society of China (English Edition),* 18**,** 1-5.

Chapter 5 Elasto-Plastic Simulations

5.1 Introduction

As demonstrated in the previous chapters, the dynamic strength of notched metals can be predicted accurately via the linear elastic PM, LM and AM, where the required stress analysis is performed by adopting a simple linear-elastic constitutive law. Having recalled this important aspect, the goals of this chapter are: (i) running elasto-plastic simulations for the tested samples Al6063-T5 subjected to dynamic loading; (ii) plotting elasto-plastic stress distributions in the vicinity of notch tip. In order to achieve these goals, a well-known multi-purpose explicit finite element program called LS-DYNA© will be used to analyse the nonlinear dynamic response of the tested Al6063-T5 cylindrical bars containing different stress raisers. In this chapter, due to the in-completed applied loading time history provided by Russian laboratory, in this chapter, only the material Al6063-T5 will be simulated.

An important advantage of LS-DYNA is that the complete stress and strain fields can be determined under different rates of loading (Hallquist and Manual, 1998). In these fast-loading LS-DYNA simulations, the uniaxial load in the form of a displacement history (with a displacement rate range from $0.05 mm \cdot s^{-1}$ to $750 mm \cdot s^{-1}$) will be applied at one end of the specimen, whilst all the degrees of freedom are constrained at the other end. By using the stress–strain data which are obtained from these simulations, a mesh convergence analysis will be conducted in order to have the results accurate enough, and at the same time, save computational time and memory space. Subsequently, two different ways of determining the constants for the Simplified Johnson–Cook material model will be used. After determining the material constants, both real and simplified displacement histories will be applied to the models, and the results obtained from these simulations will be plotted and compared in order to see the differences by applying these two different loading boundary conditions. Moreover, by plotting the elasto-plastic stress–distance curves, we also want to confirm whether it is possible to recognise an elasto-plastic critical distance value in order to estimate the dynamic strength of the tested samples. Specifically, an assumption will be made that, without considering failure criteria, the specimen is assumed as failed when the specimen reaches the maximum force. The corresponding real elastic-plastic stress fields were determined using LS/DYNA over a wide range of displacement rates. Finally, by considering the failure condition, failure effective plastic strain will be employed along with a Simplified Johnson–Cook model as the failure criterion. Crack propagation will occur once the effective plastic strain is equal to or greater than the value of the effective failure plastic strain. In this case, a time step before the initiation of the crack will be considered as the failure time, and the corresponding force will be treated as the failure force.

5.2 LS-DYNA Elastic-Plastic Simulations

LS-DYNA is a multi-purpose finite element program used to solve multi-physics problems involving solid mechanics, heat transfer and fluid dynamics. It is mainly based on explicit time integration to solve highly nonlinear transient dynamic problems (Hallquist and Manual, 1998). A large number of complex real world engineering problems, such as, for instance, crashworthiness, blast loading and high velocity impacts, have been simulated by many universities and companies using the DYNA solver.

LS-DYNA currently contains approximately 100 constitutive models and 10 equations-of-state to cover a wide range of material behaviours. A model is made up of a single executable file which is fully driven by command lines. Therefore, a command shell, executable file and enough free disk space are necessary in order to run LS-DYNA (Hallquist and Manual, 1998). The input keyword file can be prepared by using either text editors or with the help of a third party graphical pre-processor (Hallquist and Manual, 1998). Specifically, a keyword file organises the database and groups similar functions together logically; all data can be input in block form. For example, under keywords *ELEMENT, various types of elements such as solid, beam, shell, spring, etc. can be defined in a simple and logical way (Hallquist, 2007). Moreover, LS-PrePost, which has been developed by LSTC, is freely distributed software which can be used as both a graphical pre- and post-processor. In this study, Notepad++ will be used as the editor to prepare the input files, and LS-PrePost will be used as the postprocessor to analyse the simulation results.

Considering the fast deformation of the Al6063-T5 cylindrical bars described in Chapter 3, for both plain and notched samples, the uniaxial tensile load (in the form of a displacement time history in this simulation) is applied to one end of the specimen as shown in Figures 5.1 and 5.2. The displacement time histories for all tests were obtained by post-processing the high speed video recorded during testing. The distance between two corners (corner 1 and corner 2 shown in Figures 5.1 and 5.2) located at the intersection of the notch flanks with the cylindrical surface delimiting the gross volume of the specimens was tracked and used to calculate the displacement time history. Via the high speed video, axial deformation was measured. For the plain samples, because the majority of the plastic deformation occurred inside the gauge length (the circled part in Figure 5.1 (a)), there is no plastic deformation at the notch flanks, hence, the obtained displacement history can be used as the input load. Additionally, due to the use of axial-symmetric elements in the analysis, only half of the central part of the specimens was modelled (Figure 5.1 (c) and (d)). For the notched samples, since the gauge length is small compared to the length of the bar, the entire notched bar was modelled.

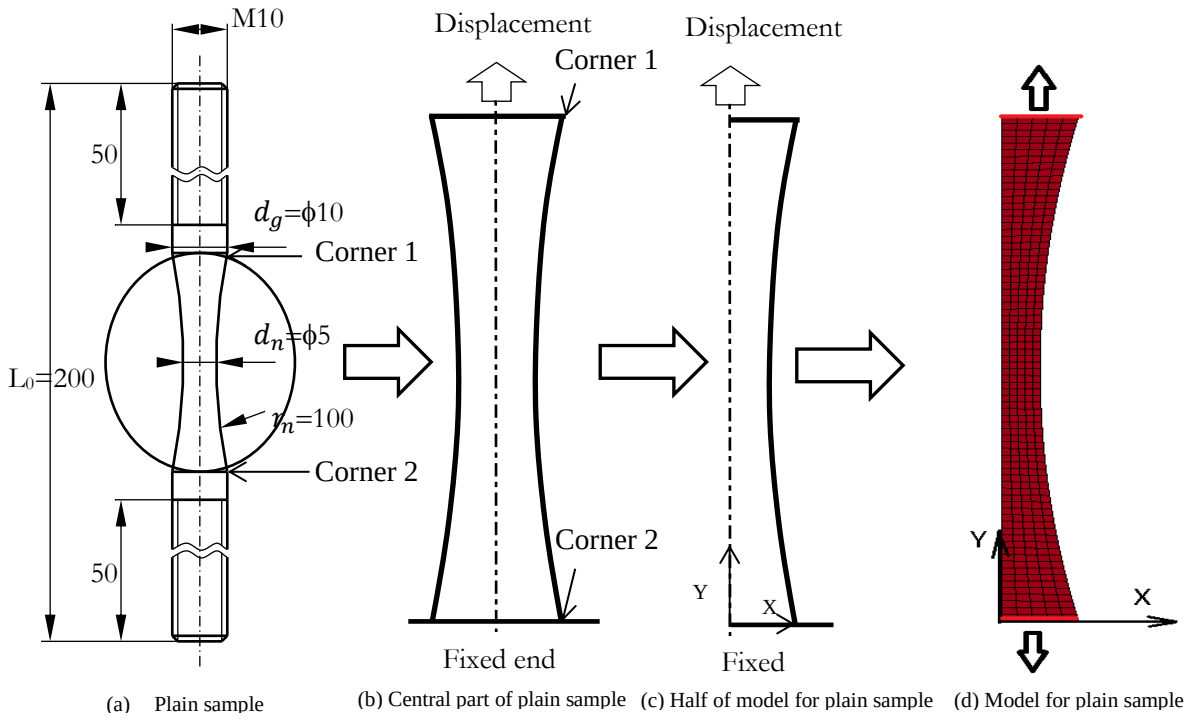

Figure 5. 1 Schematic drawing of an Al6063-T5 plain sample and FE model (dimensions in millimetres).

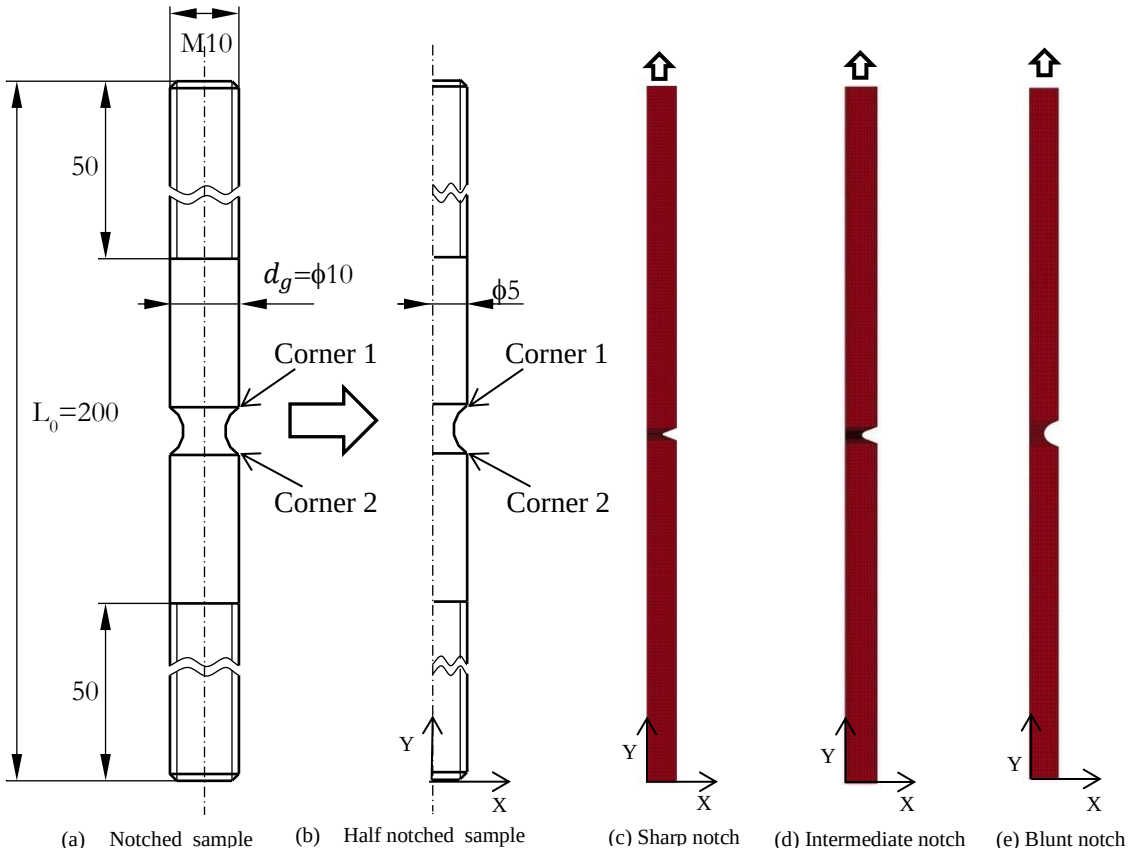

Figure 5. 2 Schematic drawing of an Al6063-T5 notched sample and FE model (dimensions in millimetres).

In order to understand the input file clearly, the keyword input file will be explained step by step and divided into four blocks in Appendix 5.

5.3 Mesh convergence

In order to reach convergence, a series of models with different element sizes were prepared. The explicit finite element solver LS-DYNA© was used to calculate the influence of the element size on the accuracy of the FEA results for the investigated tests. Thereafter, the best mesh size for each type of geometry was selected and used to model the investigated tests. Moreover, both FE models with and without the fracture criterion were analysed in order to allow us to have the mesh refined enough to generated results that are accurate enough.

As mentioned in the previous section, the investigated specimens were 200 mm long. Solely the central part of the gauge length was modelled for the plain sample. For the notched specimens, since the gauge length is relatively small, the whole length of the bar was modelled. In terms of these models, a uniaxial tensile displacement (Y-direction) history was applied to the top surface of the bar, as shown in Figure 5.3. In order to achieve convergence for all notched samples, FE models for each type of geometry were created with different mesh densities. Due to the geometry of the tested samples is cylindrical bar, all FE models involved in this study are meshed with a single integration shell element: a 4-node axis-symmetry volume-weighted shell element with one integration point through the thickness. The element behaviour was based on material model 98: the Simplified Johnson–Cook material model, which has been introduced in chapter 1.

5.3.1 Analysis of un-notched Samples

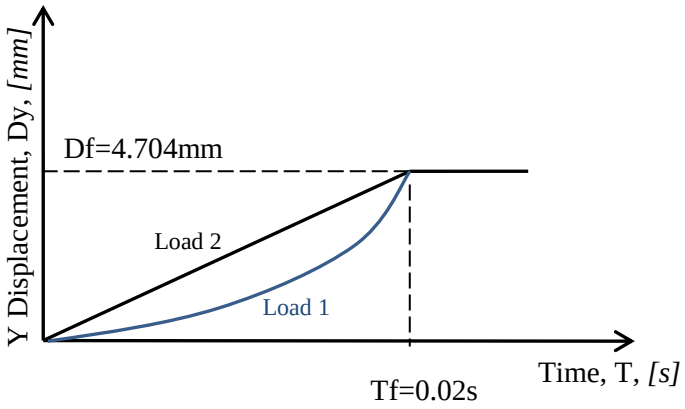

Figure 5.3 Real and simplified displacement history for plain sample S1T6.

For the plain samples, as an example, the displacement time history from the test of the S1T6 plain sample is plotted in Figure 5.3. In more detail, load 1 indicates the real displacement time history, whilst load 2 demonstrates the ramped load, which is represents a simplified version of

load 1. In this case, the ramped load in the form of a displacement time history is used as the loading boundary condition to conduct the convergence analysis. The material properties used for convergence analysis are A=143MPa, B=203.1MPa, N=0.37 and C=0 taken from the literature (Barsoum et al, 2014), the determination of these parameters will discussed later.

Figure 5.4 shows a series of meshes generated in a quadrilateral shape for the plain bar. In the radial direction (X), the element division is the same throughout the whole length. Thereafter, the mesh becomes finer as the diameter decreases. At the minimum cross section, along the redial direction, the biggest mesh size is about 1.25 mm and the finest meshing size is about 0.083 mm. During the analyses of the plain sample, the maximum axial force was computed and compared to understand the effect of mesh density on the analysis results, and the mesh was reduced until convergence occurred.

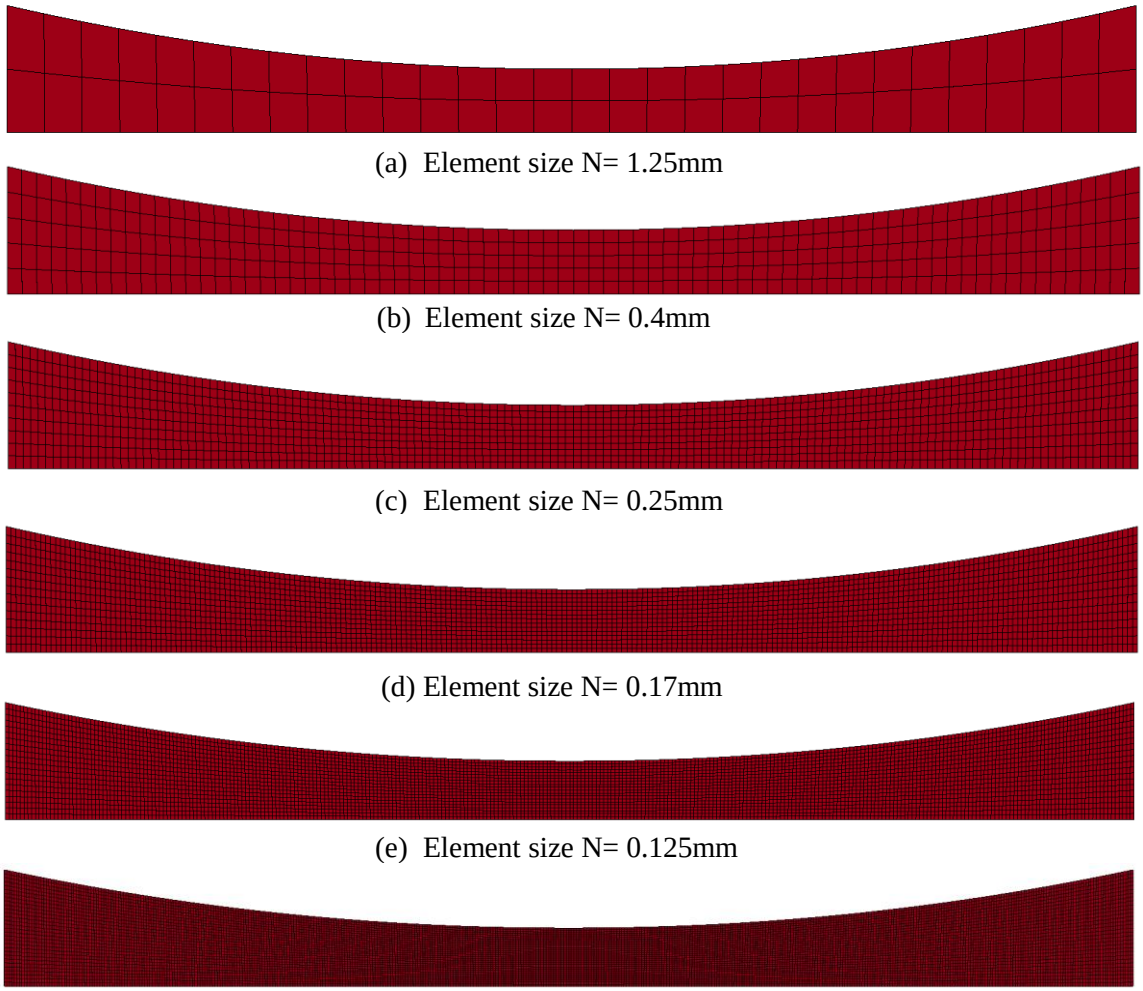

(a) Element size N= 1.25mm

(b) Element size N= 0.4mm

(c) Element size N= 0.25mm

(d) Element size N= 0.17mm

(e) Element size N= 0.125mm

(f) Element size N = 0.083mm

Figure 5.4 FE models of un-notched samples with 6 different element sizes.

Figure 5.5 shows the Von Mises effective stress distribution for 6 models with different mesh sizes at the time corresponding to the maximum force. From this graph, it can be found that when the value of element size is equal to N=1.25mm, the Von Mises stress gradient are not easy to be seen clearly. However, when the value of N is less than more than 0.4mm, the contour lines of Von Mises stress are more apparent and this does not increase significantly with a decrease in mesh size. Figure 5.6 plots the difference in the maximum axial forces obtained from the fixed ends between the plain models with coarse meshes and the finest one. It can be observed from this graph that for the plain model, convergence is achieved when the mesh size along the radial direction is 0.4mm. Additionally, the difference in maximum axial force between the model with element size N=0.4mm and N=0.25mm is 0.38%, which is acceptable for engineering simulations. Moreover, the computing time for these two models are 87 seconds and 725 seconds, and the size on disk are 126MB and 310MB respectively. Hence, the conclusion can be drawn from these figures that the plain FE model with element size N=0.4mm can be used as an efficient and suitable model for FE analyses without much loss of accuracy.

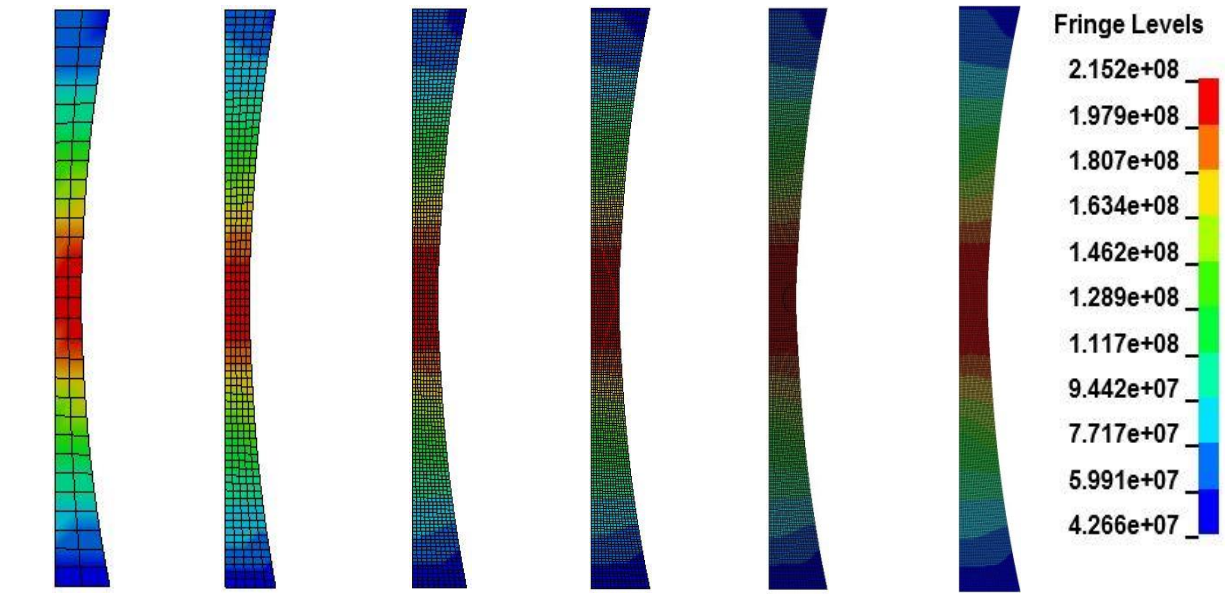

(a) N= 1.25mm (b) N = 0.4mm (c) N= 0.25mm (d) N= 0.17mm (e) N= 0.125mm (f) N = 0.083mm

Figure 5.5 Von Mises stress (Pa) contours of un-notched models for 6 different element sizes at the time of maximum force without a fracture criterion.

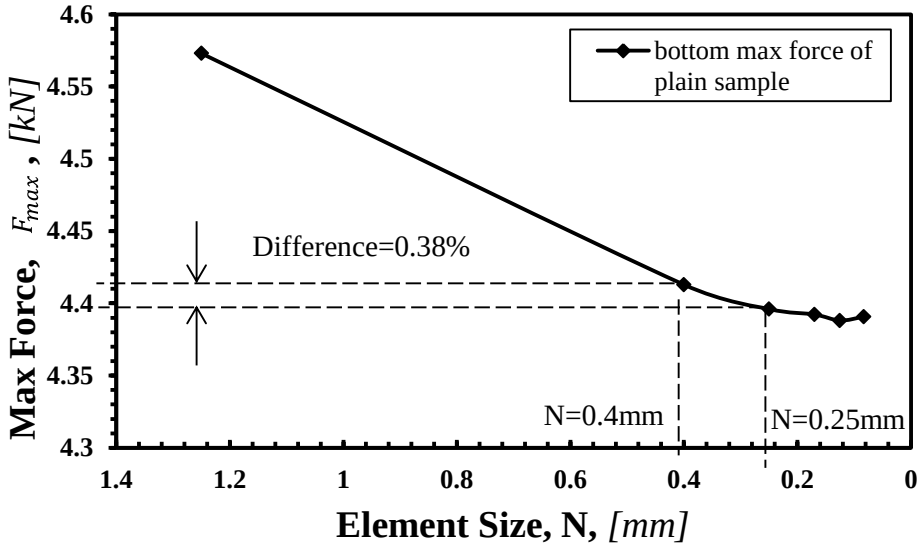

Figure 5.6 The maximum axial force vs element size for the models of un-notched samples.

5.3.2 Analysis of notched samples

A mesh convergence study for the notched samples was carried out using two kinds of model for different purposes. On one hand, without defining the fracture criterion, the models of notched samples were created. On the other hand, models with the fracture criterion defined were also analysed, and the maximum axial force obtained from these simulations was used to predict the failure force for different samples.

For the models without the fracture criterion defined, in the keyword file, a value of zero in the effective plastic strain card was included in the Simplified Johnson–Cook material model, which means that failure is not considered during the simulation (Hallquist, 2007). For notched models, because the majority of the deformation occurs in the vicinity of the notch tip, during the convergence analysis, the area around the notch tip is the critical region, and it is important to have a finer mesh around this area in order to model the large-scale deformation. As the graphs in Figure 5.7 show, the element size across the critical region is about half the size of that at the gross cross section. N indicates the element size in the critical region along the radial direction in the vicinity of the notch tip.

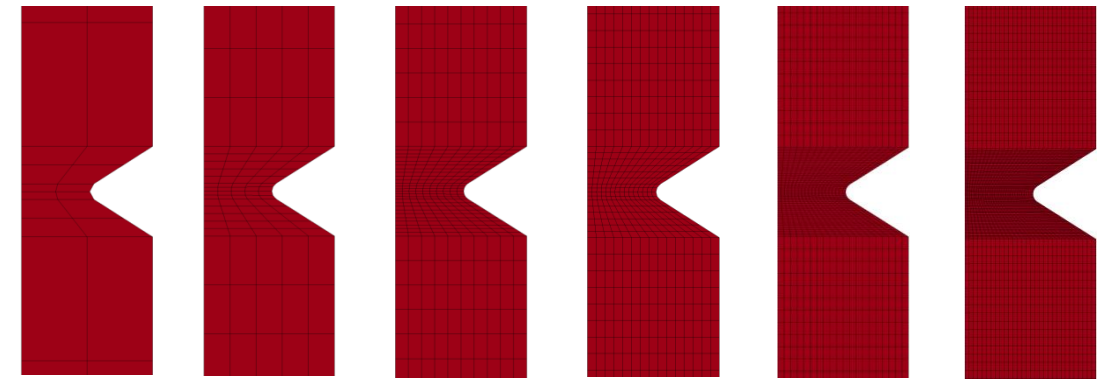

(a) N=1.3mm (b) N=0.52mm (c) N=0.26mm (d) N=0.17mm (e) N=0.13mm (f) N=0.087mm

Figure 5.7 FE models of sharply notched samples ($K_t = 2.93$) with 6 different element sizes.

Figure 5.8 shows the calculated Von Mises stress distribution for a sharply notched model from the coarsest mesh (N=1.3mm) to the finest mesh (N=0.087mm) when the cracking behaviour is not considered. From this graph, it can be found that when the element size N is smaller than 0.26mm, no significant change in the Von Mises stress contours can be observed. For the models whose element size N is bigger than 0.26mm, due to the lower mesh density, the models are not able to show a continuous and smooth Von Mises stress contour.

In Figure 5.9, the difference in the local Von Mises stress at the notch tip in the incipient failure condition between the model with element size N=0.17mm and the mesh model with element size N=0.13mm is 0.49%, which is acceptable for engineering FE simulations. When the element size decreases, this difference tends to zero.

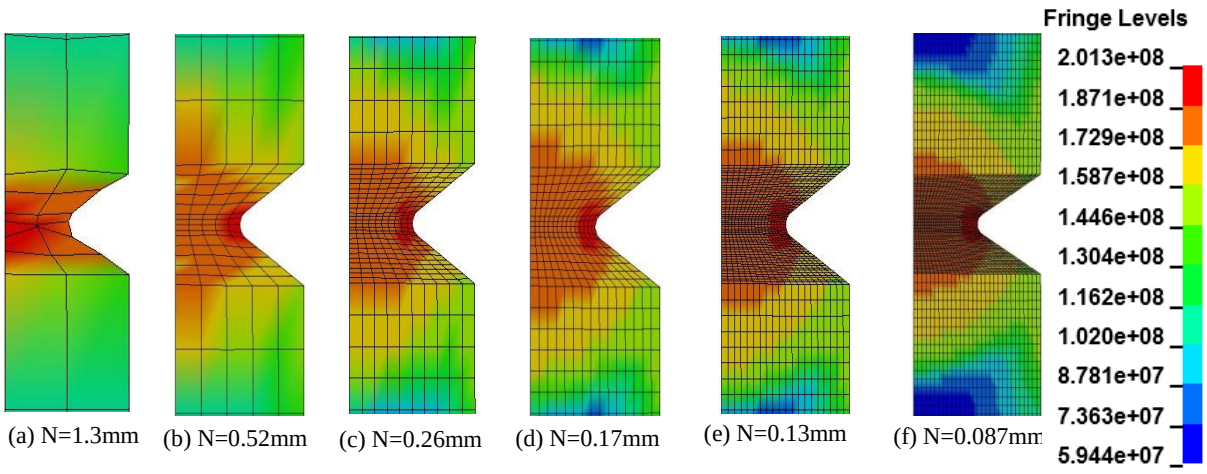

(a) N=1.3mm (b) N=0.52mm (c) N=0.26mm (d) N=0.17mm (e) N=0.13mm (f) N=0.087mm

Figure 5.8 Von Mises stress (Pa) contours of sharply notched models ($K_t = 2.93$) for 6 different element sizes at the time of maximum force without a fracture criterion.

Furthermore, the calculation time for the model with element size N=0.17mm (357 seconds) is about 3/5 of the time for the model with element size N=0.13mm (550 seconds), and the amount of the space are 3.07GB and 6.96GB respectively. Therefore, when ignoring cracking behaviour,

the conclusion can be drawn that the FE model whose element size is N=0.17mm in the critical region can provide an optimal combination of accuracy and efficiency.

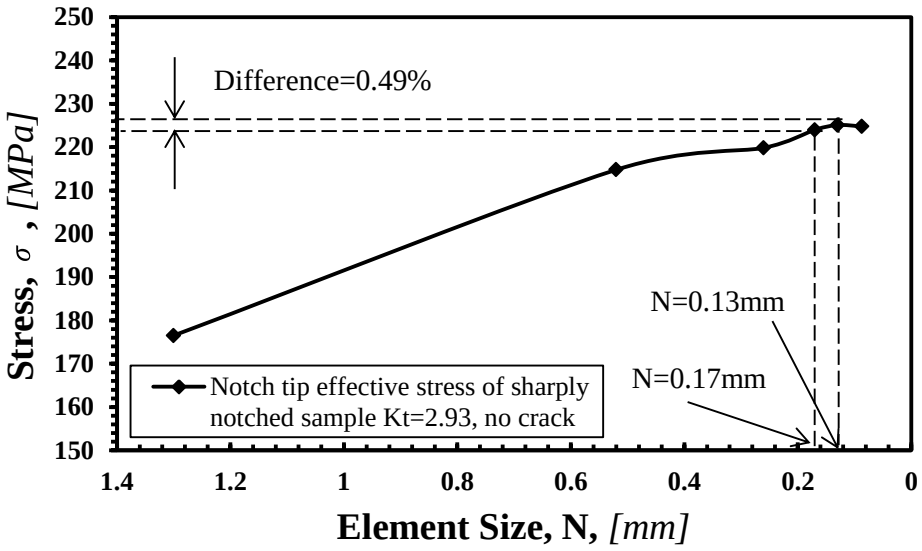

Figure 5.9 The max Von Mises stress at the notch tip vs element size for models of sharply notched sample ($K_t = 2.93$) without a fracture criterion.

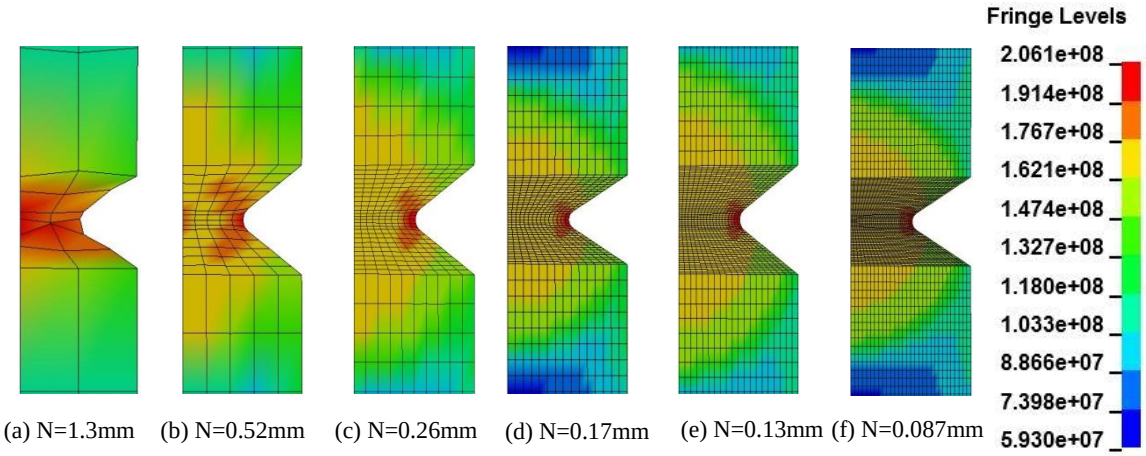

(a) N=1.3mm (b) N=0.52mm (c) N=0.26mm (d) N=0.17mm (e) N=0.13mm (f) N=0.087mm

Figure 5.10 Von Mises stress (Pa) contours of sharply notched models ($K_t = 2.93$) at the time of crack initiation for 6 different element sizes.

When considering the cracking behaviour, the failure effective plastic strain needs to be defined. An assumption was made that when the plain FE models reached the maximum axial force, the corresponding effective plastic strain at the minimum cross section was the failure effective plastic strain for this kind of material. Therefore, by applying this value of failure effective plastic strain to the Simplified Johnson–Cook material model, a new series of FE models for all notches which included cracking behaviour were generated. As long as the crack initiates, the maximum force over the time range from 0 to the time when the crack initiates was assumed as

the failure force. Figure 5.10 shows Von Mises stress distribution for various levels of mesh density just before the crack appears. There are no big changes once the size of the elements N is smaller than 0.17mm.

The difference shown in Figure 5.11 were calculated by comparing the effective stress at notch tip from the models with the element size from N=1.3mm to 0.087mm. It can be seen from this figure that the notched FE model with element size N=0.52mm can provide accurate enough results with a difference of 0.16%, and the difference tends to 0 as the element size decreases. The computing time and space for the model with element size N=0.17mm are 235 seconds and 2.45GB.

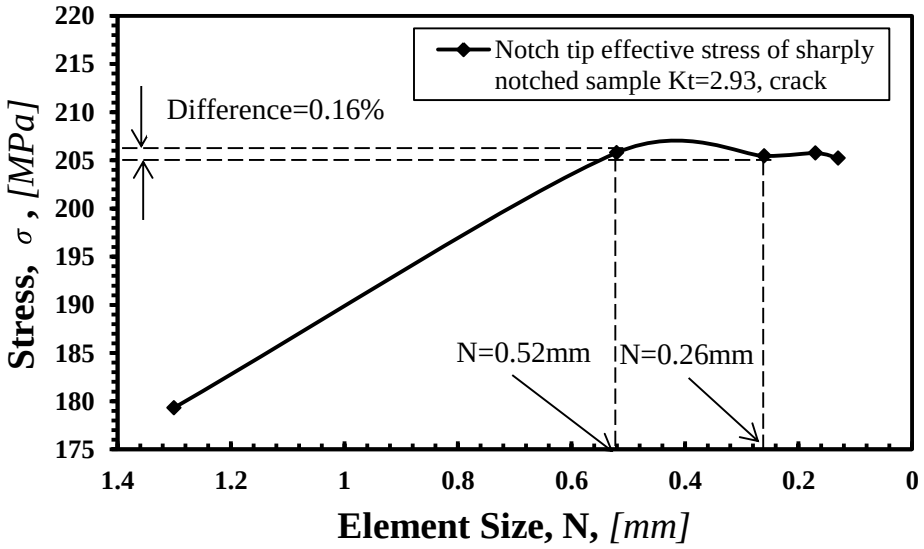

Figure 5.11 The max Von Mises stress at the notch tip vs element size for models of sharply notched sample ($K_t = 2.93$) with a fracture criterion.

Figure 5.12 shows the various levels of mesh density used for the intermediately ($K_t = 1.69$) notched models, and it is clear to see that the mesh density defined around the notch tip is much higher than the parts away from the notch. Regarding the non-fracture cases, it can be observed from Figure 5.13 that a decrease in mesh size does not increase the accuracy and smoothness of the Von Mises stress contours significantly as long as the element size N is smaller than 0.26mm. By comparing the Von Mises stress for the elements at the notch tip between the models with two adjacent element sizes, as shown in Figure 5.14, the difference is less than 1% when the element size is smaller than 0.17mm. the computing time and the amount of space of the models with element size N=0.17mm and 0.13mmm are 443 seconds, 3.17GB and 920 seconds and 5.59GB respectively. Hence, the FE model with an element size N=0.17mm in the critical region can be used as the most efficient FE model for the intermediately notched case. Moreover, from Figure 5.15 and Figure 5.16, it can be found that the FE model with element

size N=0.17mm (Computing time is 600 seconds and the amount of space is 3.17GB) is enough to properly calculate an accurate maximum axial force when fracture is taken into account.

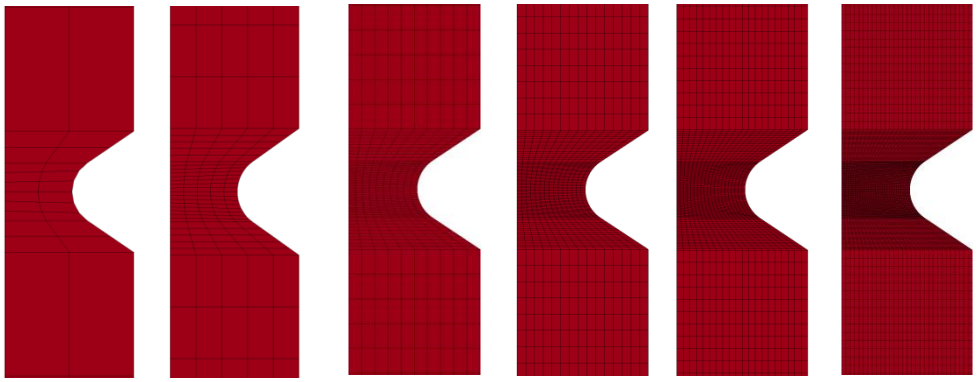

(a) N=1.3mm (b) N=0.52mm (c) N=0.26mm (d). N=0.17mm (e). N=0.13mm (f). N=0.087mm

Figure 5.12 FE models of intermediately notched sample with 6 different element sizes.

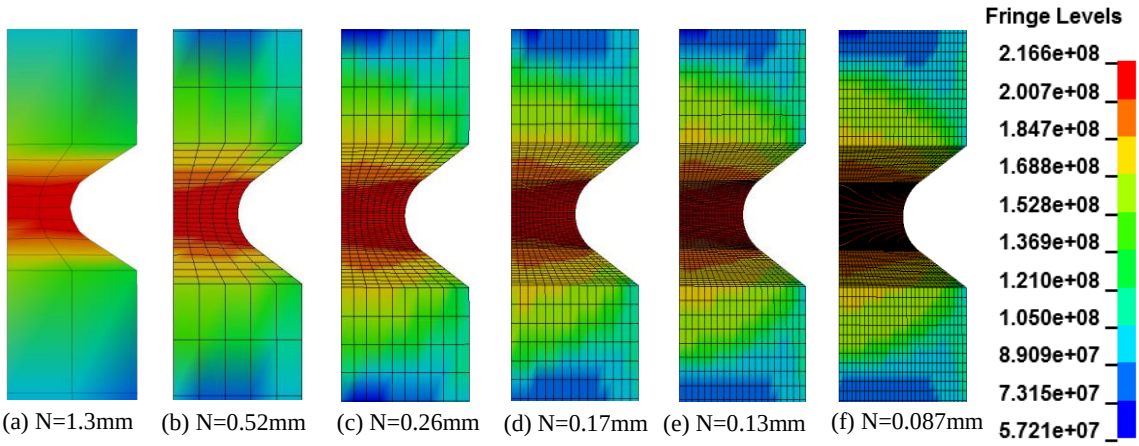

(a) N=1.3mm (b) N=0.52mm (c) N=0.26mm (d) N=0.17mm (e) N=0.13mm (f) N=0.087mm

Figure 5.13 Von Mises stress (Pa) contours of intermediately notched models (for 6 different element sizes at the time of maximum force without a fracture criterion.

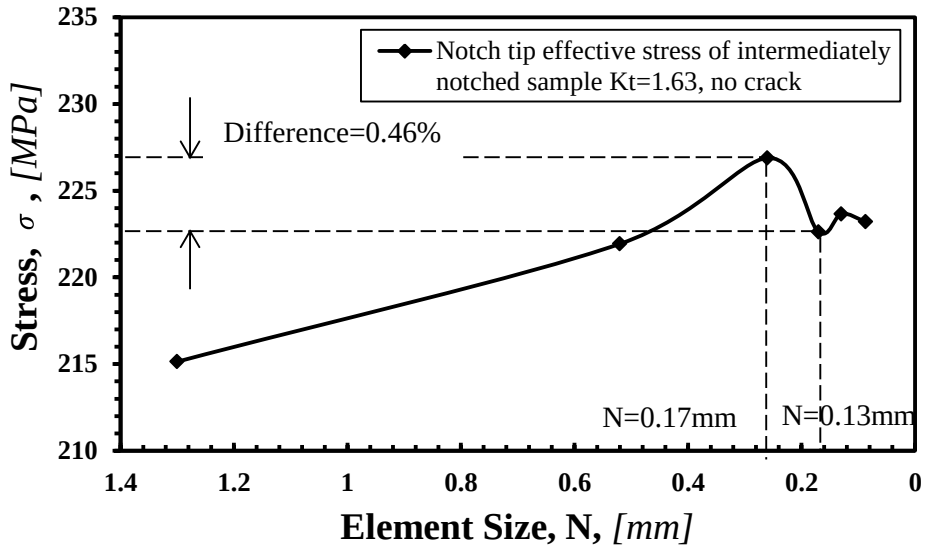

Figure 5.14 The max Von Mises stress at the notch tip vs element size for models of intermediately notched sample ($K_t = 1.63$) without a fracture criterion.

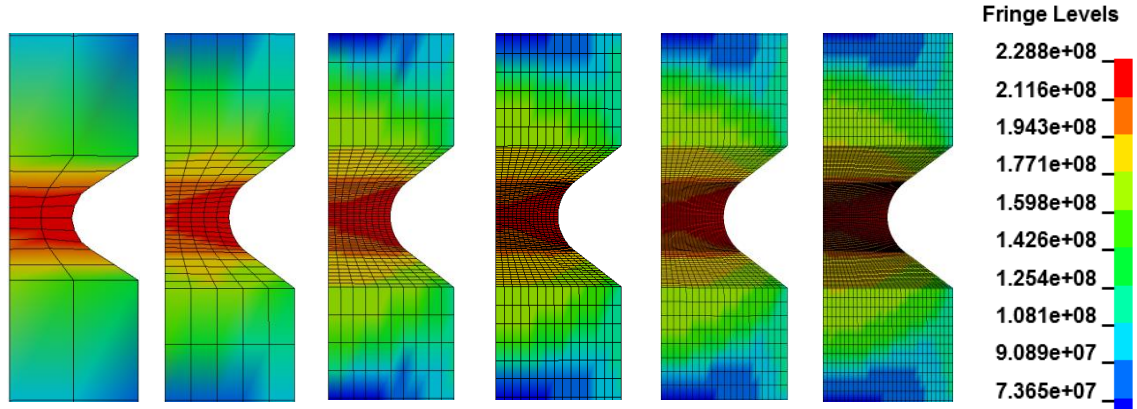

(a) N=0.13mm (b) N=0.52mm (c) N=0.26mm (d) N=0.17mm (e) N=0.13mm (f) N=0.087mm

Figure 5.15 Von Mises stress (Pa) contours of intermediately notched models at the time of crack initiation for 6 different element sizes.

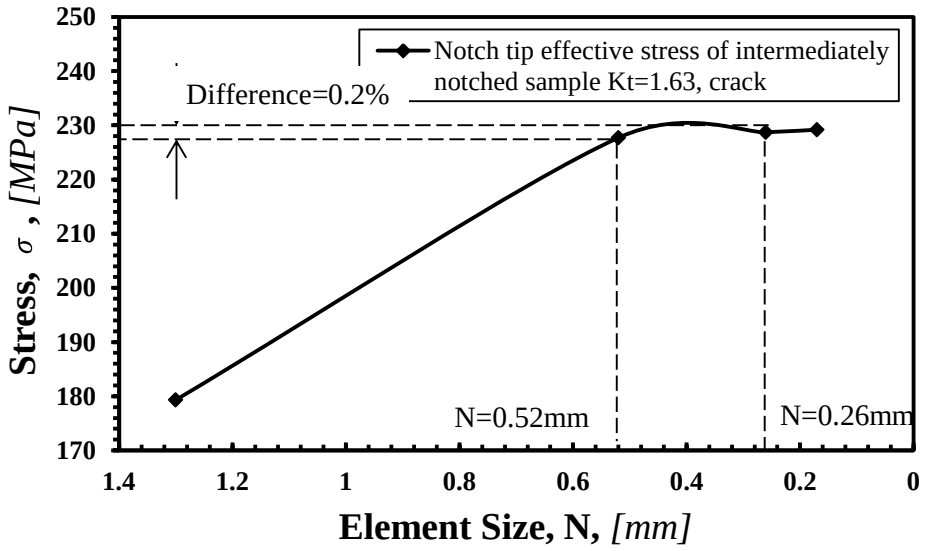

Figure 5.16 The max Von Mises stress at the notch tip vs element size for models of intermediately notched sample ($K_t = 1.63$) with a fracture criterion.

For the bluntly notched models, a range of element sizes created is shown in Figure 5.17. By running models with and without a fracture criterion, it can be observed from Figure 5.18 and Figure 5.20 that the FE models for blunt notches with an element size N=0.5mm can provide smooth and clear Von Mises distributions for models both with and without the fracture criterion (computing time and the amount of space for the two models are 381 seconds, 2.33GB and 167 seconds, 2.29GB). Moreover, Figure 5.19 is a plot of the convergence of the Von Mises stress at the notch tip for the bluntly notched FE model without a fracture criterion which falls within a difference of 1.29% between the models with element size N=0.5mm (computing time is 381 seconds, the amount of apace is 2.33GB) and 0.25mm (computing time is 327 seconds, the amount of apace is 6.13 GB). Figure 5.21 is a plot of the convergence of the effective stress with a difference of 0.46% between the models with element size N=0.5mm (computing time is 167 seconds, the amount of apace is 2.29GB) and 0.25mm (computing time is 448 seconds, the amount of apace is 6.07GB) at the same location when the fracture criterion was defined. It can be concluded that the length of N=0.5mm are selected mesh size for bluntly notched models both without and with fracture.

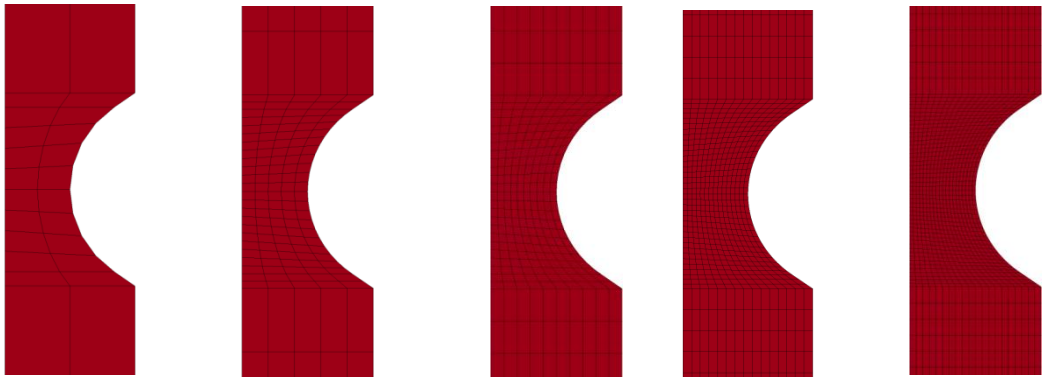

(a). N=1.25mm (b). N=0.5mm (c). N=0.25mm (d). N=0.17mm (e). N=0.125mm

Figure 5.17 FE models of bluntly notched sample with 7 different element sizes.

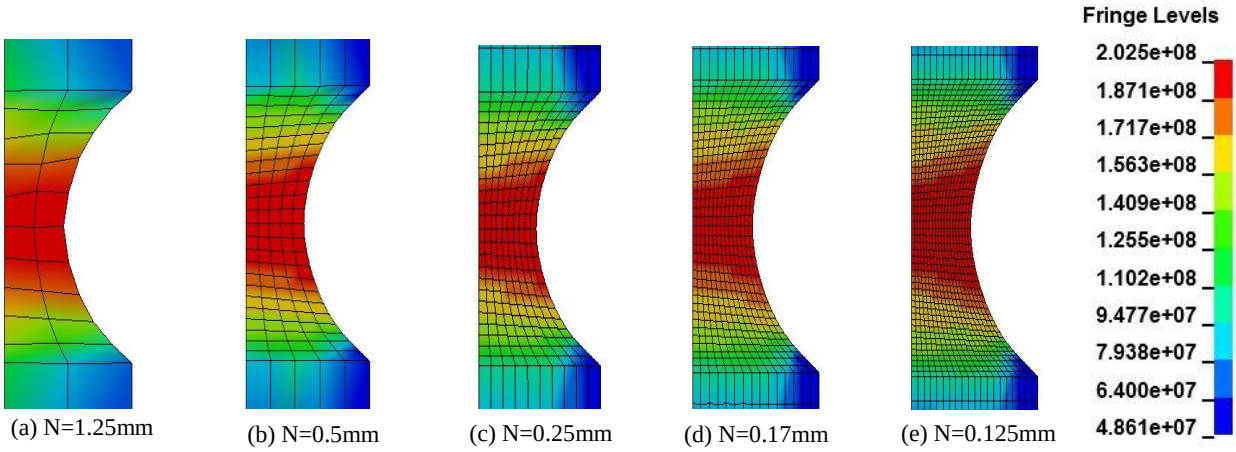

(a) N=1.25mm (b) N=0.5mm (c) N=0.25mm (d) N=0.17mm (e) N=0.125mm

Figure 5.18 Von Mises stress (Pa) contours of bluntly notched models for 7 different element sizes at the time of maximum force without a fracture criterion.

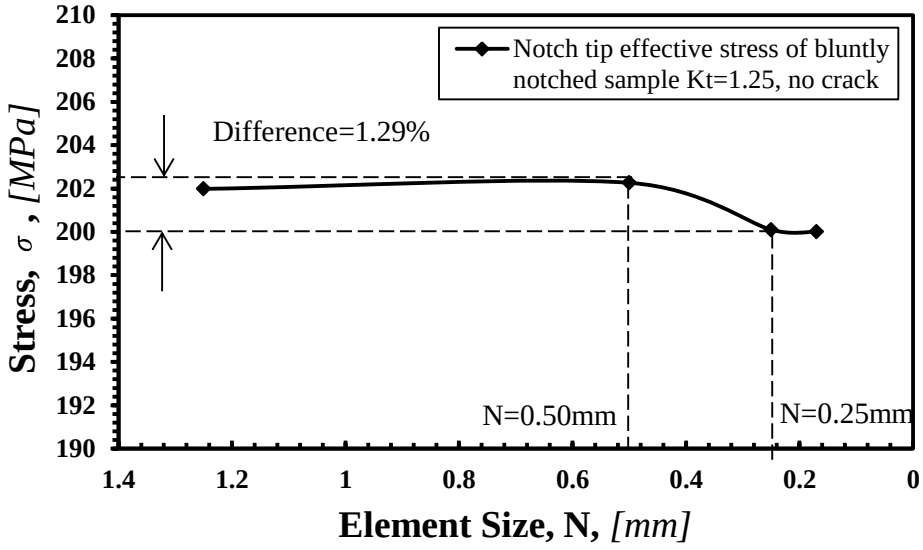

Figure 5.19 The max Von Mises stress at the notch tip vs element size for models of bluntly notched sample ($K_t = 1.25$) without fracture criterion.

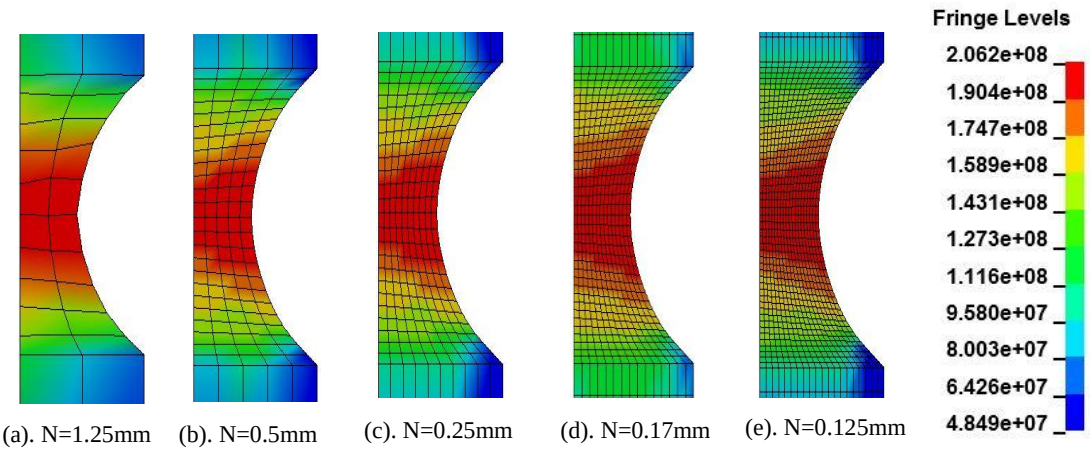

Figure 5.20 Von Mises stress (Pa) contours of bluntly notched models at the time of crack initiation for 5 different element sizes.

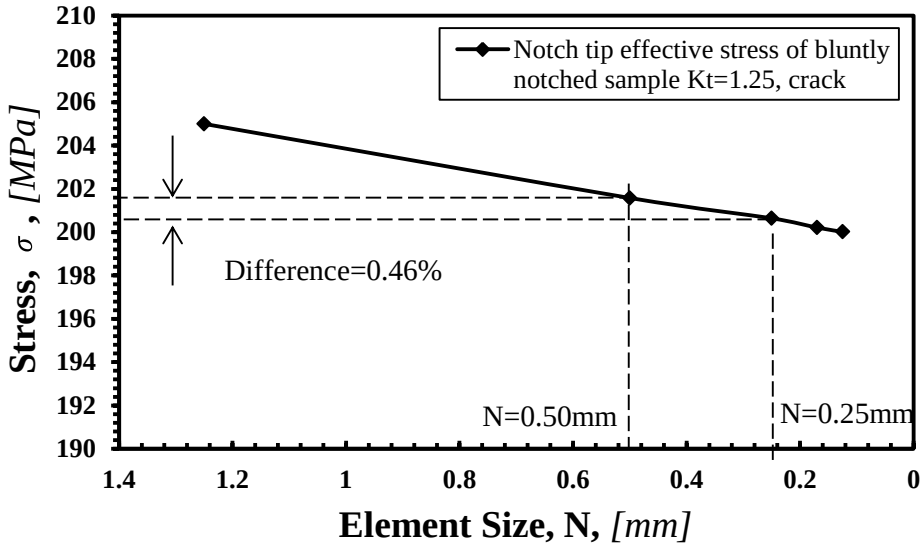

Figure 5.21 Accuracy of the maximum axial force vs element size for bluntly notched models with a fracture criterion.

To conclude, the results of the convergence study are listed in Table 5.1.

Table 5.1 Results of mesh convergence for models of Al6063-T5 samples.

Geometry	Selected mesh size with a fracture criterion , *[mm]*	Selected mesh size with no fracture criterion, *[mm]*
Un-notched	0.40	
Sharp, $K_t = 2.93$	0.52	0.17
Intermediate, $K_t = 1.63$	0.52	0.17
Blunt, $K_t = 1.25$	0.50	0.50

5.4 Determination of Material Parameters

In the FE simulations, the determination of the material parameters is key when a complex constitutive law is used during the analysis. The correct determination of the required parameters is particularly important to simulate the mechanical behaviour of structures and components which experience high loading rates and large deformations. The Simplified Johnson–Cook material model contains parameters A, B, n and C, which are used in this constitutive law to model large-scale deformation under dynamic loading. According to the technical literature, however, different mechanical behaviours for the same material can be found (Qiao and Wang, 2011, Torres-Franco et al., 2011, Varas et al., 2012, Barsoum et al., 2014). These differences can be attributed to many aspects such as the fabrication process and testing including the different level of alignment when doing dynamic axial tests, material aging, and geometries and so on.

In this subsection, two strategies to evaluate the constants in the Simplified Johnson–Cook material law will be presented as follows: 1. curve fitting techniques. By using the curve fitting tools integrated in the MATLAB program (Jiade, 2008), the parameters for the Simplified Johnson–Cook constitutive law can be obtained from experimental data taken from the literature. 2. Based on the material constants obtained from different sources, the maximum force from the experimental data can be used as the reference force to calibrate the material constants used in the numerical simulation until optimal values are determined.

5.4.1 Curve fitting techniques

As discussed in section 1.9, the material parameters of Johnson-Cook material model can be determined by fitting the model to set of experimental data. The curve fitting process has been used in many areas as a basic idea to fit the equations of approximating curves to a series of experimental data (Fang and Gossard, 1995, Maddams, 1980, Akima, 1970, Motulsky and Christopoulos, 2004, Levy, 1959, Dye and Nicely, 1971). In this case, the nonlinear least squares method was employed to fit the data taken from different sources in order to find the material constants for the Simplified Johnson–Cook constitutive law.

Turning back to Equation 1.29, according to the LS-DYNA theory manual, the flow stress σ_y is equivalent to the absolute value of the true stress in the LS-DYNA plasticity model (Dietenberger et al., 2005, Hallquist, 2006), and the effective plastic strain, ε_{EPS}, is the residual true strain when the loading is removed. Hence, in order to fit the Simplified Johnson–Cook constitutive law to the experimental data, it is essential to have the effective plastic strain, which can be calculated using Equation 5.1 (Hallquist, 2006):

$$\varepsilon_{\mathrm{EPS}} = \varepsilon_{\mathrm{T}} - \sigma_{\mathrm{T}}/\mathrm{E} \qquad (5.\ 1)$$

where ε_T and σ_T indicate true strain and true stress respectively. It can be seen from this equation that the recoverable strain σ_T/E increases as the stress σ_T increases. However, this phenomenon is not applied to metallic material due to its very large E comparing to yield stress. Therefore, value σ_T/E is taken to equal to material yield strain. The effective plastic strain is zero before the initial material yielding point; after this point, it increases as the true stress increases.

For the case of the true stress and true strain data shown in Figure 5.22, Barsoum et al. conducted uniaxial tests on 6063-T5 aluminium alloy (tempered) tubes under quasi-static conditions to investigate the ductile failure behaviour experimentally and numerically (Barsoum et al., 2014).

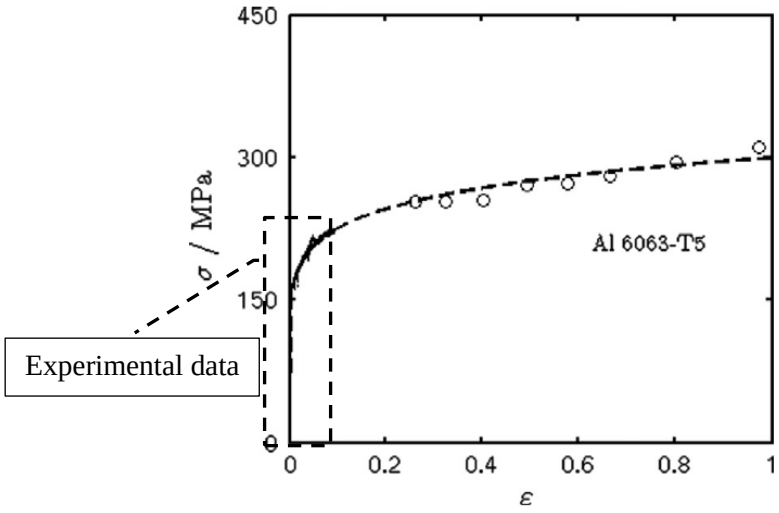

Figure 5.22 True stress-strain curve for aluminium alloy 6063 in the T5 condition (Barsoum et al., 2014).

By using the digitalisation function integrated in the commercial software MATLAB, as shown in Table 5.2, a series of experimental true stress and true strain values were digitalised from Figure 5.15 (dash square). By substituting these values into Equation 5.1, the effective plastic strain was calculated directly. All of the results are listed in Table 5.2 below, and the corresponding true stress versus effective plastic strain is plotted in Figure 5.16.

Because all of the components were tested under quasi-static loading, in this case, the rate sensitivity constant C in the Simplified Johnson–Cook constitutive law was taken equal to zero. Therefore, Equation 1.32 can be rewritten as follows:

$$\sigma_y = (A + B \cdot (\bar{\varepsilon}^p)^n) \tag{5. 2}$$

By fitting the rate insensitive constitutive law of Equation (5.2), the solid line in Figure 5.23 shows the fitted curve corresponding to the data converted from Barsoum et al. was calculated. The calculated parameters of the Simplified Johnson–Cook material model under quasi-static conditions were obtained as A=143MPa, b=203.1MPa, n=0.37, which are tabulated in Table 5.3.

Table 5. 2 Experimental data from literature of Barsoum et al.

True stress, σ_{true},*[MPa]*	True Strain, ε_{true}	Effective plastic strain, ε_{EPS}
0.000	0.000	0.000
78.862	0.001	0.000
158.382	0.003	0.001
171.284	0.006	0.004
179.447	0.013	0.010
185.503	0.019	0.016
192.349	0.025	0.022
197.747	0.033	0.030
203.935	0.041	0.038
211.439	0.052	0.048
216.837	0.065	0.061
220.260	0.077	0.074
222.894	0.088	0.084

Additionally, Al6063-T5 has also been used by many other researchers for different purposes. For example, Varas et al. (2012) used Al6063-T5 to investigate the phenomenon of the Hydrodynamic Ram (HRAM) when a fluid-filled container is penetrated by a fast object (Varas et al., 2012). In this case, the material was treated as a rate insensitive material (C=0). The data reported in Figure 5.24 (a) were generated by testing samples of Al6063-T5 to investigate the dynamic behaviour of this aluminium alloy (Qiao and Wang, 2011). Torres-Franco et al. also used material Al6063-T5 (heat treatment procedure of annealing: heated at 250^{o}C for 25 mins and slowly cooled down inside oven), whose behaviour is shown in Figure 5.24 (b), to verify a new test method to determine the loading history applied to a component (Torres-Franco et al., 2011).

By applying the same fitting procedures to the data from the literature, the digitalised data and fitted curves were plotted in Figure 5.25, and the corresponding constants of the Simplified Johnson–Cook model were calculated and are listed in Table 5.3.

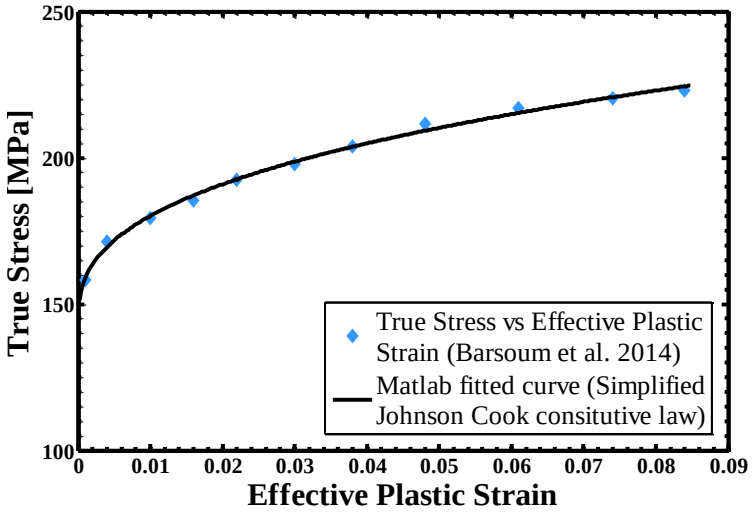

Figure 5. 23 True stress vs effective plastic strain from the literature (Barsoum et al. 2014), and the corresponding Simplified Johnson–Cook constitutive law fitted curve.

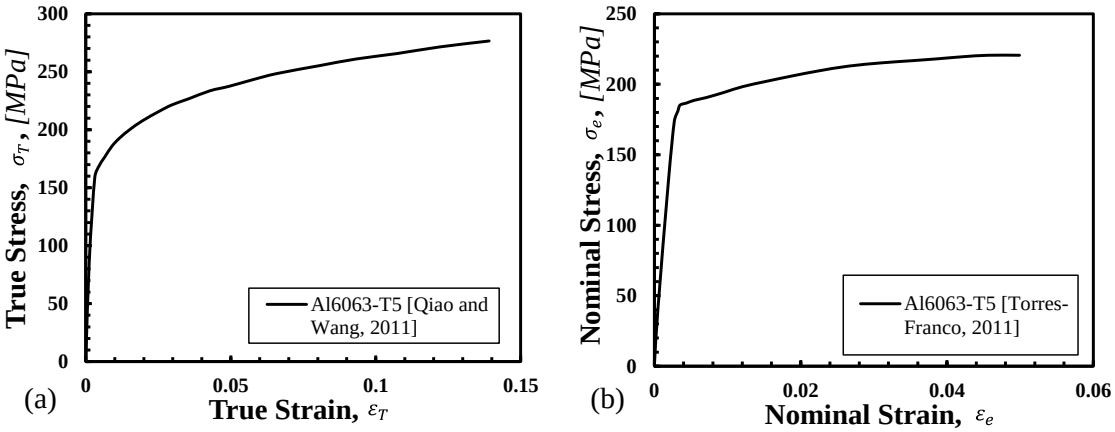

Figure 5. 24 (a) True stress vs true strain curve for Al6063-T5 (Qiao and Wang, 2011); (b) Engineering stress vs engineering strain curve for Al6063-T5 (Torres-Franco et al, 2011).

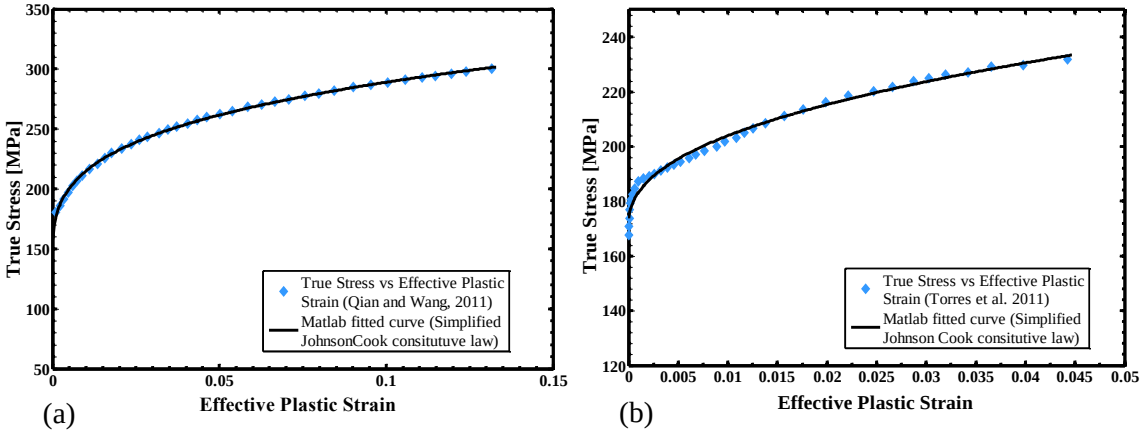

Figure 5. 25 Al6063-T5 true stress vs effective plastic strain data and corresponding fitted curves for data from the literature (a) (Qiao and Wang, 2011), and (b) (Torres-Franco, 2011).

It is clear from the values reported in Table 5.3 that, despite the fact that the tested material was nominally the same, the constants A, B and n obtained from these four studies are very different. In order to check the accuracy of the material constants in Table 5.3, a DYNA model using the Simplified Johnson–Cook model was run, and these material constants were applied together with the Simplified Johnson–Cook constitutive law to simulate the material behaviour of the plain specimens under quasi-static conditions. The results for force versus time are plotted in Figure 5.26. From this graph, it can be seen that the five sets of constants produce various material behaviours. An assumption was made here that the maximum force, F_{max}, recorded during each model was defined as the failure force, F_f. Therefore, the failure forces generated from the LS-DYNA models using material constants calculated from Barsoum et al., Varas et al., Torres-Franco et al., Qiao and Wang and our coupon tests were 4.74kN, 4.82kN, 5.37kN, 6.01kN and 5.08kN respectively. However, at the laboratory of the University of Sheffield, the average failure force for the plain samples under quasi-static conditions (S1T1 and S1T3) was calculated to be equal to 3.95kN. By comparing the failure force from numerical results with the one recorded at our laboratory, the errors were calculated and are listed in Table 5.4. From this table, it is possible to observe that the differences between the failure forces obtained from the literature data and the experiments are all equal to or greater than 20%. This means that the predictions for material performance from simulations using constants taken from the literature data give a higher material strength than the one shown by our material.

Table 5. 3 Al6063-T5 parameters from the literature and coupon tests for the Simplified Johnson–Cook material model.

Al6063-T5 References	σ_{UTS} *[MPa]*	E *[GPa]*	A *[MPa]*	B *[MPa]*	n	C
1. (Barsoum et al., 2014)	205.3	64	143.0	203.1	0.37	0
2. (Varas et al., 2012)	N/A	71	200.0	144.0	0.62	0
3. (Torres-Franco et al., 2011)	221.0	66	170.6	234.2	0.42	0
4. (Qiao and Wang, 2011)	261.8	65	130.6	297.4	0.27	0
5. (Coupon Test)	199.6	62	112.6	342.8	0.48	0

Table 5. 4 Predicted results from DYNA simulations using parameters generated from data from the literature.

Al6063-T5 References	Failure Force *[kN]* (DYNA)	Failure Force *[kN]* (Experimental data)	Error [%]
1. (Barsoum et al., 2014)	4.74	3.95	20.00
2. (Varas et al., 2012)	4.83	3.95	22.28
3. (Torres-Franco et al., 2011)	5.37	3.95	35.95
4. (Qiao and Wang, 2011)	6.01	3.95	52.15
5. (Coupon Test)	5.08	3.95	28.61

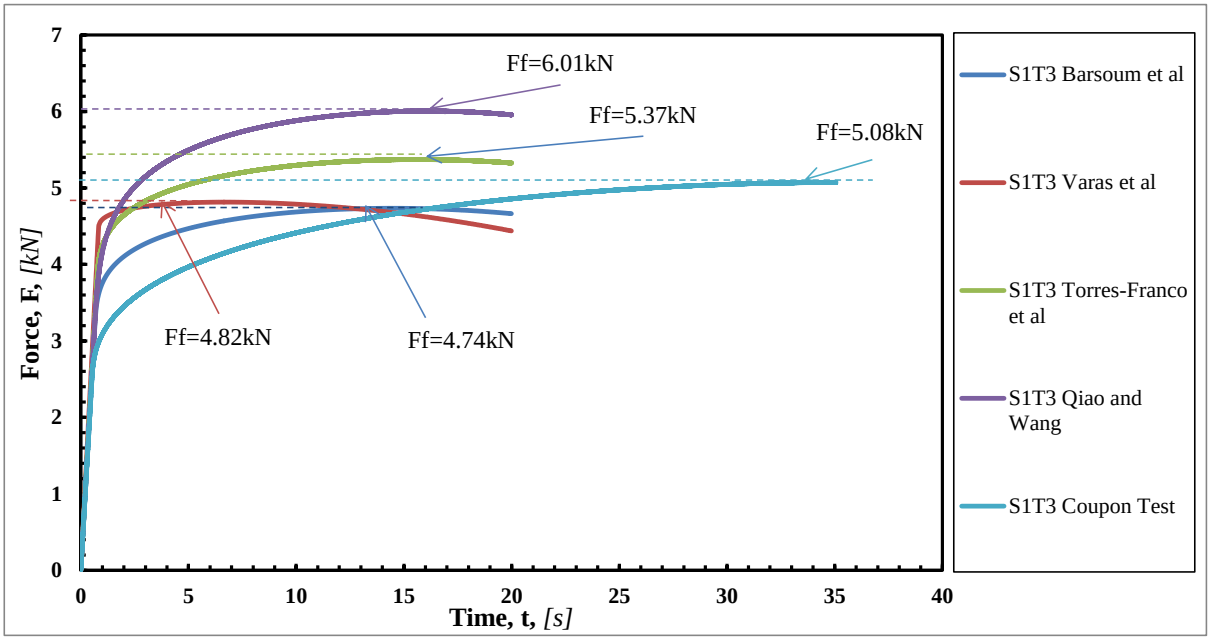

Figure 5. 26 Force vs time history of plain model under quasi-static condition (C=0) by using four different groups of parameters from literatures.

Hence, finding the right parameters for the Simplified Johnson–Cook material model for the investigated material has become one of the most important steps in this analysis. In terms of our experimental data, for example, Figure 5.27 shows the engineering stress versus engineering strain curves for plain samples under both quasi-static and dynamic loading conditions. It can be seen from this graph that the engineering stress–strain curves obtained from our experimental data for each sample are very different from each other. The elastic deformation and work hardening parts are difficult to see clearly from the curves in this figure. This situation can be ascribed to the fact that when the samples were attached to the pneumatic loading system, the alignment between the transfer bars and the sample was different for each test; at the very beginning of each test, the sample needed some time to adjust itself and be pulled straight. Moreover, in terms of the testing rig, there are no local strain gages or extensometers attached during testing, and it is very difficult to obtain the local stress–strain data for fast deforming tests. Therefore, the only information available which we could use to obtain the strain history for all of the tests was the high speed video, which was recorded by a high speed video camera. Due to the limited resolution of the high speed videos, the displacement during elastic deformation was not easy to track. Hence, the curve fitting approach is not suitable for our experimental data. Therefore, we need to find a proper way to characterise the material parameters from the experimental data.

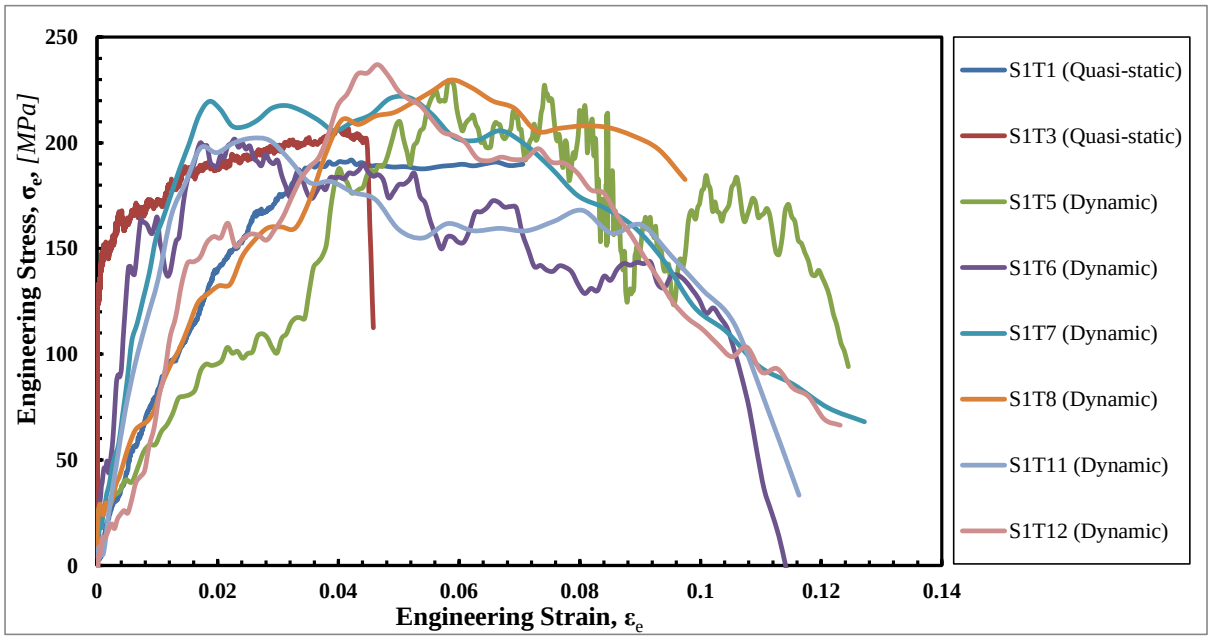

Figure 5. 27 Engineering stress vs engineering strain curves for plain samples.

5.4.2 Characterising material properties using numerical simulations

Owing to the unclear elastic deformation and work hardening effects on the stress–strain behaviour, it can be seen that the material constants for the Simplified Johnson–Cook material

from our Al6063-T5 tests are impossible to be obtained by using nonlinear curve fitting methods, so we need to find an alternative way to determine the correct values for the constitutive parameters for the tested Al6063-T5 specimens. From a design point of view, the material resistance is one of the most important features for structures and components, so the assumption was made here that the maximum force obtained during each test was taken as the reference force to characterise the material constants used for the Simplified Johnson–Cook material model.

Turning back to Table 5.3, the ultimate tensile strengths of Al6063-T5 from all of the studies are also listed. According to our experimental tests, the average ultimate tensile strength of the plain samples under quasi-static conditions is 203.7MPa, which is very close to the results from Barsoum et al. (σ_{UTS}=206.5MPa) (Barsoum et al., 2014). Hence, this set of constants has the most common set of features with our experimental results. At the very beginning, the material is assumed to be rate independent (C=0). Figure 5.28 shows the profile of the failure force, F_f, versus displacement rate, $\dot{\Delta}$, curves generated from both experiment and numerical simulations. For the tests run under quasi-static conditions, the graphs in Figure 5.28 make it evident that the prediction of failure force using the constants obtained from Barsoum et al. is poor. By trying different work hardening effect values, B, a good prediction was obtained by taking B equal to 130MPa. This value gives the best fit to the experimental data under quasi-static conditions. It can also be seen from the same figure that when C=0, the failure force, F_f, from the simulation is constant over a wide range of displacement rates.

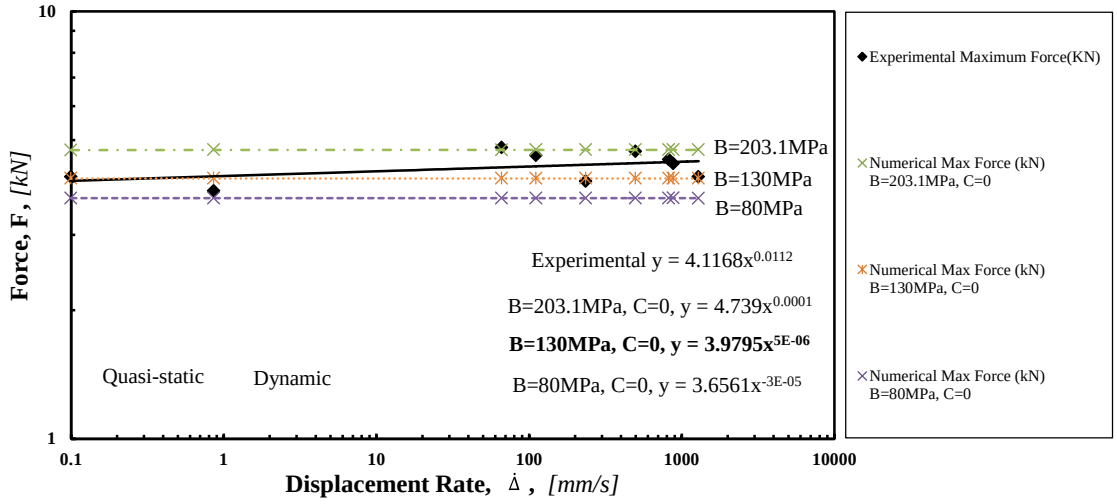

Figure 5.28 Maximum force vs displacement rate curves for plain samples.

After determining the value for B, the determination of the rate sensitivity coefficient C was carried out. Figure 5.29 shows a set of curves demonstrating the effect of the rate sensitivity coefficient C on the failure force calculated from the numerical results. Clearly, a value of

C=0.1 gives an overestimation of the experimental data, whereas, taking C=0 results in no sensitivity in the material strength as the displacement rate increases. The curve with a much smaller value (i.e. C=0.02) provides the best prediction of the experimental data.

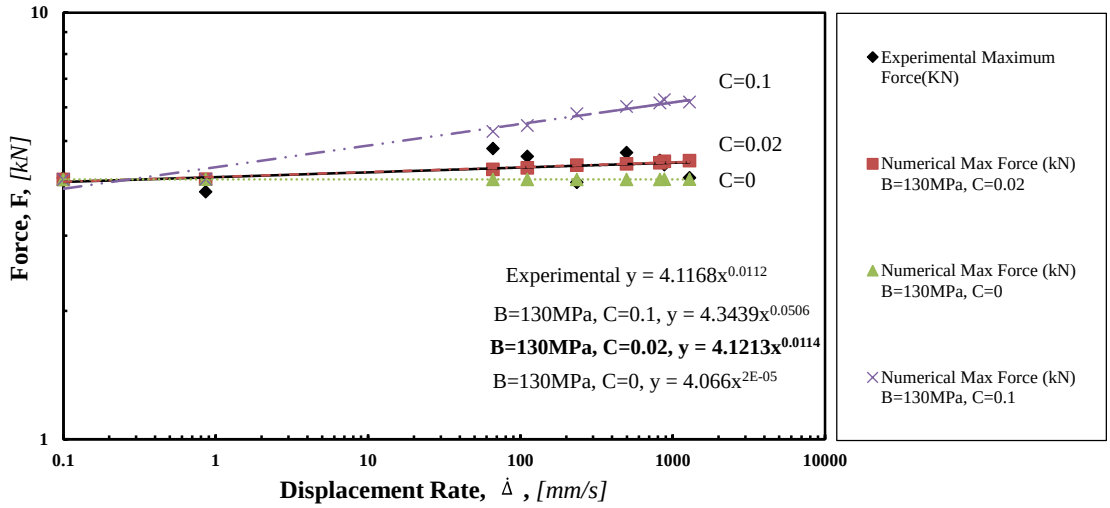

Figure 5.29 Maximum force vs displacement rate curves of plain sample with different rate sensitivity coefficients.

Table 5.5 Al6063-T5 parameters from literatures and coupon test for Simplified Johnson–Cook material model

Material	E [GPa]	A [MPa]	B [MPa]	n	C
Al6063-T5	64	143	130	0.37	0.02

To conclude, as summarised in Table 5.5, the following values of the material constants were estimated: A=143MPa, B=130MPa, n=0.37 and C=0.02. In the next section, these values will be used as material constants for the Simplified Johnson–Cook material model to carry out a series of numerical models involving different notches, and the results will be discussed in detail.

5.5 Simulation results

It is important to remember that under linear elastic analysis, the loading rate, strain rate and displacement rate used are all calculated as nominal values. However, in reality, the loading rate changes as the test progresses. Hence, it is worth verifying that the simplified ramped load history can be used as the applied load in the FE simulations instead of the actual real load history without much loss of accuracy. Moreover, the elasto-plastic FE models of all of the tested Al6063-T5 cylindrical bars were created in order to predict the behaviours of the tested samples containing different sizes of notch.

5.5.1 Comparing the results from applying ramped and real displacement histories for plain samples

As an example, Figure 5.30 shows the FE model for the plain sample, and the force time histories obtained from the model of the plain sample S1T1 corresponding to different displacement loading histories. Specifically, two types of loading boundary conditions in the form of the displacement histories (as the example S1T1 shown in Figures 5.30 (b) and (c)) were applied to the nodes across the line at the left end of the model during simulation: type 1, ramp displacement history; type 2, real displacement history. At the right end, the degrees of freedom in all directions were fixed. The nominal axial force histories (as shown in the charts reported in Figures 5.30 (d) and (e)) corresponding to load type 1 and load type 2 were obtained by post-processing the element stresses at the left-most fixed end. In this scenario, in terms of the models of plain samples, an assumption was made that the maximum nominal axial force, F_{max} obtained during the simulation was taken as the failure force F_f for the model for all plain samples.

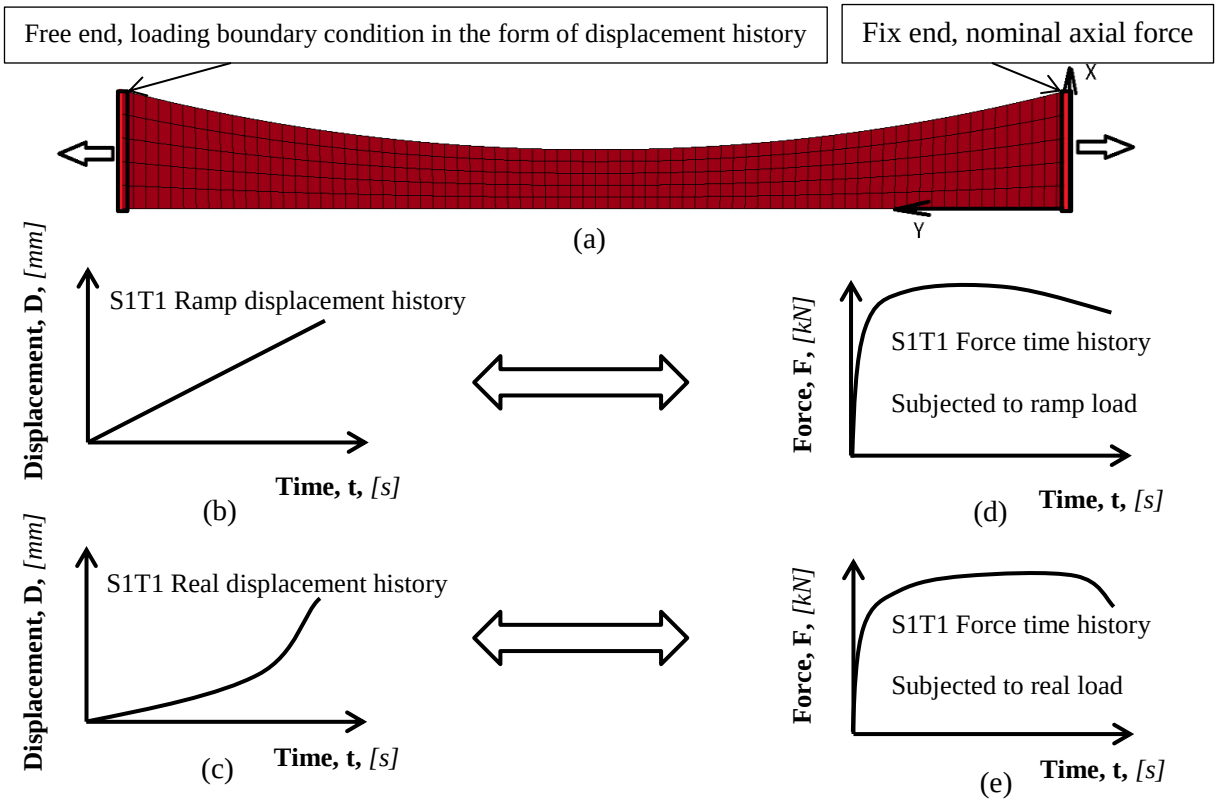

Figure 5. 30 (a) FE model of plain sample; (b) S1T1 ramped displacement history; (c) S1T1 real displacement history; (d) force time history for S1T1 subjected to ramped load; (e) force time history for S1T1 subjected to real load.

Figures 5.31 to 5.34 show the force (Y-direction) versus time histories obtained from models of all of the tested plain samples subjected to both ramped and real displacement time histories. For all of these figures, the solid lines indicate the nominal axial force, whereas the red dotted lines describe the applied displacement histories.

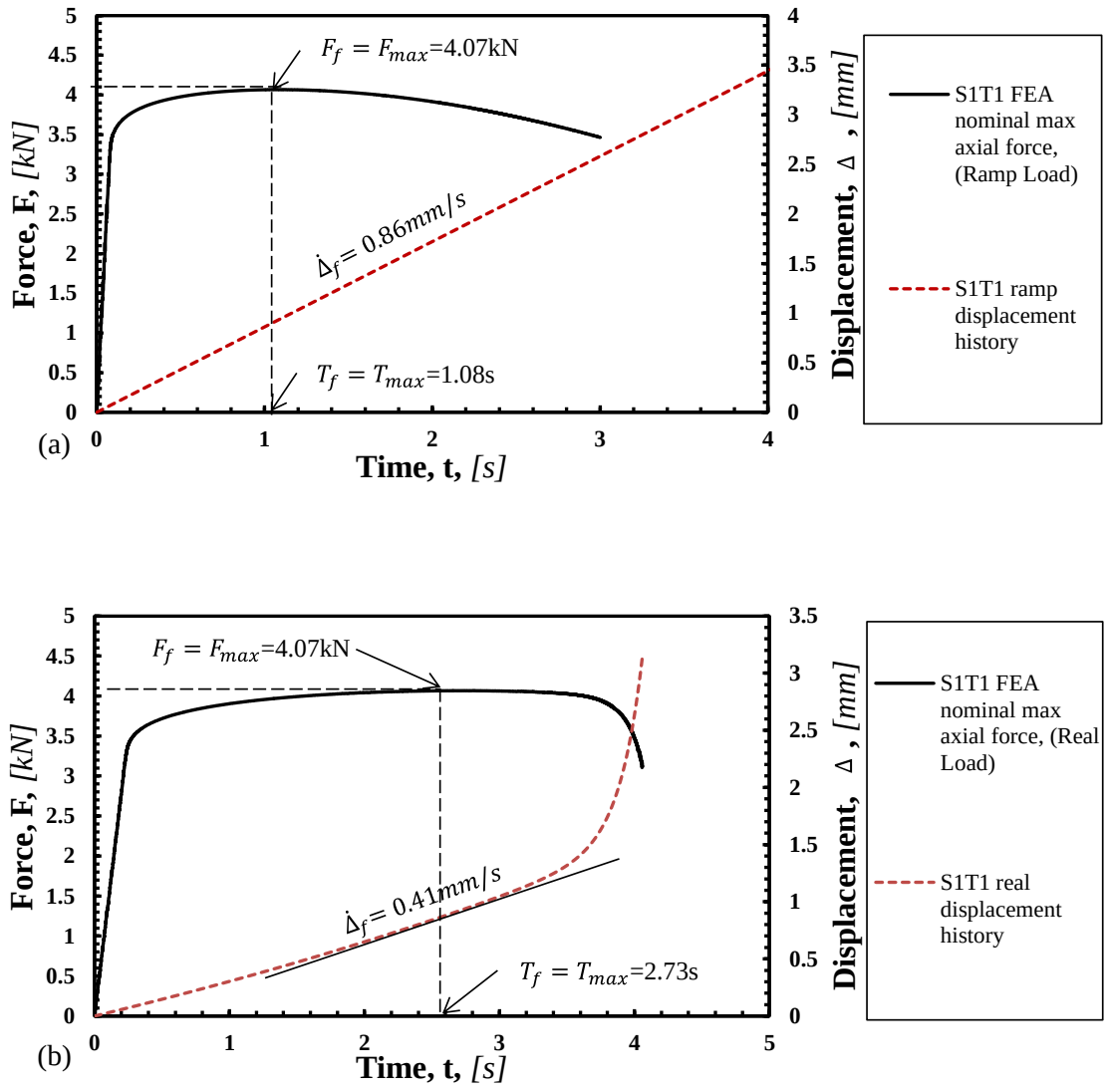

Figure 5.31 S1T1 force time histories corresponding to (a) ramped displacement history and (b) real displacement history.

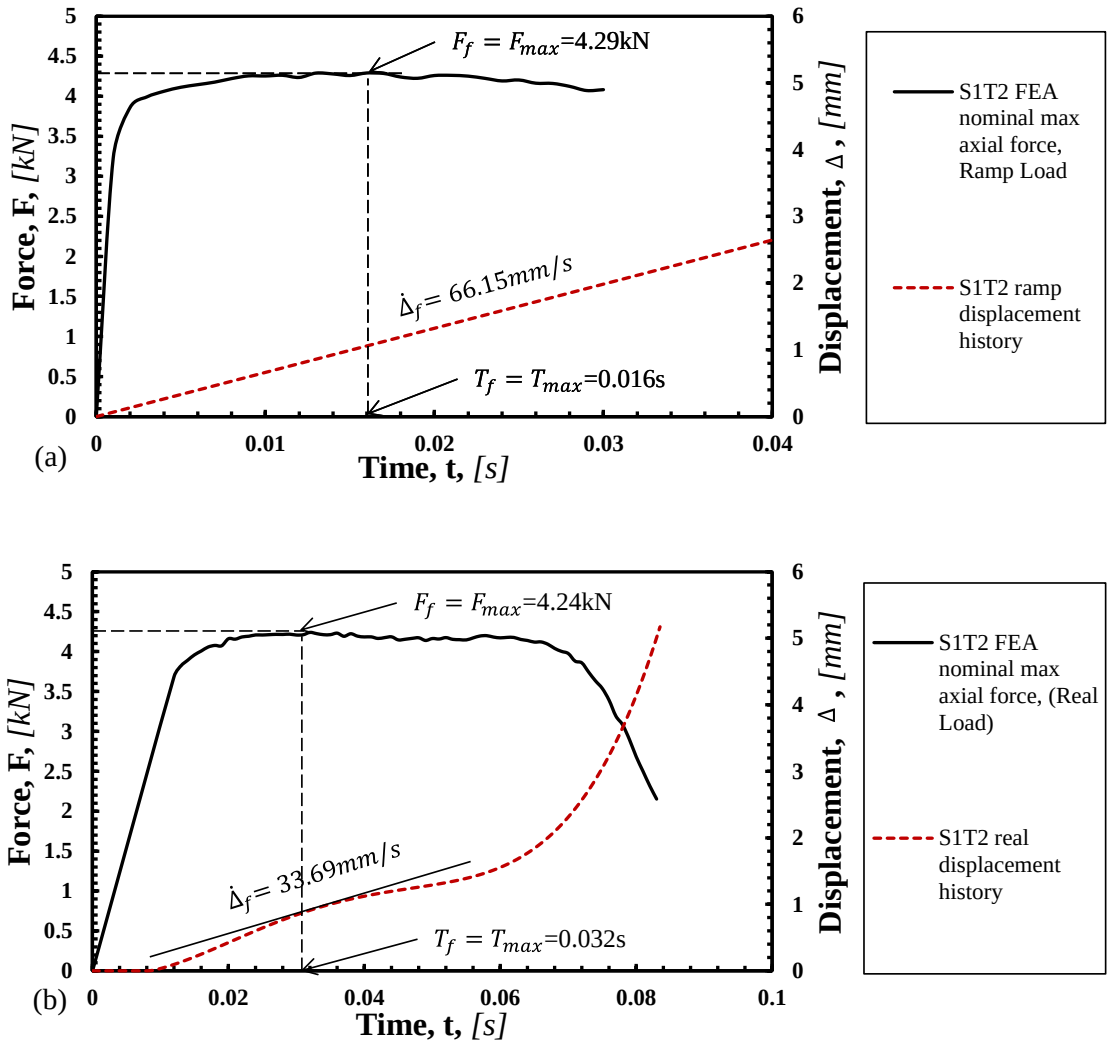

Figure 5.32 S1T2 Force time histories corresponding to (a) ramped displacement history and (b) real displacement load.

In detail, as the graphs show in Figure 5.31, the failure forces obtained by post-processing the maximum principle stresses of the elements at the fixed end for tested sample S1T1 subjected to both ramped and real displacement (red dotted lines) under quasi-static conditions are all equal to 4.07kN, and the corresponding failure times T_f are equal to 1.08s and 2.73s respectively. In terms of the model using a ramped displacement history, the nominal loading rate stays constant ($0.86mm \cdot s^{-1}$), whilst for the model using the real displacement history, the displacement rate varies as the simulation time increases, and the displacement rate corresponding to the failure time is 0.41 $mm \cdot s^{-1}$. The total CPU time of the simulations by applying ramped and real displacement history are 290 seconds and 61 seconds by taking up 199MB and 5.94GB respectively.

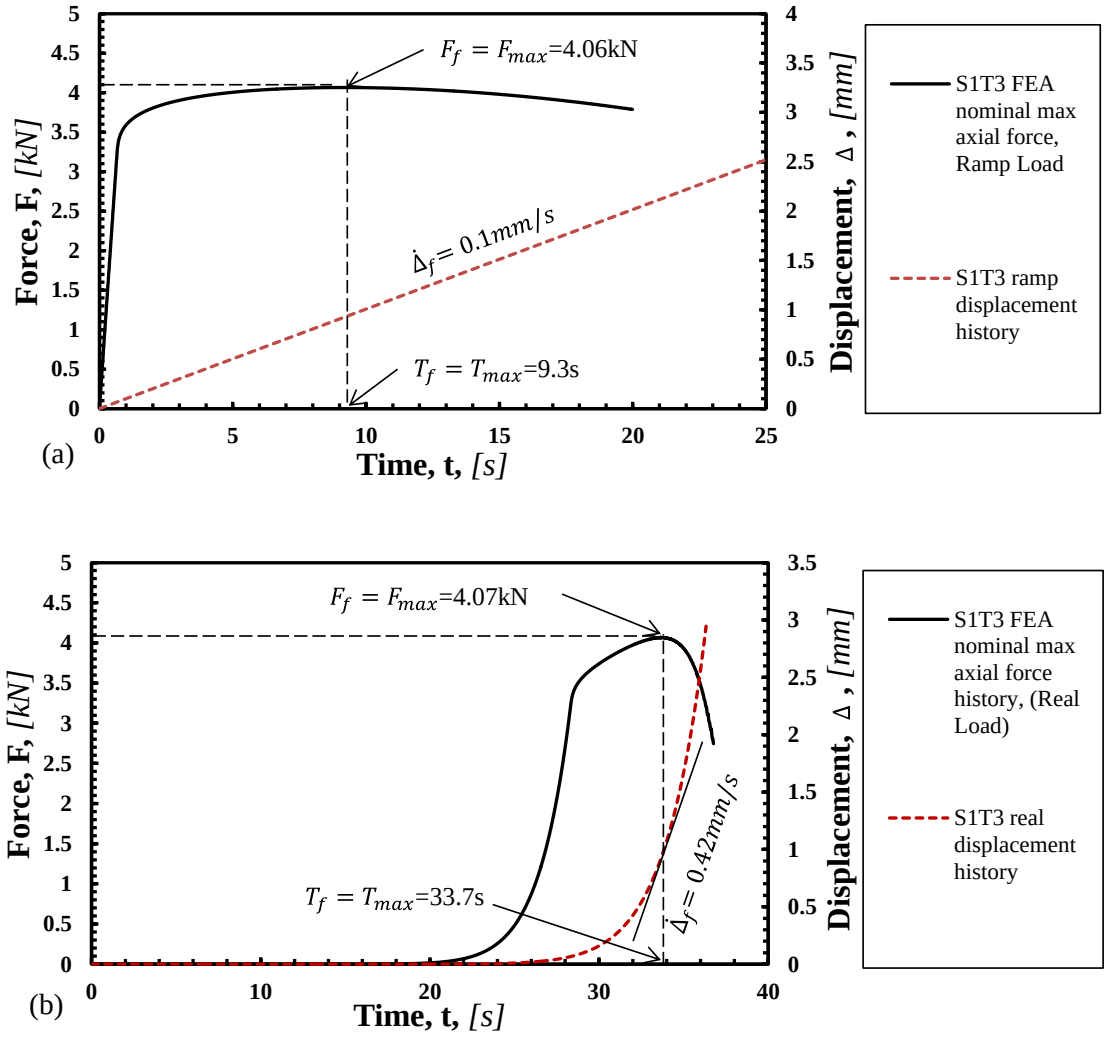

Figure 5.33 S1T3 Force time histories corresponding to (a) ramped displacement history and (b) real displacement load.

Moreover, the graphs reported in Figure 5.32 show the nominal axial force histories generated from the models of the S1T2 plain sample and the corresponding applied displacement histories. It can be seen from the graphs that the failure forces generated from the models subjected to ramped and real displacement histories are 4.29kN and 4.24kN respectively, and the corresponding displacement rates are $66.15mm \cdot s^{-1}$ and $33.69mm \cdot s^{-1}$. The computing time and space for the two models are 418 seconds, 5.11MB and 271 seconds and 2.59MB respectively.

For the model of the plain sample S1T3, quasi-static loading with a nominal displacement rate $\dot{\Delta}$= $0.1mm \cdot s^{-1}$ was employed as the loading boundary condition. As the graphs reported in Figure 5.33 show, the failure force F_f obtained from the models subjected to these both ramped (CPU time: 310 seconds, space: 50.6MB) and real displacement histories (CPU time: 601 seconds, space: 92.6MB) are 4.06kN and 4.07kN respectively.

In terms of the displacement history in Figure 5.33 (a), the displacement rate is a constant, and is equal to $0.1\,\mathrm{mm}\cdot\mathrm{s}^{-1}$. From the red dotted line in Figure 5.33 (b), at time t=25s, the displacement starts to increase from 0 to 3.528mm over 10s, and the displacement rate after 25s increases significantly. At the time of failure, the displacement rate is taken as $0.42\mathrm{mm}\cdot\mathrm{s}^{-1}$.

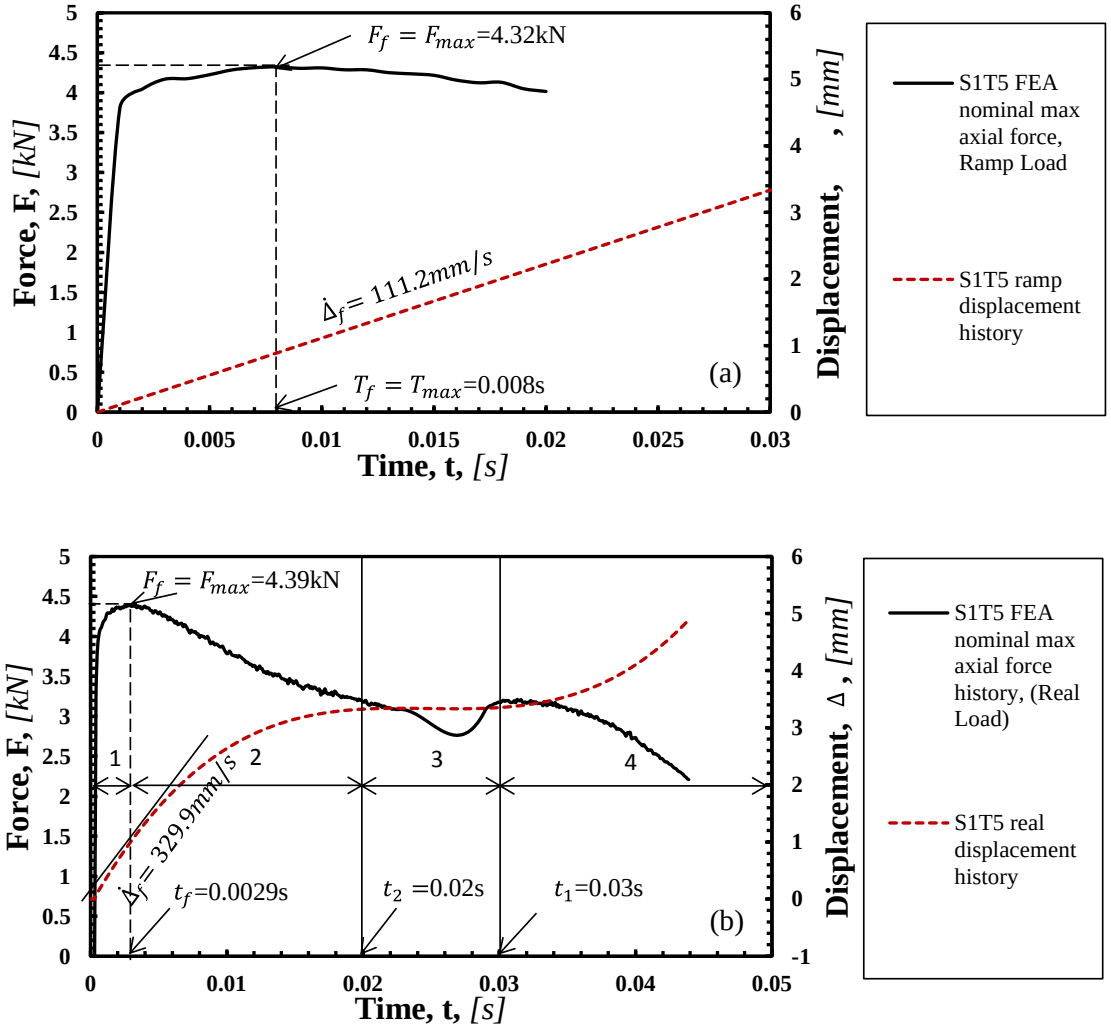

Figure 5.34 S1T5 Force time histories corresponding to (a) ramped displacement history and (b) real displacement load.

For the model of the plain sample S1T5, Figure 5.34 (a) shows the axial force and ramped displacement versus time histories. The failure force obtained in this case was F_f =4.32kN at time t=0.008s with a constant displacement rate of $\dot{\Delta}$=$111.2mm\cdot s^{-1}$ (CPU time: 464 seconds, space: 25.8MB). Moreover, the graphs reported in Figure 5.34 (b) describe the nominal axial force and real displacement against time curves. In detail, the failure force F_f=4.39kN was obtained when time t=0.0029s, and the corresponding displacement rate was equal to 329.9 $mm\cdot s^{-1}$ (CPU time: 82 seconds, space: 7.98MB). It can also be observed from this figure that, at time zone 3, the nominal axial force decreases sharply at time t=0.023s and

increases again at time t=0.028s. This behaviour can be attributed to the fact that the displacement stays constant at time zone 3, which results in a 0 strain rate. Hence, during this period, only strain influences the material behaviour, the displacement rate does not influence the strength as the strain rate temporarily becomes 0 during this time period. Once the displacement starts to increase after time t=0.028s (time zone 4), the hardening from the strain rate will be re-engaged, therefore the nominal axial force F starts to increase again. During this time, both the strain and strain rate influence the material behaviour.

By post-processing the element stresses at the same position in the models of other plain samples (S1T6, S1T7, S1T8, S1T11 and S1T12), the axial force and displacement versus time histories were obtained and are reported in Appendix from Figures A5.1 to A5.5, and the failure forces were computed and are tabulated in Table 5.6.

The log-log graphs reported in Figure 5.35 show the axial failure force, F_f, versus displacement rate, $\dot{\Delta}$, curves obtained by applying both the ramped and real load histories. In particular, the red solid squares refer to the nominal axial failure force for each plain sample calculated by applying the simplified ramped displacement history, whilst, the green markers refer to the nominal axial failure force when the real displacement history was employed to run the simulations. The graphs in this figure make it evident that the results obtained from the numerical simulations when applying the simplified ramped displacement time histories are very close to the ones obtained when applying real displacement time histories.

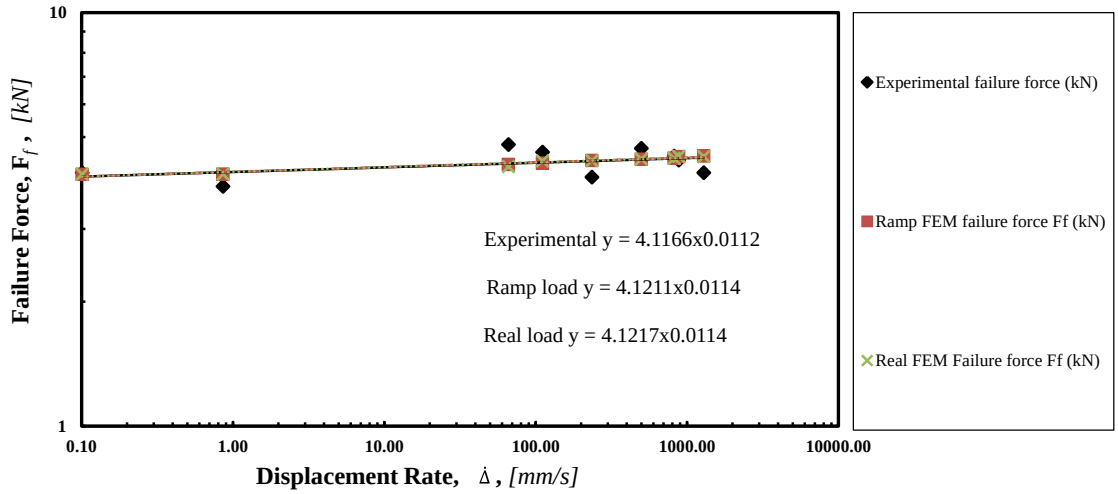

Figure 5. 35 Failure force vs displacement rate for plain samples subjected to ramped and real displacement loads.

Table 5.6 Values of failure force, failure time and corresponding failure displacement generated from FE models for plain samples.

Code	Failure force, F_f [kN]		Failure time, T_f, [s]		Displacement rate at failure time, $\dot{\Delta}_f$, $[mm \cdot s^{-1}]$	
	Ramp displacement history	Real displacement history	Ramp displacement history	Real displacement history	Ramp displacement history	Real displacement history
S1T1	4.07	4.07	1.08000	2.7300	0.86	0.41
S1T2	4.29	4.24	0.01600	0.0320	66.15	33.69
S1T3	4.06	4.07	9.30000	33.700	0.10	0.42
S1T5	4.32	4.39	0.00800	0.0290	111.20	329.90
S1T6	4.39	4.39	0.00530	0.0069	235.20	258.00
S1T7	4.48	4.49	0.01100	0.0030	881.80	1779.20
S1T8	4.45	4.44	0.00140	0.0028	823.20	864.30
S1T11	4.50	4.49	0.00077	0.0017	1290.00	1087.80
S1T12	4.42	4.43	0.00190	0.0040	498.80	452.30

In order to investigate this aspect of the numerical simulations in depth, the local stress and strain rate effects from different loading approaches have also been considered. For example, by applying both ramped and real displacement histories, the local Von Mises stress and effective strain rate data were taken from element 190 and plotted as shown in Figure 5.36. It is important to observe from the graphs and trend line equations that the overall local material strengths generated by applying a ramped displacement history are very similar to the ones generated by applying a real displacement history. It can be seen from this figure also that using the ramped displacement history results in different local strain rates compared to the ones from models applying the real displacement history. This can be attributed to the fact that, according to the Simplified Johnson–Cook constitutive law (Equation 1.32), the flow stress depends on both the effective plastic strain and the effective strain rate (Hallquist, 2007), and as the rate sensitivity factor C=0.02 for this material (Al6063-T5) is very small, which means that the strain effect plays the main role in the material strength. Hence, this level of local strain rate difference will not affect the material strength significantly.

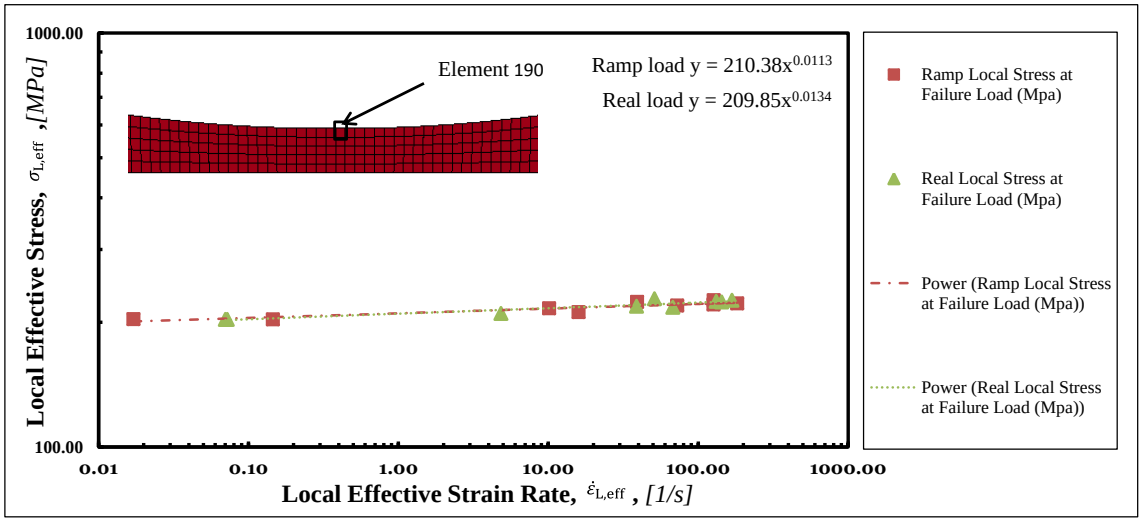

Figure 5.36 Local stress vs local strain rate for plain samples corresponding to the time of failure force under actual and simplified ramped loads.

In detail, the effective strain–displacement rate and the corresponding effective strain rate–displacement rate scatter graphs generated for both ramped and real displacement histories are shown in Figure 5.37 and Figure 5.38, and the results are listed in Table 5.7. These figures and the associated table suggest that the value of the local effective strains obtained from both simplified and real loading conditions are very close to each other, the difference is about $\pm 25\%$, which results in stress difference is less than $\pm 10\%$. For some tests, the local strain rates are slightly different. However, due to the small value of the strain rate coefficient C=0.02, the influence from the loading rate is much less than the influence from strain.

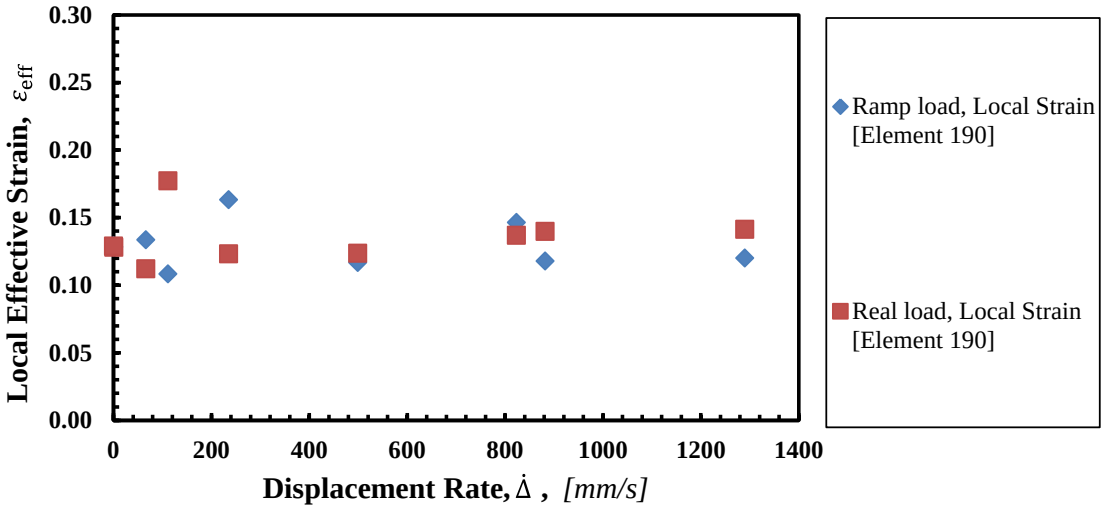

Figure 5.37 Local effective strain vs displacement rate of element 190 from the FE models of plain samples corresponding to the failure time under actual and simplified ramped loads.

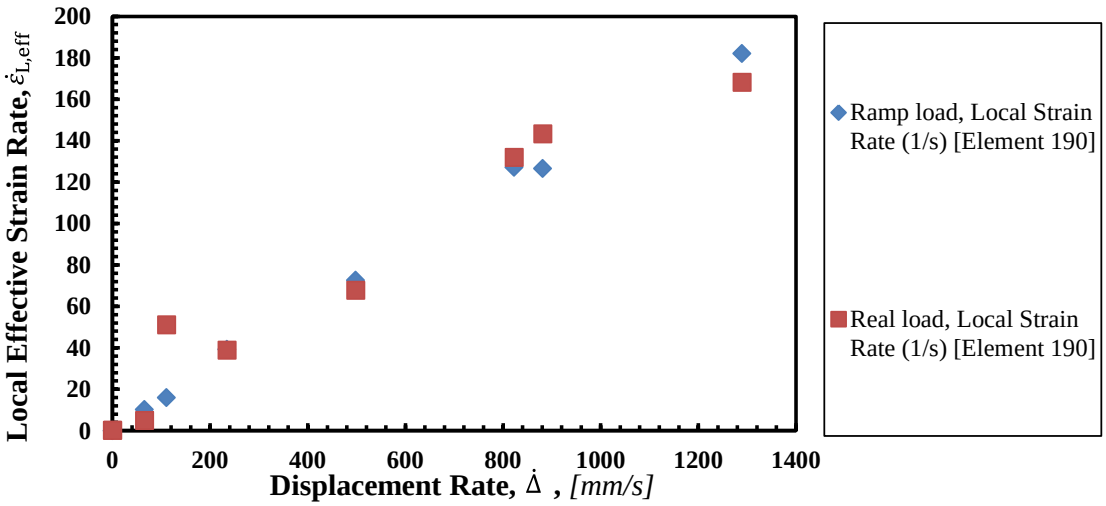

Figure 5.38 Local effective strain rate vs displacement rate for element 190 from the FE models of plain samples corresponding to the failure time under actual and simplified ramped loads.

According to the above considerations, it is possible to conclude that the numerical results calculated using the simplified ramped load histories can be used instead of the data from calculations using the real load history without much loss of accuracy, and applying the ramped load history can make the analysis simpler than the real load history.

Table 5.7 Values of local effective strain and effective strain rate generated at the time of maximum load for element 190 from the FE models of plain samples.

Test	Local Effective Strain, $\varepsilon_{L,eff}$		Local Effective Strain Rate, $\dot{\varepsilon}_{L,eff}$		Stress difference from SJC law [%]
	Ramped Load	Real Load	Ramp Load	Real Load	
S1 T1	0.13	0.13	0.15	0.07	1.61
S1 T2	0.13	0.11	10.15	4.83	4.11
S1 T3	0.13	0.13	0.02	0.07	-2.65
S1 T5	0.11	0.18	15.92	51.06	-9.61
S1 T6	0.16	0.12	39.20	38.77	4.74
S1 T7	0.12	0.14	126.48	143.20	-2.63
S1 T8	0.15	0.14	127.03	131.91	4.05
S1 T11	0.12	0.14	182.00	168.15	-2.27
S1 T12	0.12	0.12	72.54	67.76	0.13

5.5.2 Von Mises stress distributions for notched samples including crack damage

Before considering in depth the models of the notched specimens, it is important to determine the failure effective plastic strain from models of the notched samples with a failure criterion. Hence, an assumption is made here that, at the incipient failure condition, the average effective plastic strain of the elements at the minimum cross section from the models of plain samples, as shown inside the black box of Figure 5.39, is assumed as the failure effective plastic strain, $\varepsilon_{f,eps}$ (the PSFAIL value in the Simplified Johnson–Cook model) for the models of notched samples. The values of the effective plastic strain from the models of plain samples are tabulated in Table 5.8. The average value of $\varepsilon_{f,eps}$ is 0.1348, as shown in Table 5.8.

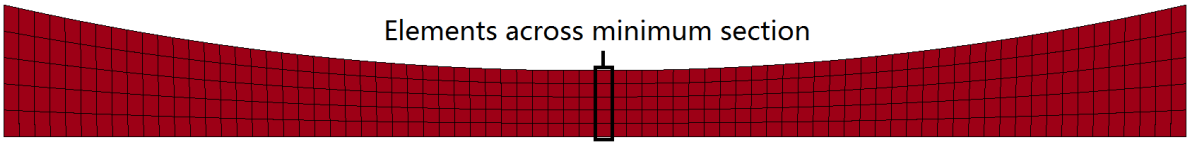

Figure 5.39 Elements along the minimum cross section of the models of plain samples.

Table 5.8 Failure effective plastic strain obtained from the plain models.

Test	Failure effective plastic strain, $\varepsilon_{f,eps}$
S1T1	0.1358
S1T2	0.1392
S1T3	0.1368
S1T5	0.1119
S1T6	0.1714
S1T7	0.1216
S1T8	0.1526
S1T11	0.1233
S1T12	0.1206
Average	0.1348

In order to better understand the elasto-plastic stress distribution in the vicinity of the notch tip at the time of crack initiation, the average effective plastic strain obtained from the plain samples was taken as the failure effective plastic strain for the models of notched samples (value of PSFAIL is taken equal to 0.1348), and the nominal axial force at the time of crack initiation was taken as the failure force. To simulate cylindrical samples of Al6063-T5 subjected to a wide range of loading rates (in the form of displacement rates from $0.001 mm \cdot s^{-1}$ to $1000\ mm \cdot s^{-1}$ as shown in Figure 5.40), the displacement time history was applied at one end

of the model, whilst, on the other end, all directions were fixed (as shown in Figure 5.41). By using the commercial software LS-PrePost 4.1, the Von Mises stress–distance curves in the vicinity of the stress raisers at the incipient failure condition were generated, as reported in the charts of Figure 5.42, to show the effect of the geometrical features (3 different sizes of notch).

Specifically, the charts reported in Figure 5.42 show the Von Mises stress–distance curves generated from the models for three different notch sizes at the time of crack initiation from models subjected to displacement rates ranging from $\dot{\Delta}= 0.001mm \cdot s^{-1}$ to $1000mm \cdot s^{-1}$. It can be seen from the graphs shown in this figure that the Von Mises stress increases as the displacement rate increases.

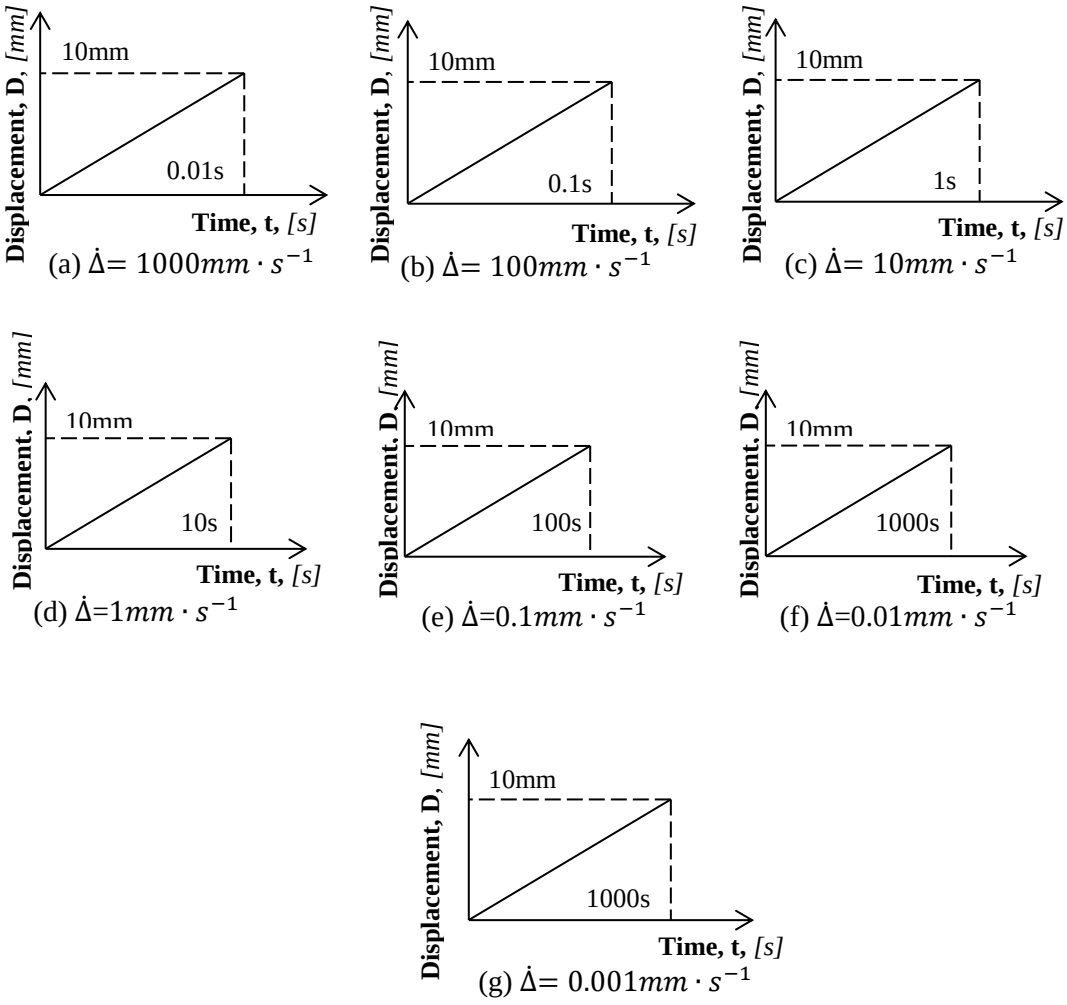

Figure 5.40 Displacement time histories with different displacement rates: (a) $\dot{\Delta}= 1000mms^{-1}$; (b) $\dot{\Delta}= 100mms^{-1}$; (c) $\dot{\Delta}= 10mms^{-1}$; (d) $\dot{\Delta}= 1mms^{-1}$; (e)$\dot{\Delta}= 0.1mms^{-1}$; (f) $\dot{\Delta}= 00.1mms^{-1}$; (g) $\dot{\Delta}= 0.001mms^{-1}$

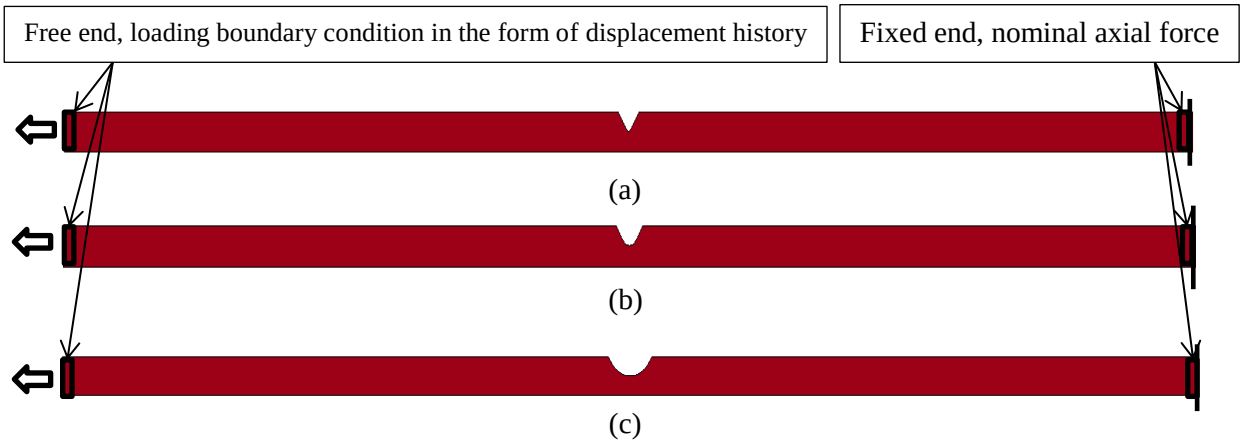

Figure 5.41 FE models for notched samples: (a) model of sharply notched sample; (b) model of intermediately notched sample; (c) model of bluntly notched sample.

For models of sharply and intermediately notched samples (Figure 5.42 (a) and (b)), the maximum Von Mises stresses are located at the notch tip $(\mathrm{d} = 0)$. The Von Mises stress becomes lower as the distance increases away from the notch tip. However, for the Von Mises stress field of the bluntly notched sample (Figure 5.42 (c)), the maximum Von Mises stress is located at the centre of the cross section (d=2.5mm), and the stress slightly increases away from the notch tip. This difference can be attributed to the fact that, in terms of the highly stress concentration for sharply and intermediately notched samples, the value of strain at notch tip increases faster than the confinement by the surrounding elastic part. However, for the bluntly notched samples, at the very beginning, the stress at notch tip is bigger than the centre part, after the plastic deformation happened, the confinement effect from elastic part plays important role in stress distribution, after a certain point, the plastic strain at notch tip is less than the strain in centre part, this results in a higher stress in the centre than notch tip for bluntly notched sample.

Moreover, it can also be observed from these graphs that, when the applied displacement rate is lower that $1mm \cdot s^{-1}$, the influence of the displacement rate is negligible, and the Von Mises stress curves overlap when the displacement rate is between $1mm \cdot s^{-1}$ and $0.001mm \cdot s^{-1}$.

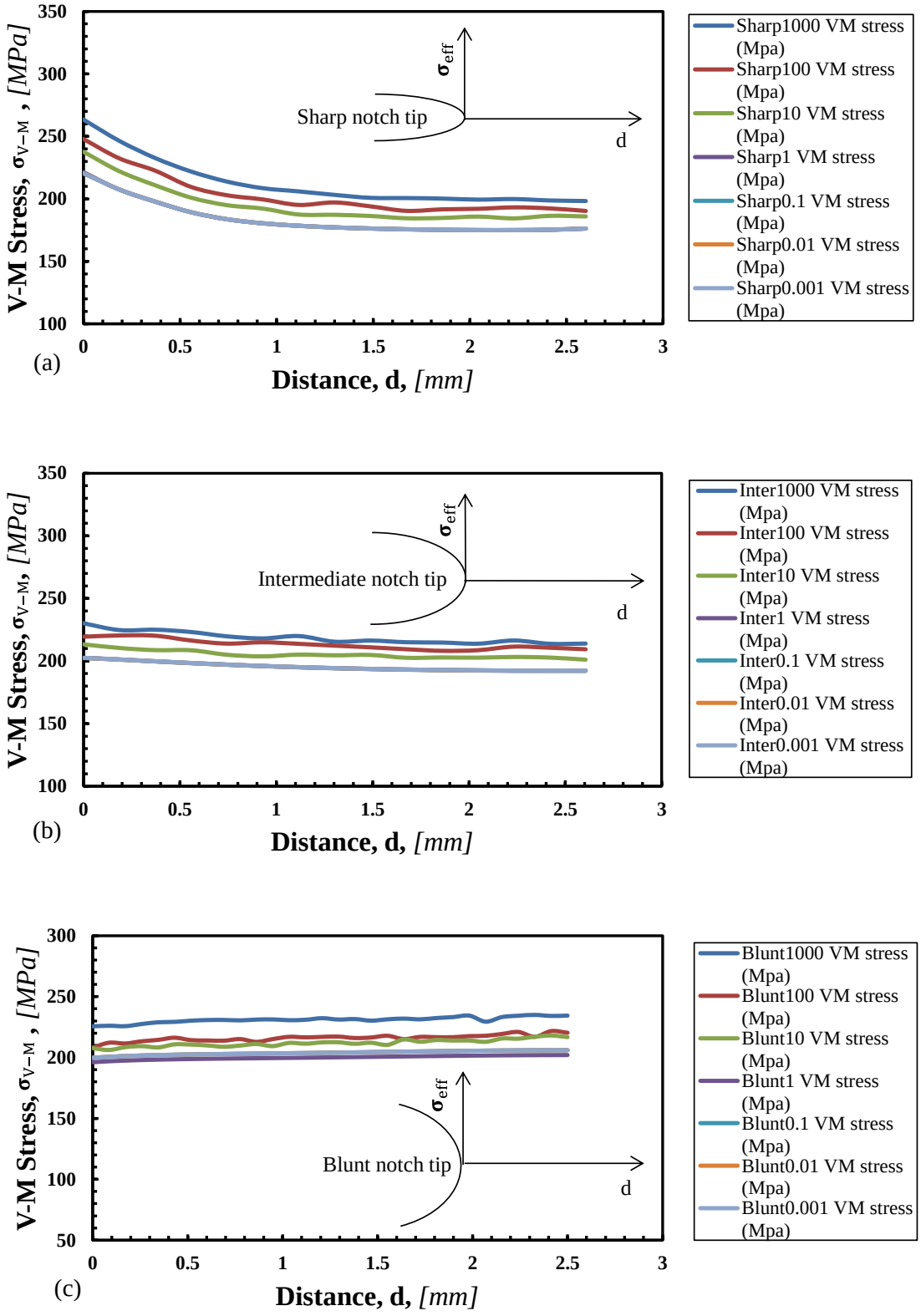

Figure 5.42 Von-Mises stress distribution for a cross section remote from the notch at the time of crack initiation over a wide range of displacement rates (from $0.001mm \cdot s^{-1}$ to $1000mm \cdot s^{-1}$), (a) sharp notch; (b) intermediate notch; (c) blunt notch.

5.5.3 Von-Mises stress distribution of notched samples ignoring crack behaviour

In order to better understand the elasto-plastic stress distribution in the vicinity of the notch tip at the time corresponding to the maximum axial force, the failure effective plastic strain was ignored (the value of PSFAIL was taken as equal to 0) during the simulations, and the maximum axial force was calculated to be the failure force. By simulating cylindrical samples of Al6063-T5 over a wide range of loading rates (displacement rates from $0.001mm \cdot s^{-1}$ to $1000mm \cdot s^{-1}$), the Von Mises stress–distance curves in the vicinity of the stress raisers at the incipient failure condition were generated and are reported in the chart of Figure 5.43. It can be highlighted here that similar Von Mises stress distributions were observed to the ones generated from the models which include a fracture criterion.

If we compare the Von Mises stress fields generated from the models with cracking behaviour with the ones without cracking, we can draw the conclusion that, at the incipient failure condition, the Von-Mises stress fields for the models which ignore crack damage provide similar stress fields as the ones obtained from the models including crack damage.

To conclude, this chapter has discussed the mesh convergence analysis of the LS-DYNA models and the stress distribution around notch tip when material components subjected to dynamic load. In the next chapter, by using these stress distribution, an attempt is made to check whether it is possible to use the TCD by post-processing the elasto-plastic stress fields to assess notched ductile materials subjected to high rates of loading.

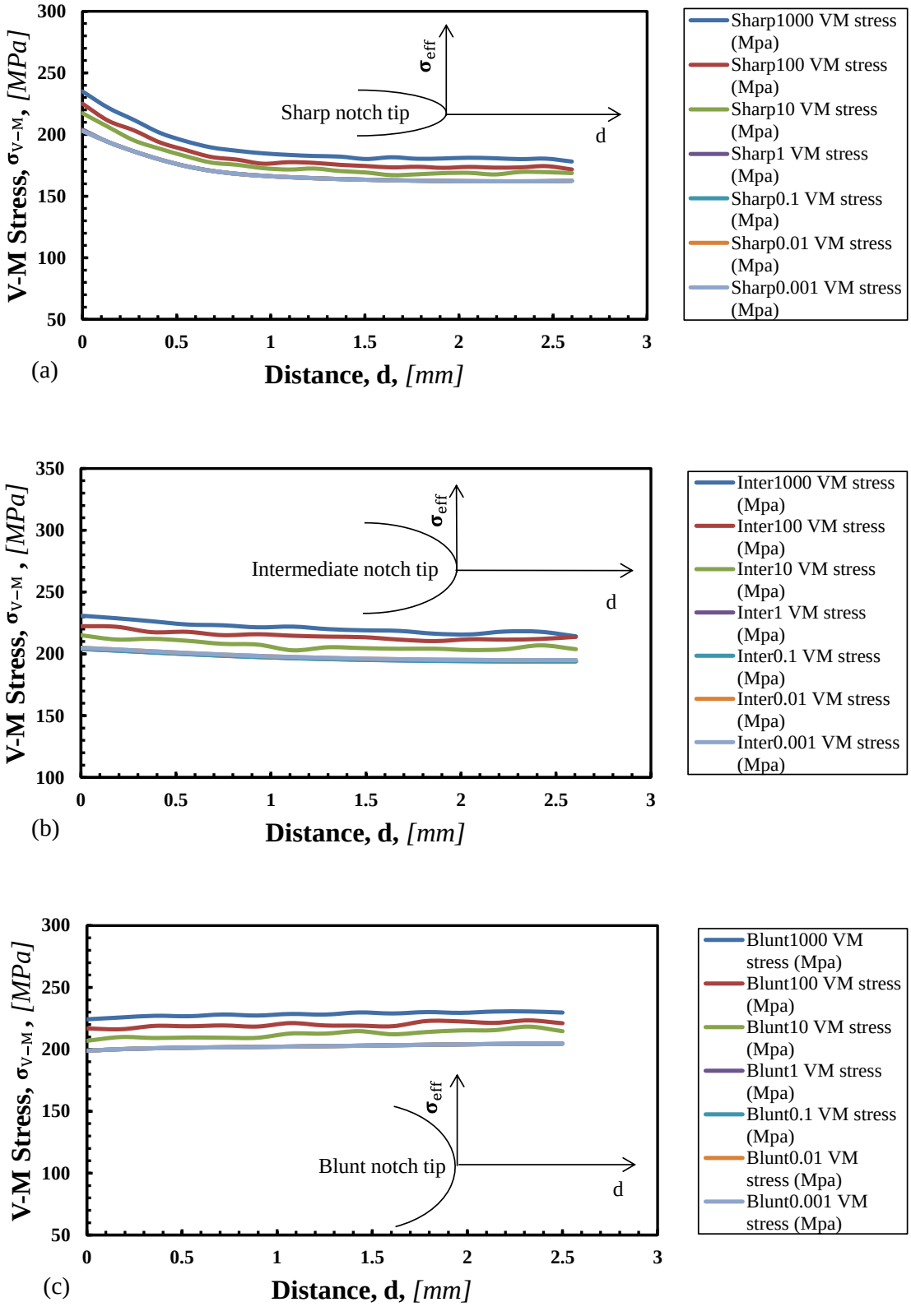

Figure 5. 43 Von-Mises stress distributions for a cross section remote from the notch at the time of maximum axial force for a wide range of displacement rates (from $0.001\text{mm} \cdot \text{s}^{-1}$ to $1000001\text{mm} \cdot \text{s}^{-1}$) for (a) a sharp notch; (b) an intermediate notch; and (c) a blunt notch.

Table 5. 9 Values of V-M stress at notch tip under a wide range of loading rate

Code	**V-M stress at notch tip, no crack** *[MPa]*	**V-M stress at notch tip, crack,** *[MPa]*
Sharp1000	198.29	178.07
Sharp100	190.34	171.64
Sharp10	185.95	168.66
Sharp1	176.23	162.10
Sharp0.1	176.30	162.48
Sharp0.01	176.31	162.47
Sharp0.001	176.31	162.47
Inter1000	213.93	214.18
Inter100	209.41	213.72
Inter10	201.09	203.75
Inter1	192.34	193.98
Inter0.1	192.21	193.83
Inter0.01	192.23	194.93
Inter0.001	192.33	194.94
Blunt1000	234.41	229.83
Blunt100	220.31	221.06
Blunt10	216.73	214.65
Blunt1	202.01	204.63
Blunt0.1	205.99	204.63
Blunt0.01	206.00	204.63
Blunt0.001	205.99	204.63

References

AKIMA, H. 1970. A new method of interpolation and smooth curve fitting based on local procedures. *Journal of the ACM (JACM)*, 17, 589-602.

BARSOUM, I., KHAN, F., MOLKI, A. & SEIBI, A. 2014. Modeling of ductile crack propagation in expanded thin-walled 6063-T5 aluminum tubes. *International Journal of Mechanical Sciences*, 80, 160-168.

DIETENBERGER, M., BUYUK, M. & KAN, C. 2005. Development of a high strain-rate dependent vehicle model. *National crash analysis center Virginia, Bamberg*.

DYE, J. L. & NICELY, V. A. 1971. A general purpose curve fitting program for class and research use. *Journal of chemical Education*, 48, 443.

FANG, L. & GOSSARD, D. C. 1995. Multidimensional curve fitting to unorganized data points by nonlinear minimization. *Computer-Aided Design*, 27, 48-58.

HALLQUIST, J. O. 2006. LS-DYNA theory manual. *Livermore software Technology corporation*, 3.

HALLQUIST, J. O. 2007. LS-DYNA keyword user's manual. *Livermore Software Technology Corporation*, 970.

HALLQUIST, J. O. & MANUAL, L.-D. T. 1998. Livermore Software Technology Corporation. *Livermore, Ca*.

JIADE, T. 2008. Nonlinear curve fitting based on MATLAB. *Comput. Modern*, 154, 15-19.

LEVY, E. 1959. Complex-curve fitting. *Automatic Control, IRE Transactions on*, 37-43.

LIU, Y. 2013. CHOOSE THE BEST ELEMENT SIZE TO YIELD ACCURATE FEA RESULTS

WHILE REDUCE FE MODE'S COMPLEXITY. *British Journal of Engineering and Technology*, 1, 13-28.

MADDAMS, W. 1980. The scope and limitations of curve fitting. *Applied Spectroscopy*, 34, 245-267.

MOTULSKY, H. & CHRISTOPOULOS, A. 2004. *Fitting models to biological data using linear and nonlinear regression: a practical guide to curve fitting*, OUP USA.

QIAO, J. & WANG, W. 2011. *Inhomogeneous Material Modeling and Characterization for Aluminium Alloys and Welded Joints*, INTECH Open Access Publisher.

TORRES-FRANCO, D., URRIOLAGOITIA-SOSA, G., URRIOLAGOITIA-CALDERON, G. M., HERNANDEZ-GOMEZ, L. H., MOLINA-BALLINAS, A., TORRES-TORRES, C. & ANGELES, B. R. Pure bending determination of stress-strain curves for an Aluminum alloy. World Congress on Engineering 2011, WCE 2011, 2011.

VARAS, D., ZAERA, R. & LÓPEZ-PUENTE, J. 2012. Numerical modelling of partially filled aircraft fuel tanks submitted to Hydrodynamic Ram. *Aerospace Science and technology,* 16, 19-28.

Chapter 6 Using Elasto-Plastic FE Simulations to Estimate the Dynamic Strength of Notched Metals

6.1 Introduction

In this chapter, the results calculated from elasto-plastic FE models will be compared with the experimental failure forces of the notched samples of Al6063-T5. Subsequently, an assumption will also be made here that the TCD is successful at assessing the dynamic strength of notched Al6063-T5 by post-processing the elasto-plastic stress fields in the incipient failure condition.

6.2 Results from LS-DYNA elasto-plastic models with crack initiation

6.2.1 Results generated by employing a ramped displacement history

By applying the average effective plastic strain, $\varepsilon_{f,eps}$=0.1348 obtained in Chapter 5 as the failure effective plastic strain, the models of all of the tested notched samples were solved to consider crack initiation. At the very beginning, the assumption was made that the nominal axial force at the time of crack initiation would be taken as the failure force F_f. The nominal axial forces for all of the tested samples were determined by post-processing the element stress at the fixed end of the samples (Figure 5.41). Figures 6.1 to 6.17 show plots of the generated nominal axial forces for all of the notched samples and the corresponding displacement time histories which were applied.

In more detail, a ramped displacement time history was applied to these models as the loading boundary condition. The graphs reported in Figures 6.1 to 6.4 describe the nominal axial force versus time histories for the models of sharply notched samples subjected to both quasi-static and dynamic conditions. For example, Figure 6.1 shows the nominal axial force history and the applied ramp displacement history of sample S1T9 which was tested under quasi-static conditions. At the time of crack initiation, T_f=6.41s, the nominal axial force $F = 6.66kN$ was taken to be equal to the failure force F_f. The graphs reported in the Figures from 6.2 to 6.4 describe the dynamic behaviour of notched samples S1T10, S2T1 and S2T2 respectively.

The nominal axial force time histories generated from the models of the intermediately notched samples are reported in Figures 6.5 to 6.15. In particular, in terms of the samples tested under quasi-static conditions (sample codes: S1T17, S2T5, S2T6, S2T11 and S2T12), the nominal axial force time histories were calculated and are shown in the graphs reported in Figures 6.5, 6.7, 6.8, 6.12 and 6.13 respectively. It can be seen from these figures that the nominal axial force increases smoothly as the time t increases. Moreover, Figures 6.6, 6.9, 6.10, 6.11, 6.14 and 6.15 describe the nominal axial force time histories of the samples subjected to dynamic loading.

Similar to the plots for the sharply notched samples under dynamic loading, oscillations can be observed in the nominal axial force time history graphs for the models of intermediately notched samples under dynamic conditions. This phenomenon can be attributed to the fact that the loading wave was passing through the cylindrical bar during the deformation.

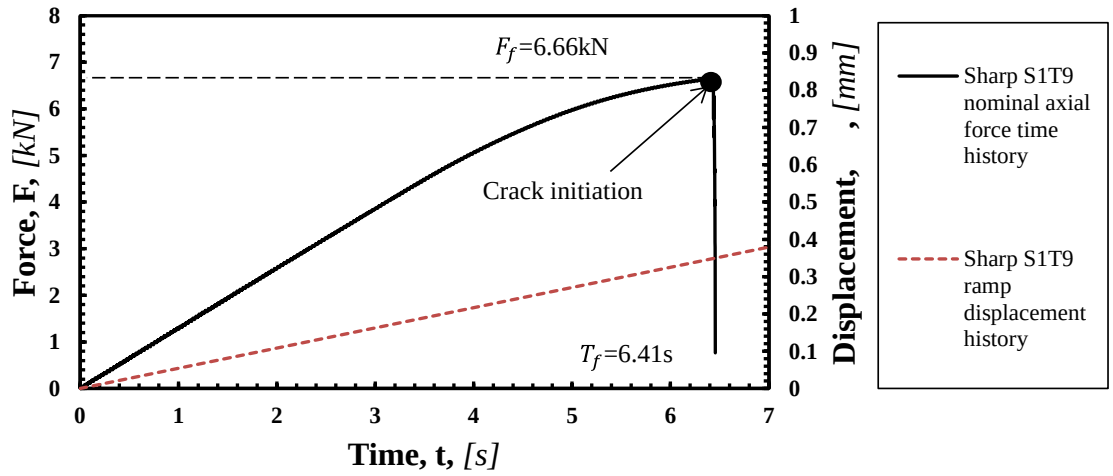

Figure 6.1 Sharply notched sample S1T9 force and ramp displacement time histories generated from the FE model.

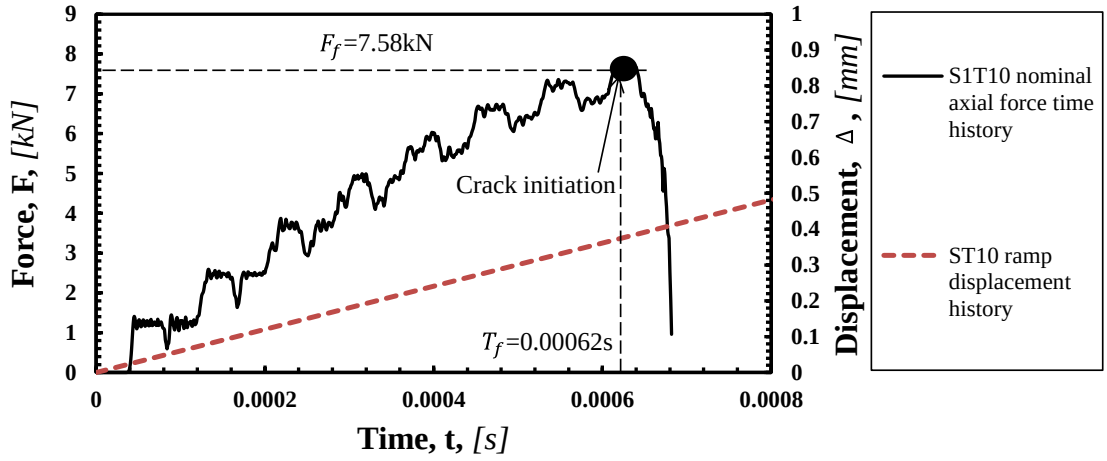

Figure 6.2 Sharply notched sample S1T10 force and ramp displacement time histories generated from the FE model.

As an example, for sample S1T18, the speed of the loading wave as it passed through the cylindrical bar can be calculated as $C_0 = \sqrt{E/\rho} = 5163m \cdot s^{-1}$ (Tyas and Watson, 2000). Hence, the duration of the loading wave transfer from the free end to the fixed end can be computed as $T_1 = L_0/C = 0.2/5163 = 0.000038s$. Once the loading wave reaches the fixed end at time T_1, the stress in the elements at the fixed end starts to increase; thereafter, the

nominal axial force at the fixed end starts to increase. After this point, the loading wave is reflected back to the free end.

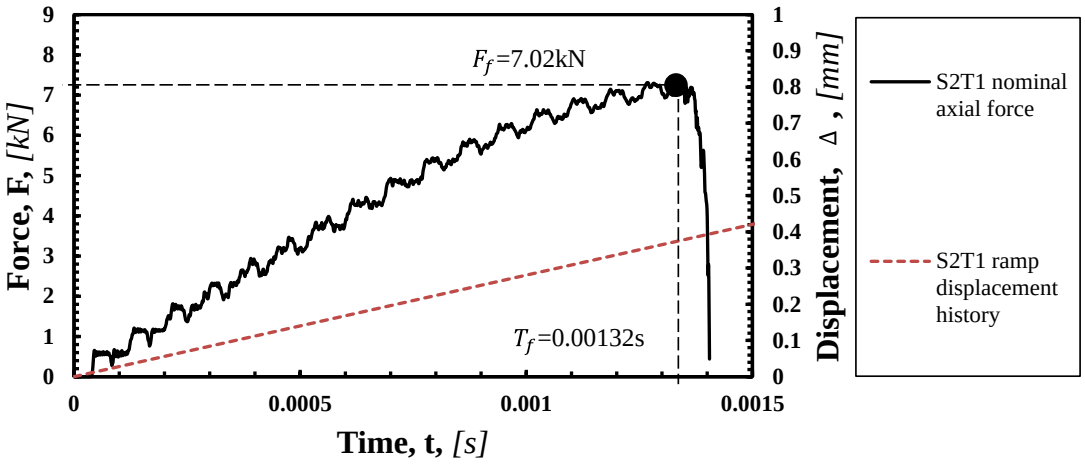

Figure 6.3 Sharply notched sample S2T1 force and ramp displacement time histories generated from the FE model.

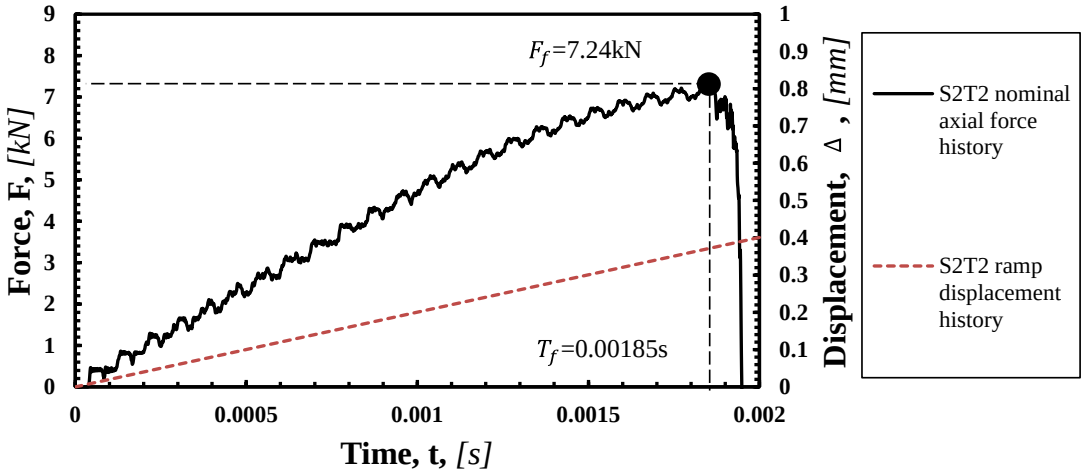

Figure 6.4 Sharply notched sample S2T2 force and ramp displacement time histories generated from the FE model.

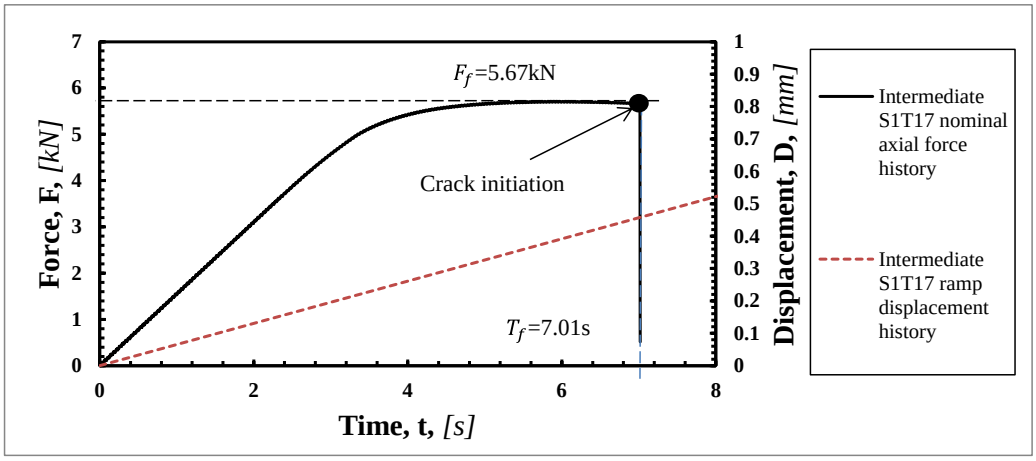

Figure 6.5 Intermediately notched sample S1T17 force and ramp displacement time histories generated from the FE model.

Figures 6.16 and 6.17 show the nominal axial force and applied ramped displacement histories for the models of the bluntly notched samples S1T15 and S1T16 subjected to quasi-static loading. The failure forces for both samples are equal to 4.38kN.

In summary, the failure nominal axial forces generated from the models of all of the notched samples are listed in Table 6.1. By comparing the numerically determined failure forces with the experimental data, the errors were also calculated (according to the Equation 6.1) and are summarised in this table.

$$Error(\%) = \frac{F_{FEM,f} - F_{exp,f}}{F_{exp,f}} * 100 \qquad (6.1)$$

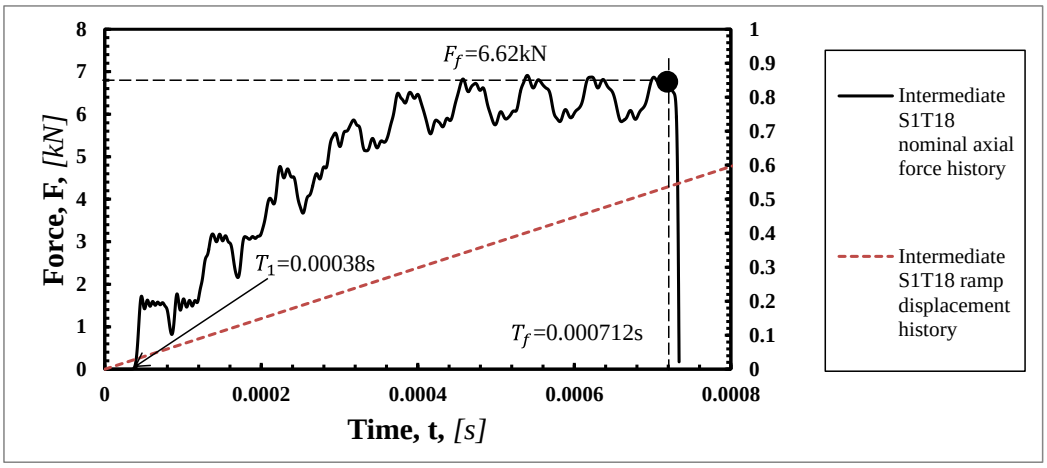

Figure 6.6 Intermediately notched sample S1T18 force and ramp displacement time histories generated from the FE model.

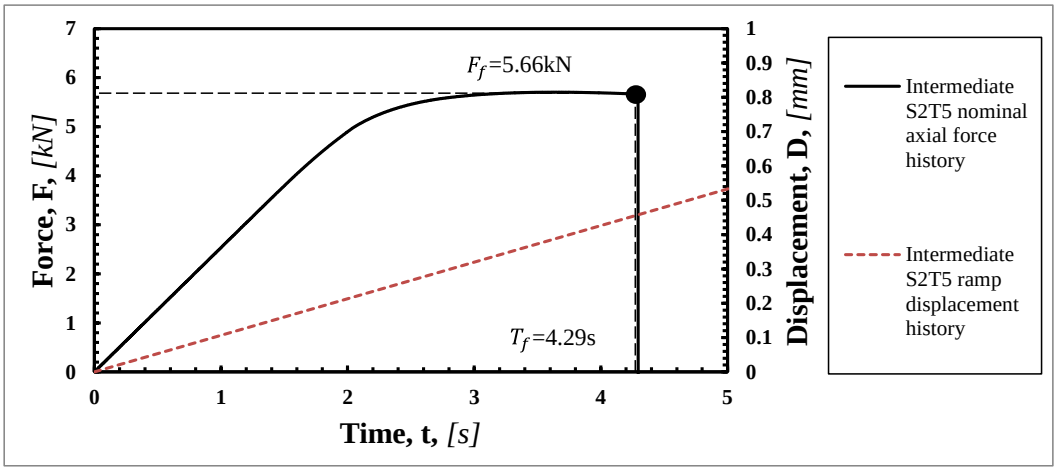

Figure 6.7 Intermediately notched sample S2T5 force and ramp displacement time histories generated from the FE model.

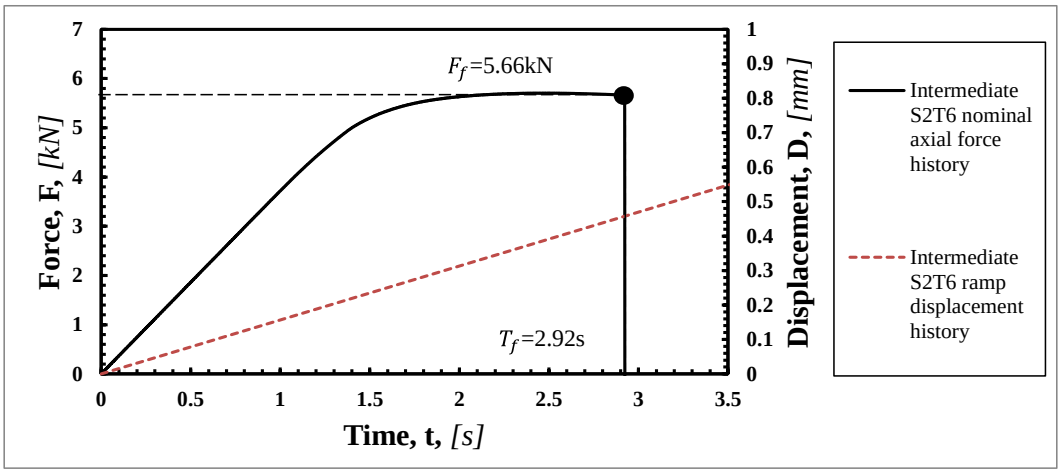

Figure 6.8 Intermediately notched sample S2T6 force and ramp displacement time histories generated from the FE model.

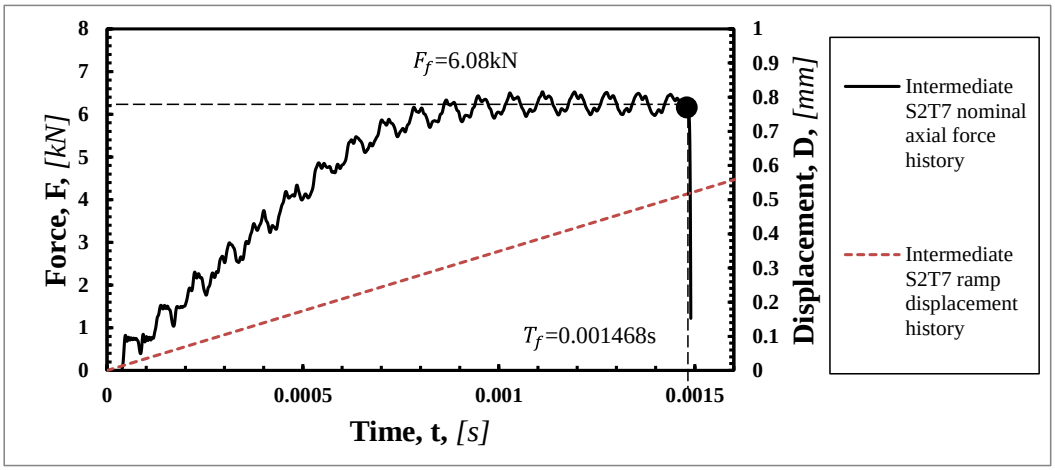

Figure 6.9 Intermediately notched sample S2T7 force and ramp displacement time histories generated from the FE model.

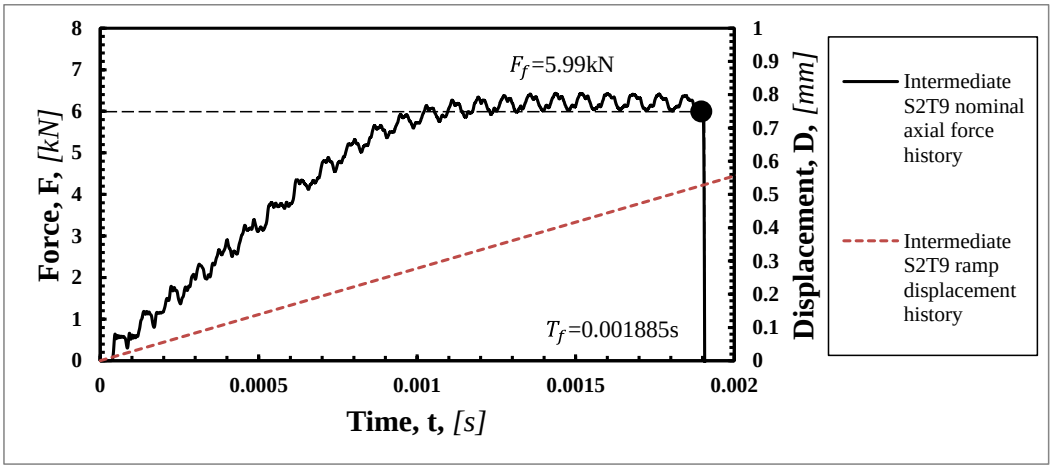

Figure 6.10 Intermediately notched sample S2T9 force and ramp displacement time histories generated from the FE model.

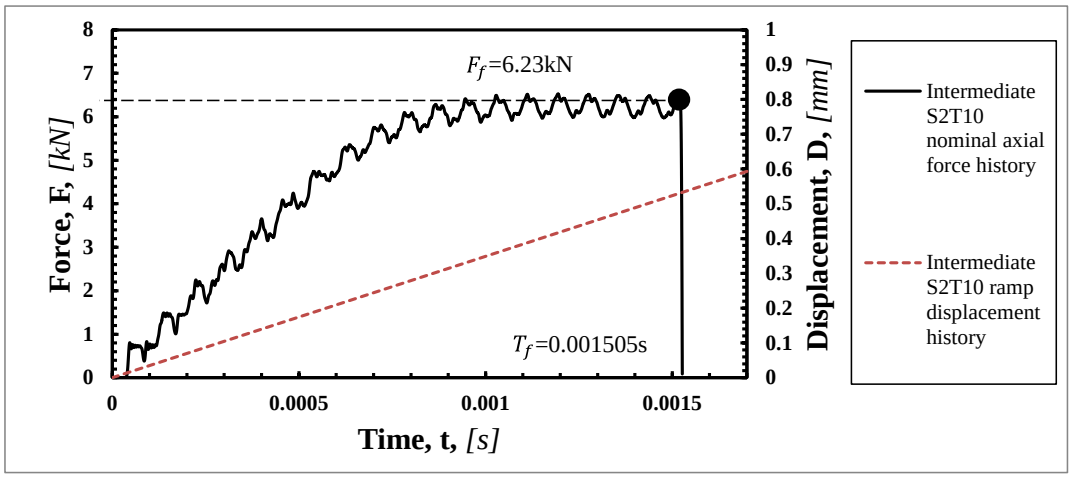

Figure 6.11 Intermediately notched sample S2T10 force and ramp displacement time histories generated from the FE model.

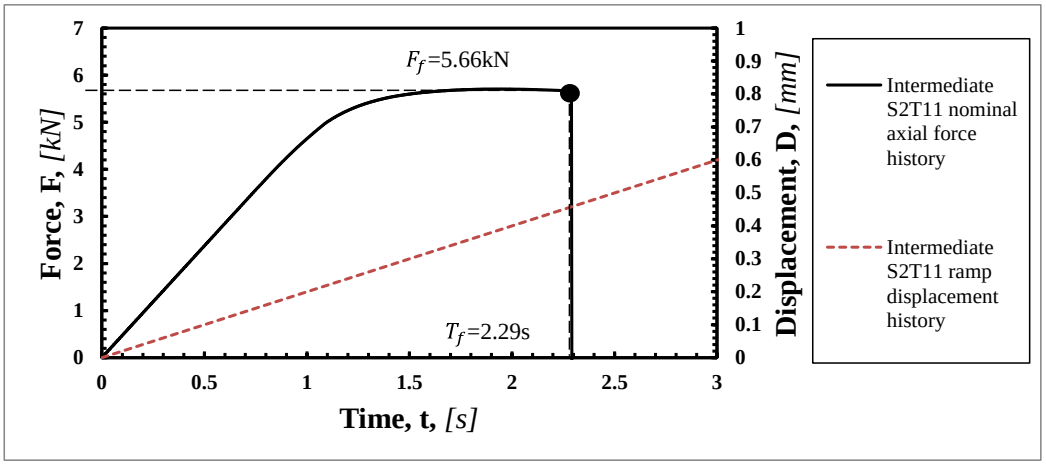

Figure 6.12 Intermediately notched sample S2T11 force and ramp displacement time histories generated from the FE model.

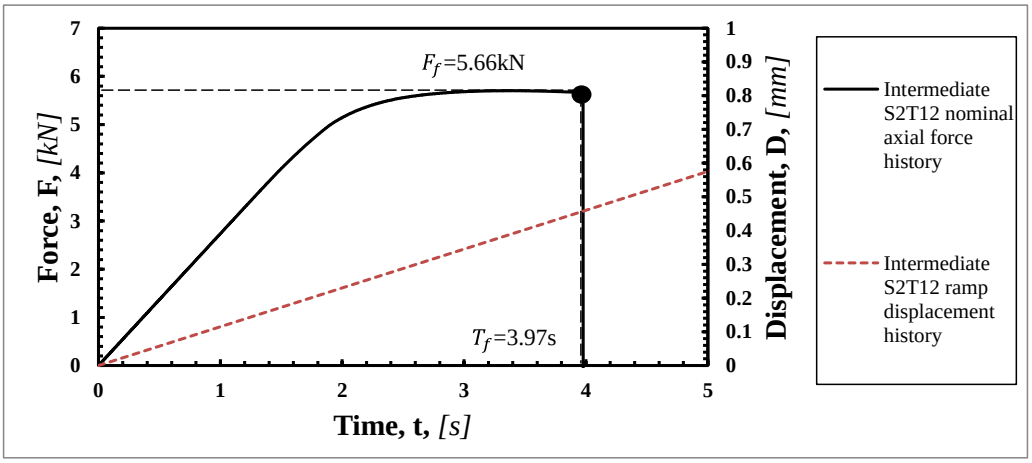

Figure 6.13 Intermediately notched sample S2T12 force and ramp displacement time histories generated from the FE model.

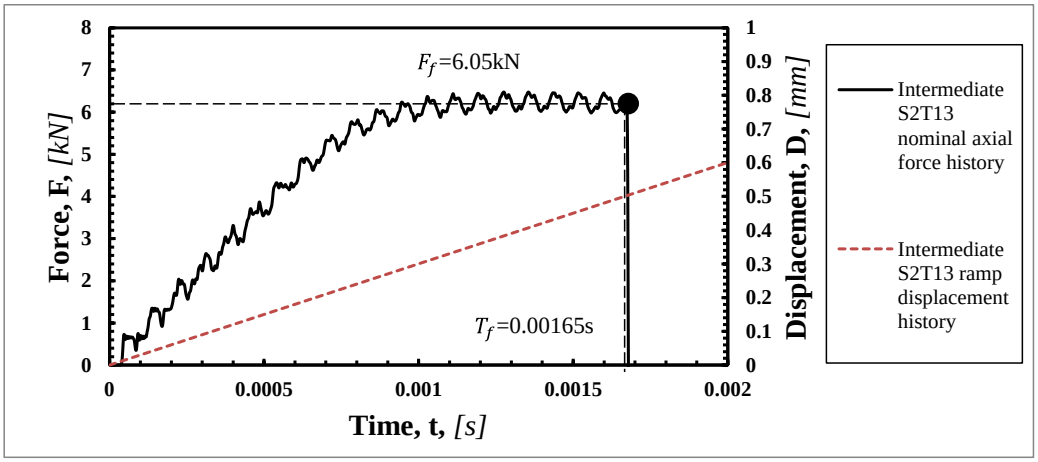

Figure 6.14 Intermediately notched sample S2T13 force and ramp displacement time histories generated from the FE model.

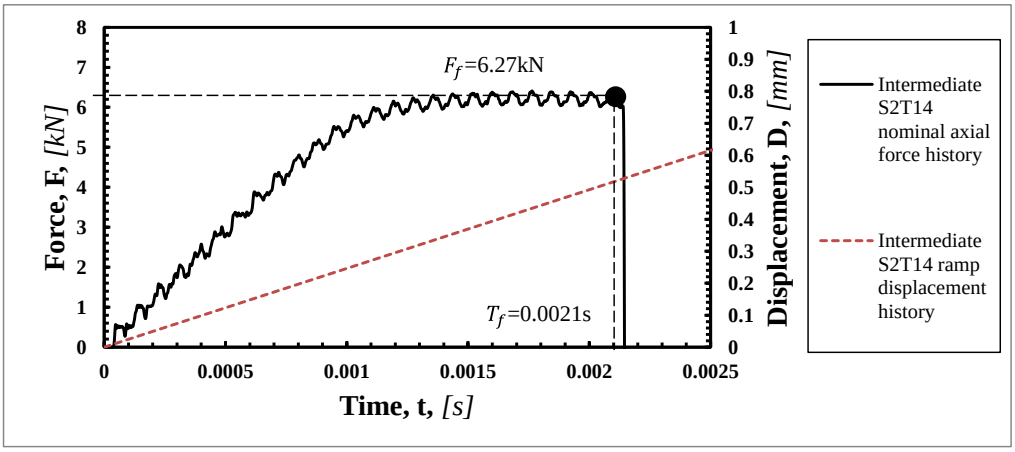

Figure 6.15 Intermediately notched sample S2T14 force and ramp displacement time histories generated from the FE model.

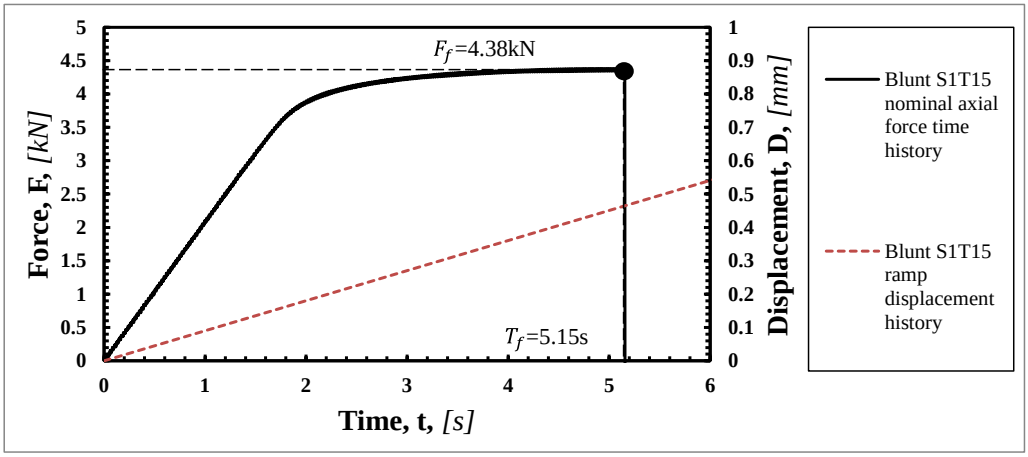

Figure 6.16 Bluntly notched sample S1T15 force and ramp displacement time histories generated from the FE model.

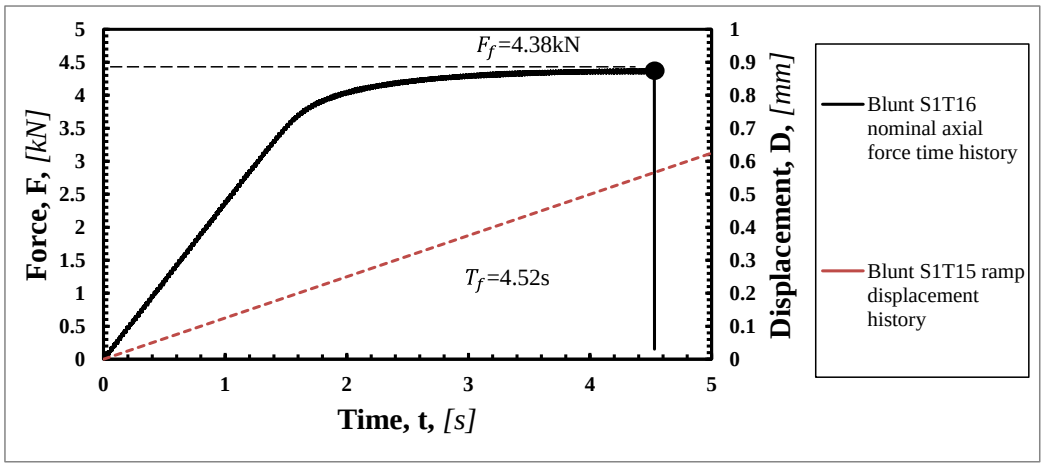

Figure 6.17 Bluntly notched sample S1T16 force and ramp displacement time histories generated from the FE model.

The errors reported in this table make it evident that the elasto-plastic FE models using simplified ramped displacement histories can be used to accurately predict the dynamic strength of samples containing different geometrical features. In the design point of view, the safety factor 1.2 can be used for the design propose.

Table 6.1 Accuracy in predicting the strength of the notched samples by applying ramped displacement histories.

Test	Experimental failure Load, $F_{exp,f}$ *[kN]*	FEM failure load $F_{FEM,f}$ *(kN)*	Error *[%]*
S1T9	5.4	6.66	23.33
S1T10	6.7	7.58	13.13
S2T1	6.8	7.02	3.24
S2T2	6.7	7.30	8.89
S1 T17	4.6	5.67	23.26
S1 T18	6.2	6.62	6.77
S2 T5	5.3	5.66	6.79
S2 T6	5.1	5.66	10.98
S2 T7	6.7	6.08	-9.25
S2 T9	6.2	5.99	-3.39
S2 T10	6.9	6.23	-9.71
S2 T11	4.9	5.65	15.31
S2 T12	5.2	5.67	9.04
S2 T13	6	6.05	0.83
S2 T14	5.9	6.27	6.27
S1 T15	3.7	4.38	18.38
S1 T16	3.5	4.38	25.14

6.2.2 Results generated by employing real displacement histories

Besides the models with simplified ramped displacement histories where crack initiation was taken into account, the real displacement history has also been used to run models for notched samples. The nominal axial force time histories and the applied real displacement histories are plotted in the graphs reported in Figures 6.18 to 6.34.

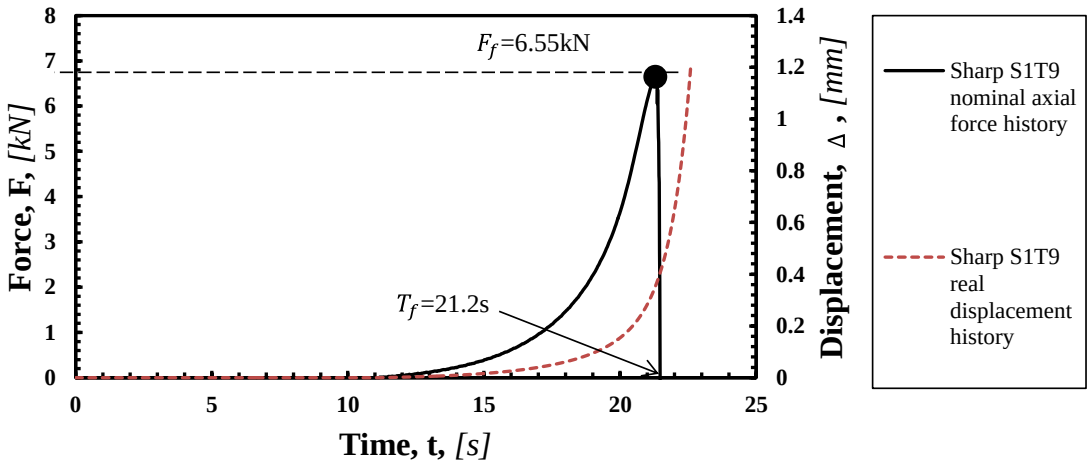

Figure 6.18 Sharply notched sample S1T9 force and real displacement time histories generated from the FE model.

The diagrams reported in Figures 6.18 to 6.21 describe the nominal axial force time histories generated from the FE models of the sharply notched samples under both quasi-static and dynamic real applied displacements. Specifically, the force and the applied real displacement histories calculated from the model of sample S1T9 are shown in the charts of Figure 6.18. The nominal axial force at time t=21.2s (crack initiation), computed from the element stresses at the fixed end, is $F_f = 6.55k$N, which is very close to the failure force ($F_f = 6.66k$N) under the ramped displacement history (Figure 6.1). The graph reported in Figure 6.19 shows the nominal axial force from the model for the sharply notched sample S1T10 under the real dynamic displacement history.

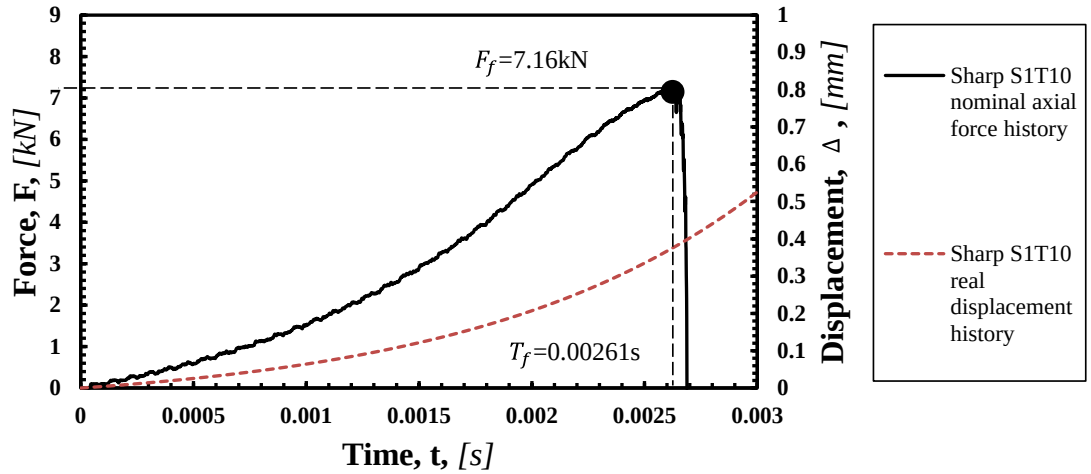

Figure 6.19 Sharply notched sample S1T10 force and real displacement time histories generated from the FE model.

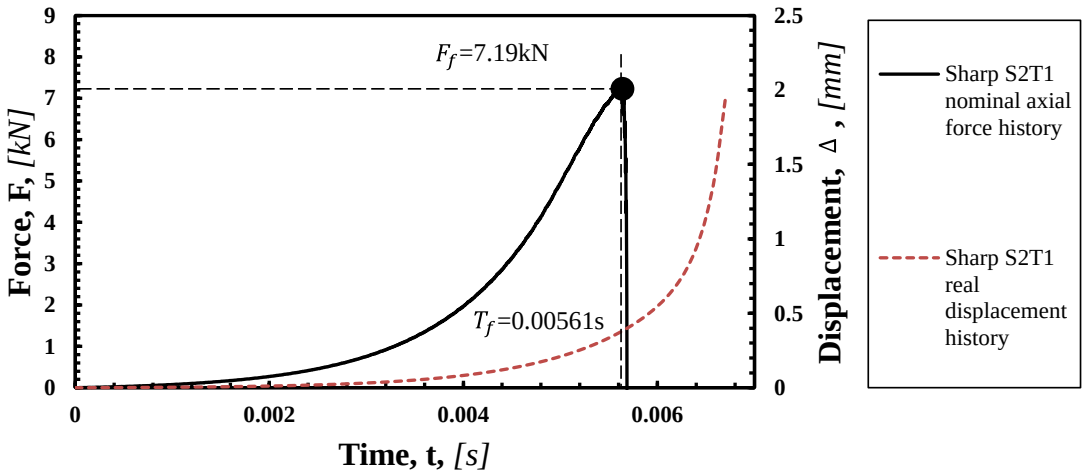

Figure 6.20 Sharply notched sample S2T1 force and real displacement time histories generated from the FE model.

The nominal axial force at the crack initiation time is $F_f = 7.16kN$, which is slightly less than the one under the ramped displacement history. Moreover, by comparing the graph with the one in Figure 6.2, it is clear that the amplitude of the oscillations under the real displacement history is much less that the one under the ramped displacement history. This phenomenon can be attributed to the fact that, for the ramped displacement history, the displacement rate is constant throughout the deformation, therefore the loading rate increases to a constant value suddenly at time 0. However, for the real displacement history, the loading rate increases progressively from 0 at time t=0. Because all of the plastic deformation occurs in the vicinity of the notch tip, the element stress at the fixed end is affected solely by the elastic wave; the particles start to move only when the elastic loading wave travels through them.

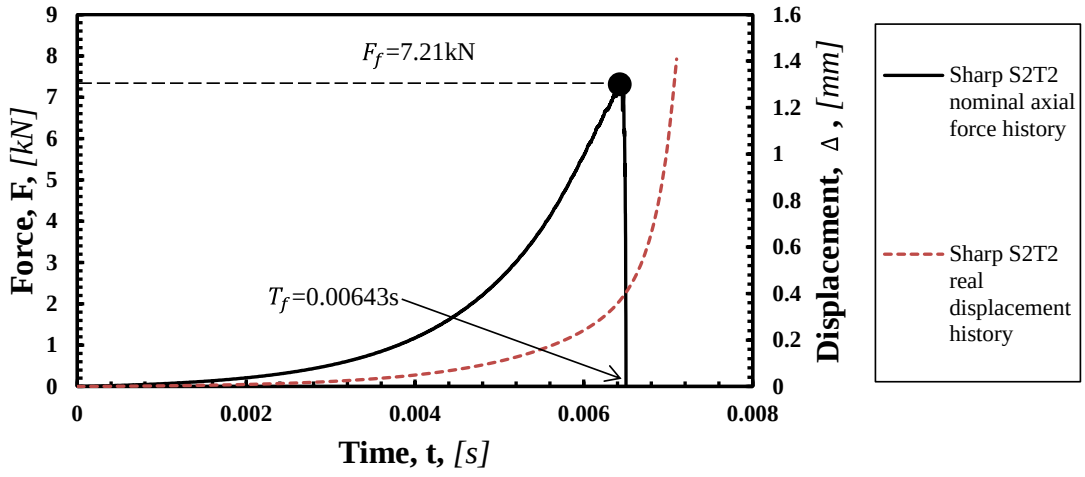

Figure 6.21 Sharply notched sample S2T2 force and real displacement time histories generated from the FE model.

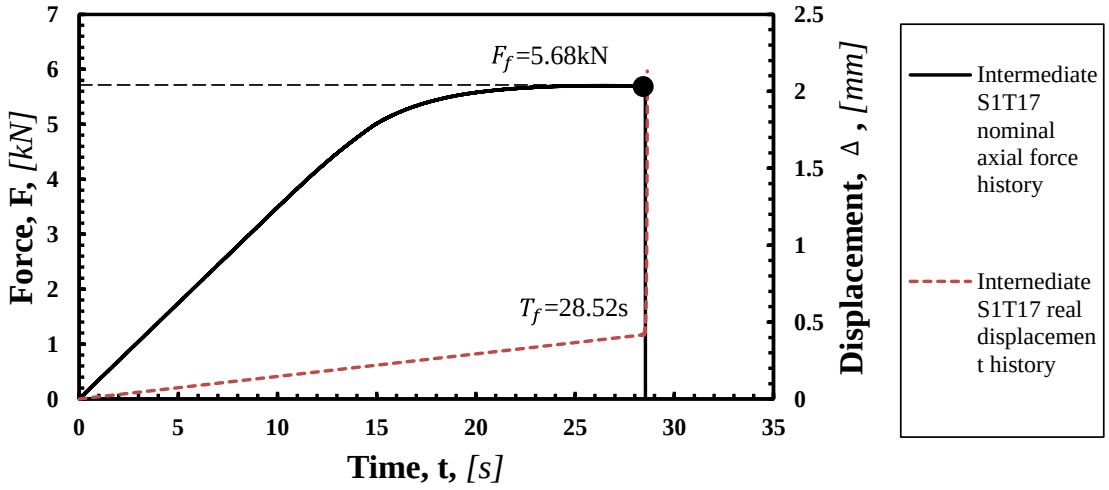

Figure 6.22 Sharply notched sample S1T17 force and real displacement time histories generated from the FE model

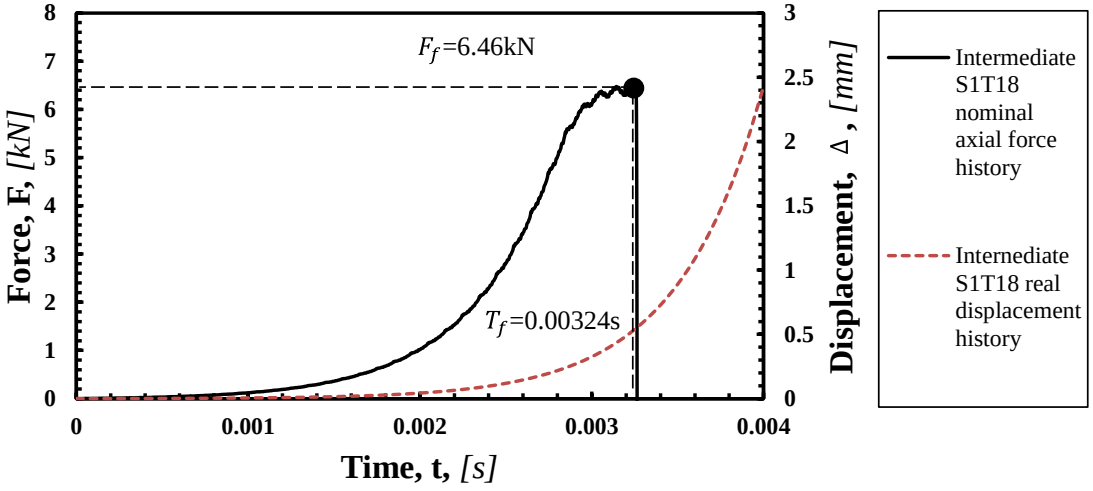

Figure 6.23 Intermediately notched sample S1T18 force and real displacement time histories generated from the FE model.

According to the conservation of momentum relationship, the uniaxial stress can be calculated by using Equation (6.1) (Meyers, 1994):

$$\sigma = \rho C U_p \qquad (6.1)$$

where ρ indicates the material density, C is the elastic wave speed, which is only dependent on the elastic modulus E and material density ρ, the particle velocity U_p is taken as equal to the displacement rate (Meyers, 1994). Hence, a higher increase in displacement rate will cause higher oscillations.

Figures 6.20 and 6.21 show the nominal axial force histories and corresponding applied real displacement histories for notched samples S2T1 and S2T2. The nominal axial forces at the time of crack initiation are 7.19kN and 7.21kN.

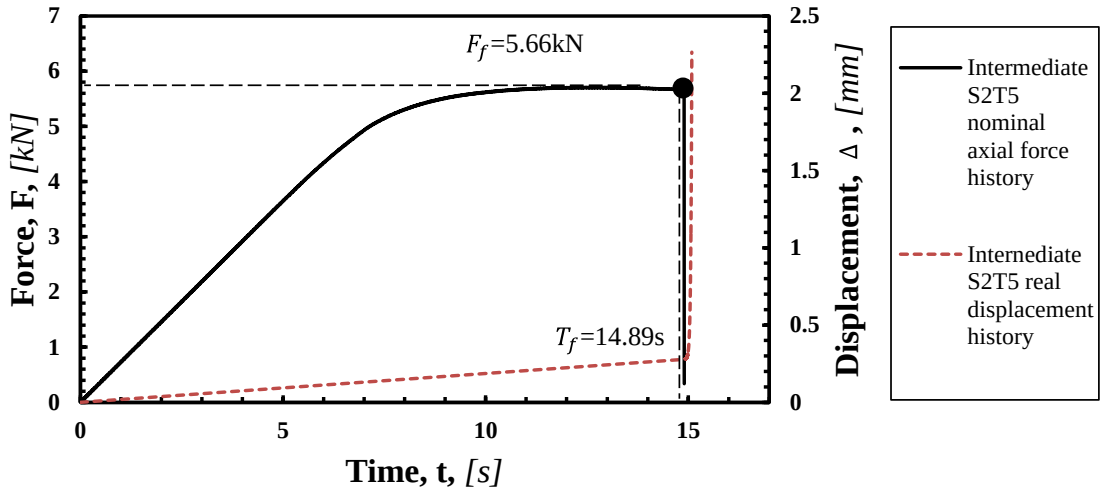

Figure 6.24 Intermediately notched sample S2T5 force and real displacement time histories generated from the FE model.

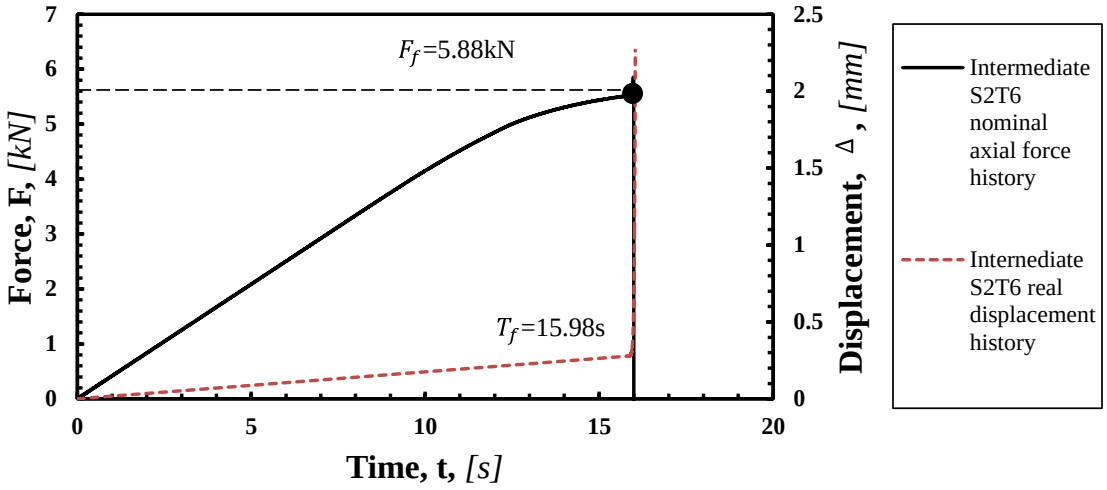

Figure 6.25 Intermediately notched sample S2T6 force and real displacement time histories generated from the FE model.

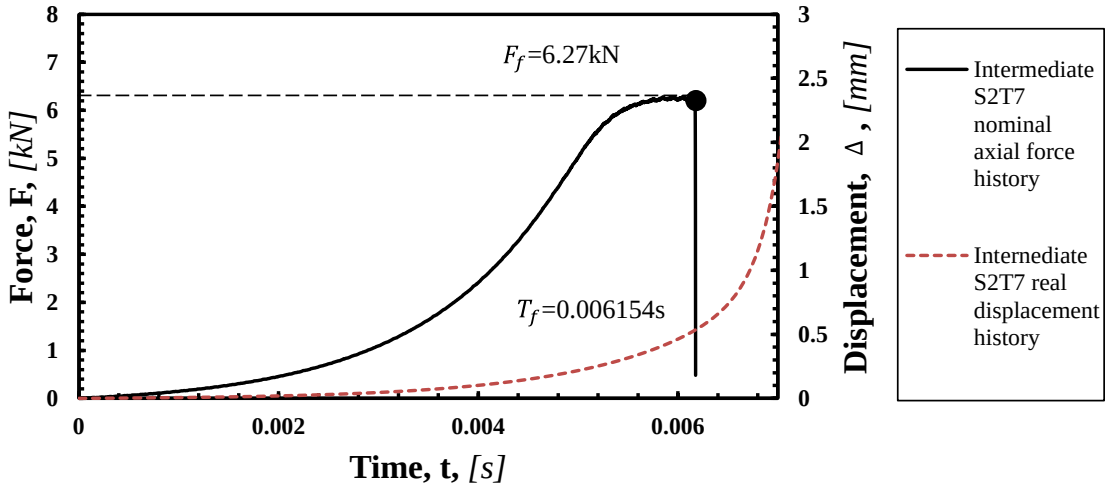

Figure 6.26 Intermediately notched sample S2T7 force and real displacement time histories generated from the FE model.

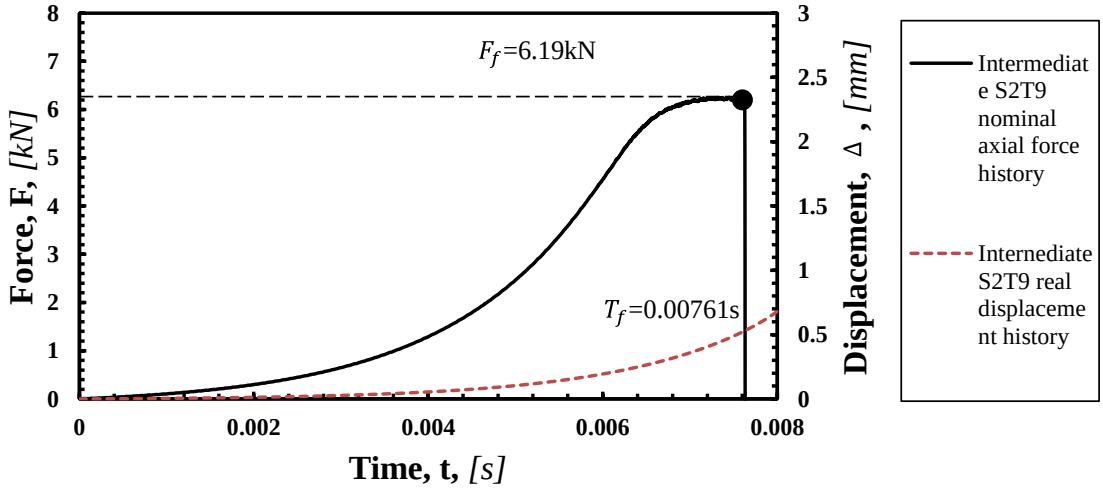

Figure 6.27 Intermediately notched sample S2T9 force and real displacement time histories generated from the FE model.

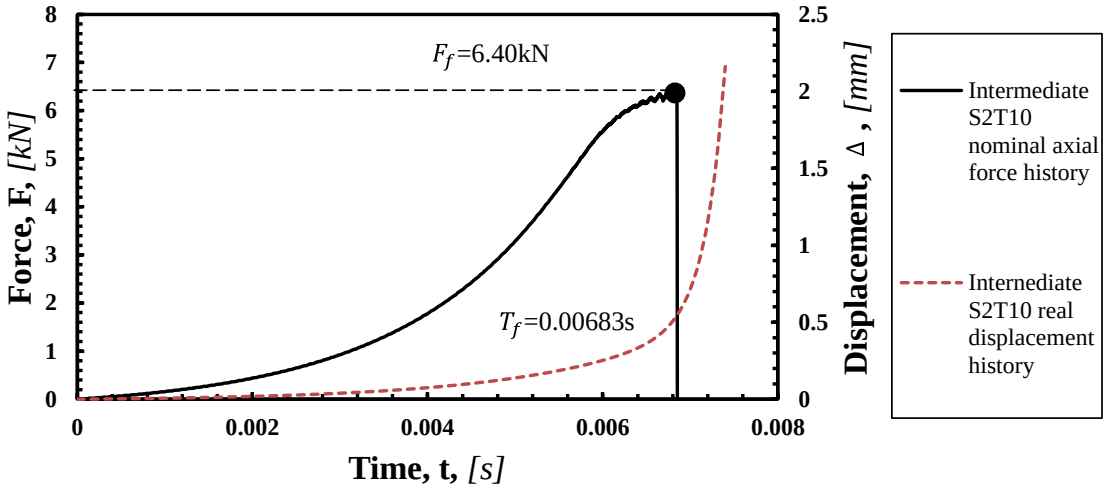

Figure 6.28 Intermediately notched sample S2T10 force and real displacement time histories generated from the FE model.

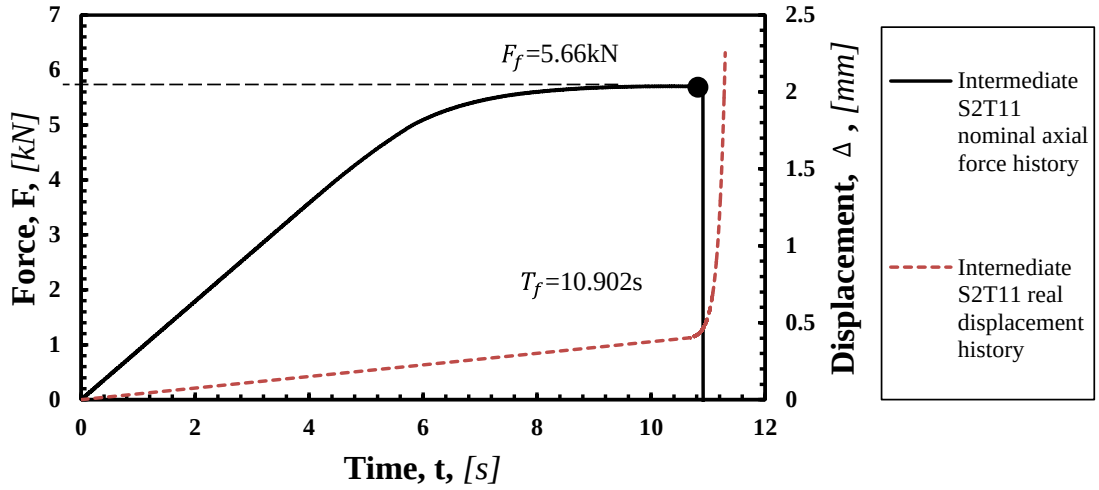

Figure 6.29 Intermediately notched sample S2T11 force and real displacement time histories generated from the FE model.

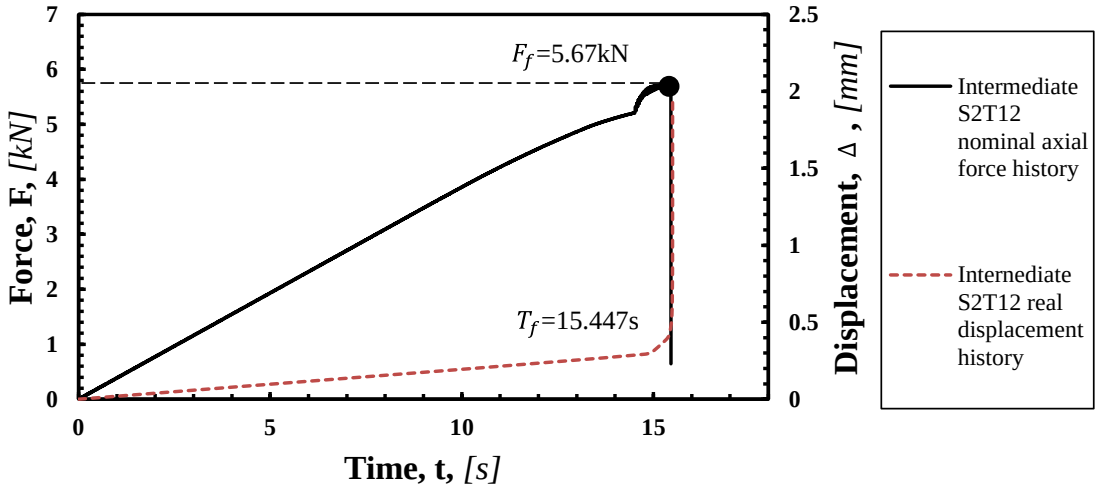

Figure 6.30 Intermediately notched sample S2T12 force and real displacement time histories generated from the FE model.

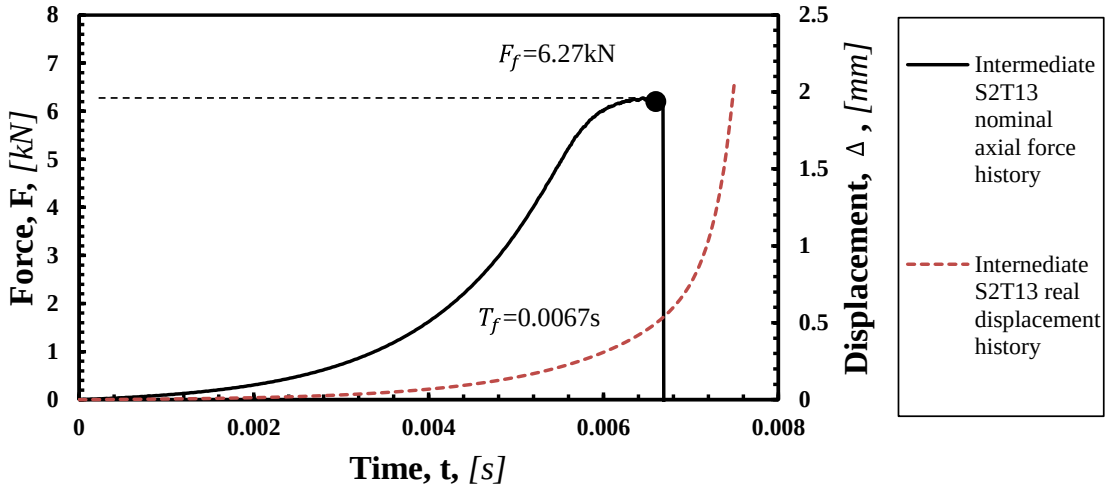

Figure 6.31 Intermediately notched sample S2T13 force and real displacement time histories generated from the FE model.

Additionally, the nominal axial force histories from the models representing the intermediate and blunt notches are shown in Figures 6.22 to 6.34. All of the numerical results computed from the FE models for all of the tested samples are summarised in Table 6.2. A comparison between the predicted numerical strengths and the experimental ones has also been carried out, and the errors were calculated and are summarised in Table 6.2. The errors in this table strongly support the idea that the failure forces calculated when applying the real load histories are also very close to the experimental results. Additionally, the values of the error calculated from the models with both ramped and real displacement histories are plotted in the diagram of Figure 6.35.

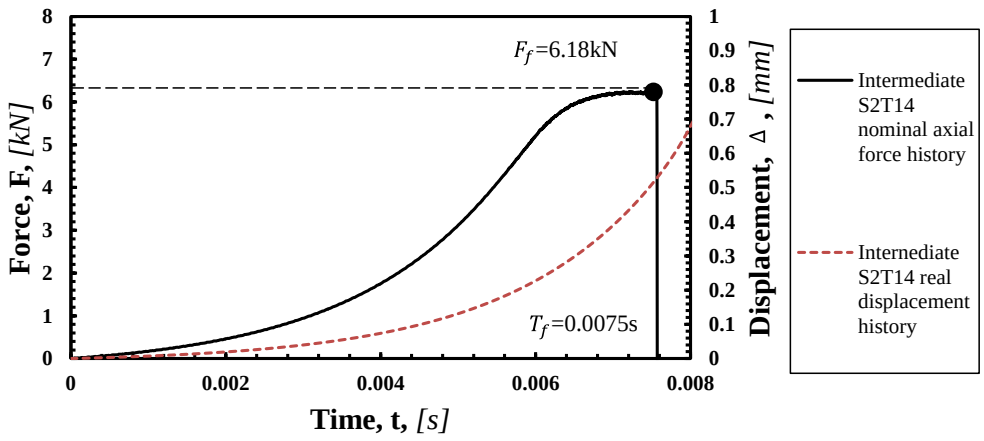

Figure 6.32 Intermediately notched sample S2T14 force and real displacement time histories generated from the FE model.

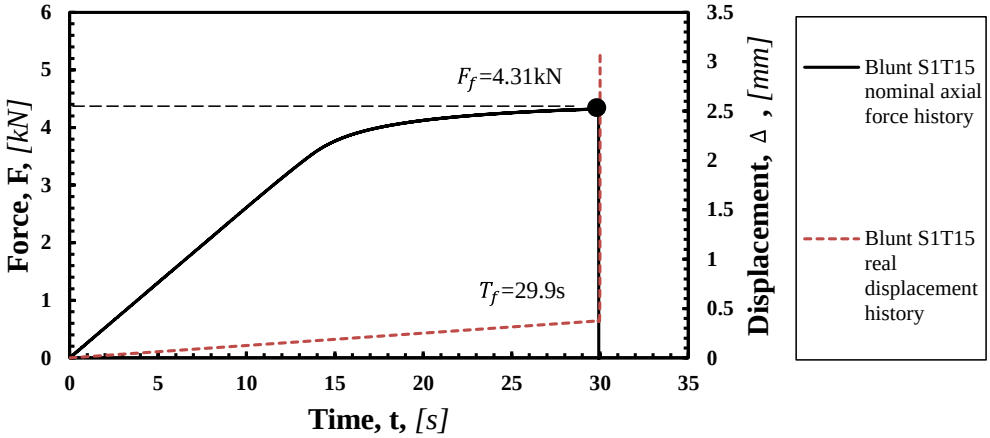

Figure 6.33 Bluntly notched sample S1T15 force and real displacement time histories generated from the FE model.

The error diagram reported in Figure 6.35 makes it evident that elasto-plastic tool LS-DYNA is highly accurate in predicting the dynamic strength of notched Al6063-T5. This holds true when the loading is applied as both a ramped load history and a real load history. In particular, it can be observed that the models using real displacement histories provide slightly more conservative results than the ones obtained by applying the ramped displacement histories.

To conclude, Table 6.1 and 6.2 show that the overall accuracy obtained by running elasto-plastic simulations is acceptable for estimating the strength of notched samples of Al6063-T5 subjected to dynamic loads. In other words, the FE models solved considering crack initiation are capable of predicting the failure strength of notched components accurately.

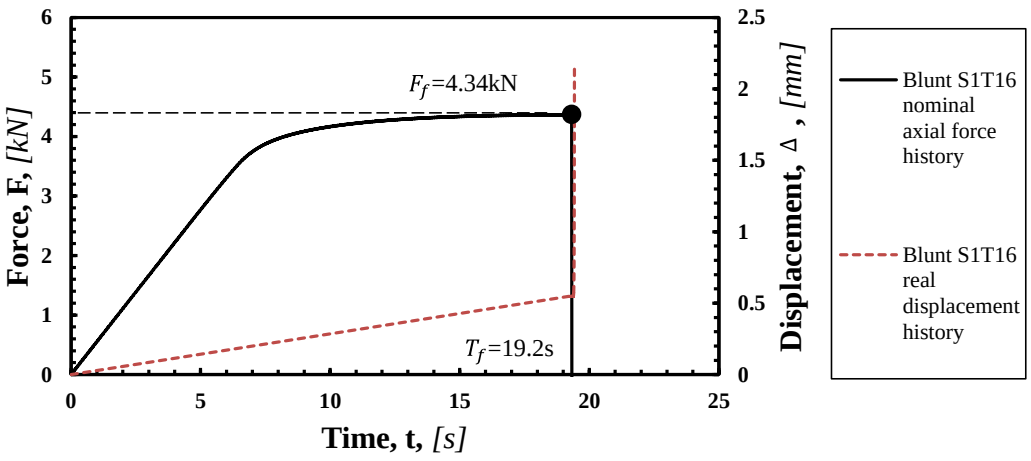

Figure 6.34 Bluntly notched sample S1T15 force and real displacement time histories generated from the FE model.

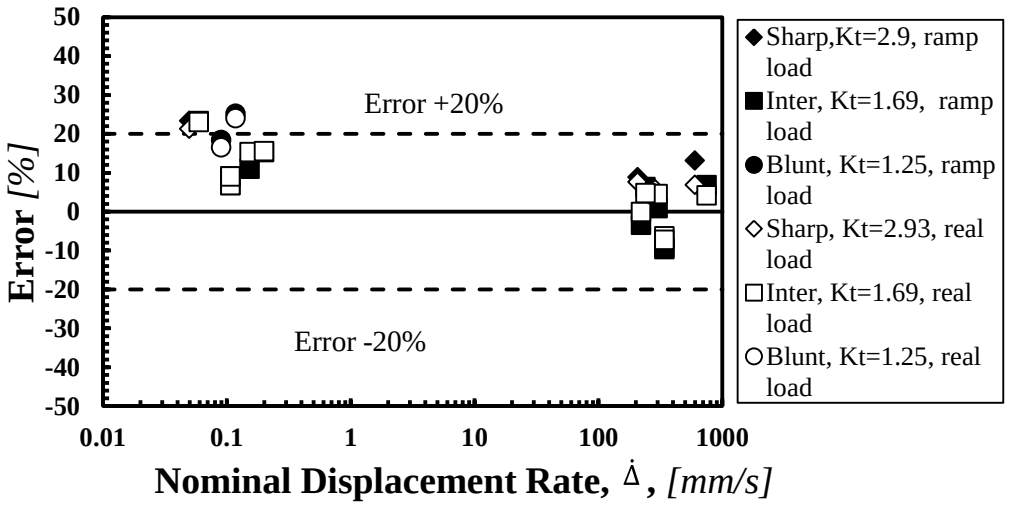

Figure 6.35 Accuracy in predicting the strength of notched Al6063-T5 when applying both ramped and real loading histories by considering crack damage.

Table 6.2 Accuracy in predicting the strength of the notched samples by applying real displacement histories

Test	Experimental failure Load, $F_{exp,f}$ *[kN]*	FEM failure load $F_{FEM,f}$ *(kN)*	Error *[%]*
S1T9	5.4	6.55	21.26
S1T10	6.7	7.16	6.87
S2T1	6.8	7.19	5.74
S2T2	6.7	7.21	7.61
S1 T17	4.6	5.66	23.04
S1 T18	6.2	6.46	4.19
S2 T5	5.3	5.66	6.79
S2 T6	5.1	5.66	10.98
S2 T7	6.7	6.27	-6.42
S2 T9	6.2	6.19	-0.16
S2 T10	6.9	6.4	-7.25
S2 T11	4.9	5.66	15.51
S2 T12	5.2	5.67	9.04
S2 T13	6	6.27	4.50
S2 T14	5.9	6.18	4.75
S1 T15	3.7	4.31	16.49
S1 T16	3.5	4.34	24.00

6.3 Using the TCD by post-processing the elasto-plastic stress fields

As described in chapter 4, the TCD has been shown to be capable of performing strength assessments for notched samples under both quasi-static and dynamic conditions by simply post-processing the linear elastic stress fields around the notch tip (Yin et al., 2015). In this case, the calculated dynamic critical distance, L, increases as the loading rate increases. Moreover, by post-processing the elasto-plastic stress fields for models subjected to quasi-static loading, the TCD can also be used to predict static failures in notched components in which final breakage is preceded by large-scale plastic deformations (Susmel and Taylor, 2008). According to these considerations, an attempt was made here to find out whether the TCD is also successful in assessing the dynamic strength of Al6063-T5 by post-processing the elasto-plastic Von Mises (V-M) stress fields at the incipient failure condition.

6.3.1 Post-processing elasto-plastic stress fields by considering crack damage

For the models which included crack damage, the graphs reported in Figure 6.36 show the Von Mises stress field distributions at the cross section away from the notch tip at the time of crack initiation for models subjected to loading with displacement rates at $1000\text{mm} \cdot \text{s}^{-1}$. Figures in Appendix from A6.1 to A6.6 show the same stress distribution subjected to displacement rates ranging from $100\text{mm} \cdot \text{s}^{-1}$ to $0.001\text{mm} \cdot \text{s}^{-1}$. The dotted horizontal lines indicate a $\pm 20\%$ error band. Overall, it is clear from the graphs in this figure that all of the stress–distance curves at the cross section fall within the $\pm 20\%$ error band. This means that the Von Mises stress–distance curves from models subjected to a wide range of displacement rates are very flat. If the TCD is used by post-processing these stress fields, and 1.2 is assumed as the engineering safety factor (it should be noted here that the value for half of the critical distance L/2 could be anywhere along the critical line), the error in the predictions from the TCD will always fall within the interval of $\pm 20\%$.

Additionally, for the FE models of notched samples under different rates of displacement which do not consider cracking behaviour, the Von Mises stress distributions are shown in the graphs reported in Figure 6.37 and Figure A6.7 To A6.12 In Appendix. From these graphs, the same result can be drawn as from Figure 6.36: that the Von Mises stress at the time of maximum nominal axial force throughout the cross section away from the notches falls within $\pm 20\%$ of the plain strength.

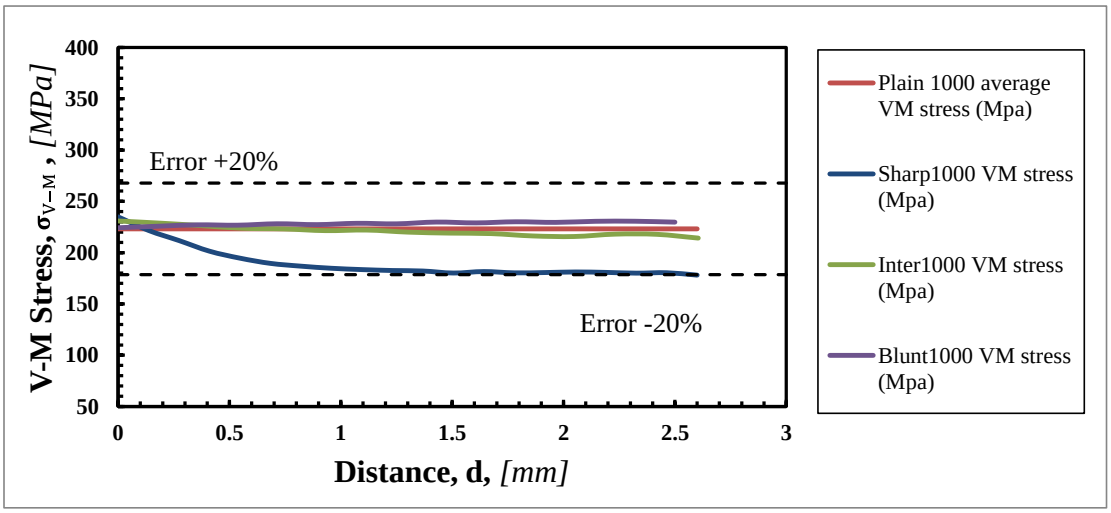

Figure 6.36 Elasto-plastic Von Mises stress vs distance curves at the time of crack initiation for displacement rates $\dot{\Delta} = 1000mm \cdot s^{-1}$.

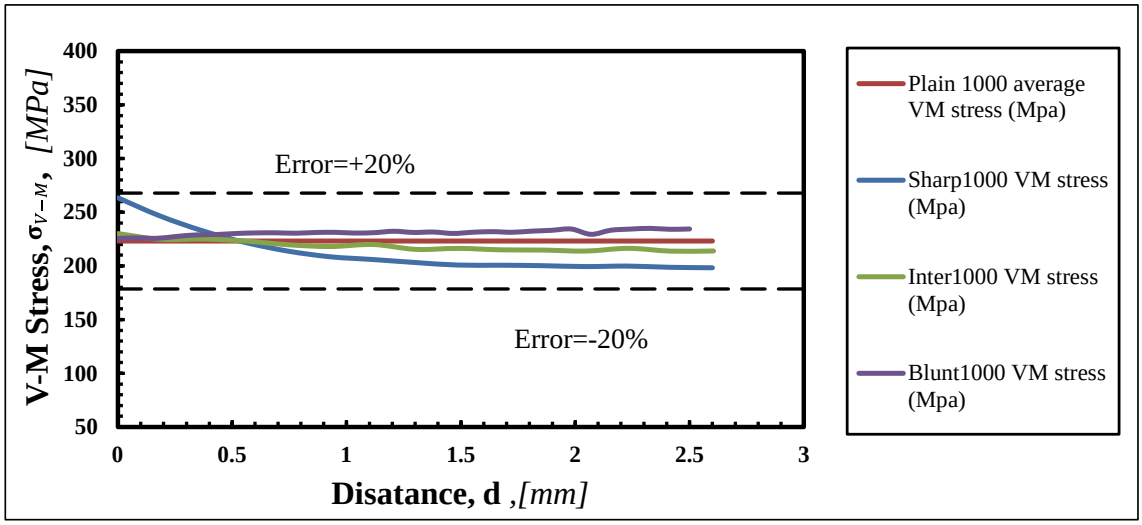

Figure 6.37 Elasto-plastic Von Mises stress vs distance curves at the time of maximum force with displacement rates $\dot{\Delta}= 1000mm \cdot s^{-1}$.

Therefore, a conclusion can be draw that for this specific material, Al6063-T5, according to Figure 6.36 and 6.37 and Figures from A6.1 to A6.12, the intersection between the elasto-plastic stress–distance curves can be obtained unambiguously from the models with and without crack initiation, and all of the stresses at the incipient failure condition along the focus path all fall within a $\pm 20\%$ error band. Owing to the successful prediction by using linear elastic approach presented in Chapter 4, in next subsection, an attempt was made to find the accuracy level of the TCD in assessing the dynamic strength of Al6063-T5 by post-processing the elasto-plastic Von Mises stress fields at the incipient failure condition.

6.3.2 Using the TCD to predict material strength by post-processing Von-Mises stress fields

By comparing the Von-Mises stress distance curves reported in Figure 6.36 and 6.37, we can see that a more clear intersections between the stress distances curves were observed when the crack initiation was not taken into account, therefore, in this scenario, the Von-Mises stress distribution from the models without crack initiation will be post-processed in order to obtain the dynamic critical distance L_d by using the PM (same strategy as shown in Figure 2.2). The elasto-plastic V-M stress–distance curves from the models of the plain and sharply notched samples were post-processed, and the distance at the intersection between the two curves was chosen as half of the dynamic critical distance $L_d/2$ (Taylor, 2007). Initially, an assumption was made here that the inherent material V-M strength $\bar{\sigma}_{0,VM}$ was taken to be equal to the plain Von Mises strength $\bar{\sigma}_{VM}$ (Susmel and Taylor, 2008). Hence, the Von Mises stress–distance curves from plain and sharply notched samples were used to determine the dynamic critical distance L_d. The Von Mises stress–distance curves generated from the models of plain and sharply notched

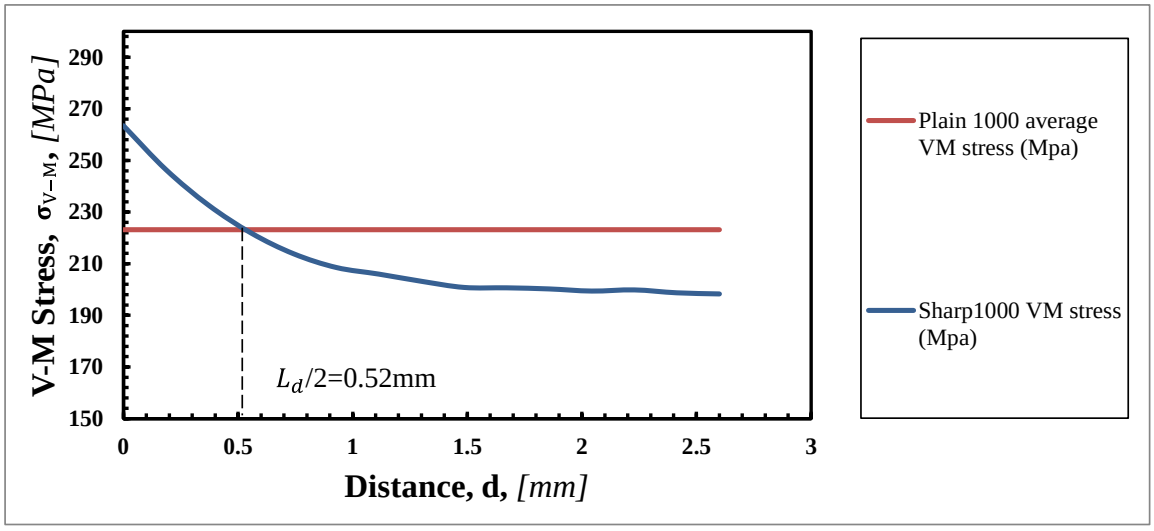

Figure 6. 38 Determination of the dynamic critical distance L_d from Von Mises stress–distance curves for models of sharply notched and plain samples under displacement rates of $\dot{\Delta}= 1000\text{mm} \cdot \text{s}^{-1}$.

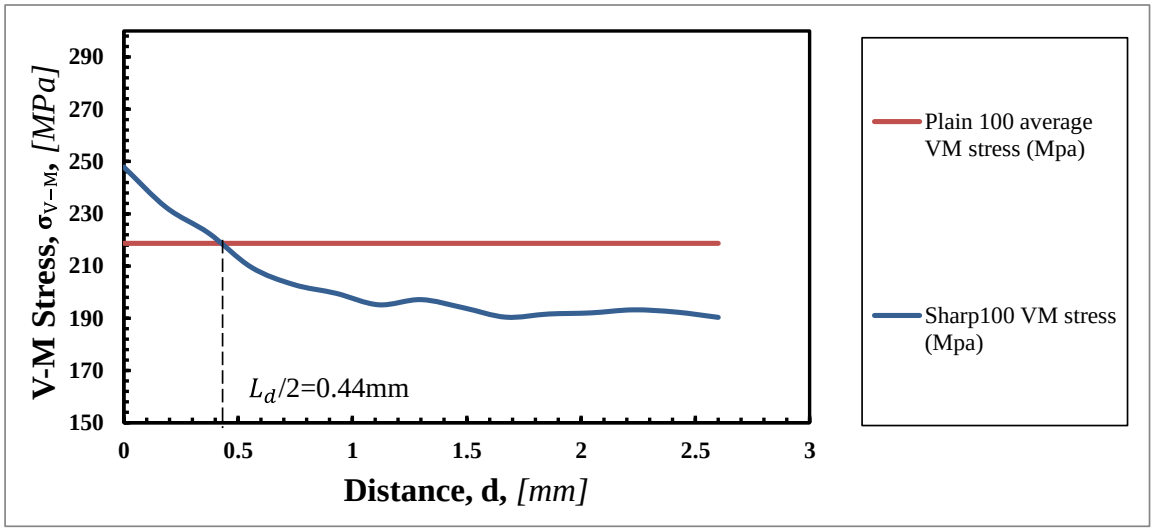

Figure 6. 39 Determination of the dynamic critical distance L_d from Von Mises stress–distance curves for models of sharply notched and plain samples under displacement rates of (a) $\dot{\Delta}= 100\text{mm} \cdot \text{s}^{-1}$.

samples subjected to a wide range of displacement rates (from $1000\text{mm} \cdot \text{s}^{-1}$ to $0.001\text{mm} \cdot \text{s}^{-1}$) are plotted in Figure from 6.38 to 6.44. Specifically, as shown in Figure 6.38, the Von Mises stress fields generated from plain and sharply notched samples subjected to a displacement rate $\dot{\Delta}= 1000\text{mm} \cdot \text{s}^{-1}$ intersect at a distance d=0.52mm, which is taken to be equal to half of the dynamic critical distance L_d/2, and the inherent material V-M strength $\bar{\sigma}_{0,VM}$ is taken to be equal to 223.17MPa at this displacement rate. Moreover, when the displacement rate is taken to be equal to $100\text{mm} \cdot \text{s}^{-1}$ (Figure 6.39), the plain Von Mises strength is $\bar{\sigma}_{VM}$=218.67MPa, and

the distance to the intersection is d=L_d/2=0.44mm. By applying the same determination process to the plain and sharply notched samples with other displacement rates (as shown in Figures 6.40 to 6.44), the plain Von Mises strength $\bar{\sigma}_{VM}$ and the dynamic critical distance L_d subjected to different rates of displacement were calculated and the results are summarised in Table 6.3.

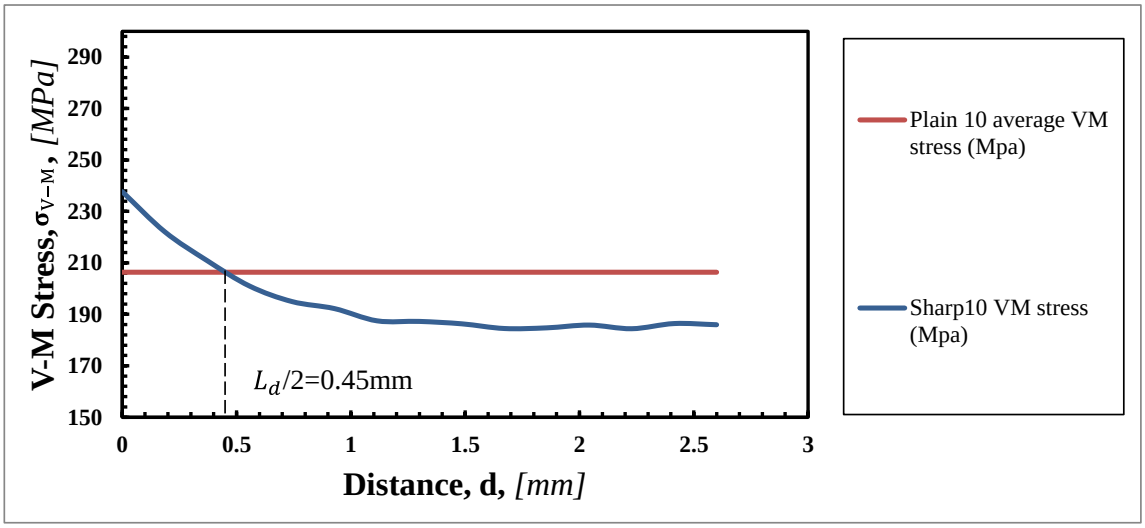

Figure 6. 40 Determination of the dynamic critical distance L_d from Von Mises stress–distance curves for models of sharply notched and plain samples under displacement rates of (a) $\dot{\Delta}$= $10\text{mm} \cdot \text{s}^{-1}$.

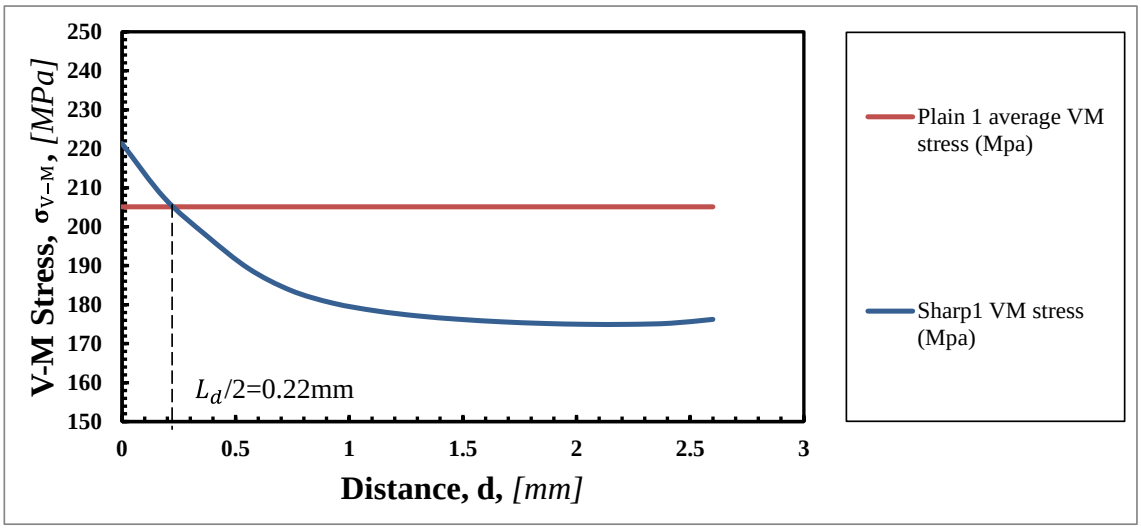

Figure 6. 41 Determination of the dynamic critical distance L_d from Von Mises stress–distance curves for models of sharply notched and plain samples under displacement rates of (a) $\dot{\Delta}$= $1\text{mm} \cdot \text{s}^{-1}$.

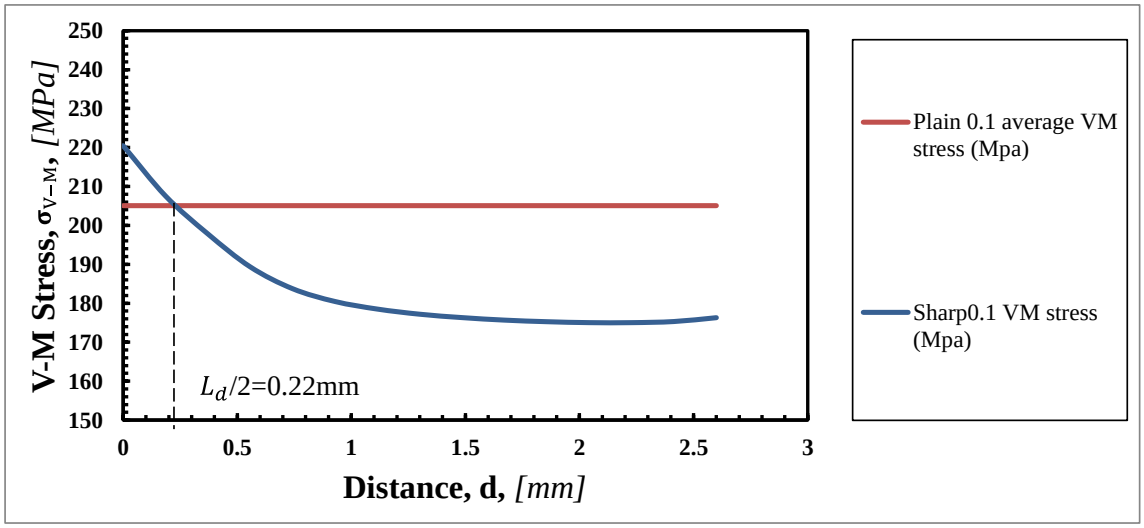

Figure 6. 42 Determination of the dynamic critical distance L_d from Von Mises stress–distance curves for models of sharply notched and plain samples under displacement rates of (a) $\dot{\Delta}= 0.1\text{mm} \cdot \text{s}^{-1}$.

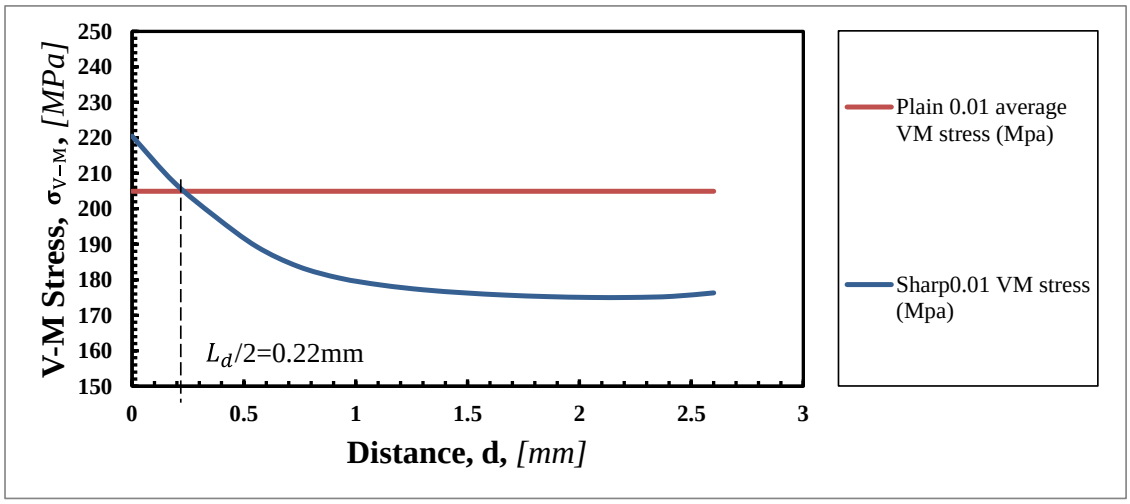

Figure 6. 43 Determination of the dynamic critical distance L_d from Von Mises stress–distance curves for models of sharply notched and plain samples under displacement rates of (a) $\dot{\Delta}= 0.01mm \cdot s^{-1}$.

According to the values listed in Table 6.3, the values of L_d under dynamic loading are larger than the ones obtained under quasi-static loading. Due to the flat stress distributions in Figure 6.37, the dynamic critical distance for this case can be taken as a constant. By averaging the dynamic critical distances generated from Figures 6.38 to 6.44, as shown in Table 6.3, the average dynamic critical distance is calculated and is taken as a material constant for material Al6063-T5.

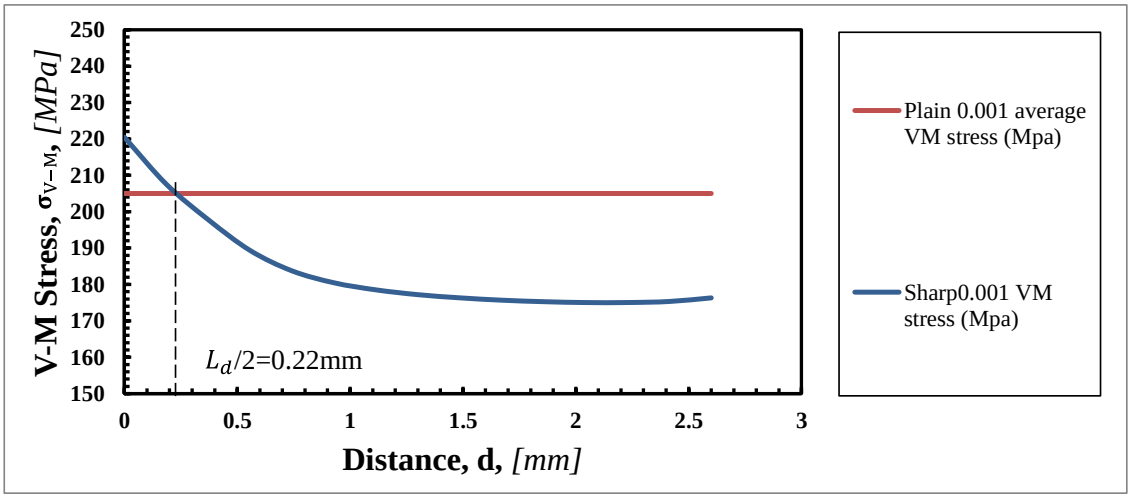

Figure 6.44 Determination of the dynamic critical distance L_d from Von Mises stress–distance curves for models of sharply notched and plain samples under displacement rates of $\dot{\Delta}= 0.001mm \cdot s^{-1}$.

Table 6.3 Values of dynamic critical distance based on PM agreement

Displacement rate, $\dot{\Delta}$, *[mm/s]*	plain Von Mises strength $\bar{\sigma}_{VM}$, *[MPa]*	Dynamic critical distance, L_d, *[mm]*
1000	223.17	1.04
100	218.67	0.88
10	206.37	0.90
1	205.09	0.44
0.1	205.06	0.44
0.01	204.93	0.44
0.001	205.00	0.44
Average		0.66

In terms of the Point Method, the graphs reported in Figure from 6.45 to 48 show the elasto-plastic V-M stress as a function of the distance from the notch tip obtained from FE models of sharply notched samples. Specifically, Figure 6.45 shows the Von-Mises stress σ_{V-M} at the incipient failure condition along the cross section remote from the notch tip generated by running models of sharply notched samples subjected to quasi-static loading (displacement rate $\dot{\Delta}= 0.05mm \cdot s^{-1}$). It can be observed from this graph that the effective stress σ_{eff} at distance L_d/2=0.33mm is 200MPa. Moreover, the plain V-M strength $\bar{\sigma}_{VM}$, which was assumed to be the inherent material Von-Mises strength under the same rate of displacement loading ($\dot{\Delta}= 0.05mm \cdot s^{-1}$), was calculated to be $\bar{\sigma}_{VM}$ =$\bar{\sigma}_{0,VM}$=191.58MPa.

The graphs reported in Figure 6.46, Figure 6.47 and Figure 6.48 show the V-M stress distributions obtained from the models of sharply notched samples subjected to dynamic loading, and the effective V-M stresses at a distance of $L_d/2$=0.33mm are 234MPa, 225MPa and 222MPa respectively.

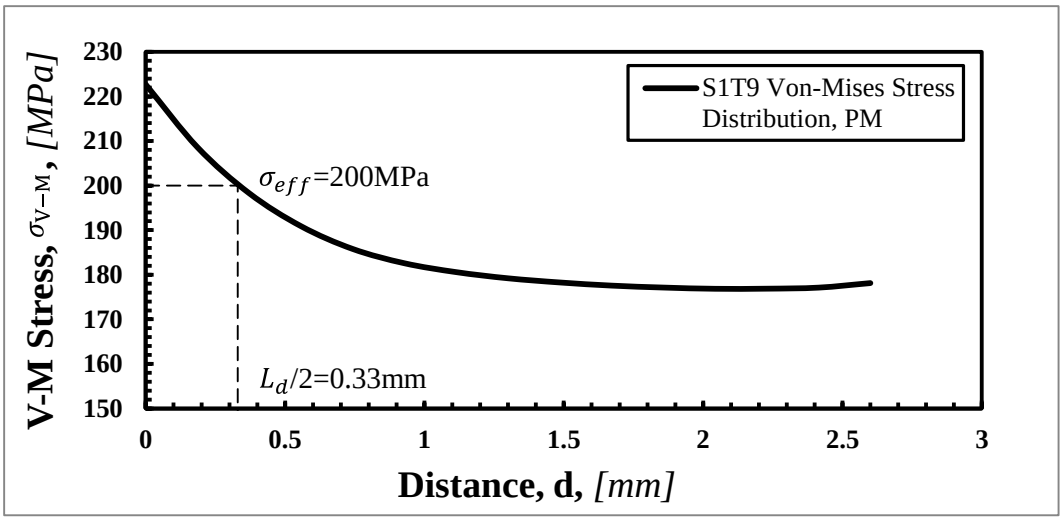

Figure 6. 45 Using the Point Method for prediction of material strength for sharply notched Al6063-T5 sample S1T9 by post-processing the elasto-plastic V-M stress field.

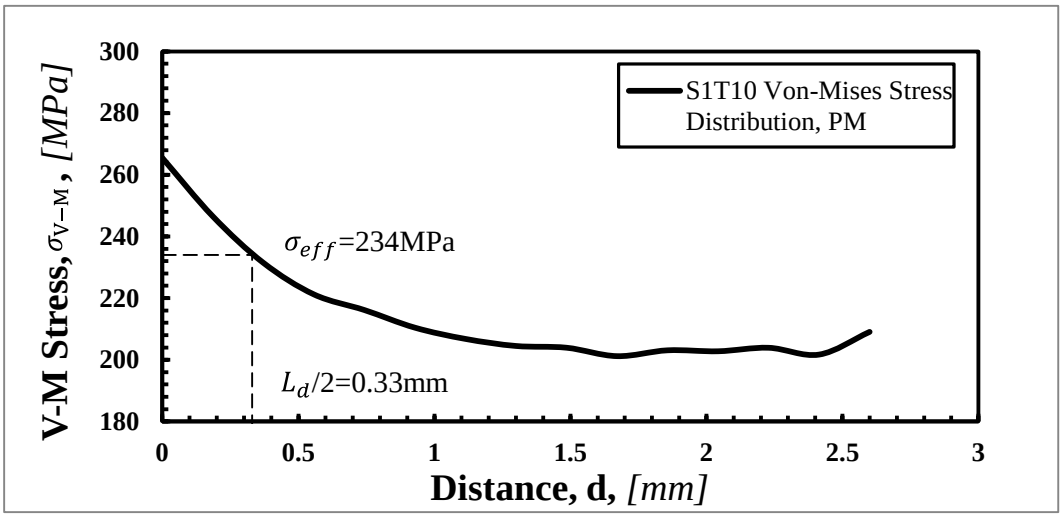

Figure 6. 46 Using the Point Method for prediction of material strength for sharply notched Al6063-T5 sample S1T10 by post-processing the elasto-plastic V-M stress field.

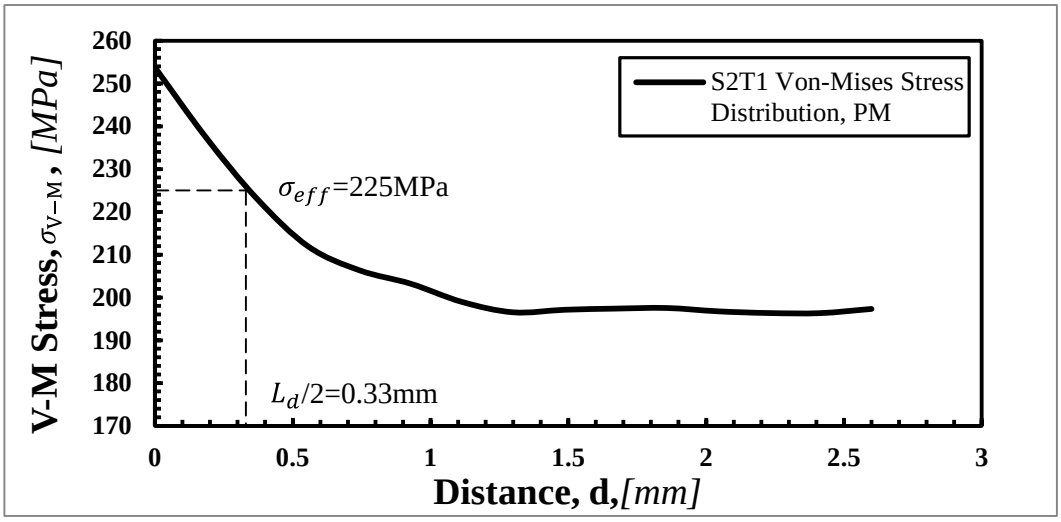

Figure 6. 47 Using the Point Method for prediction of material strength for sharply notched Al6063-T5 sample S2T1 by post-processing the elasto-plastic V-M stress field.

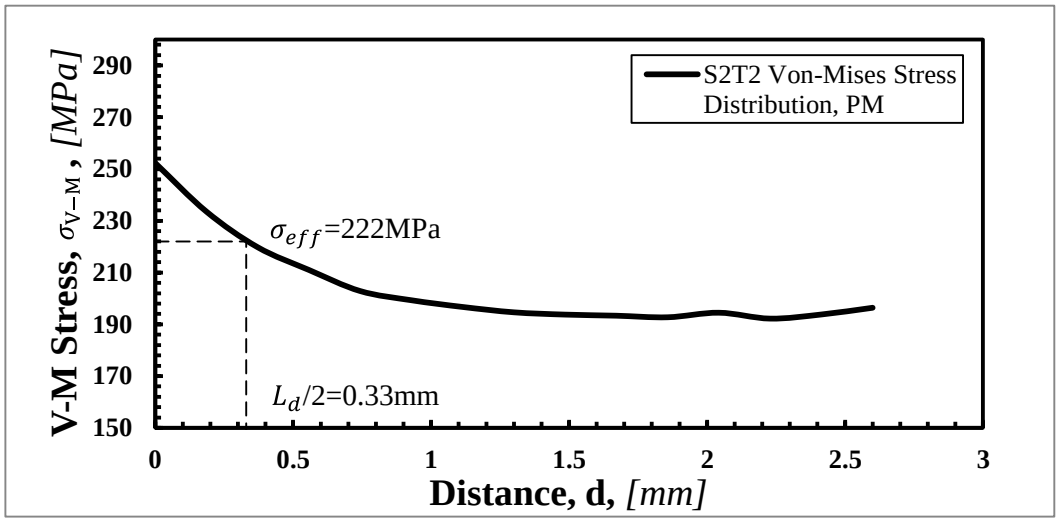

Figure 6.48 Using the Point Method for prediction of material strength for sharply notched Al6063-T5 sample S2T2 by post-processing the elasto-plastic V-M stress field.

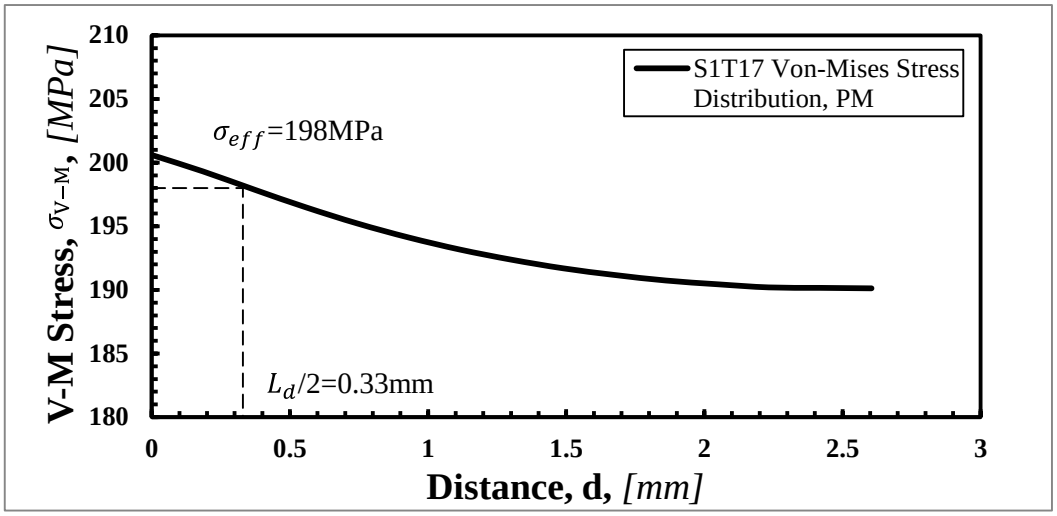

Figure 6. 49 Using the Point Method for prediction of material strength for intermediately notched Al6063-T5 sample S1T17 by post-processing the elasto-plastic V-M stress field.

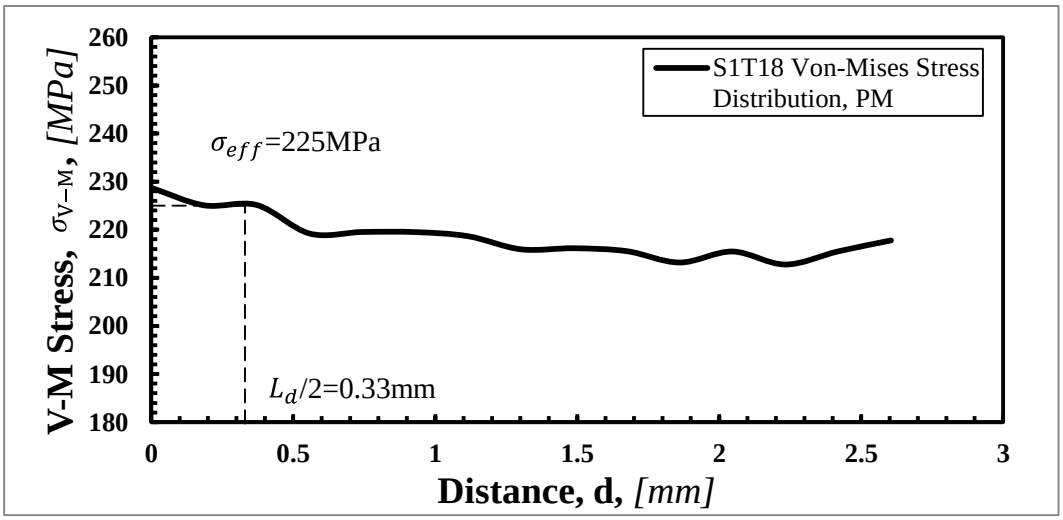

Figure 6. 50 Using the Point Method for prediction of material strength for intermediately notched Al6063-T5 sample S1T18 by post-processing the elasto-plastic V-M stress field.

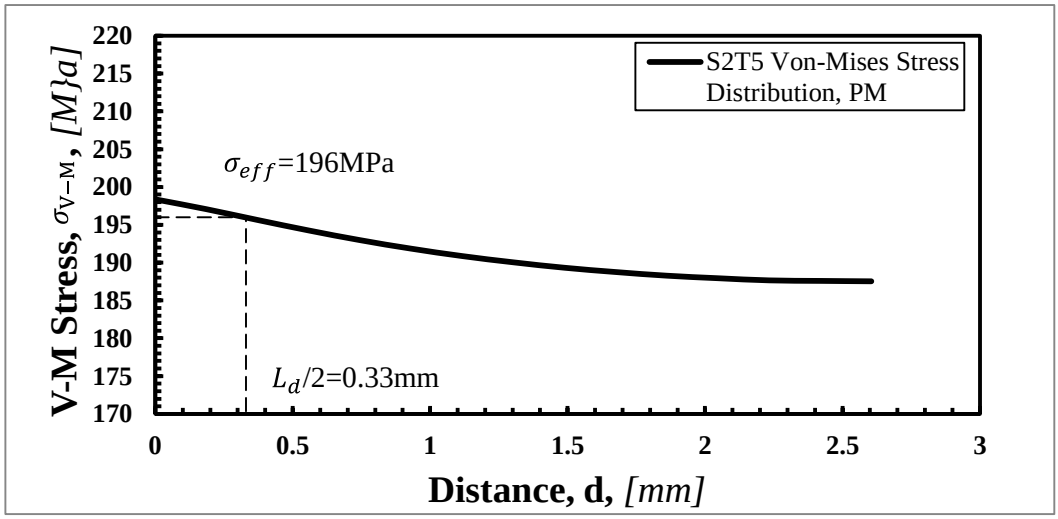

Figure 6. 51 Using the Point Method for prediction of material strength for intermediately notched Al6063-T5 sample S2T5 by post-processing the elasto-plastic V-M stress field.

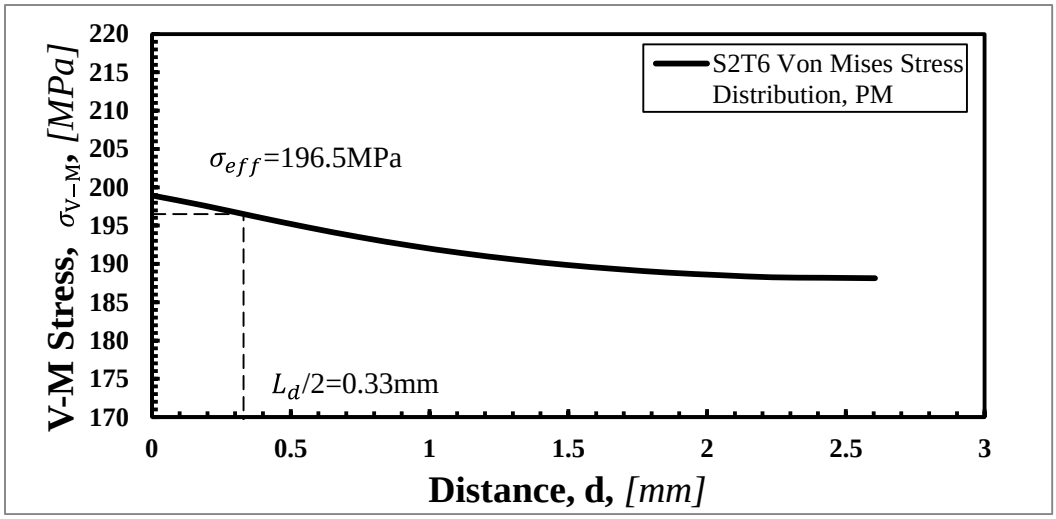

Figure 6. 52 Using the Point Method for prediction of material strength for intermediately notched Al6063-T5 sample S2T6 by post-processing the elasto-plastic V-M stress field.

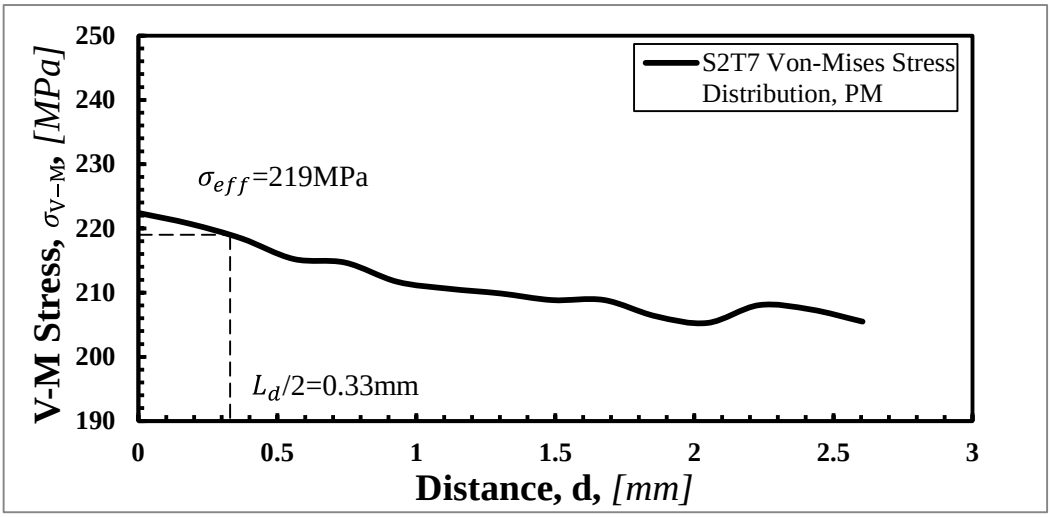

Figure 6. 53 Using the Point Method for prediction of material strength for intermediately notched Al6063-T5 sample S2T7 by post-processing the elasto-plastic V-M stress field.

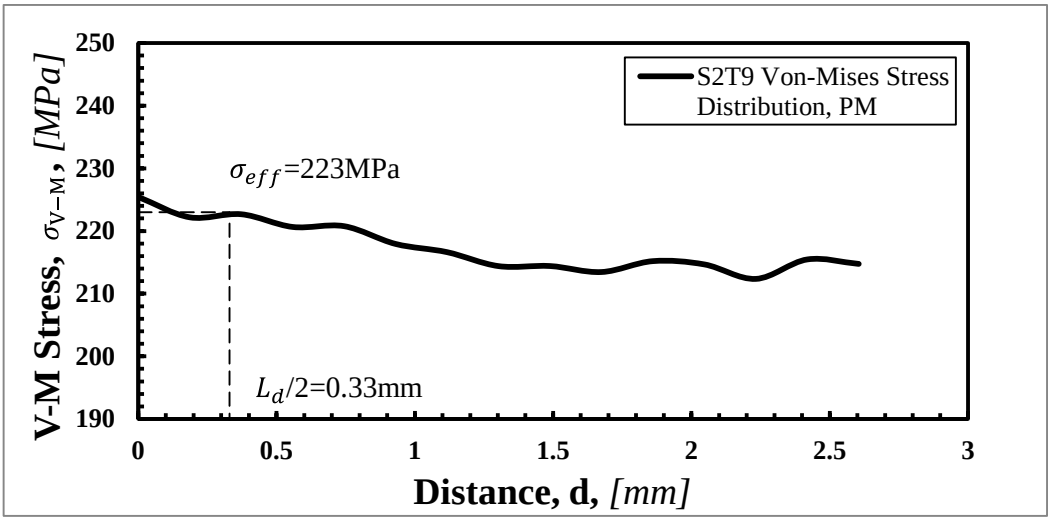

Figure 6. 54 Using the Point Method for prediction of material strength for intermediately notched Al6063-T5 sample S2T9 by post-processing the elasto-plastic V-M stress field.

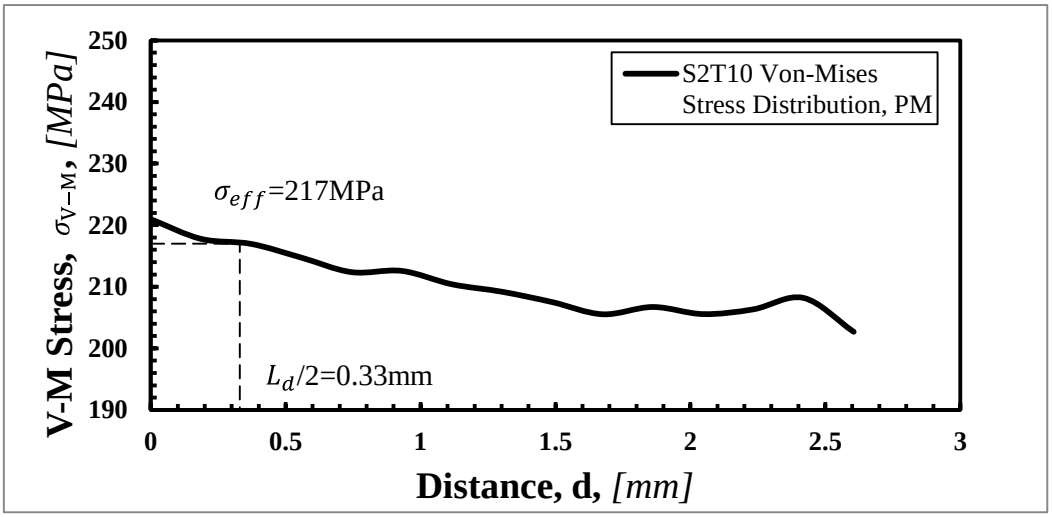

Figure 6. 55 Using the Point Method for prediction of material strength for intermediately notched Al6063-T5 sample S2T10 by post-processing the elasto-plastic V-M stress field.

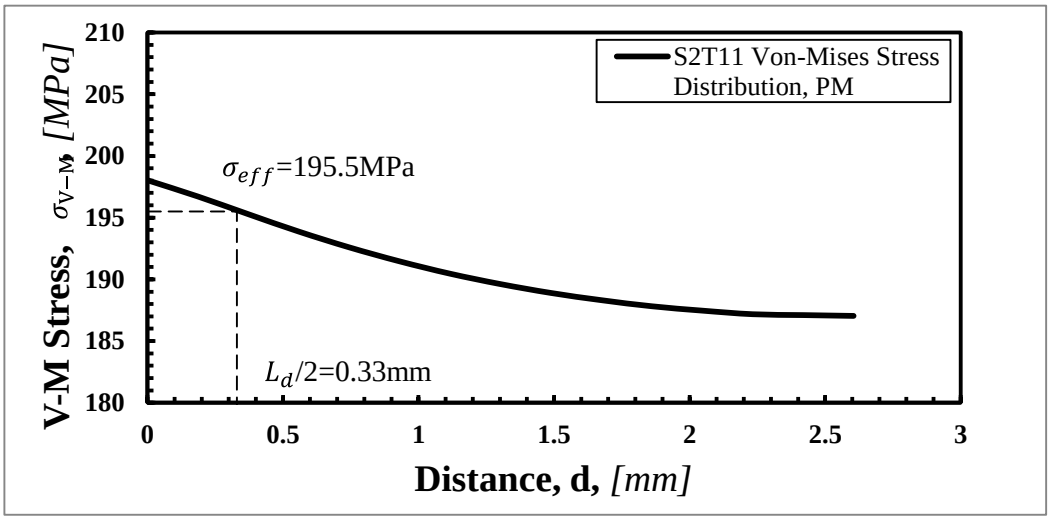

Figure 6. 56 Using the Point Method for prediction of material strength for intermediately notched Al6063-T5 sample S2T11 by post-processing the elasto-plastic V-M stress field.

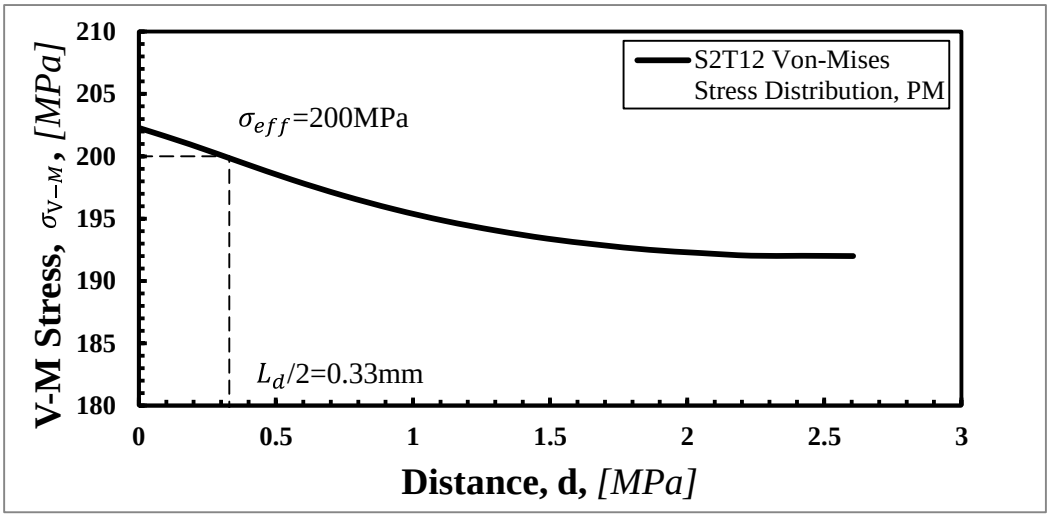

Figure 6. 57 Using the Point Method for prediction of material strength for intermediately notched Al6063-T5 sample S2T12 by post-processing the elasto-plastic V-M stress field.

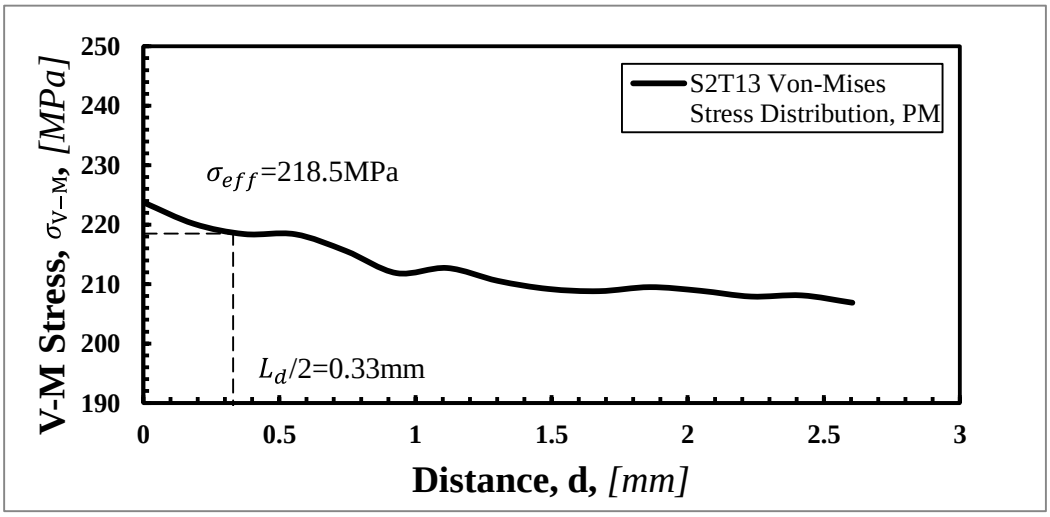

Figure 6. 58 Using the Point Method for prediction of material strength for intermediately notched Al6063-T5 sample S2T13 by post-processing the elasto-plastic V-M stress field.

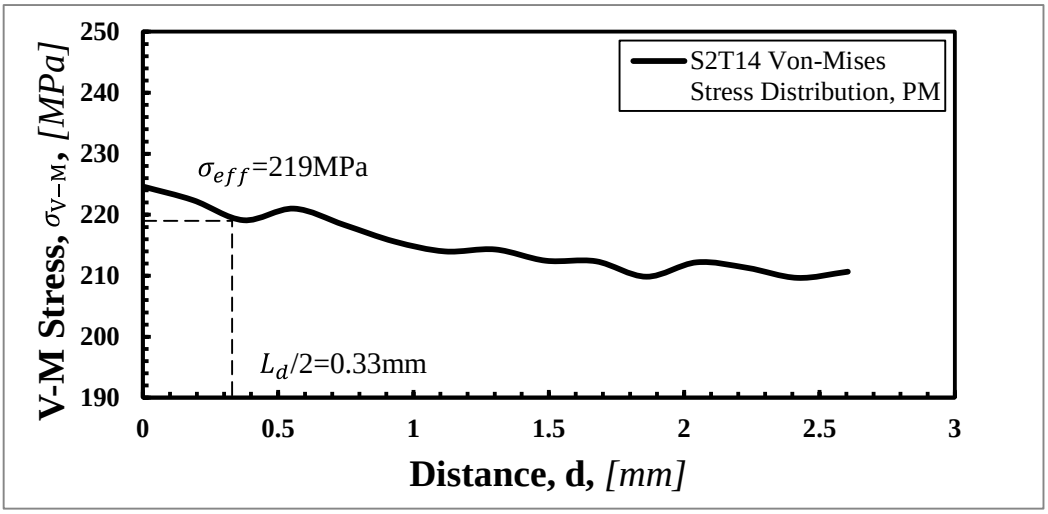

Figure 6.59 Using the Point Method for prediction of material strength for intermediately notched Al6063-T5 sample S2T14 by post-processing the elasto-plastic V-M stress field.

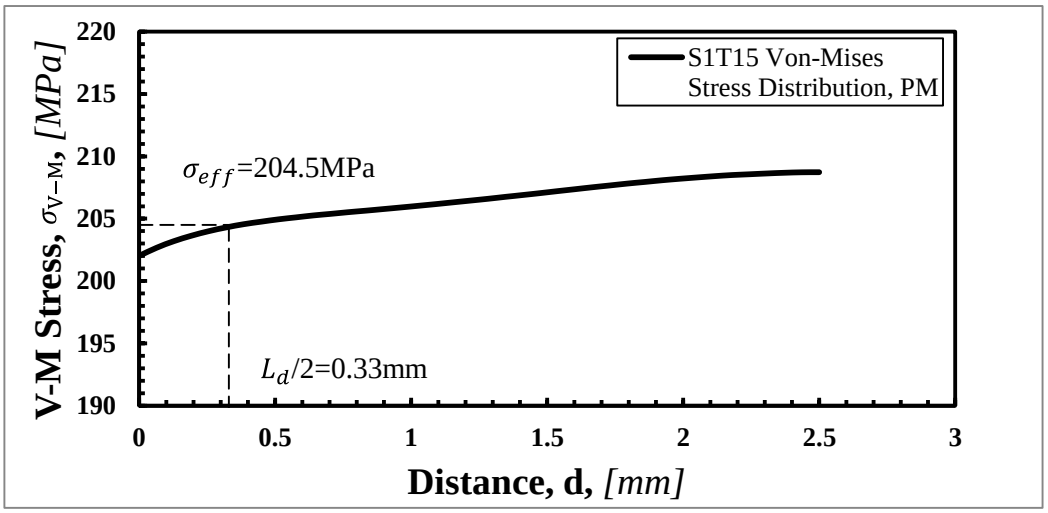

Figure 6. 60 Using the Point Method for predicting the material strength of bluntly notched Al6063-T5 sample S1T15 by post-processing the elasto-plastic V-M stress field.

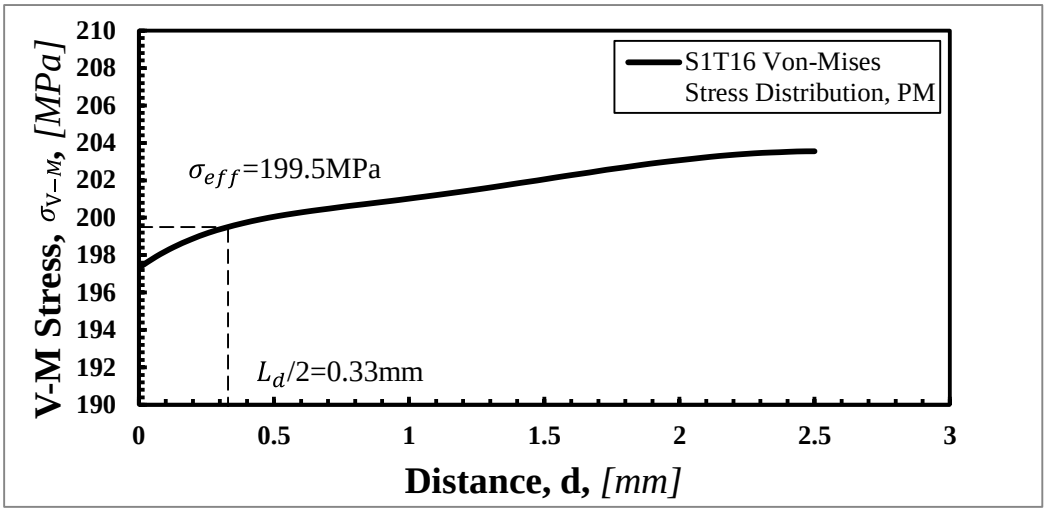

Figure 6.61 Using the Point Method for predicting the material strength of bluntly notched Al6063-T5 sample ST16 by post-processing the elasto-plastic V-M stress field.

From the FE models, the graphs reported in Figures from 6.49 to 6.59 and Figures 6.60 and 6.61 show the V-M stress distributions at the incipient failure condition for intermediately and bluntly notched samples subjected to both quasi-static and dynamic loading. The effective stresses σ_{eff} at a distance of L_d/2=0.33mm are all plotted in these figures, and the values are summarised in Table 6.4.

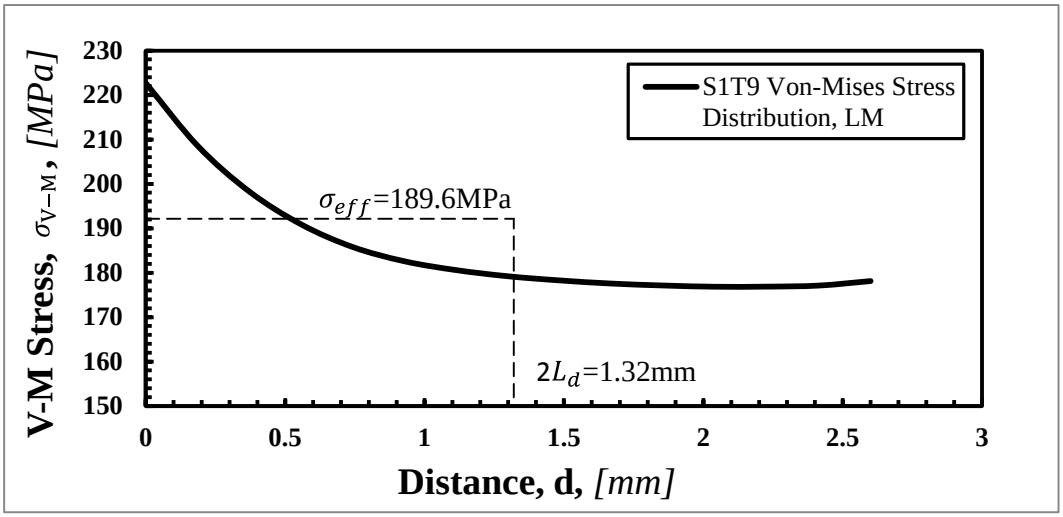

Figure 6. 62 Using the Line Method for predicting material strength of sharply notched Al6063-T5 sample S1T9 by post-processing the elasto-plastic V-M stress field.

Using the same focus path, rather than taking the stress at a particular point (PM), according to Equation 4.2 in Chapter 4 (the LM criterion), the average stress over the distance 2$\boldsymbol{L_d}$=1.32mm starting at d=0 can be used as the effective stress to assess the dynamic failure of material Al6063-T5. Specifically, The V-M stress field generated from the model of the intermediately

notched sample S1T9 under quasi-static loading conditions is shown in Figure 6.62. The effective V-M stress $\boldsymbol{\sigma_{eff}}$ over a distance of 1.32mm is 189.6MPa.

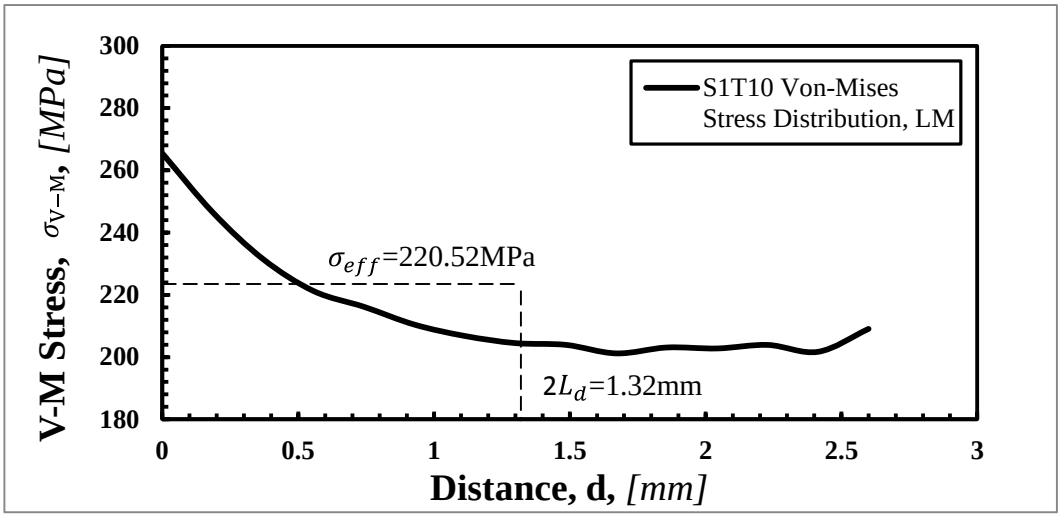

Figure 6. 63 Using the Line Method for predicting material strength of sharply notched Al6063-T5 sample S1T10 by post-processing the elasto-plastic V-M stress field.

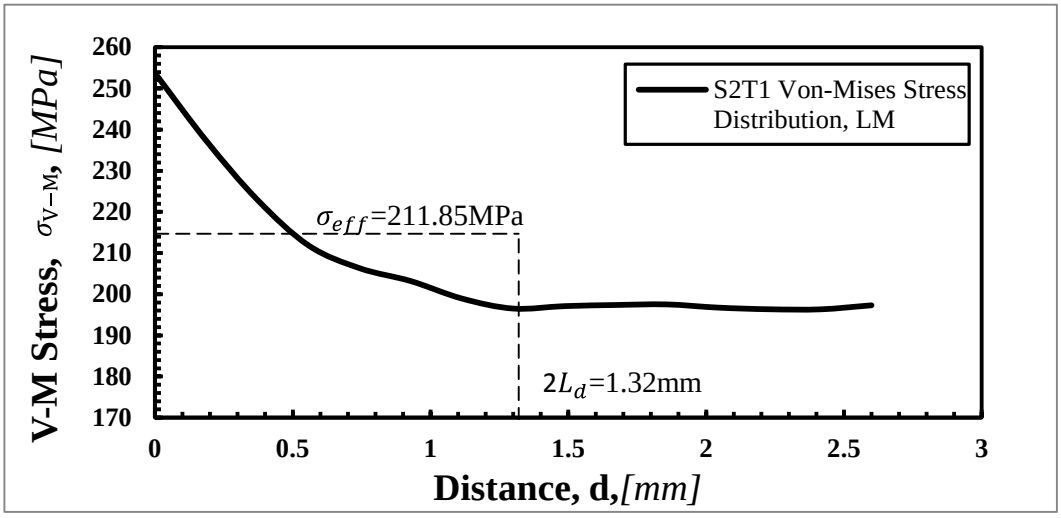

Figure 6. 64 Using the Line Method for predicting material strength of sharply notched Al6063-T5 sample S2T1 by post-processing the elasto-plastic V-M stress field.

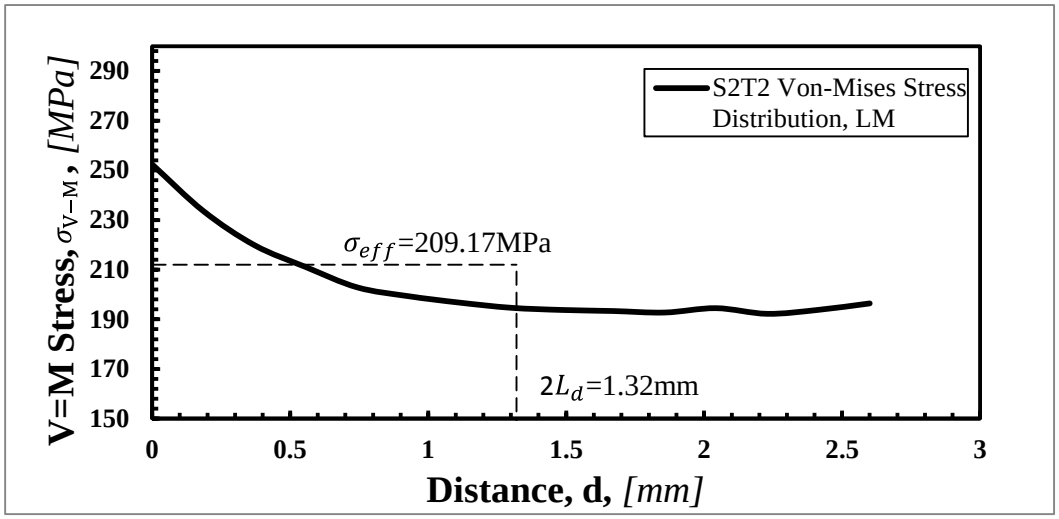

Figure 6.65 Using the Line Method for predicting material strength of sharply notched Al6063-T5 sample S2T2 by post-processing the elasto-plastic V-M stress field.

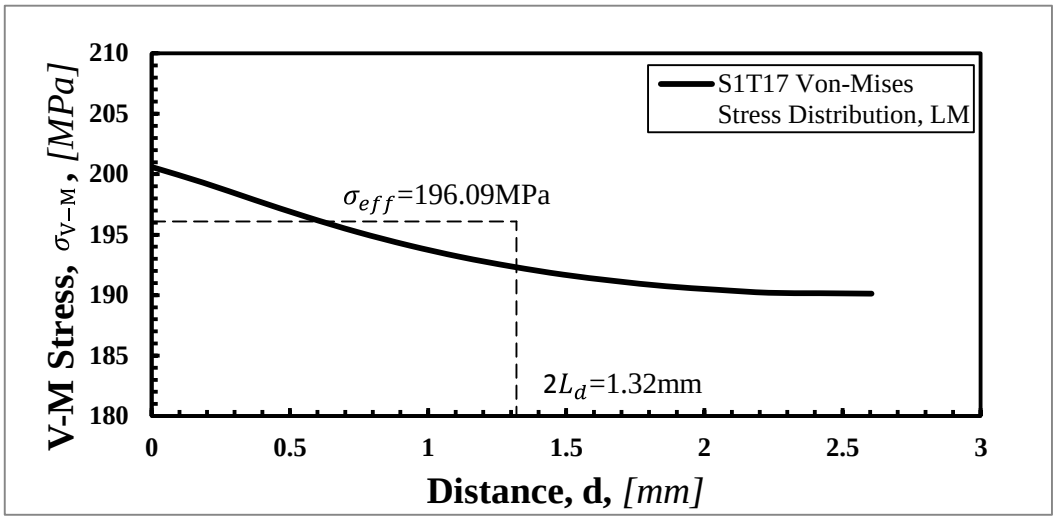

Figure 6. 66 Using the Line Method for predicting the material strength of intermediately notched Al6063-T5 sample S1T17 by post-processing the elasto-plastic V-M stress field.

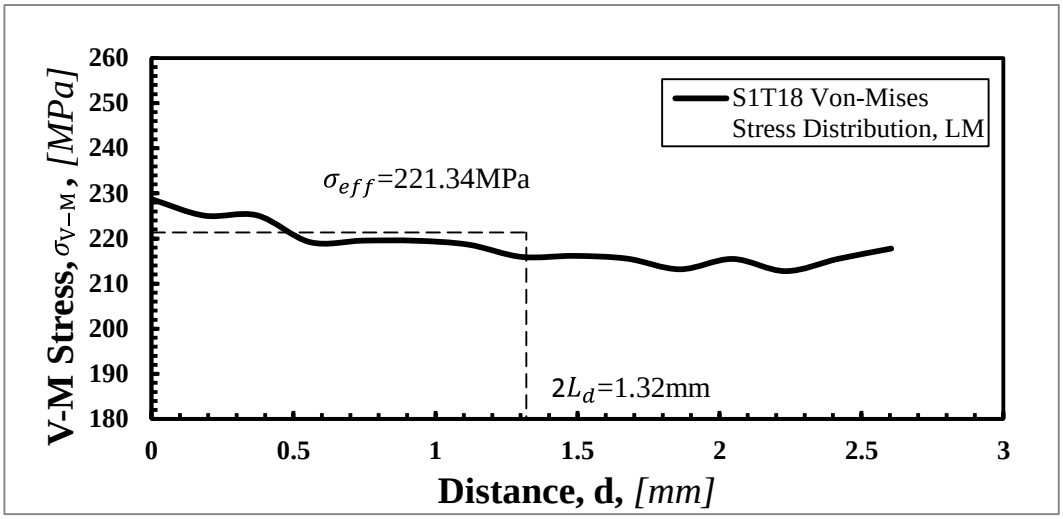

Figure 6. 67 Using the Line Method for predicting the material strength of intermediately notched Al6063-T5 sample S1T18 by post-processing the elasto-plastic V-M stress field.

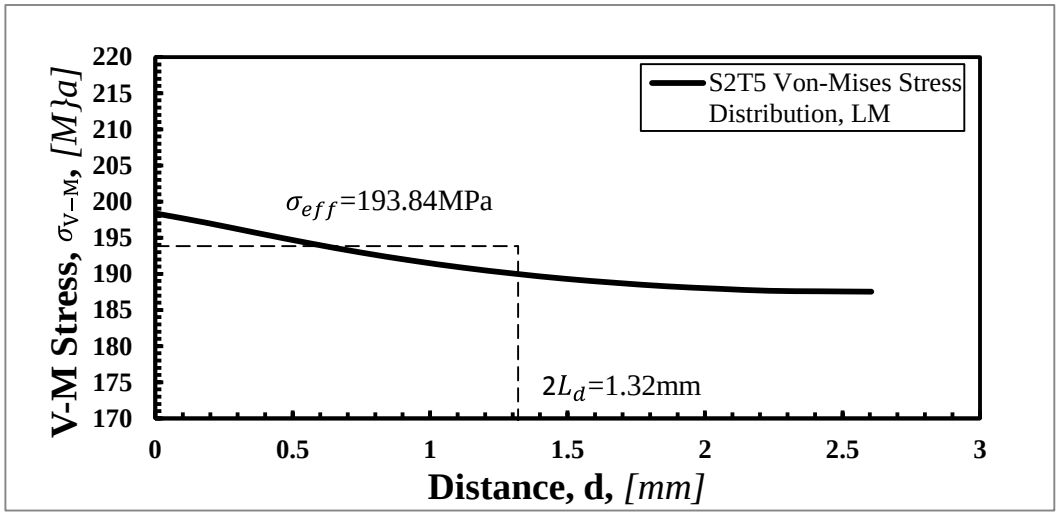

Figure 6. 68 Using the Line Method for predicting the material strength of intermediately notched Al6063-T5 sample S2T5 by post-processing the elasto-plastic V-M stress field.

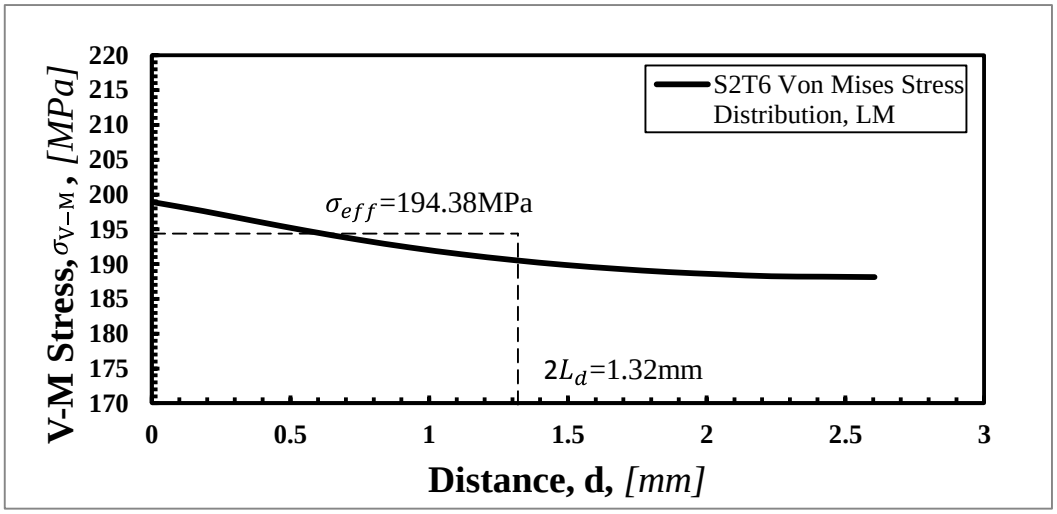

Figure 6. 69 Using the Line Method for predicting the material strength of intermediately notched Al6063-T5 sample S2T6 by post-processing the elasto-plastic V-M stress field.

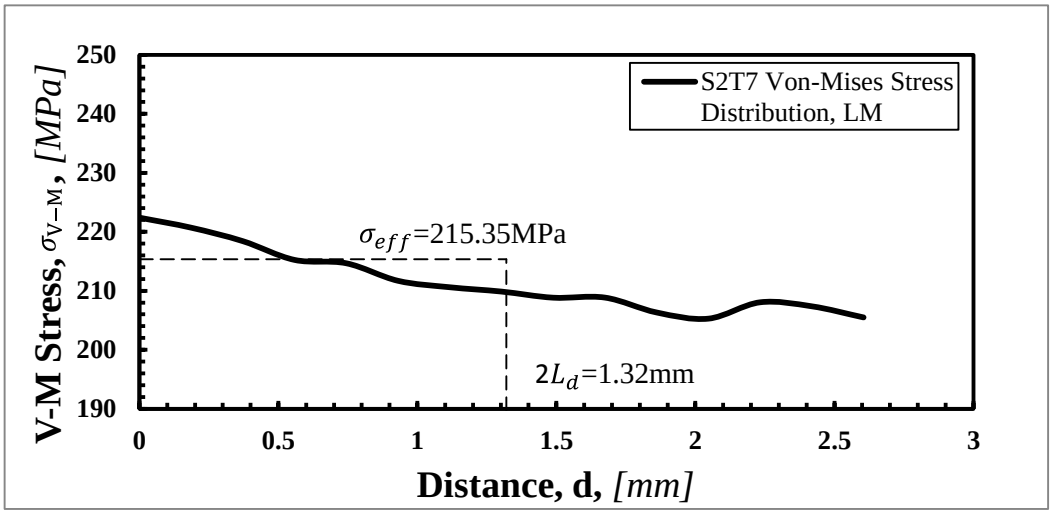

Figure 6. 70Using the Line Method for predicting the material strength of intermediately notched Al6063-T5 sample S2T7 by post-processing the elasto-plastic V-M stress field.

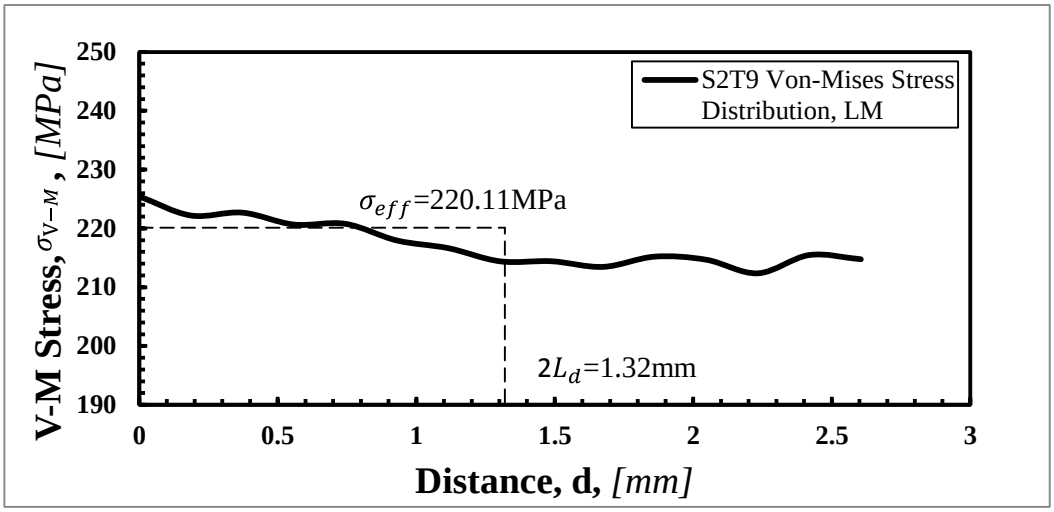

Figure 6. 71 Using the Line Method for predicting the material strength of intermediately notched Al6063-T5 sample S2T9 by post-processing the elasto-plastic V-M stress field.

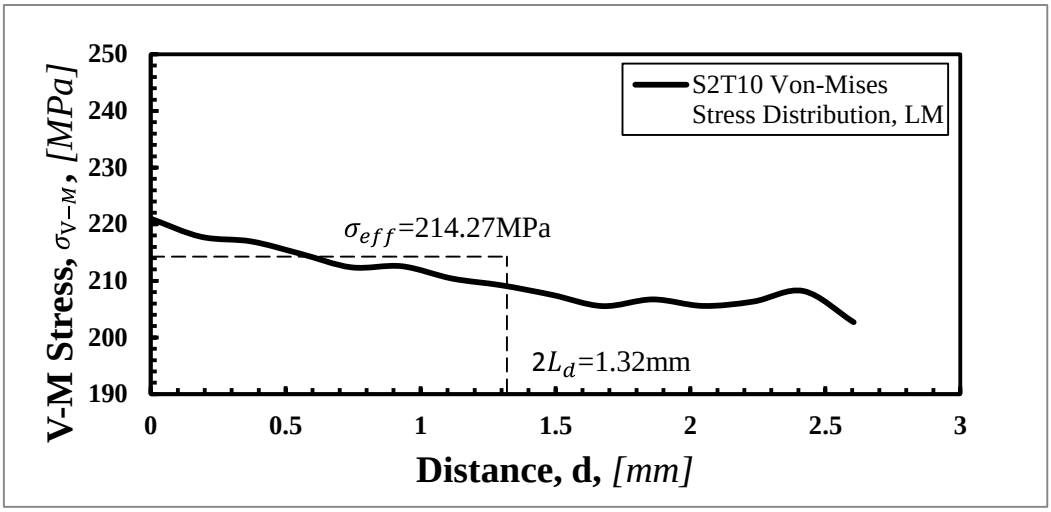

Figure 6. 72 Using the Line Method for predicting the material strength of intermediately notched Al6063-T5 sample S2T10 by post-processing the elasto-plastic V-M stress field.

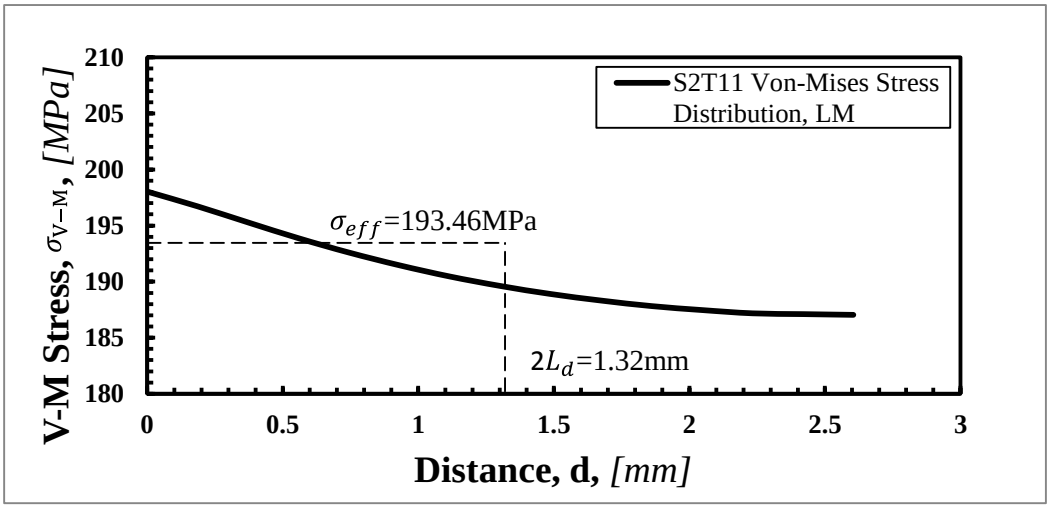

Figure 6. 73 Using the Line Method for predicting the material strength of intermediately notched Al6063-T5 sample S2T11 by post-processing the elasto-plastic V-M stress field.

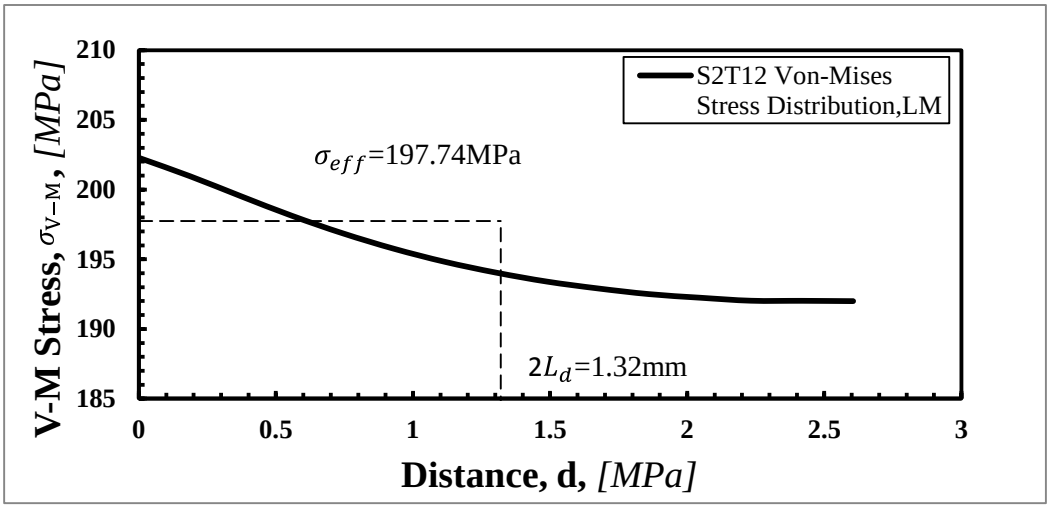

Figure 6. 74 Using the Line Method for predicting the material strength of intermediately notched Al6063-T5 sample S2T12 by post-processing the elasto-plastic V-M stress field.

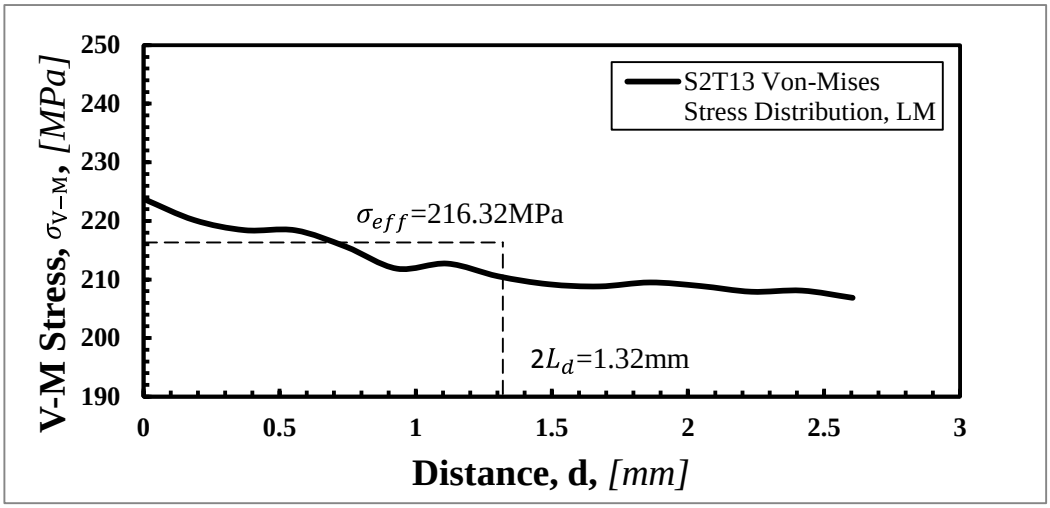

Figure 6. 75 Using the Line Method for predicting the material strength of intermediately notched Al6063-T5 sample S2T13 by post-processing the elasto-plastic V-M stress field.

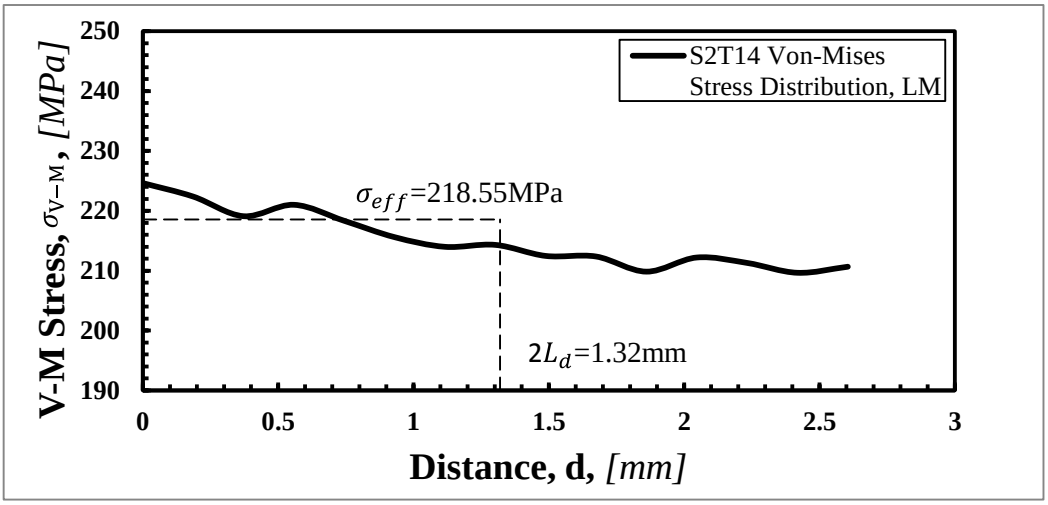

Figure 6.76 Using the Line Method for predicting the material strength of intermediately notched Al6063-T5 sample S2T14 by post-processing the elasto-plastic V-M stress field.

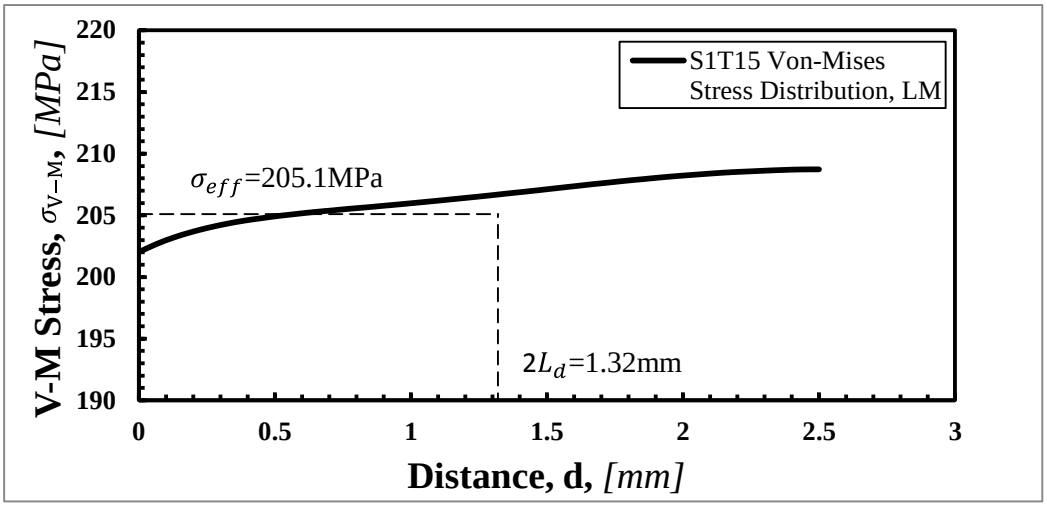

Figure 6. 77 Using the Line Method for predicting materials strength of bluntly notched Al6063-T5 sample S1T15 by post-processing the elasto-plastic V-M stress field.

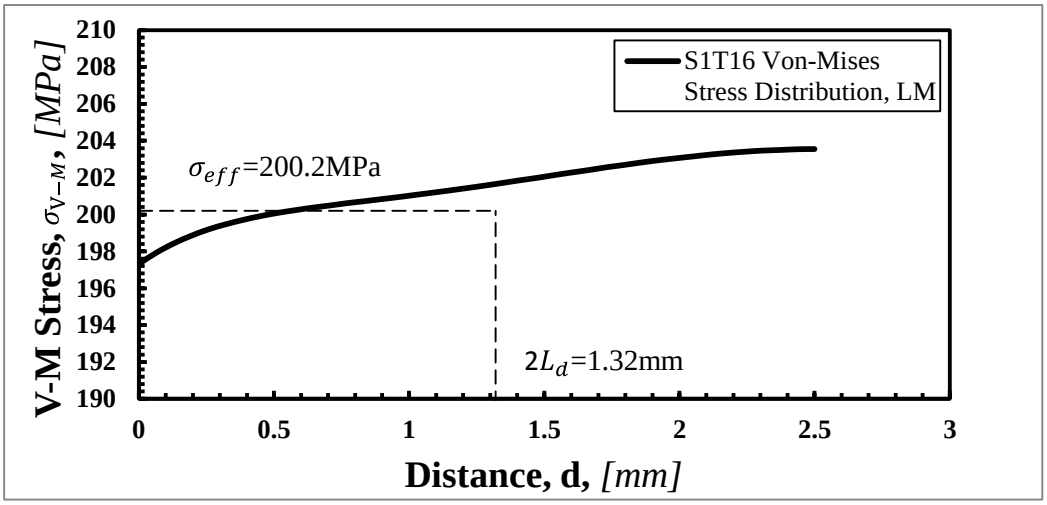

Figure 6.78 Using the Line Method for predicting materials strength of bluntly notched Al6063-T5 sample S1T16 by post-processing the elasto-plastic V-M stress field.

Moreover, from the V-M stress distributions obtained from models of sharply notched samples S1T10, S2T1 and S2T2 subjected to dynamic loading (Figure 6.63, 6.64 and 6.65), the average effective stresses were calculated as 220.52MPa, 211.85MPa and 209.17MPa respectively, and the corresponding plain V-M strengths $\bar{\sigma}_{VM}$ are 224.59MPa, 212.97MPa and 223.01MPa. According to these values, it can be seen that the difference between the average effective stress and the plain V-M strength are very small. The error can be calculated according to Equation 6.3.

$$\text{Error}(\%) = \frac{\sigma_{\text{eff}} - \bar{\sigma}_{\text{o,VM}}}{\bar{\sigma}_{\text{o,VM}}} * 100 \qquad (6.\ 2)$$

The effective stresses for intermediately and bluntly notched samples were all calculated in the same way as for the sharply notched sample, see Figures 6.43 and 6.44. The predicted results for all of the samples are summarised in Table 6.4.

The error diagram plotted in Figure 6.79 makes it evident that the TCD can be used to predict the strength of material Al6063-T5 accurately with estimates falling within an error interval of about $\pm 6\%$ when the inherent material V-M strength $\bar{\sigma}_{0,VM}$ is taken equal to the plain material V-M strength $\bar{\sigma}_{VM}$. Additionally, the difference between the predictions from the PM and LM is very small; both methods are capable of predicting the dynamic strength of material Al6063-T5.

Table 6.4 Accuracy in predicting the strength of the notched samples by applying the TCD (PM and LM)

Tests	**Plain V-M Strength, $\bar{\sigma}_{VM}$ ($=\bar{\sigma}_{0,VM}$) *[MPa]***	**Effective Stress σ_{eff} *[MPa]***		**Error *[%]***	
		PM	**LM**	**PM**	**LM**
S1 T9	191.58	200.00	192.15	4.39	0.29
S1 T10	224.59	234.00	223.49	4.19	-0.49
S2 T1	212.97	225.00	214.69	5.65	0.81
S2 T2	223.01	222.00	211.98	-0.45	-4.94
S1 T17	205.13	198.00	196.09	-3.47	-4.41
S1 T18	224.85	225.00	221.34	0.07	-1.56
S2 T5	205.51	196.00	193.84	-4.63	-5.68
S2 T6	204.85	196.50	194.38	-4.08	-5.11
S2 T7	223.24	219.00	215.35	-1.90	-3.54
S2 T9	220.18	223.00	220.11	1.28	-0.03
S2 T10	217.09	217.00	214.27	-0.04	-1.30
S2 T11	205.82	195.50	193.46	-5.01	-6.01
S2 T12	206.34	200.00	197.74	-3.07	-4.16
S2 T13	218.72	218.50	216.32	-0.10	-1.10
S2 T14	218.08	219.00	218.55	0.42	0.22
S1 T15	204.55	204.50	205.10	-0.03	0.27
S1 T16	204.91	199.50	200.20	-2.64	-2.30

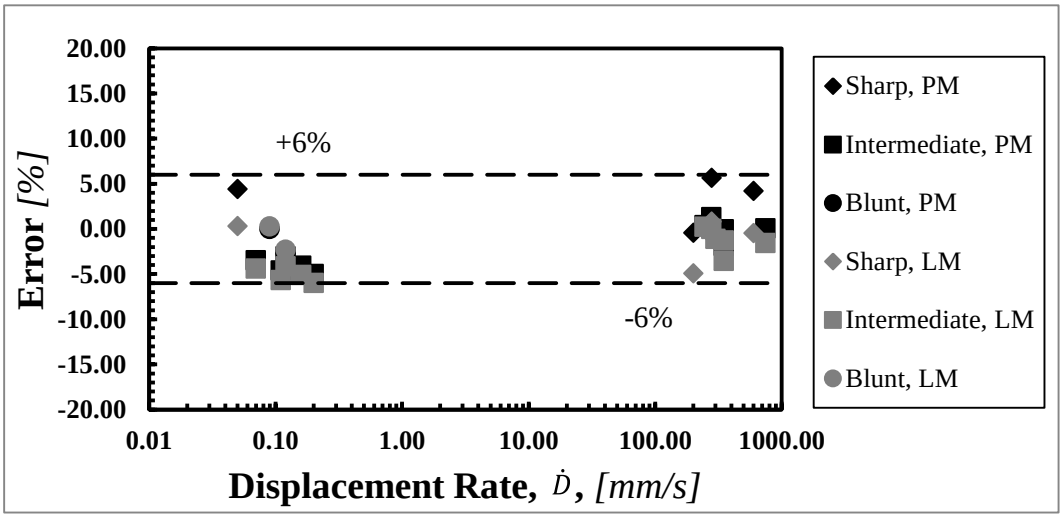

Figure 6.79 Accuracy in predicting the strength of material Al6063-T5 subjected to dynamic loading by using the TCD.

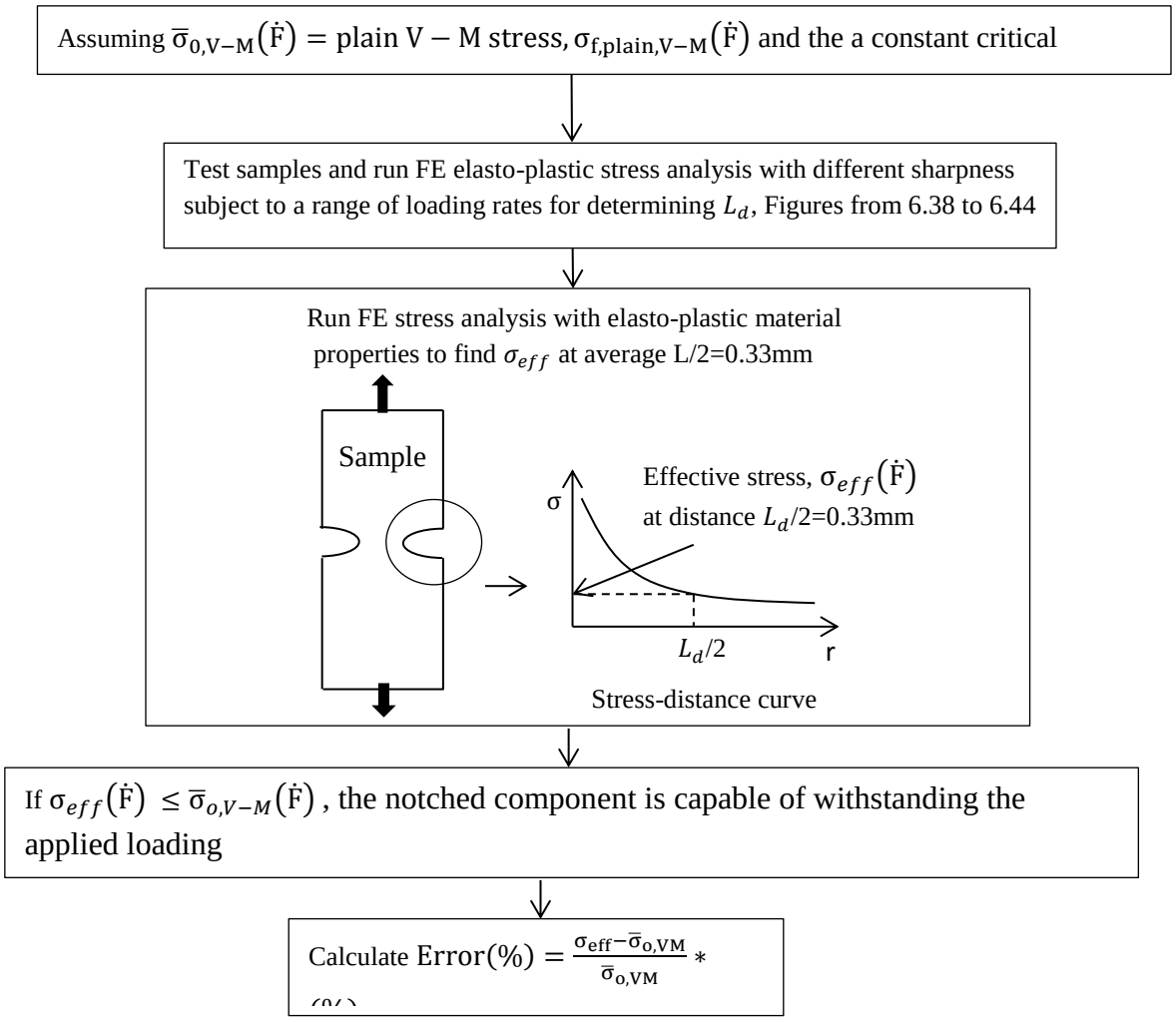

Figure 6. 80 Flow chart of Elasto-plastic TCD procedures.

The whole prediction procedure has been summarised in the flow chat as shown in Figure 6.80.

In this chapter, the predictions from using elasto-plastic simulations and the elasto-plastic TCD have been introduced. The results fully confirm that the two approaches can predict the dynamic strength of notched samples successfully and accurately. In the next chapter, a comparison between the results obtained using the linear elastic TCD, elasto-plastic simulations and the elasto-plastic TCD will be carried out in order to find out the advantages and disadvantages of these methods.

References

MEYERS, M. A. 1994. *Dynamic behavior of materials*, John wiley & sons.

SUSMEL, L. & TAYLOR, D. 2008. On the use of the Theory of Critical Distances to predict static failures in ductile metallic materials containing different geometrical features. *Engineering Fracture Mechanics,* 75**,** 4410-4421.

TAYLOR, D. 2007. *The Theory of Critical Distances: A New Perspecive in Fracture Mechanics,* Elsevier Science Limited.

TYAS, A. & WATSON, A. J. 2000. Experimental evidence of Pochammer-Chree strain variations in elastic cylinders. *Experimental Mechanics,* 40**,** 331-337.

YIN, T., TYAS, A., PLEKHOV, O., TEREKHINA, A. & SUSMEL, L. 2015. A novel reformulation of the Theory of Critical Distances to design notched metals against dynamic loading. *Materials & Design,* 69**,** 197-212.

Chapter 7: Discussion and Conclusions

7.1 Comparison of the results from the linear-elastic TCD, LS-DYNA modelling and the elastic-plastic TCD

In this thesis it has been demonstrated that the dynamic strength of notched metallic specimens can be predicted successfully by using a reformulated linear elastic TCD, LS-DYNA elasto-plastic simulations and an elasto-plastic TCD. A comparison between these three approaches is discussed below.

With regard to the accuracy of the predictions, the diagram in Figure 7.1 shows a comparison between the errors from the simple linear elastic TCD and the more sophisticated elasto-plastic dynamic FE modelling done using LS-DYNA. It is clear that the predictions from the linear elastic solution are slightly more accurate than those from the elasto-plastic LS-DYNA solutions, although the LS-DYNA predictions are more conservative.

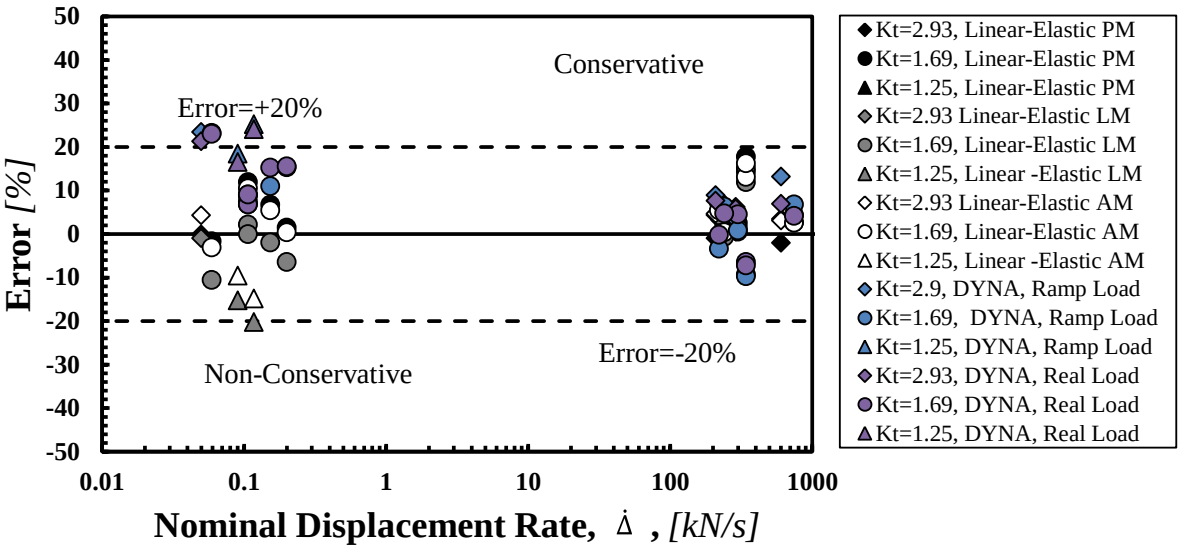

Figure 7.1 Accuracy of predictions for the strength of notched Al6063-T5 from both the linear elastic TCD and elasto-plastic LS-DYNA modelling.

A similar comparison between the accuracy of the predictions from the linear elastic TCD with those from the elasto-plastic TCD is shown in Figure 7.2. It is clear from this figure that the elasto-plastic TCD gives more accurate predictions than the linear elastic TCD solution. The error band for the elasto-plastic TCD calculations is approximately $\pm 6\%$, whereas the error band for the linear elastic TCD predictions is approximately $\pm 20\%$.

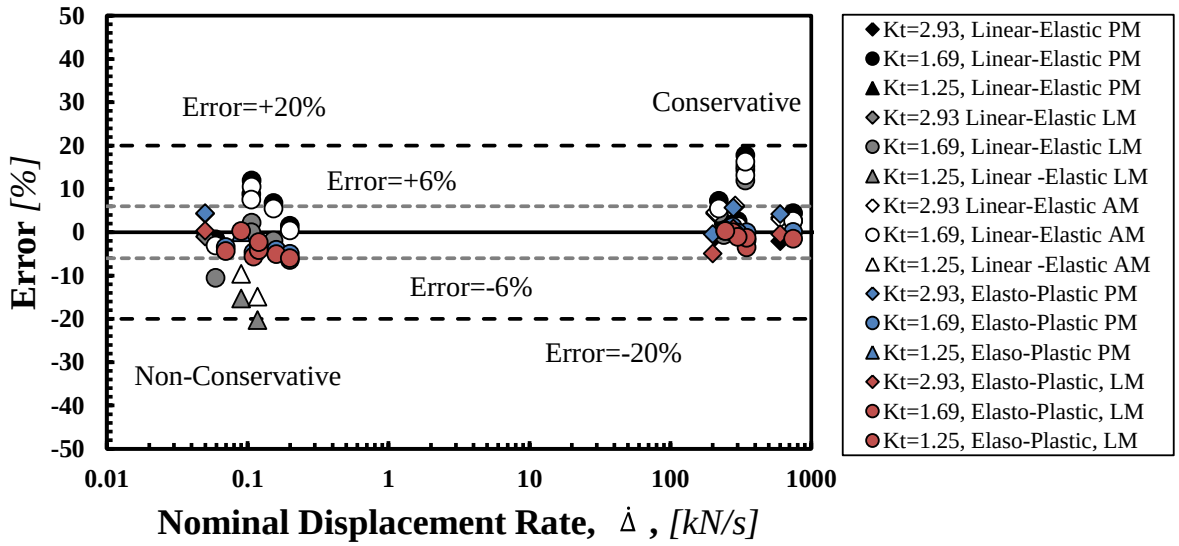

Figure 7.2 Accuracy in predicting the strength of notched Al6063-T5 by using both linear elastic TCD solution and elasto-plastic TCD solution.

From a practical point of view, an important consideration regarding both the LS-DYNA elasto-plastic simulations and the elasto-plastic TCD is that they are very time-consuming and are therefore not readily applicable to industrial design. Even for the simple geometries considered in the present investigation, the elasto-plastic calculations took considerably longer to solve and required significantly more computing power than the simple linear elastic TCD analyses. In engineering design, structures and components have more complex geometries than the samples modelled here which would significantly increase the time and cost of LS-DYNA simulations and the required optimisation of the elasto-plastic analyses.

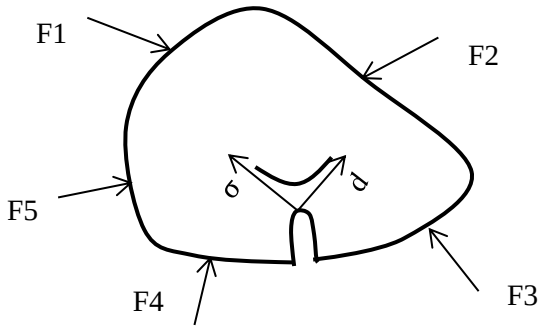

Figure 7.3 Irregular geometry of notched structural component with multi-directional applied dynamic loads.

For example, in order to model an irregular notched structural component with dynamic loads applied from more than one direction, as shown in Figure 7.3, the boundary conditions for an

LS-DYNA model would be much more complicated than those for the simple cylindrical bar loaded in tension considered in this study. This would dramatically increase the computing time. However, using the modified linear elastic approach to address the same problem, a large number of iterations can be completed in the same time period, which makes it a more useful design tool. In addition, the predictions from the simple linear elastic TCD method are slightly more accurate than those from the LS-DYNA elasto-plastic simulations. Therefore from the design point of view, the linear elastic approach is the obvious choice as it offers engineers and designers a quick, simple approach with improved accuracy over the more modern but time consuming FE simulations.

In summary, the simplified linear elastic solution developed here could decrease both the time and cost of the design process, as it gives faster, more accurate results than more complex dynamic FE modelling. It has been demonstrated that the levels of accuracy offered by this novel approach are sufficient for engineering design. However, if more accurate results are required, the use of the elasto-plastic TCD method should be considered. In addition, the simplified linear elastic approach has proven to be useful for fully understanding the development of damage in the critical regions in the components investigated in terms of loading and boundary conditions.

However, this area is still need to be investigated in more detail. For example, due to the limitation of the testing rig, the tested loading rates are focusing on low and high range, there is a big gap in intermediate loading rate. Hence, lots of material components with both same and different notches need to be tested in order to have more results to fill the strain rate gap and further validate the proposed TCD. Moreover, the accuracy of the testing rig at university of Sheffield need to be upgraded in order to record more accurate results to have clear strain and strain rate history. Additionally, in this thesis, the analysis is only focusing few types of metallic materials, and it is really worth to expand our theory to other kinds of materials, such as other types of metallic material, concrete, ceramic and so on. Moreover, the micro-structure behaviour of material subjected to dynamic loading is also an important aspect in understanding complex dynamic material behaviours, and it is also needed to be considered in the further work. Additional, the testing rig we used for our experimental test need to be upgraded in order to have better results. Specifically, due to the low definition video clips recorded by high speed camera, the elastic deformation was very difficult to be spotted, in further work, a proper stain gauge might be essential for further tests.

7.2 Conclusions

In this thesis, a novel reformulation of the linear-elastic TCD suitable for designing notched metallic materials under dynamic loading was developed and validated by experiment.

Predictions from LS-DYNA elasto-plastic FE simulations and the elasto-plastic TCD were also made for comparison. The main conclusions can be summarised as follows:

1. The proposed design methodology allows components to be designed for dynamic loading based on the stress fields determined via conventional linear-elastic FE modelling. Sufficiently accurate estimates of failure loads can be obtained without the need for explicitly modelling the mechanical response under dynamic loading.

2. Comparison with experimental results demonstrated that the proposed reformulation of the TCD gives reliable estimates for the strength of notched metallic components subjected to dynamic loading.

3. The same degree of accuracy was achieved using the linear elastic TCD with the PM, LM, or AM approach.

4. The estimates for dynamic strengths calculated using the linear elastic TCD were within ±20% of the measured values. It is therefore recommended that for the future design of notched metallic components, a safety factor greater than 1.25 should be adopted.

5. It has been demonstrated that LS-DYNA elasto-plastic simulations can predict the dynamic strength of notched metallic components within an error of approximately ±20%.

6. The elasto-plastic TCD analyses predicted the dynamic strength of the notched metallic components within an error of approximately ±6%.

7. For the elasto-plastic TCD analyses, the same degree of accuracy was achieved using both the PM and LM approaches.

8. In terms of required computational time, the novel linear elastic TCD method presented here is the best tool for designing components subjected to dynamic loading. If higher accuracy is required, the use of the elasto-plastic TCD should be considered.

9. It is recommended that further research be carried out to extend the use of the proposed methodology to cases involving both axial and multiaxial dynamic loading.

Appendix 3

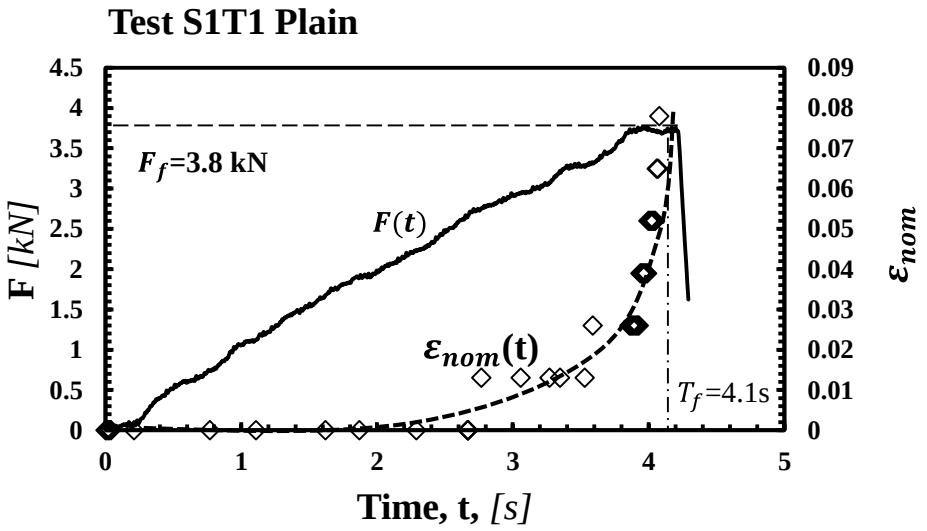

Figure A3. 1 Force vs. time and nominal strain vs. time curve for test S1 T1.

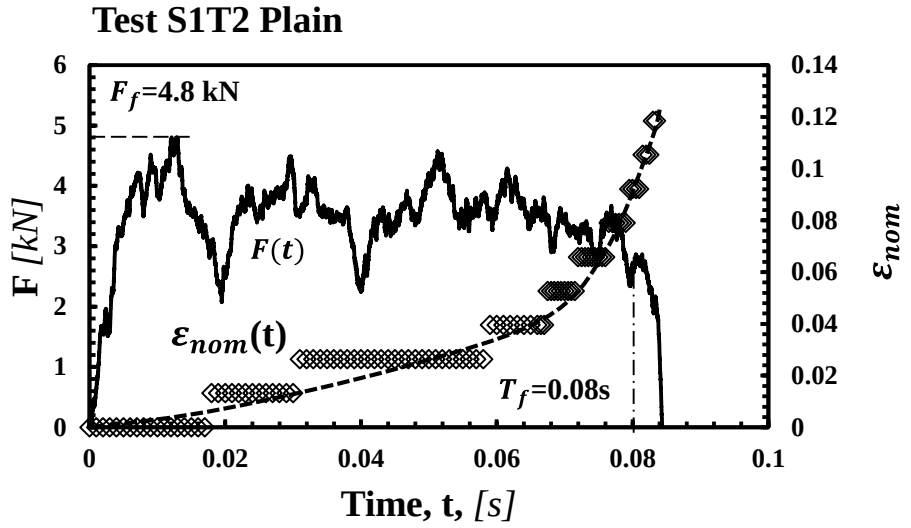

Figure A3. 2 Force vs. time and nominal strain vs. time curve for test S1 T2.

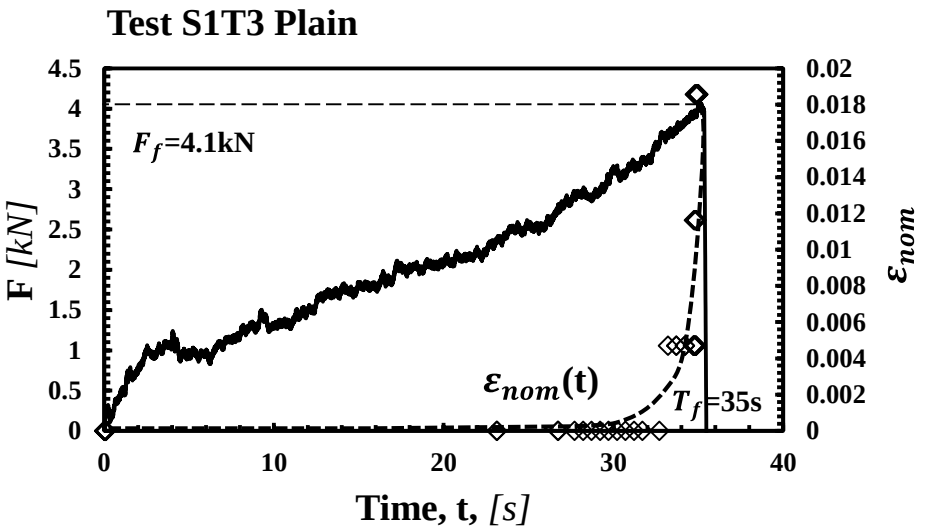

Figure A3. 3 Force vs. time and nominal strain vs. time curve for test S1 T3.

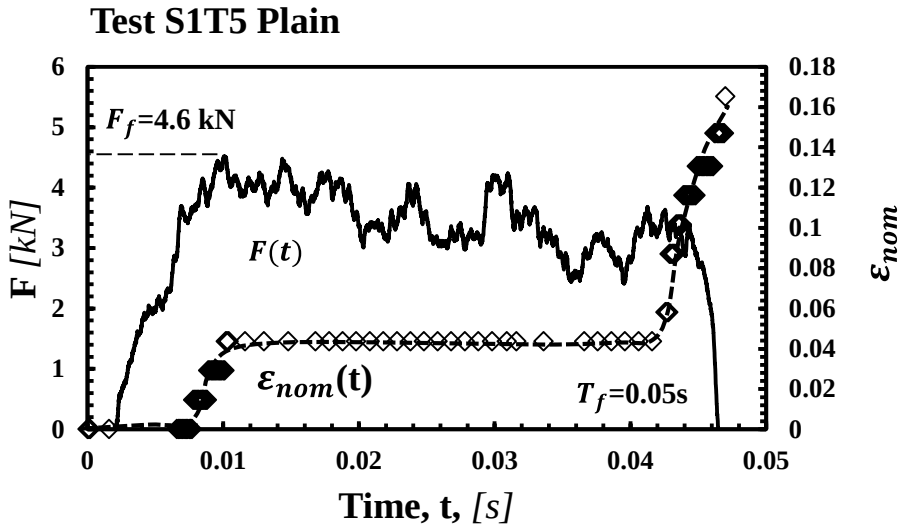

Figure A3. 4 Force vs. time and nominal strain vs. time curve for test S1 T5.

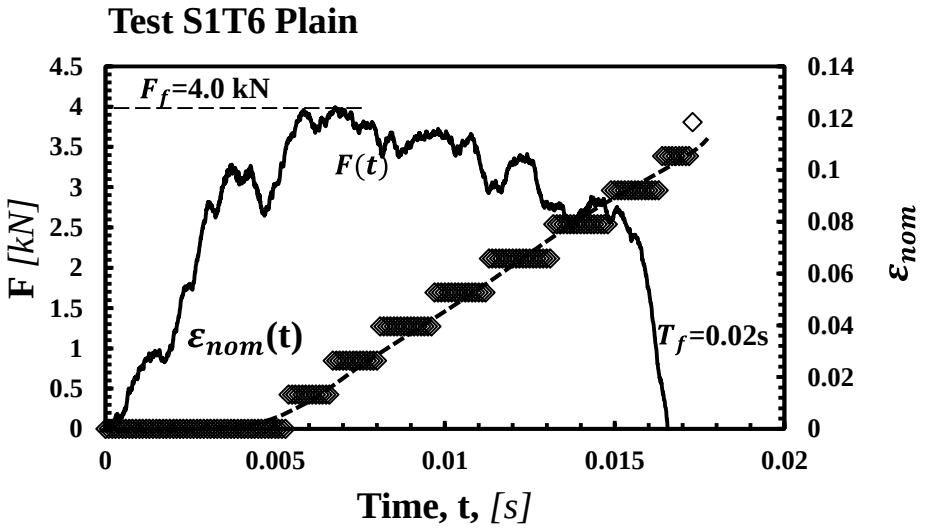

Figure A3. 5 Force vs. time and nominal strain vs. time curve for test S1 T6.

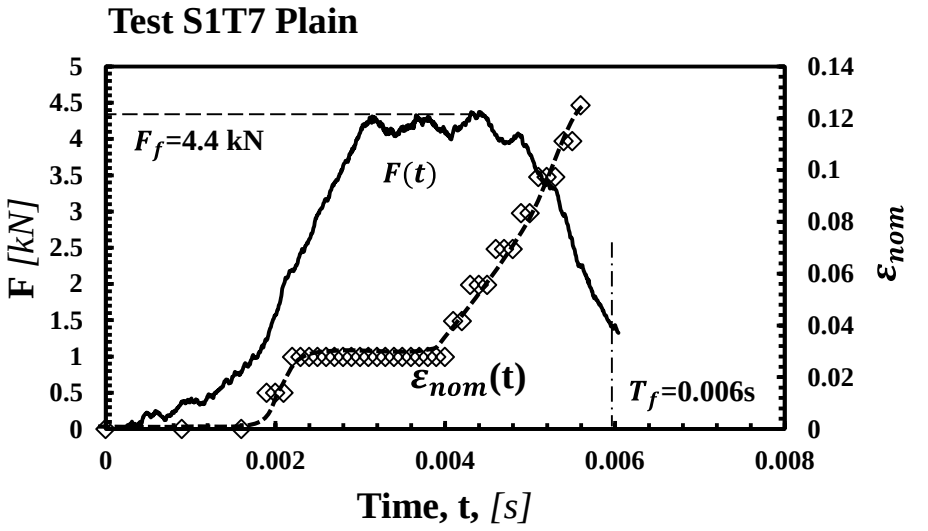

Figure A3. 6 Force vs. time and nominal strain vs. time curve for test S1 T7.

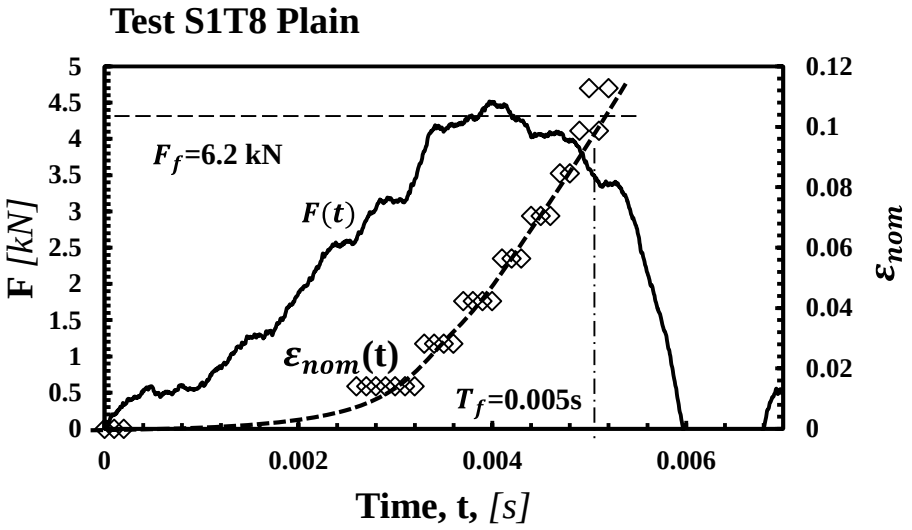

Figure A3. 7 Force vs. time and nominal strain vs. time curve for test S1 T8.

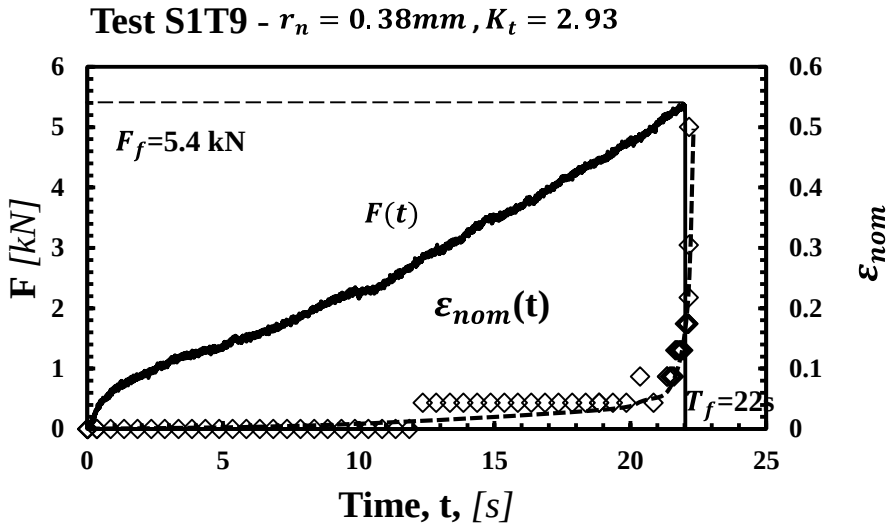

Figure A3. 8 Force vs. time and nominal strain vs. time curve for test S1 T9.

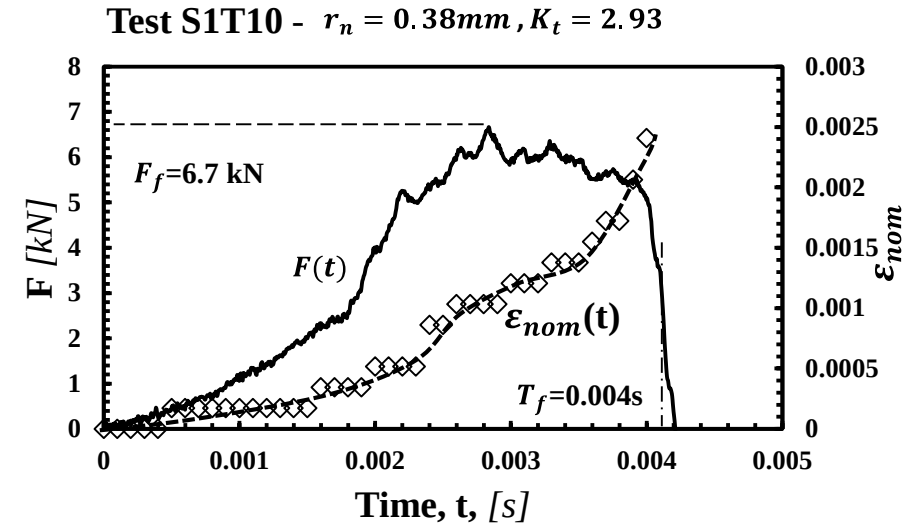

Figure A3. 9 Force vs. time and nominal strain vs. time curve for test S1 T10.

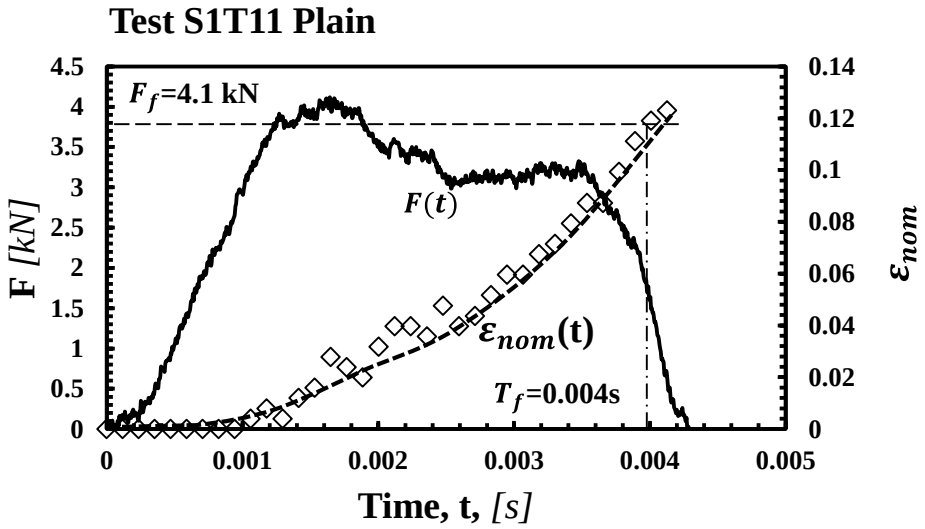

Figure A3. 10 Force vs. time and nominal strain vs. time curve for test S1 T11.

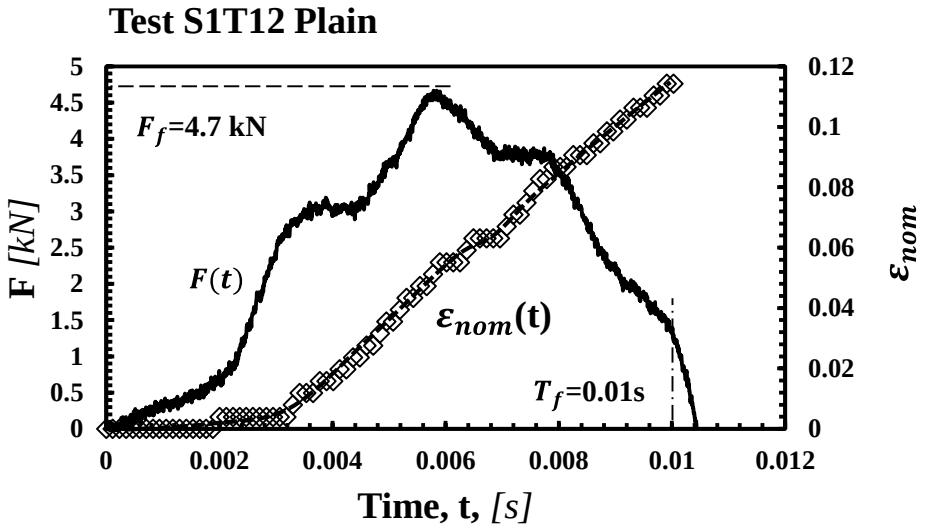

Figure A3. 11 Force vs. time and nominal strain vs. time curve for test S1 T12.

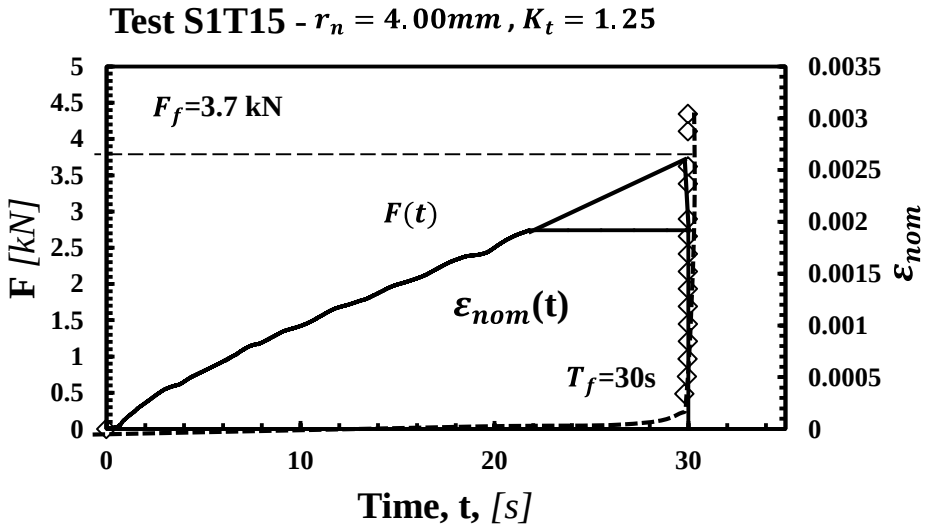

Figure A3. 12 Force vs. time and nominal strain vs. time curve for test S1 T15.

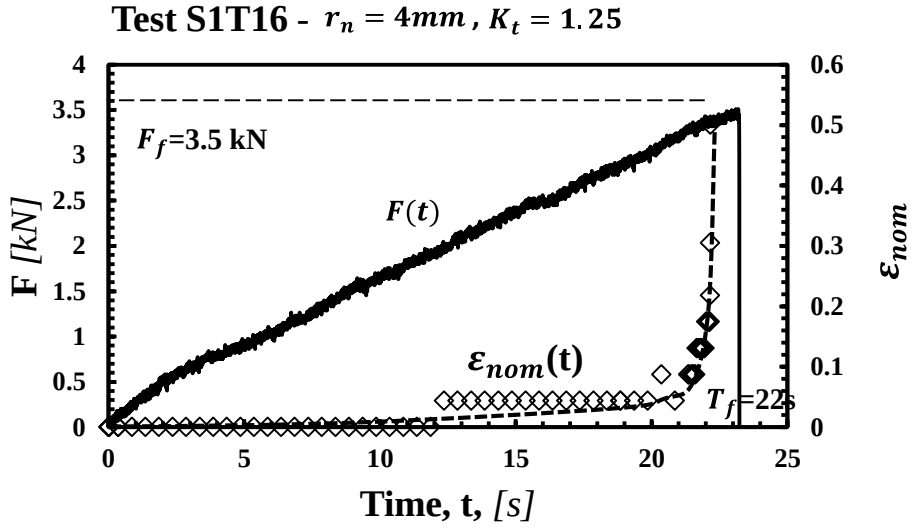

Figure A3. 13 Force vs. time and nominal strain vs. time curve for test S1 T16.

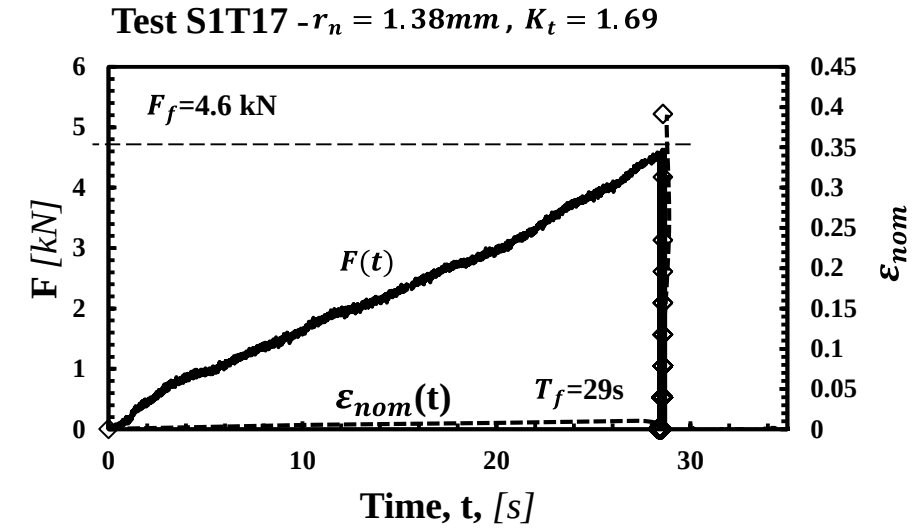

Figure A3. 14 Force vs. time and nominal strain vs. time curve for test S1 T17.

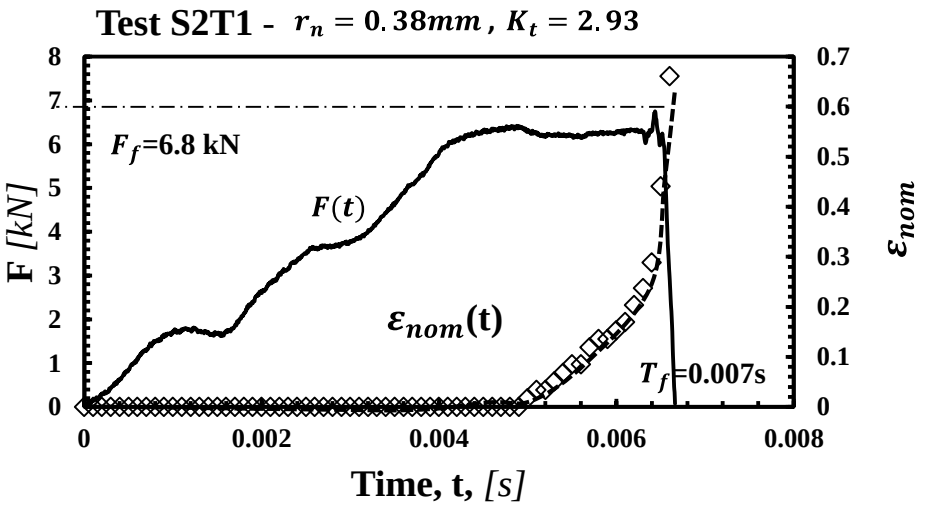

Figure A3. 15 Force vs. time and nominal strain vs. time curve for test S2 T1.

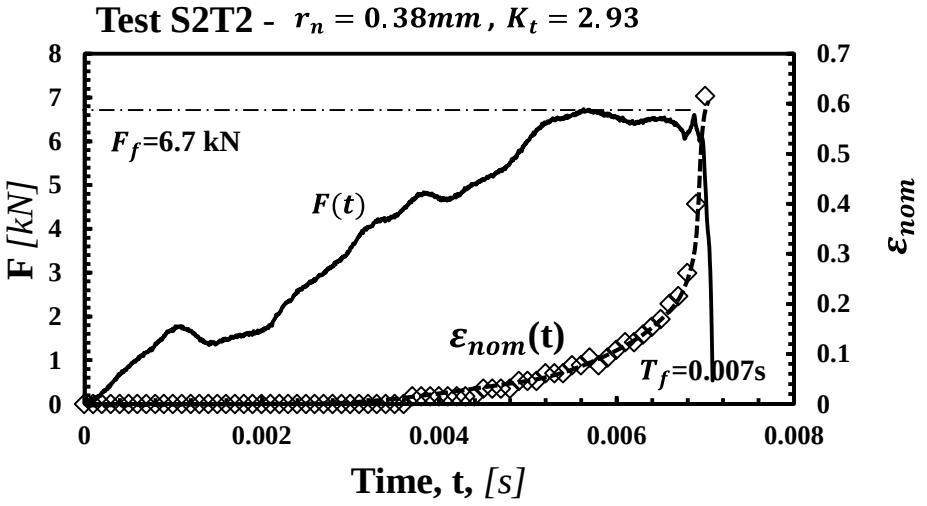

Figure A3. 16 Force vs. time and nominal strain vs. time curve for test S2 T2.

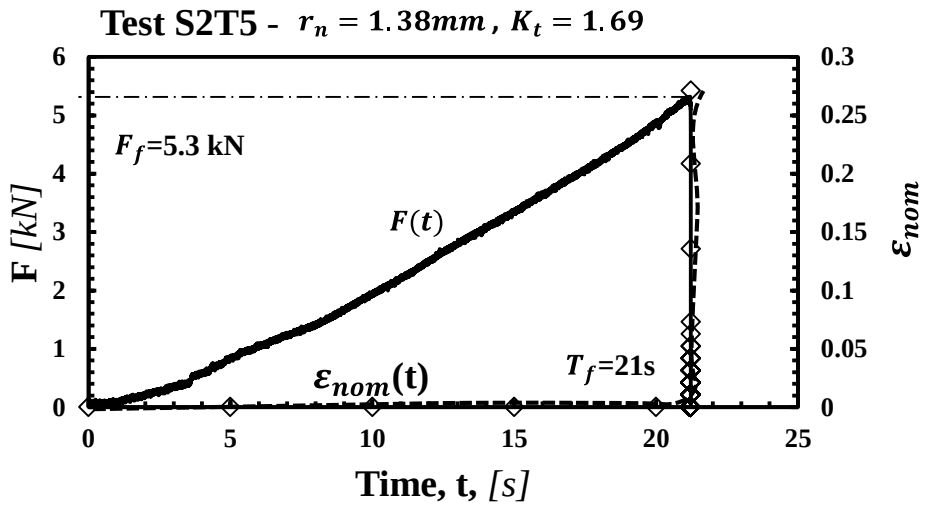

Figure A3. 17 Force vs. time and nominal strain vs. time curve for test S2 T5.

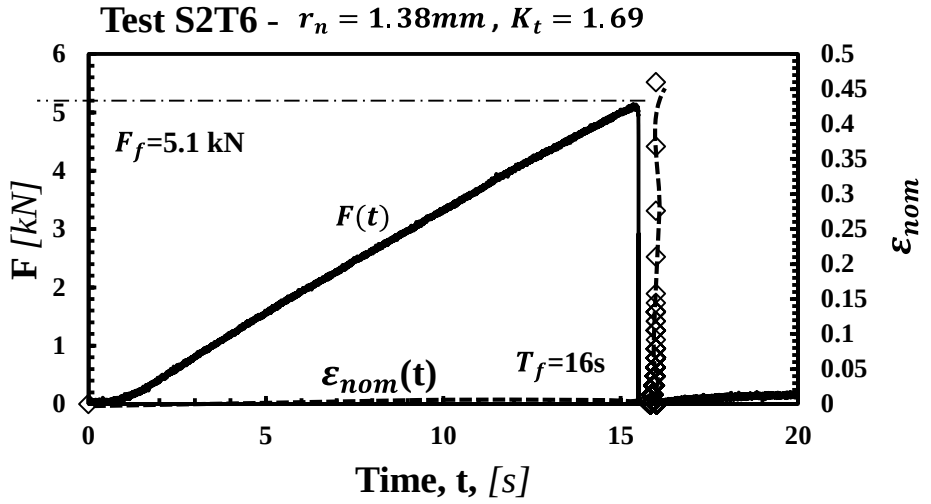

Figure A3. 18 Force vs. time and nominal strain vs. time curve for test S2 T6.

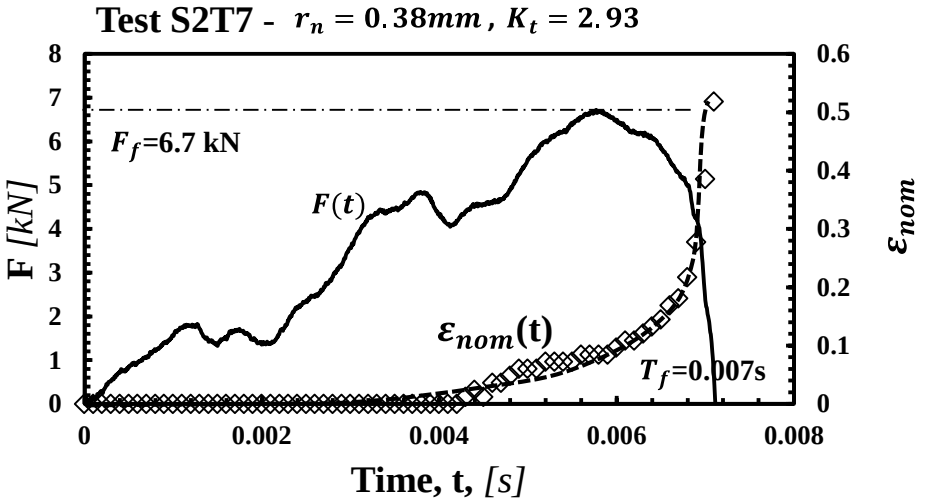

Figure A3. 19 Force vs. time and nominal strain vs. time curve for test S2 T7.

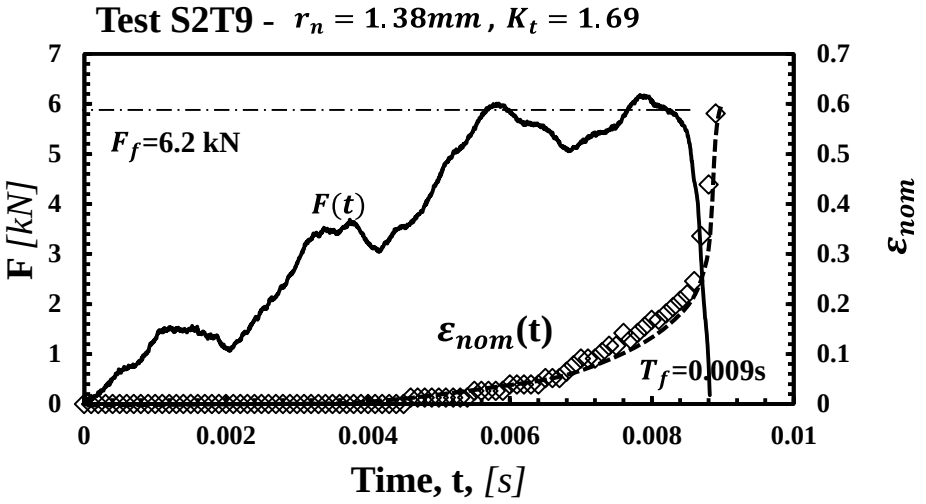

Figure A3. 20 Force vs. time and nominal strain vs. time curve for test S2 T9.

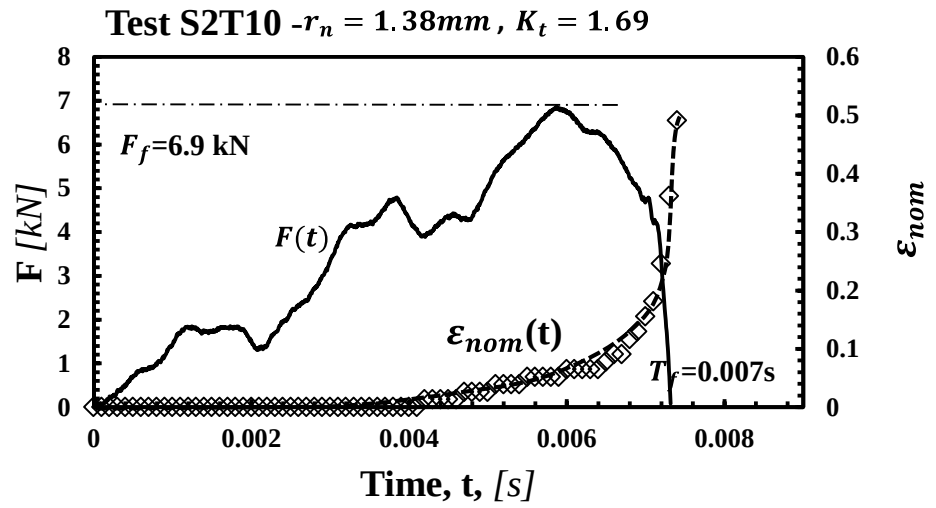

Figure A3. 21 Force vs. time and nominal strain vs. time curve for test S2 T10.

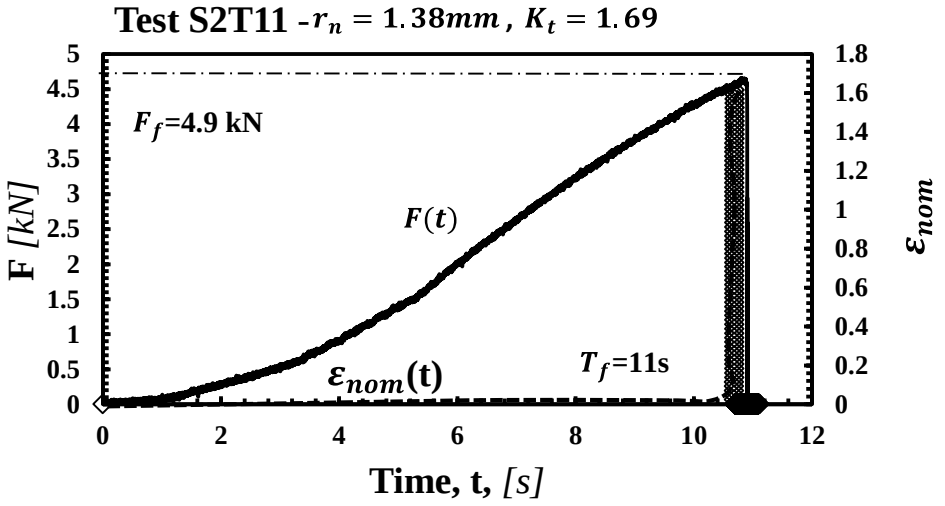

Figure A3. 22 Force vs. time and nominal strain vs. time curve for test S2 T11.

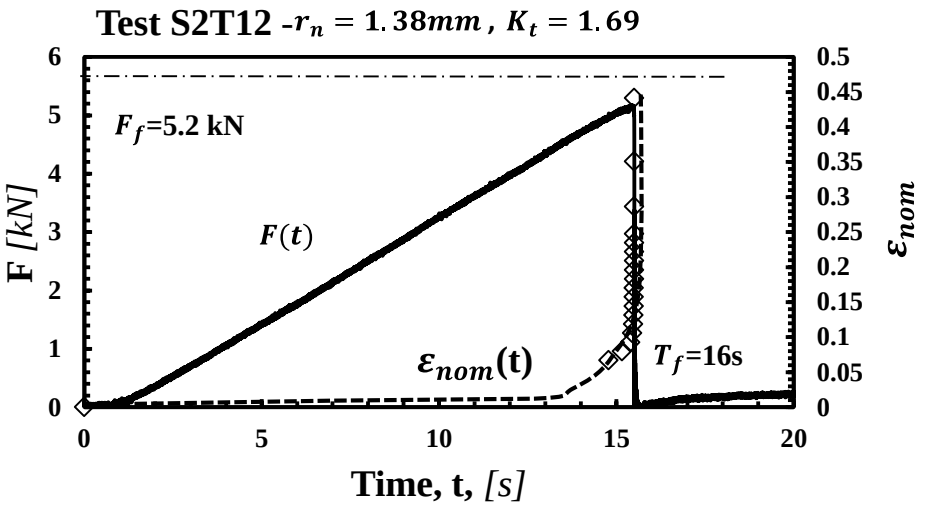

Figure A3. 23 Force vs. time and nominal strain vs. time curve for test S2 T12.

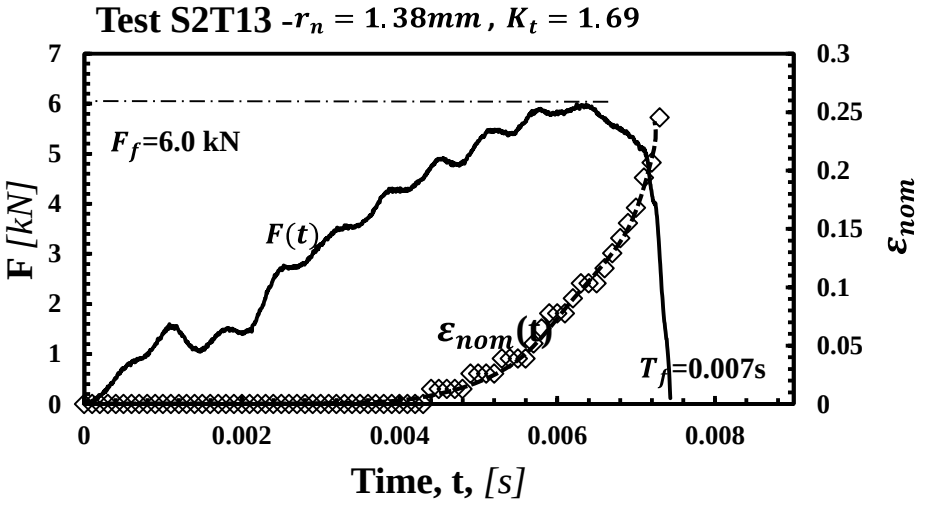

Figure A3. 24 Force vs. time and nominal strain vs. time curve for test S2 T13.

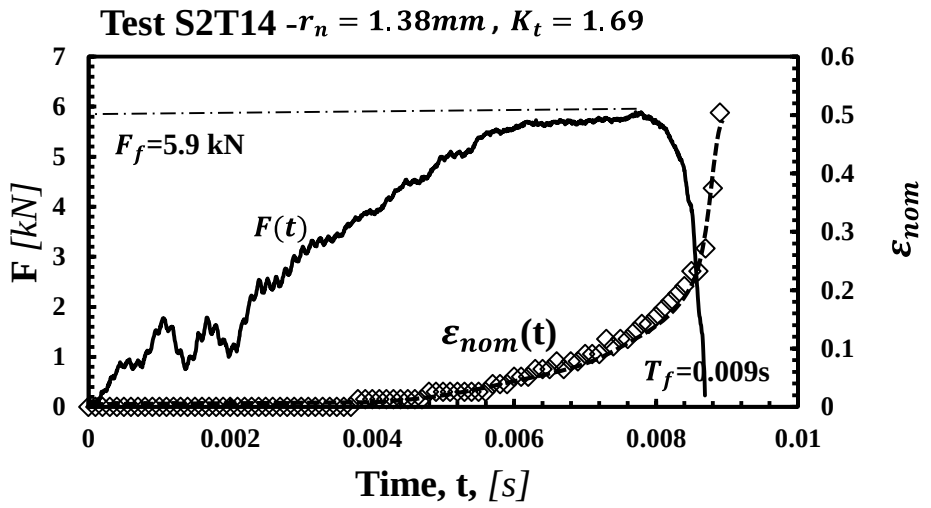

Figure A3. 25 Force vs. time and nominal strain vs. time curve for test S2 T14.

Appendix 4

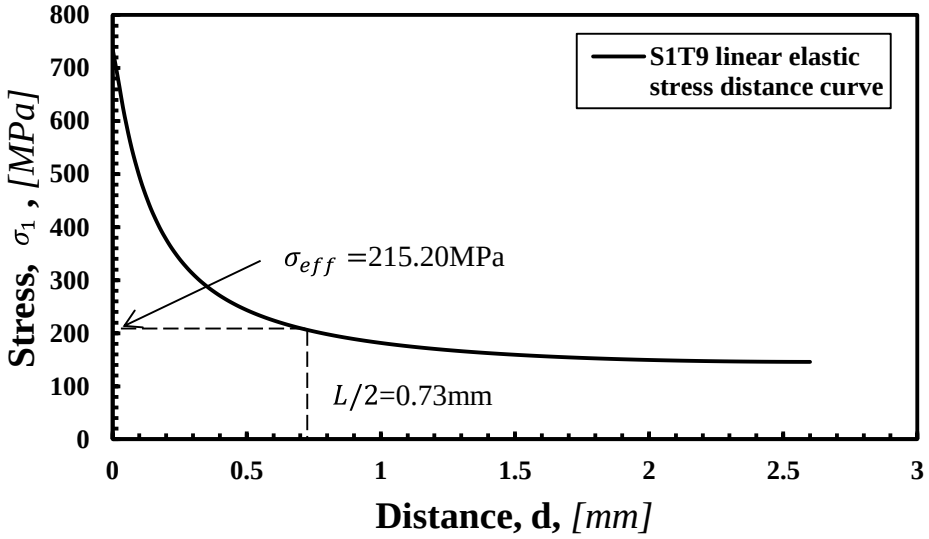

Figure A4. 1 Linear elastic stress distance curve of S1T9 in the incipient failure condition.

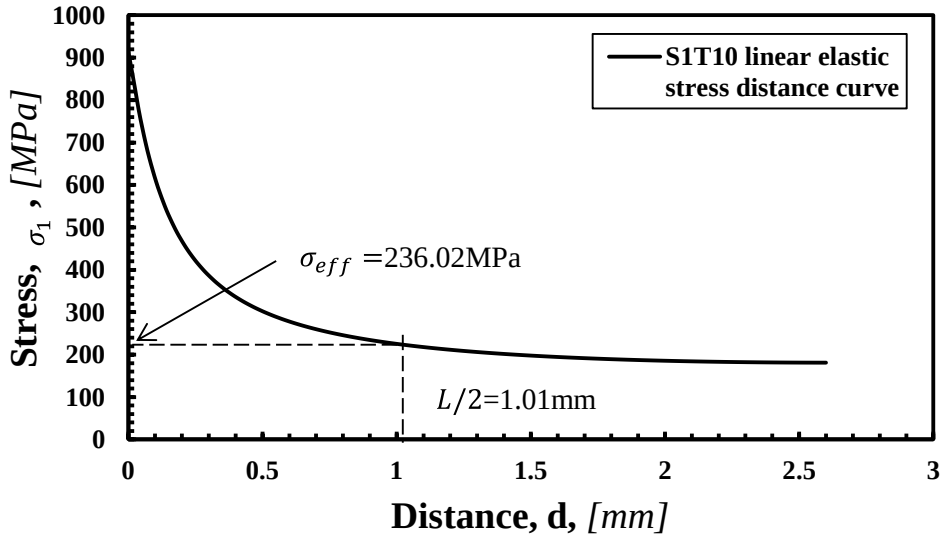

Figure A4. 2 Linear elastic stress distance curve of S1T10 in the incipient failure condition.

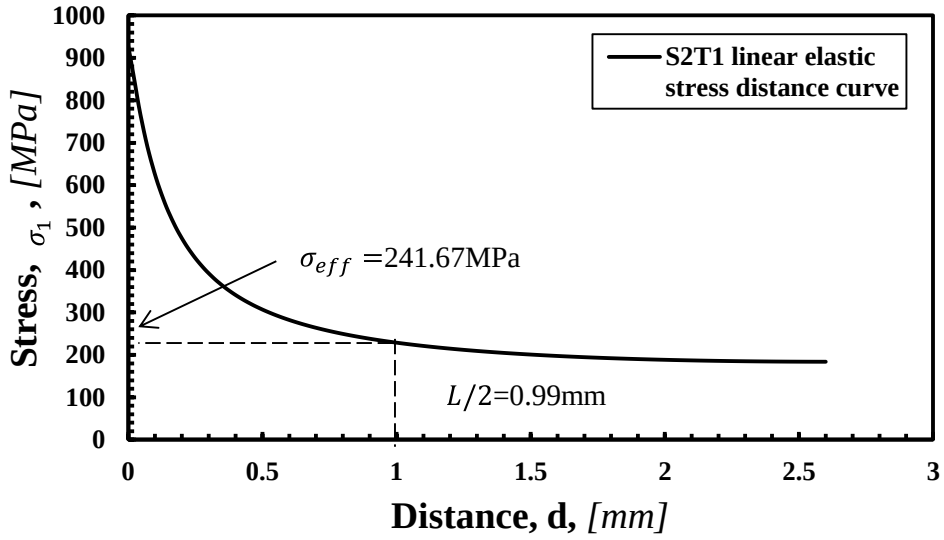

Figure A4. 3 Linear elastic stress distance curve of S2T1 in the incipient failure condition.

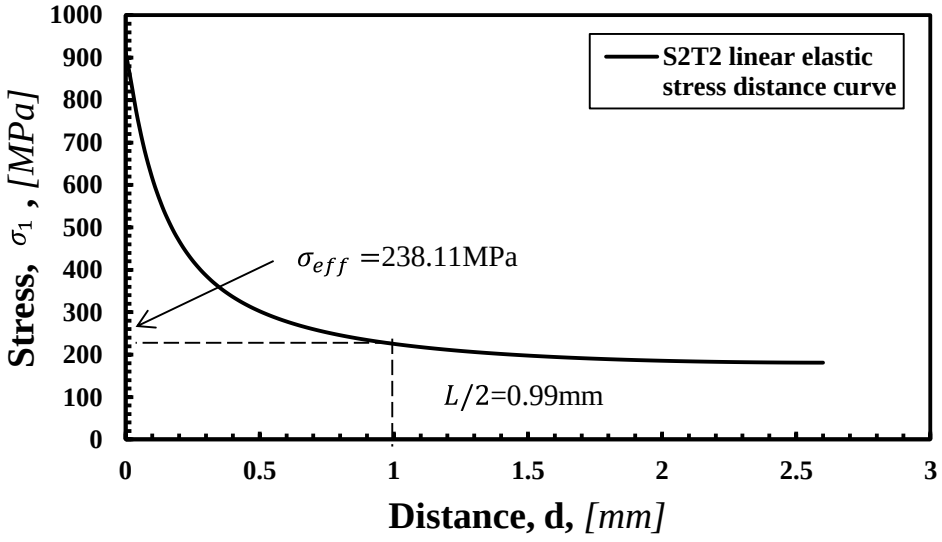

Figure A4. 4 Linear elastic stress distance curve of S2T2 in the incipient failure condition.

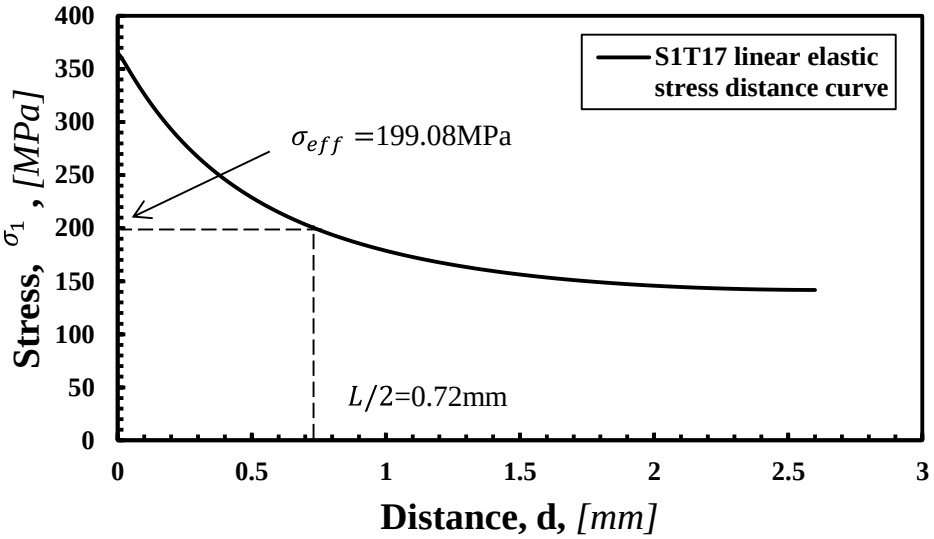

Figure A4. 5 Linear elastic stress distance curve of S1T17 in the incipient failure condition.

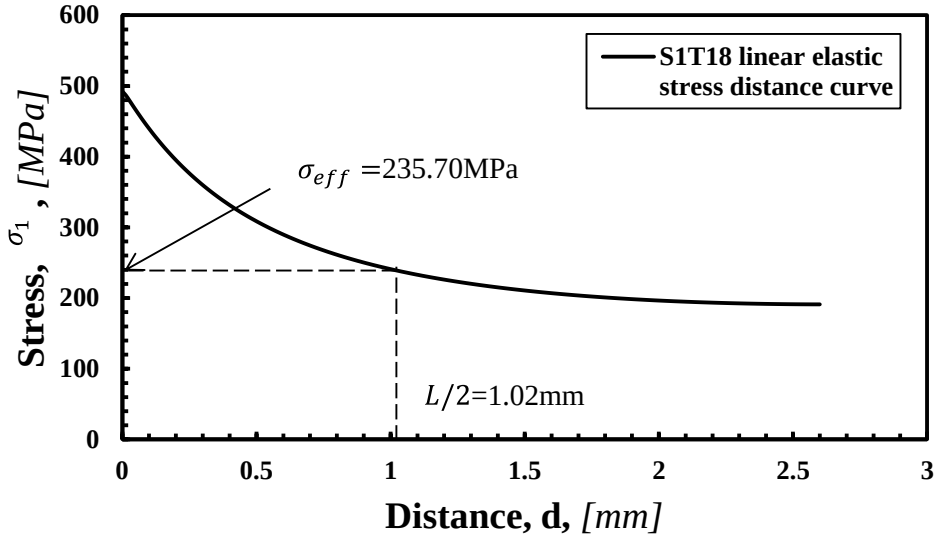

Figure A4. 6 Linear elastic stress distance curve of S1T18 in the incipient failure condition.

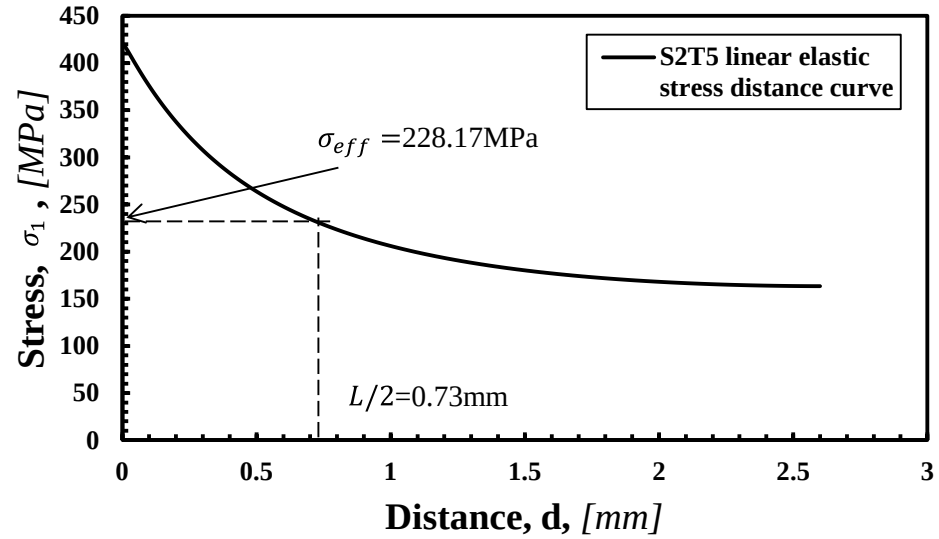

Figure A4. 7 Linear elastic stress distance curve of S2T5 in the incipient failure condition.

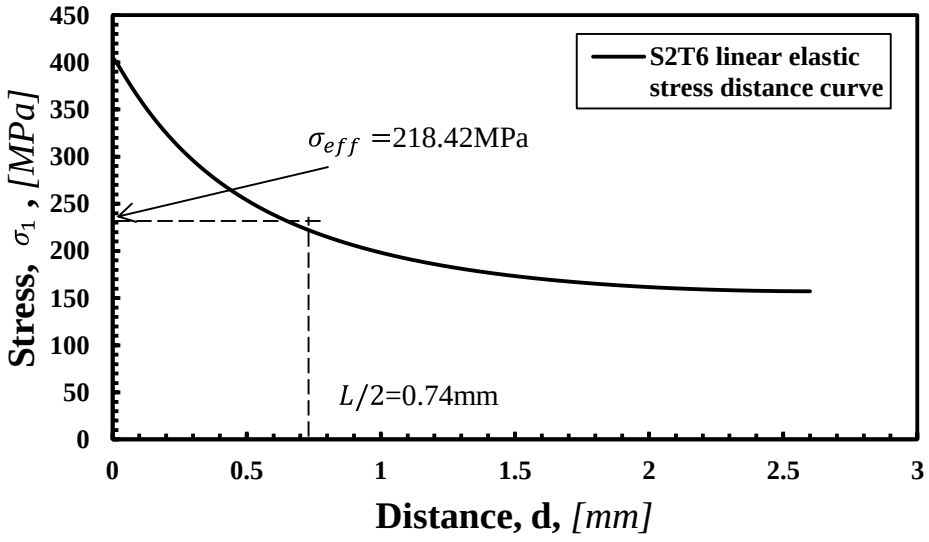

Figure A4. 8 Linear elastic stress distance curve of S2T6 in the incipient failure condition.

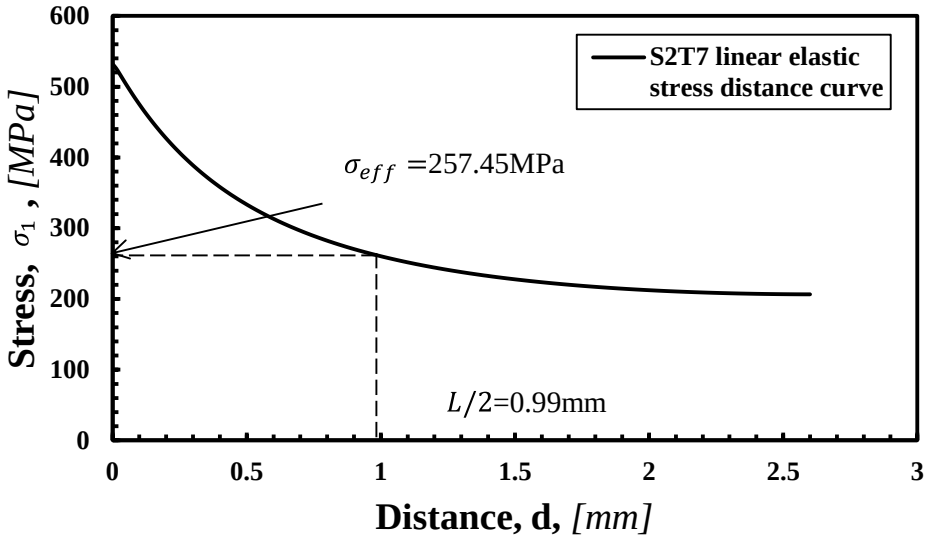

Figure A4. 9 Linear elastic stress distance curve of S2T7 in the incipient failure condition.

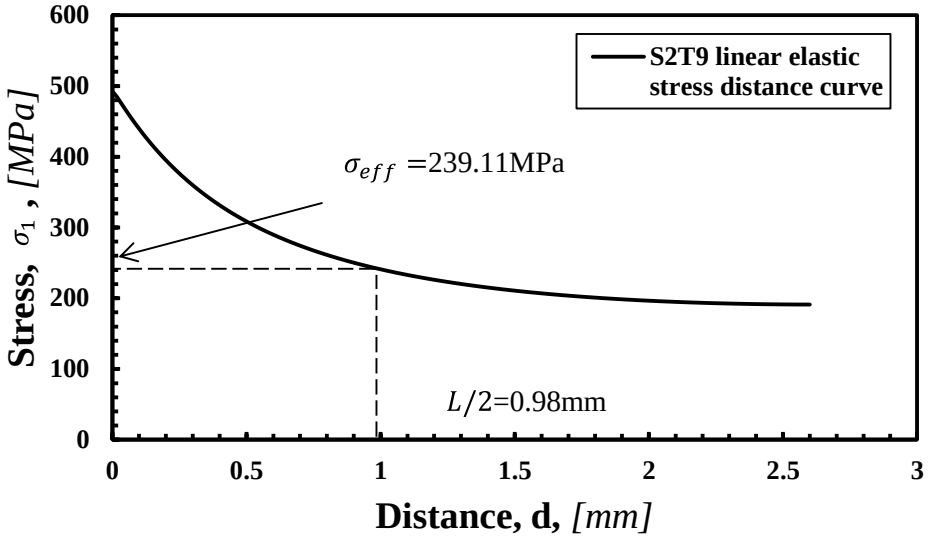

Figure A4. 10 Linear elastic stress distance curve of S2T9 in the incipient failure condition.

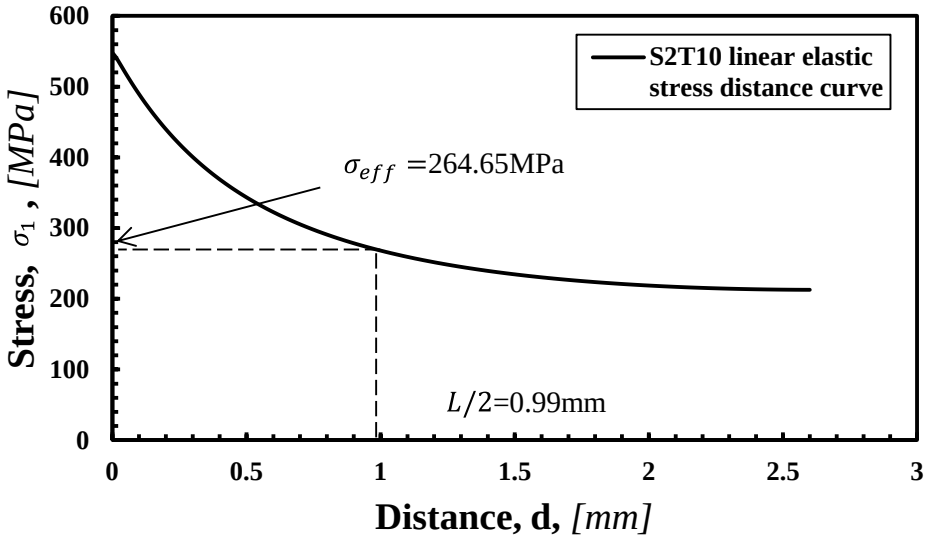

Figure A4. 11 Linear elastic stress distance curve of S2T10 in the incipient failure condition.

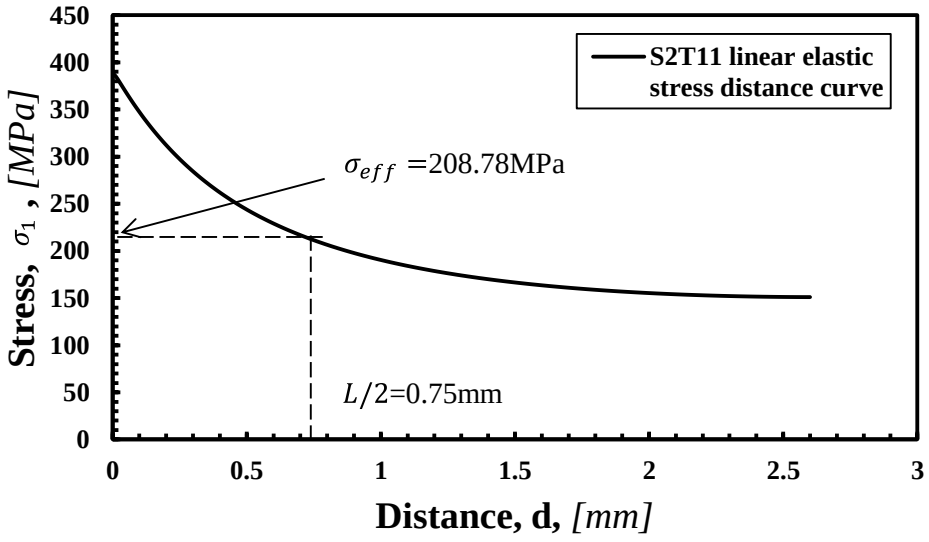

Figure A4. 12 Linear elastic stress distance curve of S2T11 in the incipient failure condition.

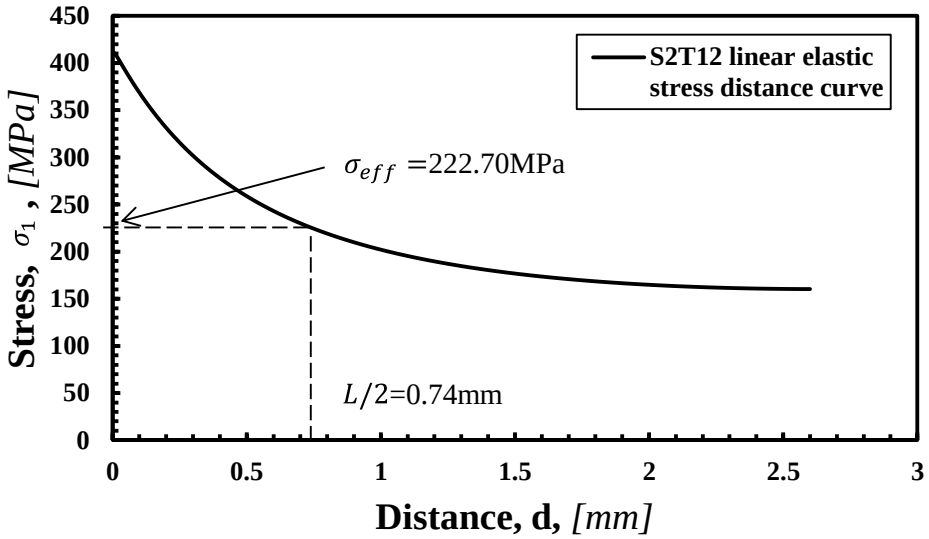

Figure A4. 13 Linear elastic stress distance curve of S2T11 in the incipient failure condition.

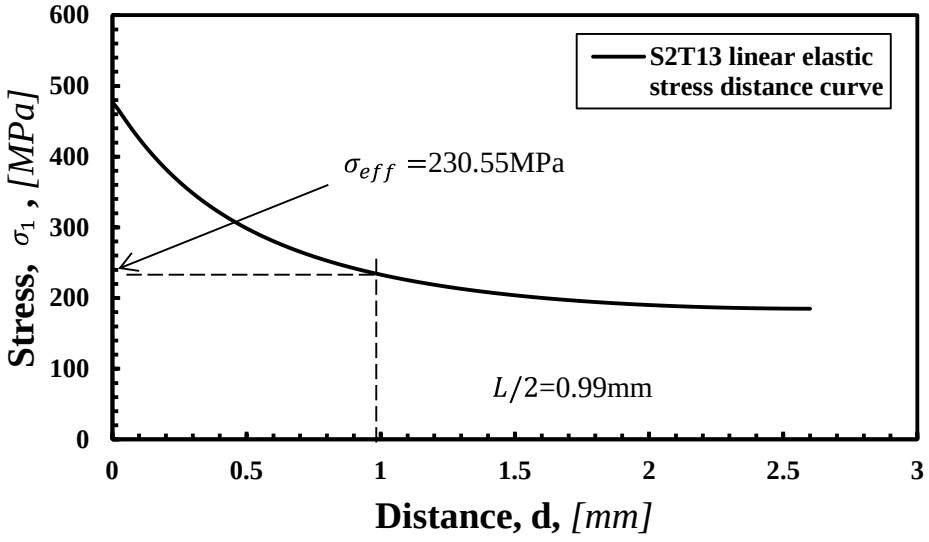

Figure A4. 14 Linear elastic stress distance curve of S2T11 in the incipient failure condition.

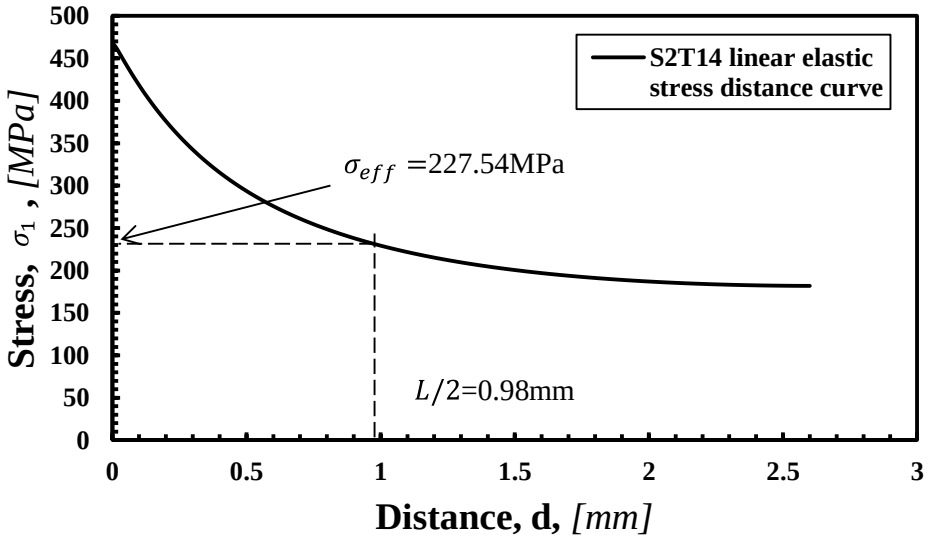

Figure A4. 15 Linear elastic stress distance curve of S2T11 in the incipient failure condition.

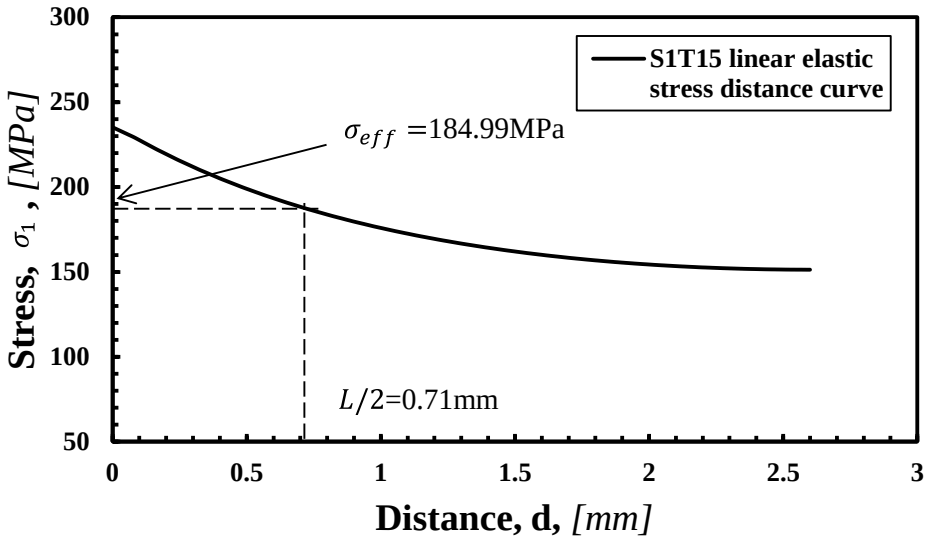

Figure A4. 16 Linear elastic stress distance curve of S2T11 in the incipient failure condition.

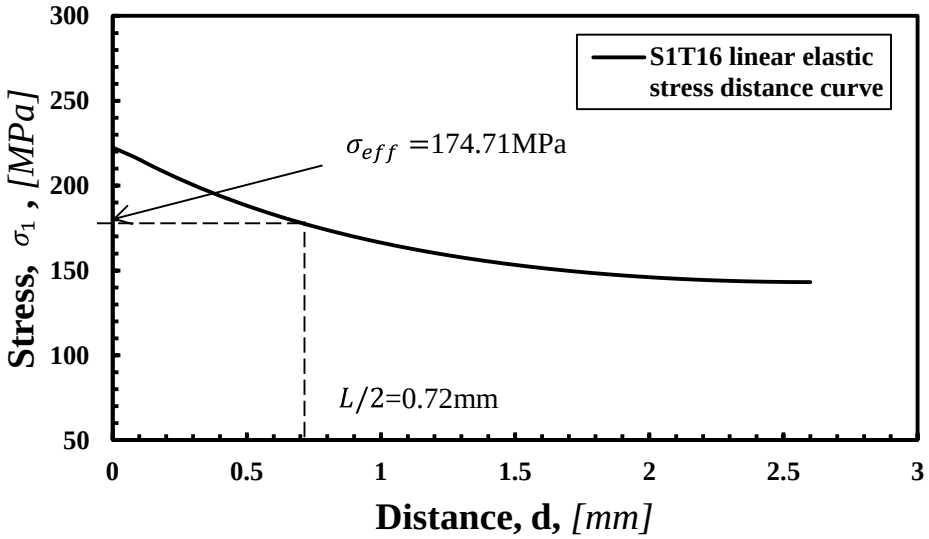

Figure A4. 17 Linear elastic stress distance curve of S2T11 in the incipient failure condition.

Appendix 5

A5.1 LS-DYNA keywords file explanation

The first input block is used to specify the keyword format, title and output format. The first line in the input file must be *KEYWORD, which indicates that the input file is in a keyword format rather than a structured format (Hallquist, 2007). After that, the title of the simulation and the output format are defined using the keywords *TITLE and *DATABASE_FORMAT respectively as shown in the following 1st block; the default LS-DYNA database format

(IFORM=0) and 64 bit format for binary output files (IBINARY=0) are selected for this keyword.

$ Define keyword format *1st block*

```
*KEYWORD
$ Define simulation title
*TITLE
Al6063-T5 cylindrical bar
$ Define the output format for binary files
*DATABASE_FORMAT
$ IFORM, IBINARY
      0,         0
```

In the second input block, the model geometry, mesh information and material parameters for the chosen material model are defined. Specifically, when using ANSYS/LS-DYNA software, the element and node coordinates are generated and described using the keywords *NODE and *ELEMENT_SHELL in the input file. For example, in keyword *NODE, NID, N1, N2, N3 indicate the identification number and coordinates of the nodes in the global coordinate system, and TC and RC mean translational and rotational constraints respectively. Through keyword *SECTION_SHELL (SECID=1, ELFORM=15, NIP=1), the element formulation, integration rule, nodal thickness and cross section properties can be defined. Furthermore, in this study, the mesh is created by using 2D, 4-node (SHELL), axisymmetric volume weighted solid elements (ELFORM=15) with reduced 1-point integration (NIP=1), hence, only half of the specimen was modelled (as Figure 5.1(c) shows). According to the theory manual, in LS-DYNA, a 2D axisymmetric geometry is defined in the X-Y plane, and the X-axis corresponds to the radial direction and the Y-axis is assumed to be the axis of symmetry. All nodes must have an X coordinate ≥ 0 (Hallquist, 2006). In the next step, Keyword *MAT is used to specify the material ID and corresponding parameters. As the tests were carried out at room temperature and the thermal effect was ignored, in this study, the Simplified Johnson–Cook material model was selected as the material constitutive law to model the rate sensitivity of Al6063-T5. The material model can be referenced by either a number or descriptive designation, which are

*MAT_SIMPLIFIED_JOHNSON_COOK or *MAT_98. Card 1 under this keyword defines the material ID (MID), density (RO), elastic modulus (E), Poisson's ratio (PR) and formulation for the rate effects (VP=1) for the tested material. Card 2 defines material parameters A, B, n, C and PSFAIL for the Simplified Johnson–Cook material model, where A indicates the material yield stress under quasi static loading, B and n are material constants modelling the work hardening effect, and C is the rate sensitivity of the material. The determination of these values will be discussed in the following sections in detail. Additionally, only one part (part ID PID=1) was used for the cylindrical bar which was defined by using the *PART keyword, the function of this keyword is to group all attributes of the part together, such as material information (MID=1) and section properties (SECID=1). Moreover, thermal properties and the flag for the part were set as default values (Hallquist, 2007).

$ Defines parts and groups all of the material information, section properties and hourglass type together. *2nd block*

```
*PART
$ Card 1 defines heading
$ HEADING
    S1T10
$ Card 2 combines material information, section properties and hourglass type etc.
$ PID, SECID, MID, EOSID, HGID, GRAV, ADPOPT, TMID
     1,      1,      1,      0,        0,        0,        0
$ Defines section properties for shell elements
*SECTION_SHELL
$ Card 1
$ SECID, ELFORM, SHRF, NIP, PROPT, QR/IRID, ICOMP, SETYP
     1,        15,       1,     1,        0,        0,        0,        3
$ Card 2
$ T1, T2, T3, T4, NLOC
```

```
  0,   0,  0,  0,   0
$ Defines material model
*MAT_SIMPLIFIED_JOHNSON_COOK (or *MAT_98)
$ Card 1
$ MID,  RO,      E,         PR,   VP
    1,  2700, 6.4E+10, 0.33,   1
$ Card 2
$      A,              B,              N,            C,          PSFAIL
 1.462E+08,  1.3E+08,        0.39,       0.02,      0.137556
$ Defines four-noded 2D axisymmetric solid elements
*ELEMENT_SHELL
$ EID,   PID,  N1,  N2,  N3,    N4
     1     1     1     3    341    340
     2     1     3     4    490    341
     3     1     4     5    639    490
     4     1     5     6    788    639
$ Define node IDs and coordinates
*NODE
$ NID,    X,     Y,     Z,   TC,    RC
    1,     0,     0,     0,    0,     0
```

The keywords in the third input block are used to define the boundary conditions and the time dependent load curves. The purpose of keyword *DEFINE_CURVE is to define two-column data, which indicate the time and the load applied to the top end of the specimen as shown in Figure 5.3. In card 1, a unique number has to be defined for the curve ID (LCID=1); the default values are used for the other parameters in this card. Card 2 is used to define the loading curve in the form of time versus displacement. A bi-linear time displacement curve was used in this

example. The real displacement history was also employed when running the simulations, and the results calculated from these two different loading histories will be discussed and compared in the final section of this chapter. Keyword *SET_NODE_LIST is used to select a group of nodes as a set. Keyword *BOUNDARY_PRESCRIBED_MOTION_SET here indicates that the displacement time curve (LCID=1) is imposed on a nodal set 1 (SID=1) in the Y-direction. In keyword *BOUNDARY_SPC_SET, single point constraints can be applied to a single node or a set of nodes. In this case, all of the degrees of freedom are constrained at the bottom end of the specimen.

```
$ Define a displacement history curve                                    3rd block

*DEFINE_CURVE

$ Card 1

$ LCID, SIRD, SFA, SFO, OFFA, OFFO, DATTYP

     1,      0,     1,     1,     0,         0

$ Card 2, 3, 4, define displacement history

$       TIME,                    DISPLACEMENT

0.000000000000E+00 0.000000000000E+00

8.000000000000E-03  4.816000000000E-03

10.00000000000E-03  4.816000000000E-03

$ Define nodal set 1

*SET_NODE_LIST

$ Card 1

$ SID, DA1, DA2, DA3, DA4

    1,    0,     0,      0,    0                                    3rd Continue

$ Card 2, 3, define node list

     6852     7001     7002     7003     7004     7005     7006     7007

     7008     7009     7010     7011     7012     7013     7014     7015
```

```
$ Define an imposed nodal motion (velocity, acceleration, or displacement) on a set of nodes.
*BOUNDARY_PRESCRIBED_MOTION_SET
$ typeID, DOF, VAD, LCID, SF, VID, DEATH, BIRTH
      1,      2,      2,      1,    1,    0,        0,       0
$ Define nodal set 2
*SET_NODE_LIST
      2    0.000    0.000    0.000    0.000
$ Define nodal set constraints
*BOUNDARY_SPC_SET
$ NID/NSID, CID, DOFX, DOFY, DOFZ, DOFRX, DOFRY, DOFRZ
      2,          0,      1,      1,      1,        1,        1,          1
```

The energy dissipation options, solution control and output parameters are defined in the fourth block. In more detail, the energy dissipation options card *CONTROL_ENERGY is employed to define the hourglass energy, rigidwall energy, sliding interface energy dissipation and Rayleigh energy dissipation. In this study, all of the energy dissipations were computed and included in the energy balance. Keyword *CONTROL_SHELL is used to define the section properties for the shell elements; the shell formulation defined in *SECTION_SHELL can be overridden by THEORY in this keyword. Keyword *CONTROL_TERMINATION must be used to designate the ending time for the calculation. The interval for the reporting of results will be defined through the keyword *DATABASE. As an example, the keyword *DATABASE_BINARY_D3PLOT defines a results database for the entire model, whilst, *DATABASE_BINARY_D3THDT indicates the time interval for a database containing time histories for subsets of elements and nodes. Selected element and nodal results are included in an ASCII file as defined by the keywords *DATABASE_ELOUT and *DATABASE_NODOUT respectively. We can only define much smaller output time steps for the element or nodal results in which we are interested. Keyword *DATABASE_HISTORY controls which node or element results are output into the ASCII file NODOUT and ELOUT.

```
$ Provide controls for energy dissipation options
```
4th block

```
*CONTROL_ENERGY
$ Provide controls for energy dissipation options
$ HGEN, RWEN, SLNTEN, RYLEN
      2,         2,          2,         2
$ Provide controls for computing shell response
*CONTROL_SHELL
$ WRPANG, ESORT, IRNXX, ISTUPD, THEORY
         20,          1,        -1,          1,          15
*CONTROL_TIMESTEP
0, 0.9, 0, 0, 0
*CONTROL_TERMINATION
0.010E+00, 0, 0, 0, 0
$
*DATABASE_NODOUT
0.1000E-05
*DATABASE_ELOUT
0.1000E-05
*DATABASE_GLSTAT
0.1000E-05
*DATABASE_MATSUM
0.1000E-05
*DATABASE_HISTORY_NODE                                    4th Continue
       1       2       3       4       5       6       7       8
*DATABASE_HISTORY_SHELL
```

```
      1       2       3       4       5       6       7       8

*DATABASE_BINARY_D3PLOT

0.1000E-04

*DATABASE_BINARY_D3THDT

0.1000E-04

*DATABASE_EXTENT_BINARY

      0       0       3       1       0       0       0       0

      0       0       4       0       0       0

*END
```

Finally, at the end of the input file, keyword *END must be typed to indicate the end of the input process. In the next section, we will make a change to this keyword file to do the mesh convergence study in order to find the most suitable meshes for the investigated geometries.

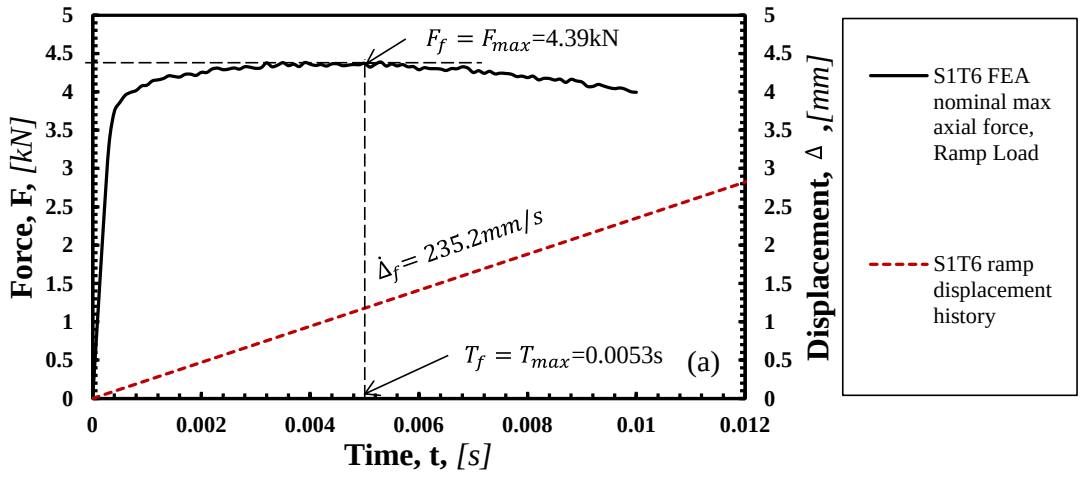

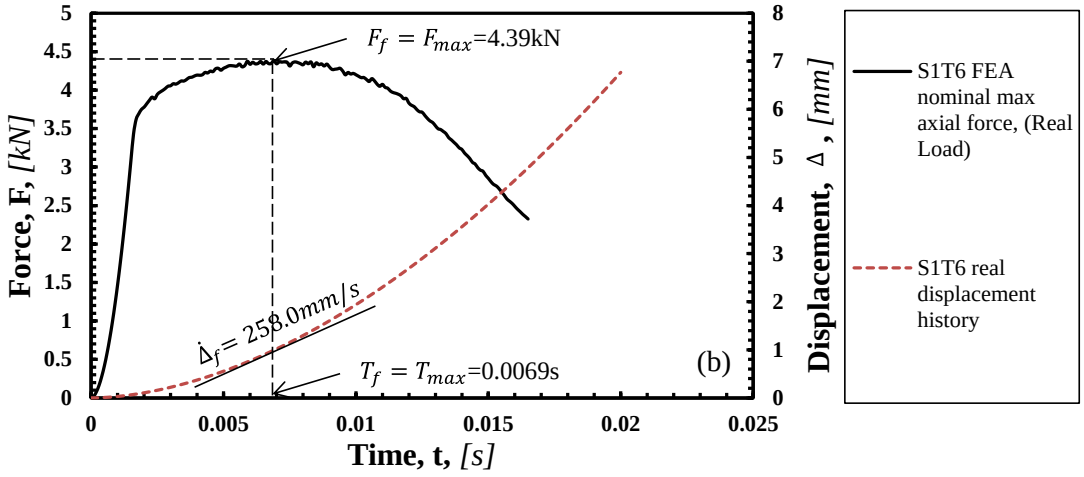

Figure A5. 1 S1T6 Force time histories corresponding to (a) ramped displacement history and (b) real displacement load.

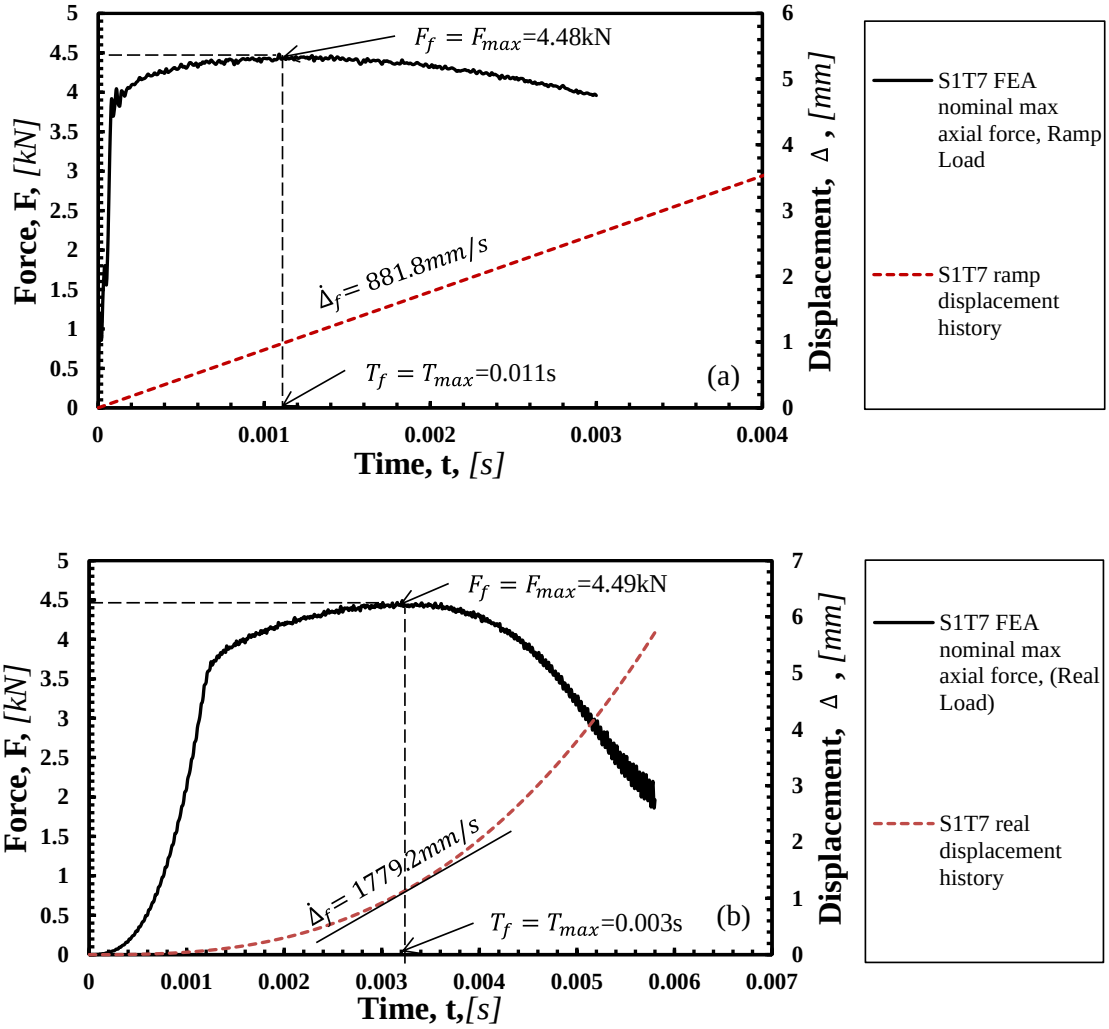

Figure A5. 2 Force time histories corresponding to (a) ramped displacement history and (b) real displacement load.

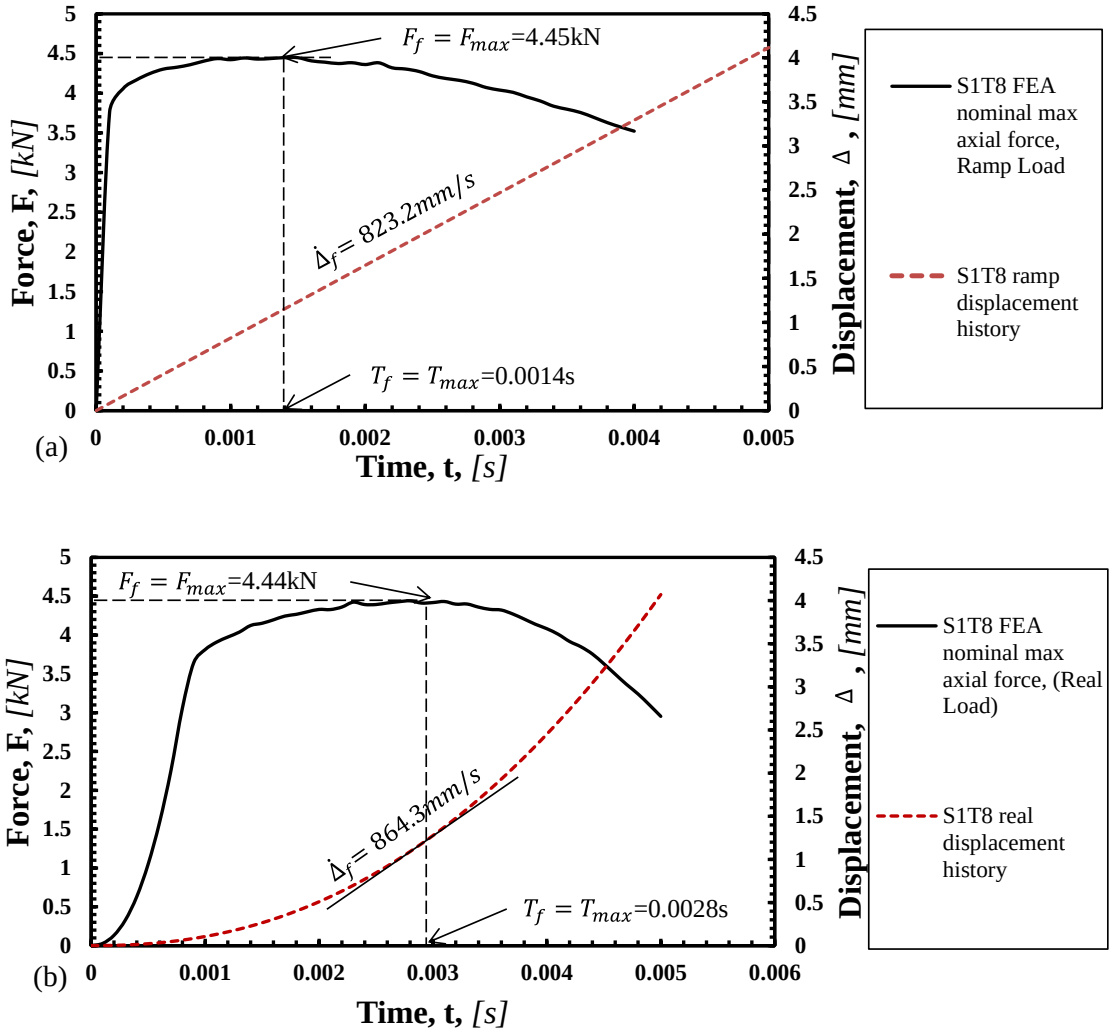

Figure A5. 3 S1T8 Force time histories corresponding to (a) ramped displacement history and (b) real displacement load.

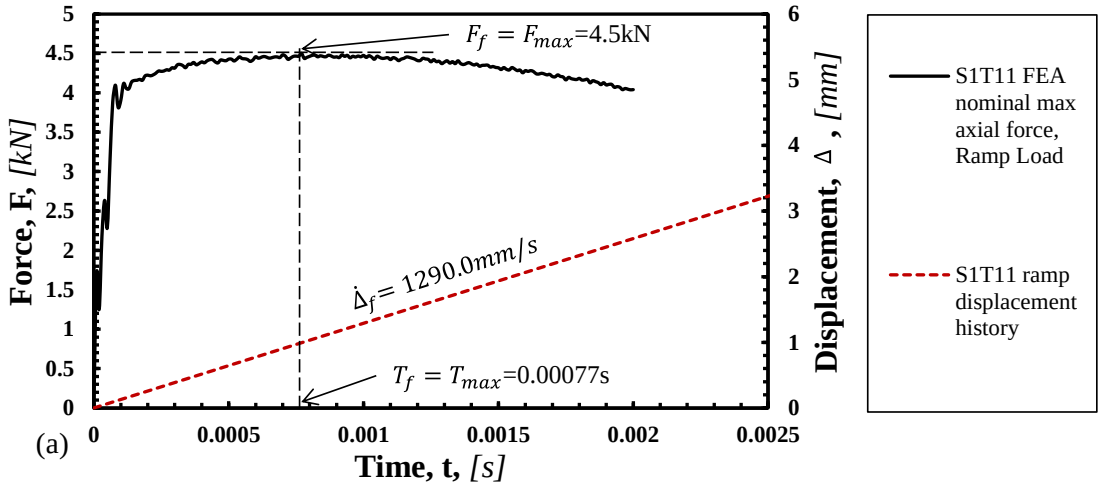

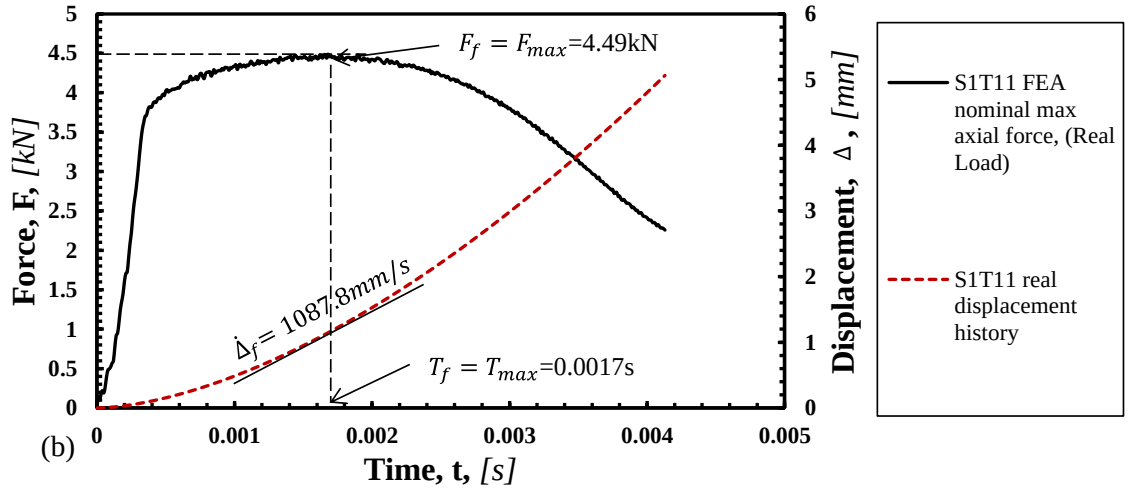

Figure A5. 4 Force time histories corresponding to (a) ramped displacement history and (b) real displacement load.

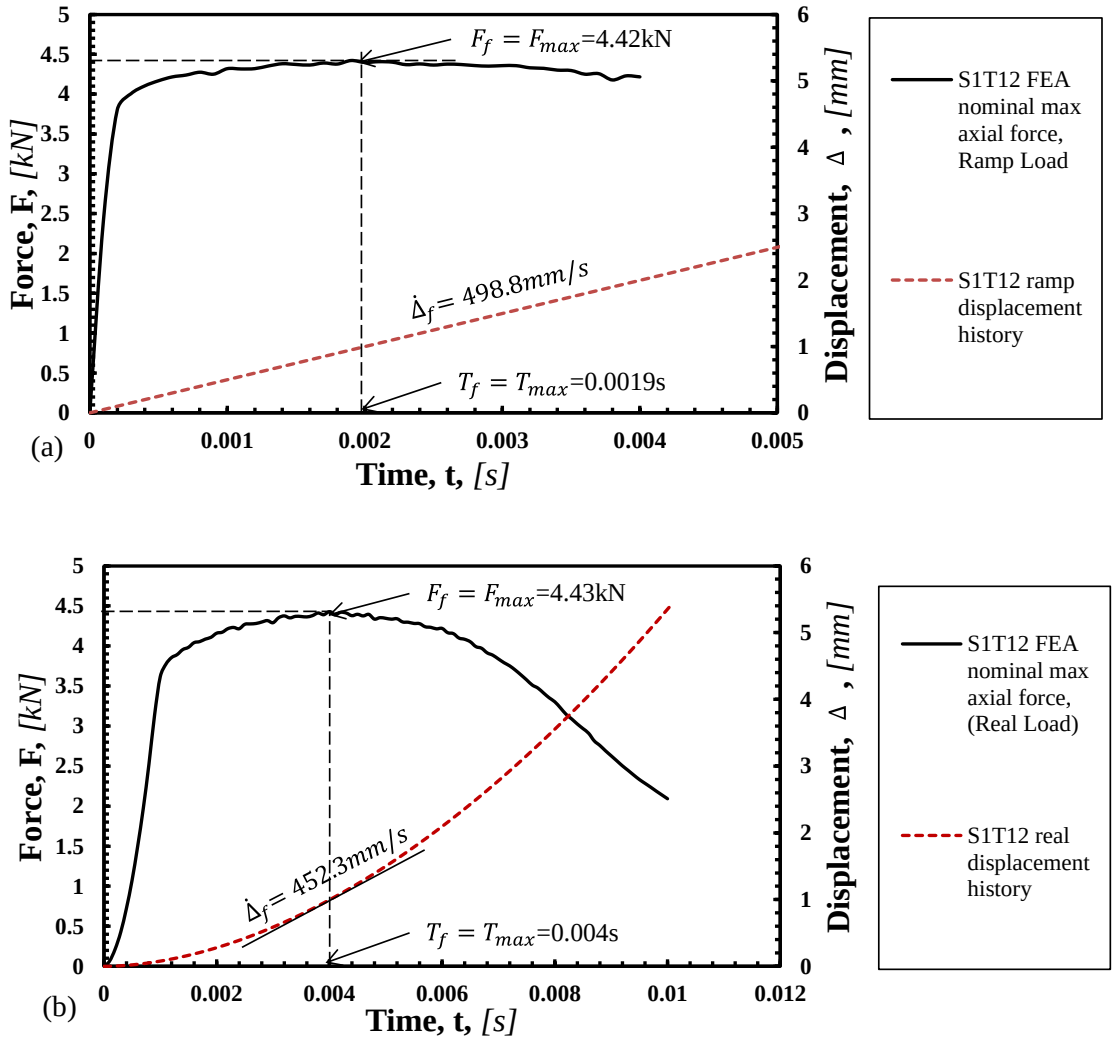

Figure A5. 5 S1T12 Force time histories corresponding to (a) ramped displacement history and (b) real displacement load.

Appendix 6

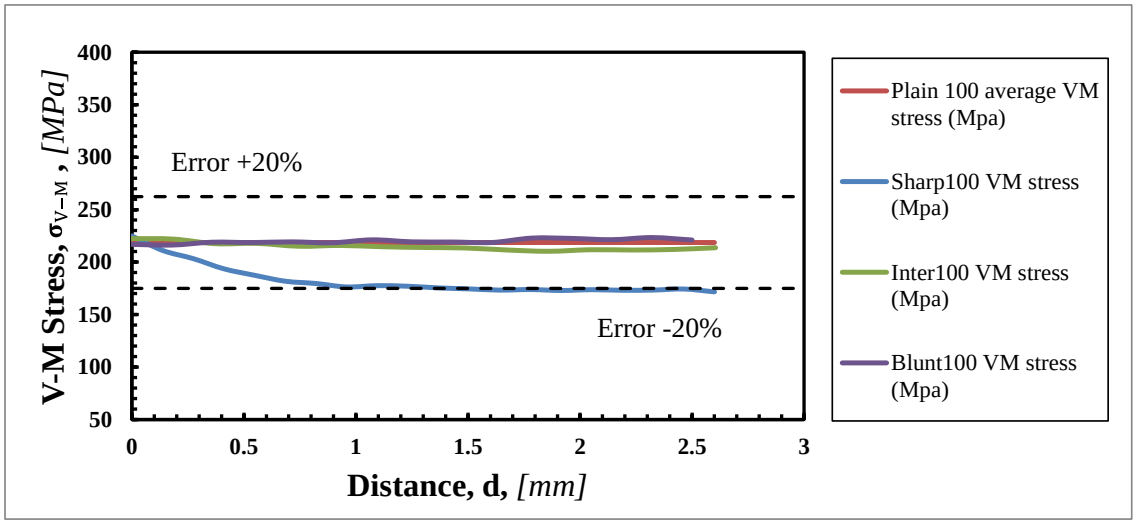

Figure A6. 1 Von Mises stress vs distance curves at the time of crack initiation for displacement rates $\dot{\Delta}= 100mm \cdot s^{-1}$.

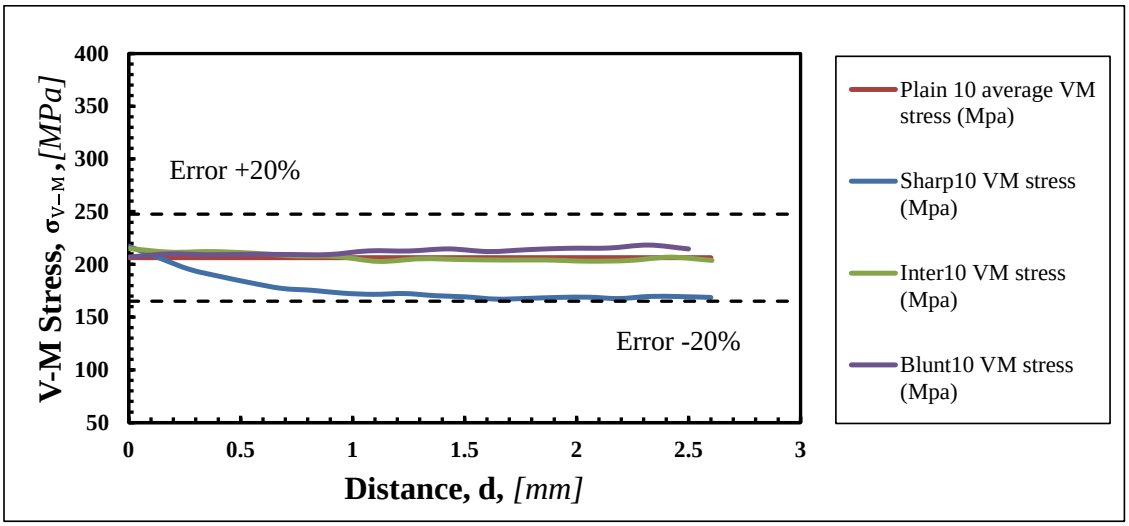

Figure A6. 2 Von Mises stress vs distance curves at the time of crack initiation for displacement rates $\dot{\Delta}= 10\text{mm} \cdot \text{s}^{-1}$.

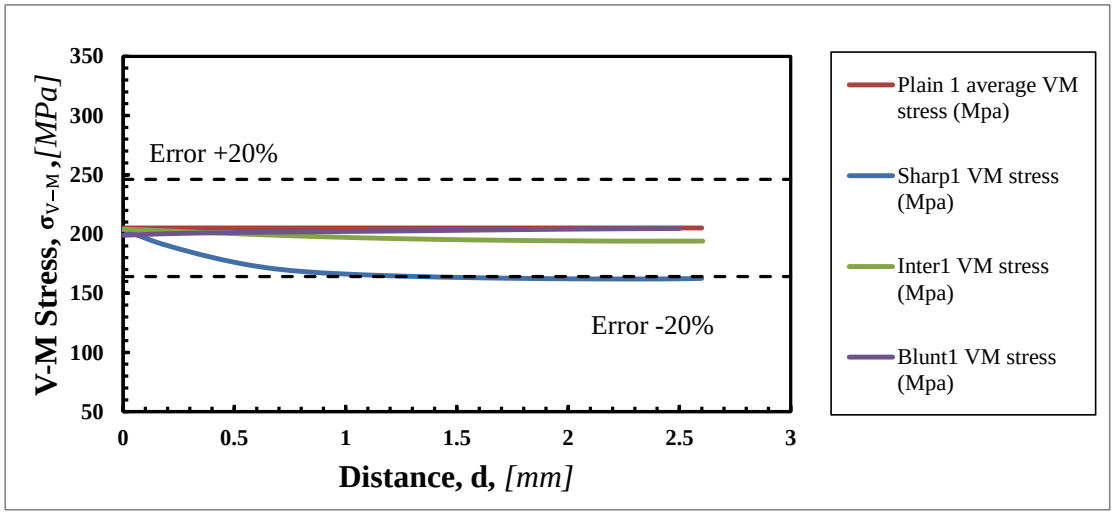

Figure A6. 3 Von Mises stress vs distance curves at the time of crack initiation for displacement rates $\dot{\Delta} = 1\text{mm} \cdot \text{s}^{-1}$.

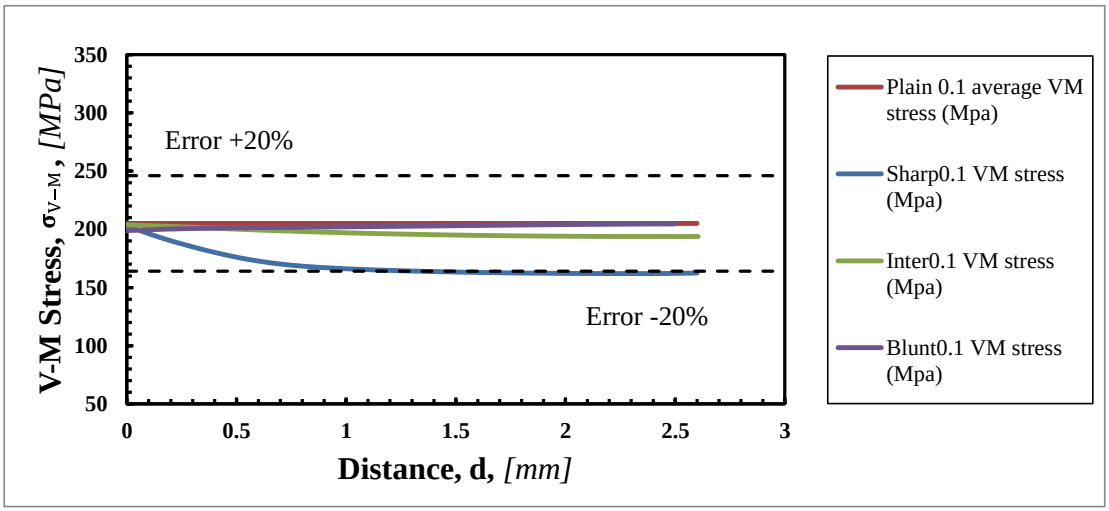

Figure A6. 4 Von Mises stress vs distance curves at the time of crack initiation for displacement rates $\dot{\Delta} = 0.1\text{mm} \cdot \text{s}^{-1}$.

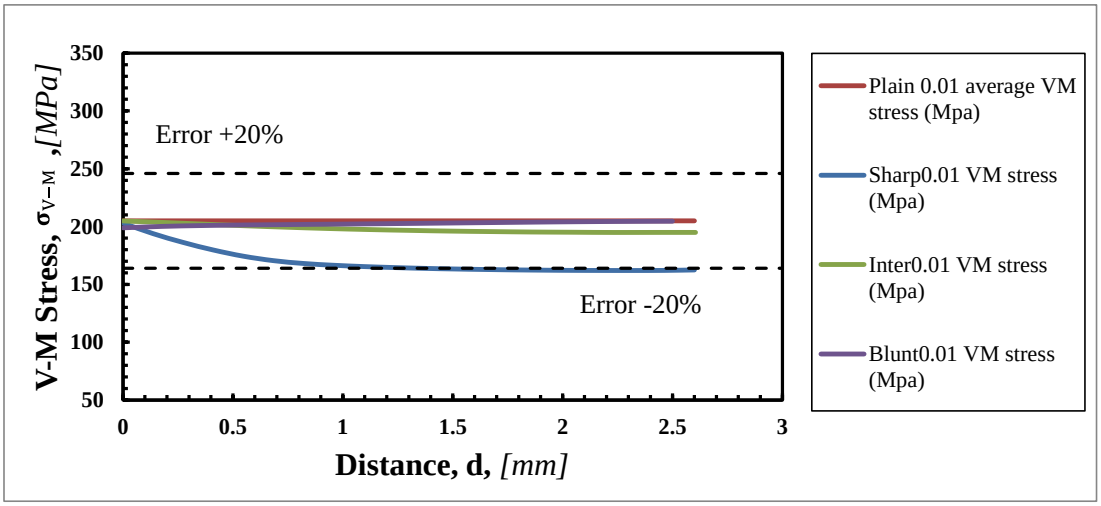

Figure A6. 5 Von Mises stress vs distance curves at the time of crack initiation for displacement rates $\dot{\Delta} = 0.01\text{mm} \cdot \text{s}^{-1}$.

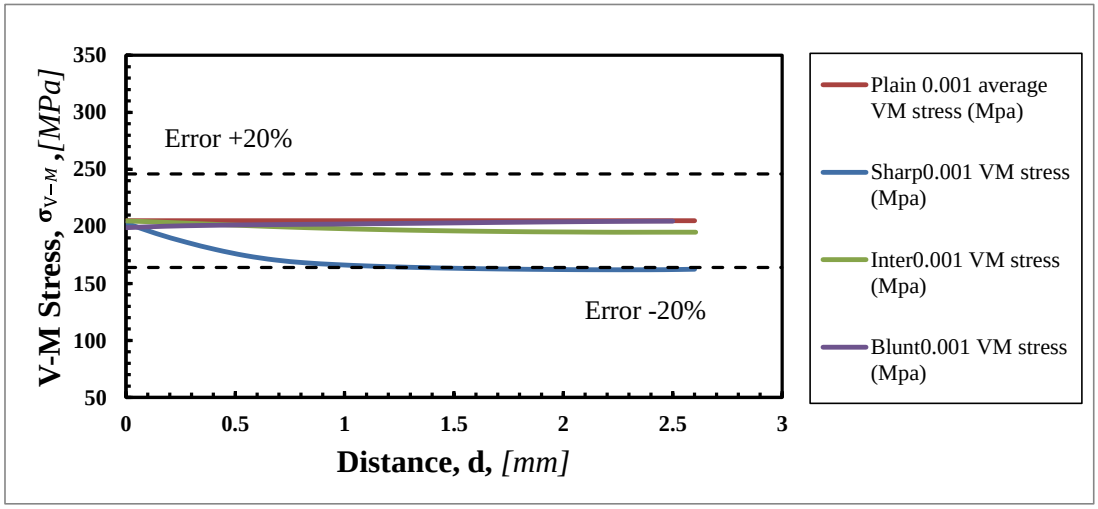

Figure A6. 6 Von Mises stress vs distance curves at the time of crack initiation for displacement rates $\dot{\Delta} = 0.001\text{mm} \cdot \text{s}^{-1}$.

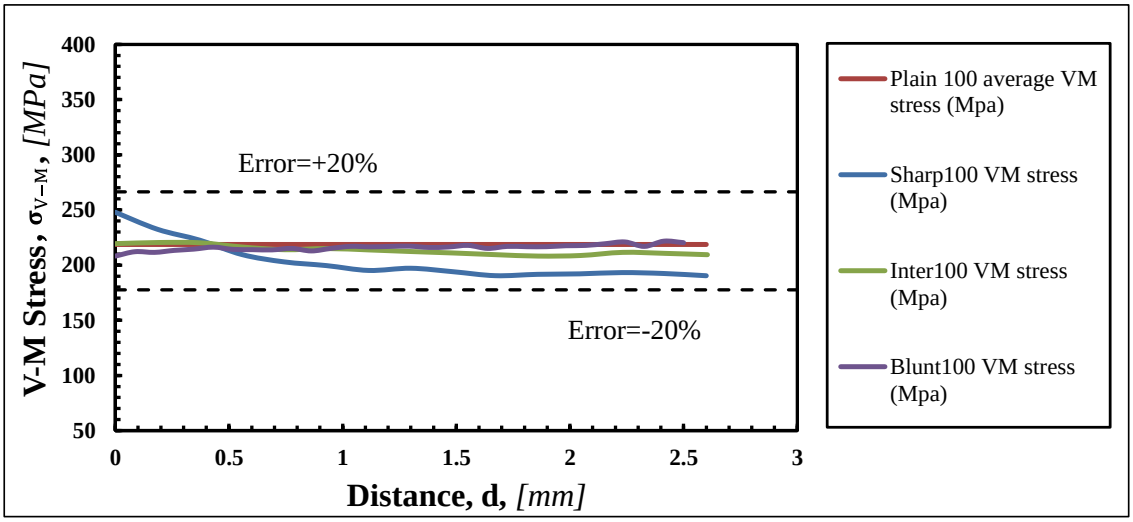

Figure A6. 7 Elasto-plastic Von Mises stress vs distance curves at the time of maximum force with displacement rates $\dot{\Delta}= 100mm \cdot s^{-1}$.

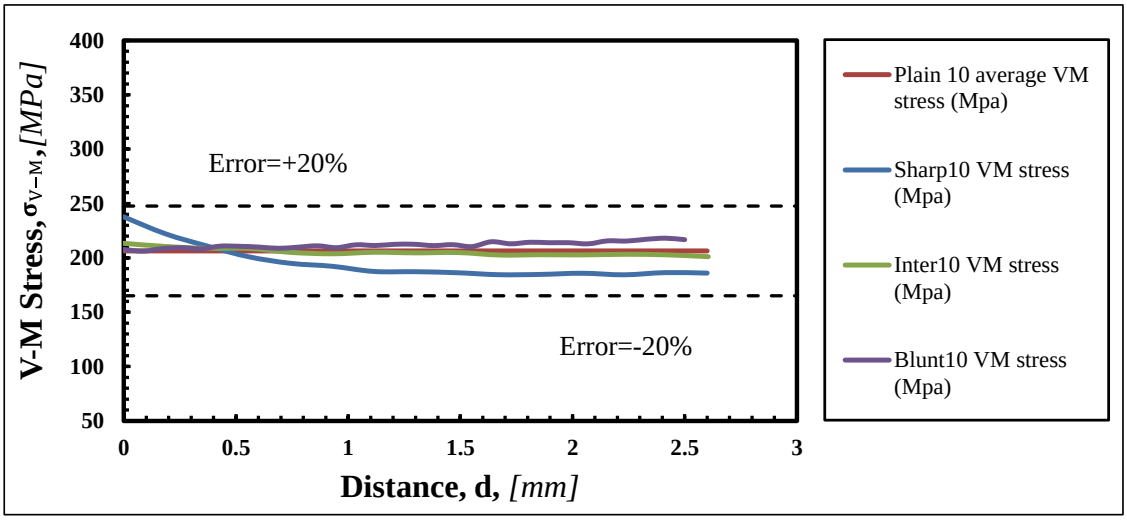

Figure A6. 8 Elasto-plastic Von Mises stress vs distance curves at the time of maximum force with displacement rates $\dot{\Delta}= 10\text{mm} \cdot \text{s}^{-1}$.

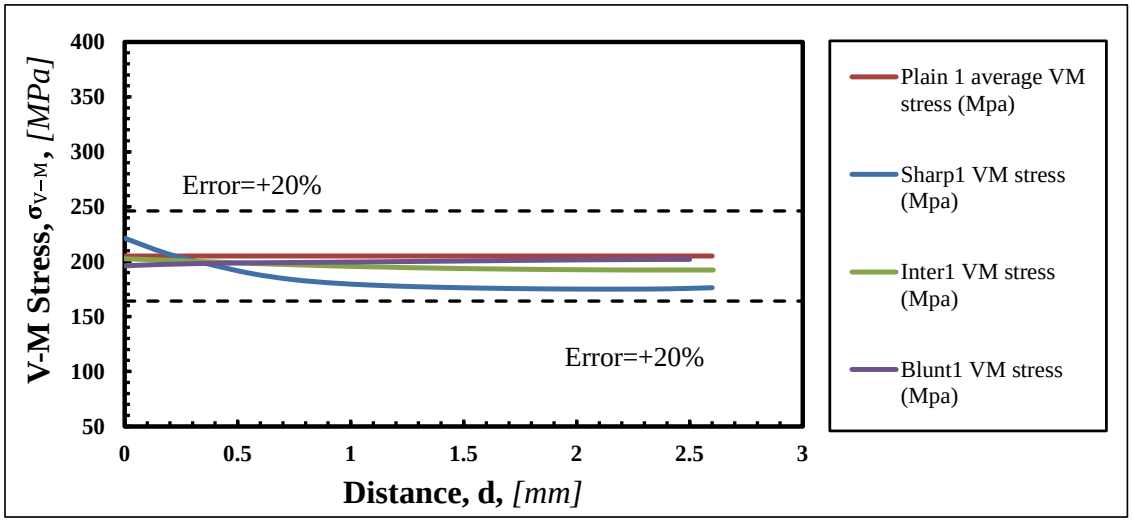

Figure A6. 9 Elasto-plastic Von Mises stress vs distance curves at the time of maximum force with displacement rates $\dot{\Delta} = 1\text{mm} \cdot \text{s}^{-1}$.

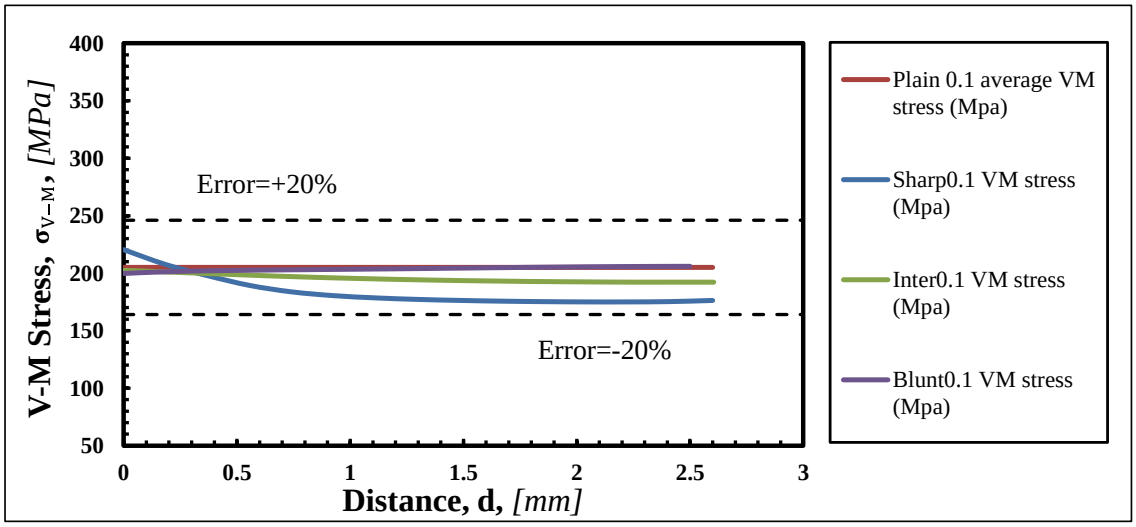

Figure A6. 10 Elasto-plastic Von Mises stress vs distance curves at the time of maximum force with displacement rates $\dot{\Delta} = 0.1\text{mm} \cdot \text{s}^{-1}$.

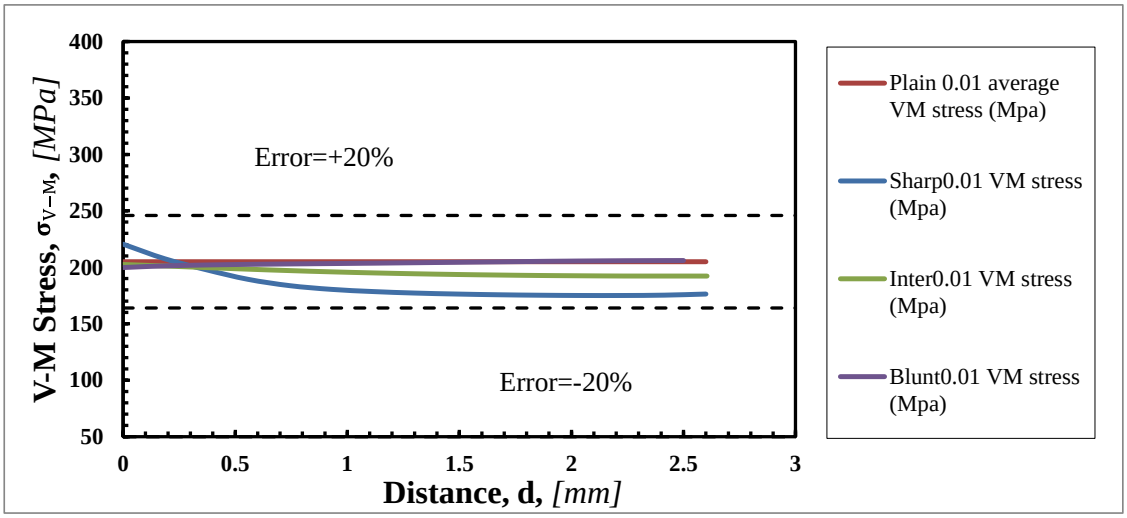

Figure A6. 11 Elasto-plastic Von Mises stress vs distance curves at the time of maximum force with displacement rates $\dot{\Delta} = 0.01\text{mm} \cdot \text{s}^{-1}$.

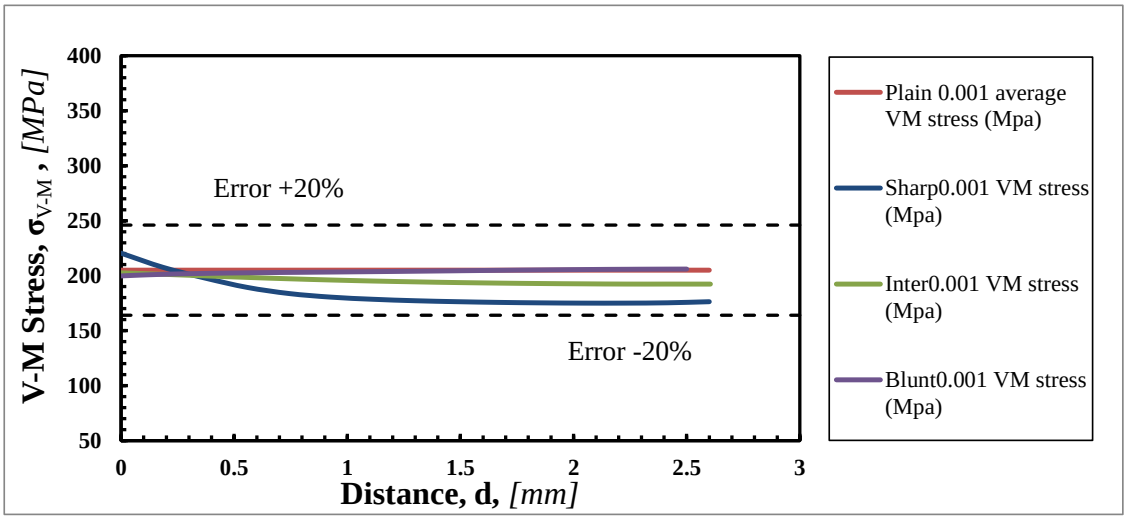

Figure A6. 12 Elasto-plastic Von Mises stress vs distance curves at the time of maximum force with displacement rates $\dot{\Delta} = 0.001\text{mm} \cdot \text{s}^{-1}$.